Relaxation of quasiparticles injected above the Fermi sea of a Quantum Hall edge channel

Ramiro H. Rodriguez

université PARIS-SACLAY

NNT : 2019SACLS063

Thèse de doctorat

Relaxation of Quasiparticles Injected Above the Fermi Sea of a Quantum Hall Edge Channel

Thèse de doctorat de l'Université Paris-Saclay
préparée à l'Université Paris-Sud

Ecole doctorale n°564 Physique en Île-de-France (EDPIF)
Spécialité de doctorat: Physique

Thèse présentée et soutenue à Gif-Sur-Yvette, le 28 Février 2019, par

RAMIRO H. RODRIGUEZ

Composition du Jury :

Gwendal Fève Professeur des Universités, Université Pierre et Marie Curie (Laboratoire Pierre Aigrain)	Président
Christopher Bäuerle Directeur de recherche, Université Grenoble Alpes (Institut Néel)	Rapporteur
Jérôme Rech Chargé de recherche, Aix-Marseille Université (Centre de Physique Théorique)	Rapporteur
Anne Anthore Maîtresse de Conférences, Université Paris-Diderot – Université Paris-Saclay (Centre de Nanosciences et de Nanotechnologie)	Examinatrice
Thomas Ihn Professeur, ETH Zurich (Department of Physics)	Examinateur
Patrice Roche Directeur de Recherche, CEA Saclay (Service de Physique de l'Etat Condensé)	Directeur de thèse
François Parmentier Chargé de Recherche, CEA Saclay (Service de Physique de l'Etat Condensé)	Co-directeur de thèse

To my loved brothers

To my dear parents

Acknowledgments

The whole PhD project was to me, no doubts, a unique experience which I deeply value for how it enriched my appreciation of things. With few but honest words, I would like to thank to the people who, in different ways, were next to me with their support throughout the duration of this project. They made it possible to overcome the difficulties and to prosperously arrive at the last phase of this scientific and personal adventure.

I would like to express my deepest gratitude to Patrice Roche and Francois Parmentier for their guidance all along this thesis. I realize that their critic and constructive opinions in our discussions have influenced in many ways my scientific thinking for the best. Patrice, I'm extremely grateful to you for your belief, your patience and attention to my opinions since our first discussions, even when language was an unavoidable barrier. You gave me the tools, the space and the time to explore with freedom my ideas making the everyday life in the lab and the experience of "being a scientist" very enjoyable to me. François, I honestly appreciate very much your constant motivation, support and encouragement. Your advises, your teachings and the great amount of assistance you provided to me have been essential for the successful completion of this thesis. I am certainly very glad that I had the opportunity to be part of this project under your combined advise. Science has never been so exciting like during these three years, I really had a great time and a lot of fun being part of your team.

I would like to extend my sincere thanks to the rest of the Nanoelectronic group for welcoming as a PhD student. I found a very kind and stimulating atmosphere in the lab, where discussions and debates are always enlightening moments for the students. Special thanks to Patrice Jacques and also to the Cryogenic group for all the technical assistance during this period.

I also wish to thank to the Quantronic group for the continuous and fruitful exchange of ideas and for all the invitations to share a cake whenever there was something to be celebrated. In particular I would like to thank to Cristián Urbina, Marcelo Goffman and Leandro Tosi who were the ones who first opened the door of their labs and their homes to welcome me when I first arrived in Europe back in 2015.

Finally, I would like to write some words to my friends. Many thanks to my PhD fellows, with which I have been sharing most of my days, between coffees and all type of

discussions. Special thanks to Maëlle, who started her PhD the same year than me and who was always up to give me a hand with the bureaucracy at the university. Maëlle, I very much appreciate your friendship, your empathy and all your tips that made me progress in my french. No questions that "friendship" came to have a huge meaning to me after these years away from home. This is why I could not finish this words without expressing my deepest gratitude to the small group of close argentine friends who has been a heartwarming and uplifting family here. I will always be grateful for your invaluable support and for your unconditional company.

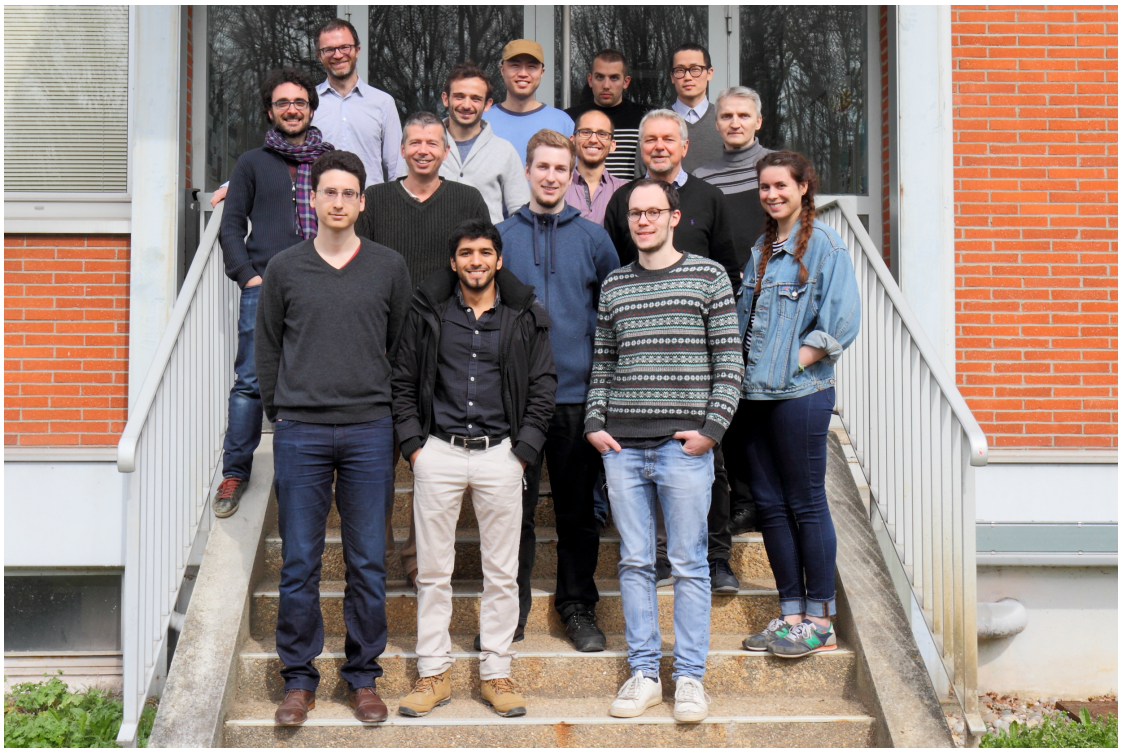

Nanoelectronics Group in 2017. From left to right, ***Top row:*** Fabien Portier, Preden Roulleau, Myunglae Jo, Matthieu Santin, Minky Seo; ***Middle row:*** Carles Altimiras, Patrice Roche, Mueller Jonas, François Parmentier, Christian Glattli, Patrice Jacques; ***Bottom row:*** Ambroise Peugeot, Ramiro Rodriguez, Paul Brasseur and Maëlle Kapfer. Also Zubair Iftikhar, Imen Taktak and Iouri Moukharski, who were not present at the moment of the picture.

Acronyms

2DEG ..... 2-Dimensional Electron Gas
EC ..... Edge channel
FS ..... Fermi Sea
HOM ..... Hong-Ou-Mandel
IQHE ..... Integer Quantum Hall effect
LL ..... Landau Level
MZI ..... Mach-Zehnder Interferometer
QD ..... Quantum Dot
QPC ..... Quantum Point Contact

Content

Abstract

The one-dimensional, chiral and dissipationless edge channels of the quantum Hall effect form the electrical analogue of optical fibers, allowing the implementation of electron quantum optics experiments where one coherently manipulates the trajectories of single electronic wave packets [i]. A recent series of experimental and theoretical works have put into light strong effects of decoherence and energy relaxation caused by interactions with quasiparticles present in neighboring edge channels, capacitively coupled to the edge channel in which the experiment is performed [ii, iii]. This coupling leads to new eigenstates challenging the usual representation of excitations in the quantum Hall effect.

We have experimentally investigated the energy relaxation of electrons emitted at a well-defined energy in a quantum Hall edge channel, in presence of a second edge channel co-propagating along the former. Our setup relies on a pair of electrostatically defined quantum dots, used as energy-resolved emitter and detector. The emitter is realized by applying a finite drain-source voltage on the first quantum dot, with a single resonant level in the bias window, the position of which sets the energy at which electrons are emitted above the drain Fermi energy. After a tunable propagation length in the micrometer scale, we perform an energy spectroscopy of the emitted electrons using the second quantum dot as an energy filter [iv]. This detection technique was previously used to characterize the energy relaxation for an out-of-equilibrium energy distribution of electrons generated in a quantum point contact [v].

Our results, obtained at filling factor 2 of the quantum Hall effect, show that although the propagation over submicron lengths leads to sizable energy relaxation, a small portion of quasiparticles are not affected by energy relaxation even at relatively high energies, up to 150 μeV. Additionally, we investigated simultaneously the charge current and the heat current propagating in the edge channel while relaxation takes place. Surprisingly, we observe that the amount of energy lost during propagation is markedly larger than expected [vi], suggesting that relaxation mechanisms towards external degrees of freedom play an important unexpected role in electron quantum optics experiments.

Furthermore, we have experimentally demonstrated that the relaxation of the quasiparticle peak injected in the outer edge channel can be strongly suppressed by decou-

pling the edge channel of the neighboring inner co-propagating edge channel. Clear signatures of a reduced relaxation rate have been observed both in the decaying amplitude of the quasiparticle peak and in the amount of energy leaking out of the edge channel.

To conclude, in this experiment we captured the limitations imposed by the energy relaxation in quantum Hall edge channels and circumvent them by considerably extending the lifetime of finite energy excitations.

[i] E. Bocquillon, et al., Annalen der Physik 526, 1 (2014).
[ii] I. Levkivskyi, et al., PRB 85, 075309 (2012).
[iii] E. Bocquillon, et al., Nat. Commun. 4, 1839 (2013).
[iv] C. Altimiras, et al., Nature Physics 6, 34 (2009).
[v] H. le Sueur, et al., PRL 105, 056803 (2010).
[vi] C. Grenier et al, Mod. Phys. Lett. B 25, 1053 (2011).

Keywords: RELAXATION, SPECTROSCOPY, EDGE CHANNEL, QUANTUM HALL EFFECT, QUANTUM DOTS

Résumé

Les canaux de bord unidimensionnels et chiraux de l'effet Hall quantique forment l'analogue électrique des fibres optiques, permettant la réalisation d'expériences d'optique quantique électronique où l'on manipule de manière cohérente les trajectoires de paquets d'ondes électroniques uniques [i]. Une série récente de travaux expérimentaux et théoriques a mis en lumière de forts effets de décohérence et de relaxation en énergie provoqués par des interactions avec des quasiparticules présentes dans des canaux voisins, couplés capacitivement au canal dans lequel l'expérience est réalisée [ii, iii]. Ce couplage conduit à des nouveaux états propres du transport rendant caduque la représentation habituelle des excitations dans l'effet Hall quantique.

Nous avons étudié expérimentalement la relaxation en énergie d'électrons émis à une énergie bien définie dans un canal de bord de l'effet Hall quantique, en présence d'un second canal de bord co-propageant le long du premier. Notre méthode repose sur une paire de boites quantiques electrostatiquement définies, utilisées comme émetteur et détecteur à énergie résolue. L'émetteur est réalisé en appliquant une tension de drain-source finie sur la première boite quantique, avec un seul niveau discret dans la fenêtre de transport, dont la position définit l'énergie à laquelle les électrons sont émis au-dessus de l'énergie de Fermi du drain. Après une longueur de propagation ajustable à l'échelle micrométrique, nous effectuons une spectroscopie des électrons émis en utilisant la deuxième boite quantique [iv]. Cette technique de détection a déjà été utilisée pour caractériser la relaxation en énergie pour une distribution électronique hors d'équilibre générés dans un contact ponctuel quantique [v].

Nos résultats, obtenus au facteur de remplissage 2 de l'effet Hall quantique, montrent que même si la propagation sur des longueurs submicroniques conduit à une relaxation en énergie importante, une petite partie des quasiparticules ne sont pas affectées par la relaxation, même à des énergies relativement élevées, jusqu' à 150 μeV. De plus, nous avons étudié simultanément le courant de charge et le courant de chaleur se propageant dans le canal de bord pendant que la relaxation a lieu. Étonnamment, nous observons que la quantité d'énergie perdue pendant la propagation est nettement plus importante que prévu [vi], ce qui suggère que les mécanismes de relaxation vers des degrés de liberté externes jouent un rôle inattendu et important dans les expériences d'optique quantique électronique.

Nous avons en outre démontré expérimentalement que la relaxation du pic des quasiparticules injecté dans le canal de bord extérieur peut être fortement supprimée en découplant le canal de bord du canal de bord voisin interne. Des signes évidents d'un taux de relaxation réduit ont été observés tant dans l'évolution de l'amplitude du pic des quasiparticules que dans la quantité d'énergie s'échappant du canal de bord.

En conclusion, dans cette expérience, nous avons capturé les limitations imposées par la relaxation en énergie dans les canaux de bord de l'effet Hall quantique et nous les circonvenons en prolongeant considérablement la durée de vie des excitations à énergie finie.

[i] E. Bocquillon, et al., Annalen der Physik 526, 1 (2014).
[ii] I. Levkivskyi, et al., PRB 85, 075309 (2012).
[iii] E. Bocquillon, et al., Nat. Commun. 4, 1839 (2013).
[iv] C. Altimiras, et al., Nature Physics 6, 34 (2009).
[v] H. le Sueur, et al., PRL 105, 056803 (2010).
[vi] C. Grenier et al, Mod. Phys. Lett. B 25, 1053 (2011).

Mots Clés: RELAXATION, SPECTROSCOPIE, ÉTATS DE BORD, L'EFFET HALL QUANTIQUE, BOITE QUANTIQUES

Chapter 1

Introduction (French)

Ce chapitre est un résumé des investigations menées au cours de cette thèse. La première partie présente le contexte général du transport électronique mésoscopique. Je décris brièvement l'effet Hall quantique et les propriétés des canaux de bord. Elle est suivie d'une discussion sur les mécanismes de décohérence et de relaxation qui peuvent avoir lieu dans ce régime et comment ces processus ont été étudiés expérimentalement dans le cadre de l'optique quantique électronique. Plusieurs observations inattendues sur ces expériences ainsi que quelques questions ouvertes au niveau le plus fondamental sur les différents modèles théoriques ont motivé ce travail. Dans ce qui suit, je présente l'expérience dont nous avons réalisé une spectroscopie à énergie résolue de la relaxation des quasiparticules dans un canal de bord de l'effet Hall quantique. Enfin, je discute des principaux résultats et observations de cette expérience au cours de laquelle le pic de quasiparticules a été mesuré directement pour la première fois dans un canal de bord chiral unidimensionnel.

1.1 Transport mésoscopique dans les semiconducteurs

Les semiconducteurs sont des systèmes fascinants pour étudier le transport électronique dans la matière condensée. Une des raisons est qu'il est possible de fabriquer ces matériaux avec un haut niveau de contrôle de la pureté et du désordre de la structure cristalline. Ainsi, plusieurs de leurs propriétés électroniques intrinsèques peuvent être conçues à la demande. Une autre raison est qu'il existe déjà une technologie très mature pour réduire les dimensions de ces systèmes jusqu'à l'échelle nanométrique où une description quantique est nécessaire puisque la théorie classique du transport commence à échouer. Ces degrés de tunabilité ouvrent la voie à l'exploration du transport électronique dans une grande variété de régimes.

En particulier, dans les gaz électroniques bidimensionnels (2DEG) obtenus dans les hétérostructures semiconductrices, la densité des électrons, typiquement de l'ordre

de $n_s \sim 10^{11}$ cm^{-2}, est suffisamment faible pour que les interactions ne puissent être efficacement criblées mais suffisamment élevées pour mettre ces interactions en jeu, de manière non négligeable, en provoquant de fortes corrélations quantiques entre les particules. De plus, la mobilité elevé obtenue sur ces systèmes, typiquement de l'ordre de $\mu_\tau \sim 10^6$ cm^2/Vs, permet de concevoir des dispositifs électroniques avec des dimensions inférieures à certaines des échelles de longueur caractéristiques du transport électronique, telles que: le *longueur élastique* l_e où les particules se propagent sans perte d'énergie, le *libre parcours moyenne* $\bar{l}$ où les particules se propagent de façon balistique sans avoir des collisions ou même la longueur de cohérence l_φ qui définit la distance à laquelle elles maintiennent la phase liée à leur nature ondulatoire. Par conséquent, les signatures du caractère quantique du transport électronique se reflètent sur des quantités macroscopiques mesurables telles que le courant et la résistance. Ce régime est mieux connu sous le nom de régime de transport mésoscopique.

Dans le gaz d'électron bidimensionnel (2DEG) à base de GaAs/AlGaAs, de nombreux phénomènes mésoscopiques caractéristiques ont été observés. Par exemple la quantification de la conductance dans un régime balistique [1, 2, 3] ; l'effet du blocage de Coulomb dans des systèmes très confinés comme les boîtes quantiques et l'interférence quantique des ondes electroniques comme dans l'effet Aharonov-Bohm observé sur des systèmes en géométrie annulaire [6, 7] ou l'effet de localisation faible observé dans des systèmes désordonnés [8]. ***L'effet Hall quantique entier*** [9], qui est observé lorsqu'un 2DEG est sous un fort champ magnétique perpendiculaire et à une température suffisamment basse, est d'un intérêt particulier pour cette thèse. Il s'agit d'un phénomène quantique robuste et remarquable qui change radicalement les lois classiques habituelles pour décrire le transport électronique, même dans le circuit résistif le plus simple.

1.2 L'effet Hall quantique

Dans la théorie semi-classique, les particules chargées se déplaisant sous un champ magnétique décrivent des trajectoires circulaires, les orbites cyclotron, comme conséquence de la force de Lorentz. Alors que la fréquence du cyclotron ω_c n'est fixée que par le champ magnétique B, le rayon de l'orbite r_c dépend tant du champ magnétique que de l'énergie E de la particule:

$$w_c = \frac{eB}{m} \qquad r_c = \frac{v}{w_c} = \frac{\sqrt{2Em}}{eB} \tag{1.1}$$

Puisque les particules dans un conducteur ont une énergie maximale de l'ordre de l'énergie Fermi E_F, en augmentant le champ magnétique le rayon peut être rendu si petit qu'il devient comparable à la longueur d'onde *de Broglie* de la particule. On s'attend donc à observer des effets de quantification de l'énergie et du rayon orbital dans la lim-

ite des champs magnétiques élevés. En fait, les principales propriétés électroniques d'un 2DEG sous un fort champ magnétique perpendiculaire sont décrites par la théorie quantique en termes de niveaux de Landau. Ce sont des niveaux d'énergie discrets, séparés par $\hbar\omega_c$ comme représenté sur la Fig. 1.1a, qui résultent directement de la quantification du mouvement cyclotron.

Afin d'observer les effets de la quantification de Landau sur les propriétés de transport, deux conditions principales doivent être satisfaites: Premièrement, les électrons doivent être capables d'effectuer au moins une orbite cyclotron complète avant d'être dispersés, ce qui implique que $\omega_c\tau = B\mu_\tau \gg 1$; Deuxièmement, la température électronique T doit être suffisamment petite pour qu'un seul niveau de Landau soit excité thermiquement à la fois: $k_bT \ll \hbar\omega_c$.

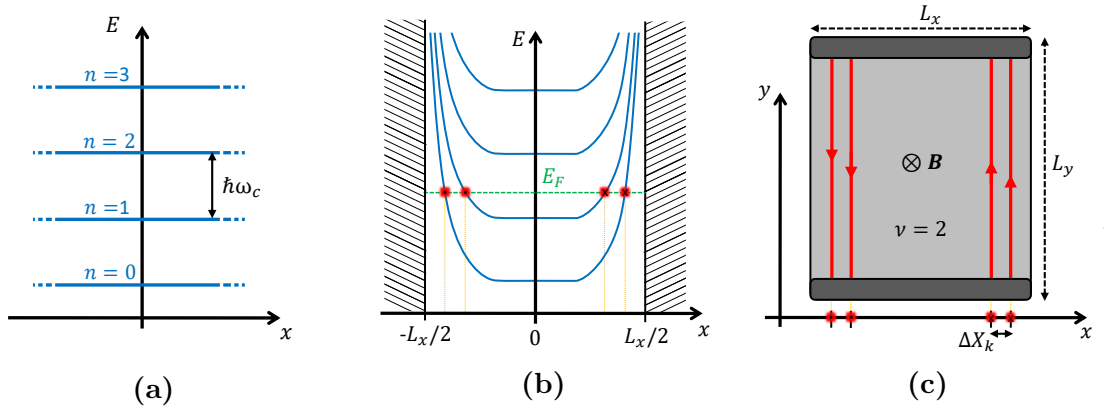

Figure 1.1: **(a)** Niveaux de Landau plats $E_n = \hbar\omega_c(n + 1/2)$ formés dans un 2DEG infini sous un champ magnétique uniforme $\boldsymbol{B}$. **(b)** Niveau de Landau formé dans un système de taille finie L_x dans la direction $\hat{x}$. Le potentiel de confinement créé aux frontières (ici représentées sous forme de murs durs) fait monter les niveaux de Landau. **(c)** Chaque fois qu'un niveau de Landau croise le niveau de Fermi E_F en **b**, un état de bord chiral se développe situé dans l'échantillon à la position du croisement des niveaux. Le nombre d'états de bord est donné par le nombre de niveaux de Landau remplis dans le coeur (*bulk*) du système.

De plus, lorsqu'un 2DEG de taille finie est considéré, les niveaux de Landau sont modifiés près des frontières du système: ils sont pliés vers le haut en raison du potentiel de confinement qui définit les frontières (Fig 1.1b). Néanmoins dans le coeur (*bulk*) du système, les niveaux de Landau restent plats (s'il n'y a pas de désordre) et séparés par l'énergie du cyclotron $\hbar\omega_c$.

De plus, l'énergie des niveaux de Landau peut être réglée avec le champ magnétique pour faire en sorte que l'énergie de Fermi E_F se situe entre deux niveaux de Landau dans le coeur (*bulk*) du système. Dans cet condition, le coeur (*bulk*) devient isolante et les seules excitations à faible énergie qui sont possibles se situent près des bords du système. Cela signifie que dans ce régime, les électrons ne peuvent se propager que le long des frontières du système dans les ***états de bord*** [10]. Comme détaillé dans les Fig 1.1b et 1.1c un état de bord est développé chaque fois qu'un niveau de Landau croise l'énergie de Fermi et il est situé dans la position où le croisement a lieu.

Dans cette représentation simple, le nombre de canaux de bord est donné par la partie entière du facteur de remplissage $\nu = n_s h/eB$, qui correspond au nombre de niveaux de Landau qui sont en dessous du niveau de Fermi.

La chiralité traditionnelle imposée par le champ magnétique dans un mouvement cyclotron se reflète ici par le fait que les états de bord se propageant dans des directions opposées sont situés dans des côtés opposés du système, généralement séparés par une distance macroscopique. En conséquence, la rétrodiffusion est supprimée et la propagation des électrons résulte robuste contre les impuretés et le désordre. Dans ce régime, le transport est dit chiral et topologiquement protégé: les particules se propagent de façon balistique sur les canaux de bord. Pour ces raisons, les états de bord de l'effet Hall quantique ont été considérés comme de bons candidats pour l'obtention des *fils quantiques unidimensionnels idéals* où les particules peuvent se propager de manière cohérente et sans dissipation.

1.3 Optique quantique électronique

Les propriétés particulières de la propagation des électrons dans les canaux de bord dans le régime de l'effet Hall quantique entier ont incité les physiciens à effectuer des expériences semblables à l'optique quantique où les électrons sont utilisés pour imiter la propagation des photons. Les progrès faits dans cette direction ont conduit au développement récent d'un champ spécifique dans le domaine du transport mésoscopique qui est connu sous le nom de *optique quantique électronique*.

Au cours des dernières décennies, un effort considérable a été fait pour déterminer dans quelle mesure cette analogie peut être étendue. Alors que les propriétés balistiques des canaux de bord assurent le mouvement des électrons en forme de faisceau, il a également été démontré que des nanostructures électrostatiques comme les contacts ponctuels quantiques (QPC) et les boîtes quantiques (QD) pouvaient être efficacement mises en œuvre comme analogues électroniques des diviseurs de faisceau et des filtres des particules resolus en énergie. De plus, récemment, plusieurs types de sources d'électrons uniques ont été développés afin de réaliser ces expériences avec des particules individuelles [11, 12, 13, 14, 15, 16, 17].

En physique de la matière condensée, le caractère fermionique des électrons ainsi que l'interaction de Coulomb ont un rôle important à jouer. Les expériences d'optique quantique électronique permettent de sonder l'analogie entre la propagation cohérente des électrons et des photons, mais aussi de mettre en évidence leurs différences. Une aspiration majeure de ce domaine est d'étudier et de comprendre l'importance des interactions électroniques afin de pouvoir manipuler l'état quantique des excitations individuelles dans les canaux de bord de l'effet Hall quantique. Cela fournirait une base prometteuse pour la mise en œuvre de qubits volants électroniques pour l'information quantique [18, 19]. Dans le domaine de l'information quantique, les qubits volants sont

nécessaires pour la transmission cohérente de l'information entre les parties séparées du réseau physique [20, 21]. La propagation chirale et robuste des électrons dans le régime de l'effet Hall quantique offre de grands avantages à cette fin puisque les trajectoires des électrons peuvent être facilement manipulées par des grilles électrostatiques. De plus, il a été proposé de mettre en œuvre des qubits volants électroniques, non seulement pour transférer l'information mais aussi pour effectuer des opérations logiques puisque l'information peut également être codée dans les trajectoires des électrons [21]. Par conséquent, une étape fondamentale consiste à déterminer jusqu'à quel point les électrons peuvent se propager de façon cohérente et sans relaxation le long des canaux de bord de l'effet Hall quantique.

Dans cette thèse, nous abordons cette question en étudiant expérimentalement la relaxation des quasiparticules émises à une énergie bien définie au-dessus de la mer de Fermi d'un canal de bord, dans le régime de l'effet Hall quantique entier au facteur de remplissage $\nu = 2$. Cette expérience sonde la importance des interactions qui permet aux particules d'échanger de l'énergie et donc de relaxer dans le régime IQHE.

1.4 Le rôle des interactions

La simple quantification du mouvement cyclotron des électrons est suffisante pour expliquer de nombreuses observations expérimentales du transport électronique dans le régime de l'effet Hall quantique entier, mais ce n'est qu'une description sans interactions. Comme elle ne tient pas compte des interactions, on sait peu de choses sur la relaxation et la décohérence des quasiparticules.

Le rôle de les interactions dans les systèmes électroniques est une question très fondamentale qui a été considérée originellement dans la théorie de Landau des liquides Fermi [22, 23, 24]. Il décrit un gaz de Fermi où les interactions de Coulomb entre les particules sont allumées de façon adiabatique à partir du cas non interactif. Il en résulte un système, le liquide de Fermi, dont l'état fondamental est toujours une mer de Fermi et les excitations à faible énergie sont encore décrites par des états des particules uniques à longue durée de vie qui suivent une statistique de Fermi.

Cependant, *l'hypothèse adiabatique* n'est pas toujours valide. Un exemple bien connu est le cas d'un supraconducteur, dont l'état fondamental est radicalement différent de celui d'une mer Fermi. Par conséquent, il ne peut pas être décrit par cette théorie. Un autre cas où l'hypothèse adiabatique est susceptible d'échouer est celui des systèmes de faible dimension car les effets des interactions sont généralement renforcés en raison du confinement supplémentaire; par conséquent, de nombreux effets inhabituels des particules fortement corrélées ont été suggérés de se développer. La théorie du liquide de Luttinger [25, 26] décrit un gaz de Fermi unidimensionnel avec des interactions et prédit plutôt que les excitations dans ce système sont mieux représentées par des quasiparticules bosoniques qui se composent des excitations collectives [27, 28].

Dans ce contexte, la nature même des quasiparticules se propageant dans les canaux de bord chiraux de l'effet Hall quantique est encore sous investigation [29, 30, 31]. En raison de son caractère unidimensionnel, il n'est pas clair dans quelle mesure les excitations fondamentales de basse énergie peuvent être représentées comme des quasiparticules de Landau stables. Dans les expériences menées dans le cadre de cette thèse, nous sondons directement dans quelle mesure les quasiparticules peuvent se propager avant de se décomposer en excitations collectives.

1.5 Décohérence dans les canaux de bord

Au cours des deux dernières décennies, plusieurs expériences ont été réalisées pour étudier les propriétés des états de bord dans le régime de l'effet Hall quantique entier, principalement au facteur de remplissage $\nu = 2$.

Des interféromètres de Mach-Zehnder (MZI) ont été conçus pour étudier les propriétés de cohérence du canaux de bord en produisant une interférence quantique qui reflète la propagation balistique et cohérente des électrons [32, 33, 34, 35, 36]. Des interférences avec une visibilité aussi élevée que 90% ont été obtenues [37] et des longueurs de cohérence de l'ordre de $20\,\mu m$ à une température de $20\,mK$ ont été déterminées expérimentalement [33]. Ultérieurement, il a également été démontré que le bruit électronique présent dans le canal de bord voisin co-propagation et dans l'environnement contitue une source de décohérence qui peut être manipulée expérimentalement[38, 39].

Le développement d'une source d'électrons unique à la demande qui assure un bon contrôle du temps d'émission et de la résolution en énergie d'un paquet d'ondes a ouvert la voie à l'étude de la décohérence au niveau des particules individuelles [11, 40]. Des interférences à deux particules dans la configuration de Hong-Ou-Mandel ont été mises en œuvre, suggérant que la décohérence des particules individuelles résulte en effet de l'émergence d'excitations collectives induites par l'interaction de Coulomb entre les deux canaux de bord co-propageants [41, 42, 43].

Certaines de ces observations concordaient bien avec le modèle théorique qui décrit les deux canaux de bord co-propageant couplés par l'interaction de Coulomb en terme de la théorie du liquide de Luttinger [44, 45, 46]. Cependant, d'autres expériences récentes réalisées avec des MZI, où des particules ont été injectées au-dessus de la mer de Fermi à une énergie bien définie, ont démontré une cohérence quantique robuste à haute énergie: il a été observé qu'au-dessus d'une énergie seuil, la visibilité des franges d'interférence reste constante et indépendante de l'énergie [47]. Ces résultats sont en forte contradiction avec les modèles théoriques qui prédisent plutôt une diminution continue de la visibilité en fonction de l'énergie d'injection.

Les explications de ces observations inattendues dans les expériences d'interférence font encore l'objet d'un débat. De plus, puisque les interactions permettent d'échanger

de l'énergie entre les particules du système, l'étude des mécanismes de relaxation dans les canaux de bord peut donner de nouvelles perspectives pour mieux comprendre le rôle des interactions au niveau le plus fondamental.

1.6 Relaxation dans les canaux de bord

Les expériences qui étudient la relaxation en énergie consistent essentiellement à mettre le système hors équilibre, d'une manière contrôlable, puis à mesurer comment il revient à l'état d'équilibre. Ce faisant, nous pouvons étudier le mécanisme de relaxation et sonder ses dépendances avec d'autres paramètres tels que la température électronique, la distance de propagation ou l'environnement électromagnétique. Cette idée a été mise en œuvre pour étudier le rôle des interactions dans divers systèmes mésoscopiques comme des fils métalliques diffusifs [48], des nanotubes de carbone [49], des nanostructures dans les semiconducteurs [50] et récemment dans les canaux de bord de l'effet Hall quantique entier au facteur de remplissage $\nu = 2$ [51, 52]. Puisque la propagation dans le régime de l'effet Hall quantique est chirale, l'évolution de l'état hors équilibre peut être suivie le long du bord de l'échantillon: le temps et la distance sont liés simplement par la vitesse de dérive v_d.

Dans la Réf. [51] il a été démontré qu'une mesure directe de la fonction de distribution $f_r(E)$ dans le canal de bord peut être obtenue à partir du courant tunnel I_{QD} à travers une boîte quantique qui est faiblement couplé au canal de bord. Cette technique de spectroscopie repose sur l'effet tunnel des électrons à travers un seul niveau discret dans une boîte quantique, dans le régime de transport élastique et séquentiel, dont l'énergie du niveau dicret E_2 peut être manipulée électrostatiquement pour sonder la fonction de distribution du canal de bord à différentes énergies. Si le canal de bord à étudier se trouve à la source de la boîte quantique, le courant tunnel est simplement:

$$I_{QD}(E_2) = I_{max}\Big(f_r(E_2, \mu_r) - F_d(E_2, \mu_d)\Big) \tag{1.2}$$

où I_{max} est une constante déterminée par les caractéristiques de la boîte quantique et F_d est la fonction Fermi au réservoir de drain de la boîte sur lequel une tension de polarisation V_d est appliquée afin de séparer le potentiel électrochimique des réservoirs de drain (μ_d) et de source (μ_r): $|eV_d| = \mu_r - \mu_d$.

Comme nous le verrons au chapitre 5, cette méthode a été mise en œuvre pour mesurer la relaxation d'un état hors-équilibre injecté sur un canal de bord qui consiste en une fonction de distribution $f_i(E)$, avec une forme en double marche, générée avec un contact ponctuel quantique à une transmission intermédiaire $\tau_{qpc} \sim 0.5$ et polarisé avec une tension V_1. Ainsi, le QPC mélange les distributions de Fermi[1] $F(E)$ d'un contact ohmique mis à la masse avec la distribution de Fermi $F(E - eV_1)$ du contact

ohmique biaisé.

$$f_i(E) = \tau_{qpc} F(E - eV_1) + (1 - \tau_{qpc}) F(E) \tag{1.3}$$

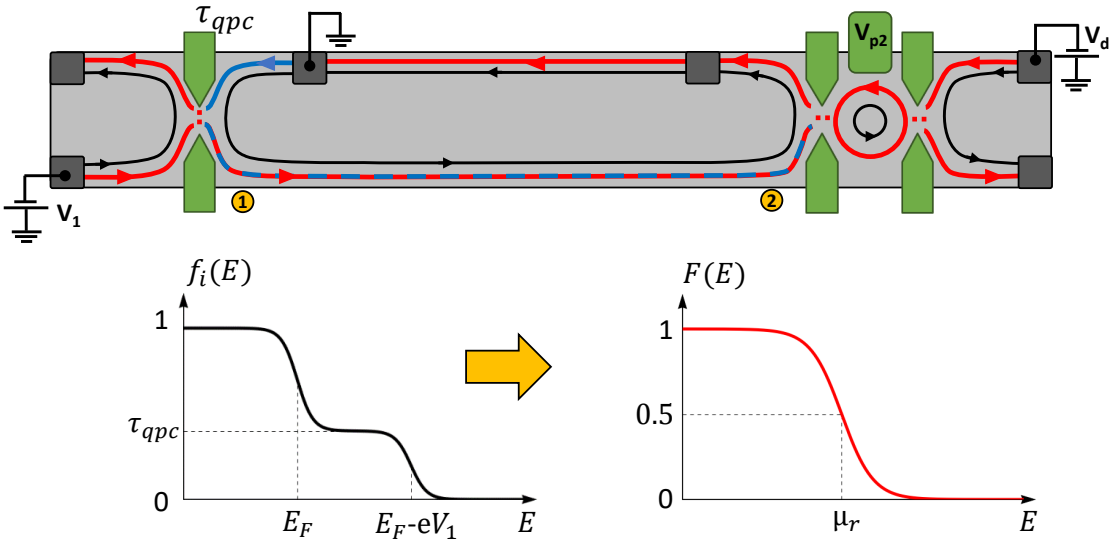

Figure 1.2: Top: Représentation schématique de la configuration expérimentale implémente pour étudier la relaxation d'une fonction de distribution qui a une forme en double marche dans le régime IQHE au facteur de remplissage $\nu = 2$. Le QPC biaisé a une transmission intermédiaire τ_{qpc} crée une fonction de distribution avec une forme en double marche f_i dans le canal du bord extérieur. Après quelques micromètres de propagation, là où la relaxation peut avoir lieu, la distribution f_r résultante est mesurée à l'aide d'une boîte quantique implémenté comme filtre d'énergie. (**Bottom:**) État initial et final de la fonction de distribution avant et après le processus de relaxation.

La figure 1.2 illustre la configuration expérimentale pour l'étude de la relaxation de une fonction de distribution avec une forme en double marche injectée dans le canal du bord extérieur obtenue dans le régime de l'effet Hall quantique entier à facteur de remplissage $\nu = 2$. Sur ces expériences, il a été démontré qu'après une courte distance de propagation, d'environ $0.8\,\mu$m, l'état de déséquilibre injecté ne se relâche pas du tout. Des expériences ultérieures ont montré que le processus de relaxation s'effectue progressivement tandis que les particules se propagent sur quelques micromètres. Une relaxation complète vers un régime d'électrons chauds a été mesurée après une distance de $10\,\mu$m [52] et il reste inchangé à plus grande distances, jusqu'à $30\,\mu$m.

L'interaction de Coulomb entre les deux canaux de bord co-propageant, qui sont seulement couplés capacitivement, a été identifiée comme la principale source de relaxation. En fait, un échange d'énergie direct a été observé entre les deux canaux de bord et il a été démontré que cet échange d'énergie pouvait être empêché en forçant le canal de bord intérieur à former des boucles. Lorsque le canal de bord intérieur forme des boucles, sa densité d'état devient discrète comme dans une boîte quantique,

[1] Les fonctions de distribution de Fermi sont représentées en majuscule $F(E)$ tandis que les autres fonctions de distribution sont représentées en minuscule $f(E)$.

ainsi le canal de bord extérieur est maintenant couplé à un système avec un spectre d'énergie quantifié au lieu d'un spectre continu. Cela limite les énergies auxquelles ils peuvent échanger de l'énergie en réduisant la relaxation de la fonction de distribution hors équilibre qui a été injectée dans le canal du bord extérieur [53].

Bien que certaines des observations concordent bien avec le scénario de couplage capacitif de deux canaux de bord en interaction, il a été également observé que 25% du courant de chaleur injecté s'échappe du système constitué par les deux canaux de bord, ce qui suggère qu'il pourrait y avoir des degrés de liberté supplémentaires qui jouent un rôle imprévu dans le mécanisme de relaxation et dont les modèles théoriques précédents n'ont pas tenu compte [52, 54, 55].

Au chapitre 5 nous présentons des mesures que nous avons effectuées dans le même régime, pour étudier la relaxation d'une fonction de distribution avec une forme en double marche, qui sont en accord avec les principaux résultats des expériences réalisées à l'origine par l'équipe Phynano du laboratoire C2N(LPN) [51, 52]. Dans ces expériences, nous avons vérifié que sur nos échantillons, qui ont une géométrie différente, nous observons le même taux de relaxation pour la fonction de distribution à double marche, ce qui signifie que le processus de relaxation n'est pas fortement affecté par le désordre particulier dans l'échantillon, ou la configuration géométrique spécifique des électrodes métalliques qui définissent l'appareil. Nos mesures sont en accord avec le fait que la fonction de distribution en double marche se relaxe vers un régime d'électrons chauds à une distance de 10 μm de propagation.

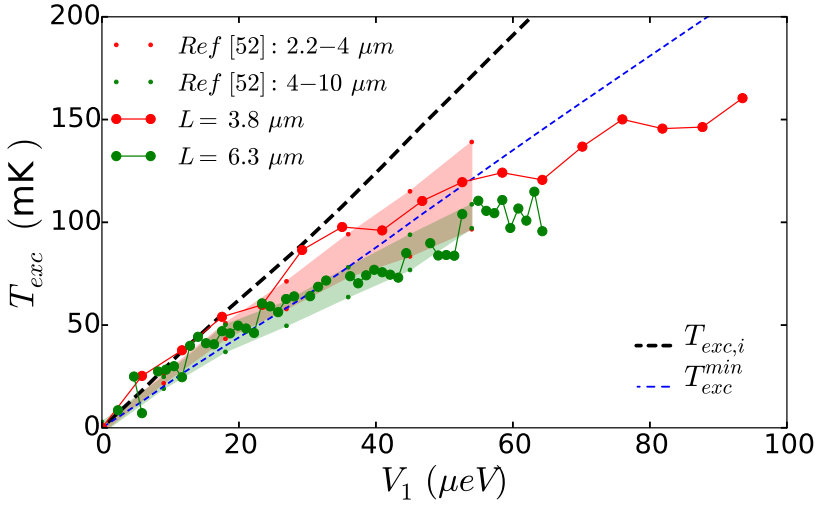

Figure 1.3: Température d'excès mesurée après une courte (longue) distance de propagation tracée avec les gros symboles remplis en rouge (verts) en fonction de la tension de polarisation V_1 dans le QPC. Nos mesures se situent dans la zone ombrée en rouge (verte) pour la courte (longue) distance. Ces régions ombrées ont été déterminées à partir des données présentées dans la Réf. [52] (Voir chapitre 5 pour plus de détails). *La conservation de l'énergie dans le canal de bord* est indiqué par la ligne pointillée noire épaisse ($T_{exc,i}$), tandis que *la conservation de l'énergie sur le système de deux canaux couples* est indiqué par la ligne pointillée bleue mince (T_{exc}^{min}) qui est la limite inférieure prévue par la théorie.

De plus, nous avons observé la même fuite d'énergie de $\sim$ 25% de l'ensemble du

système constitué par les deux canaux de bord en interaction. Il s'agit d'une vérification importante de l'observation faite en premier lieu dans la Réf. [52] que nous reproduisons quantitativement pour la première fois et qui suggèrent qu'il s'agit en fait d'une caractéristique intrinsèque du mécanisme de relaxation. Cette fuite d'énergie est mis en evidence en regardant la température d'excès T_{exc}, qui est proportionnelle à la racine carrée du courant de chaleur dans le canal de bord. Celle-ci est présentée dans la figure 1.3 en fonction de la tension de polarisation V_1 dans le QPC pour deux longueurs de propagation, $L = 3.8\mu$m (rouge) et $L = 6.3\mu$m (verte). Ici, la fuite d'énergie se manifeste par l'augmentation de l'écart observé entre les points mesurés, à grande tension de polarisation et à grande distance, et la ligne diagonale T_{exc}^{min} (ligne bleue en pointillés fins) qui est la limite inférieure prévue par tous les modèles théoriques.

1.7 Relaxation á des énergies définies

Bien que les expériences décrites jusqu'à présent aient clairement démontré que les interactions entre les canaux de bord sont la principale source de décohérence et de relaxation, elles ont également montré que ces processus pouvaient être contrôlés et supprimés jusqu'à un certain niveau. Cependant, l'énergie manquante suggère également que la compréhension actuelle du mécanisme de relaxation n'est pas complète. En outre, il reste encore des questions fondamentales auxquelles ces expériences n'ont pas permis de répondre: ***Comment un pic de quasiparticules, bien défini en énergie, se relaxera-t-il vers la mer de Fermi?*** et ***Jusqu'á quelle distance les excitations résolues en énergie peuvent-elles se propager dans un canal de bord avant de se relaxer?*** Ce sont là des questions fondamentales abordées à l'origine dans la théorie de Landau des liquides de Fermi, qui sont d'une importance fondamentale pour la manipulation cohérente des quasiparticules dans le régime de l'effet Hall quantique entier pour des applications futures.

Dans cette thèse, nous abordons ces questions et apportons des preuves expérimentales de la désintégration d'un pic des quasiparticules en effectuant une spectroscopie résolue en énergie de la relaxation des quasiparticules injectées, à une énergie bien définie, audessus de la mer de Fermi dans un canal de bord dans l'effet Hall quantique. Les expériences sont réalisées sur un 2DEG à base de GaAs/AlGaAs avec des densités d'électrons allant de $n \approx 2.5 \times 10^{11}$ cm^{-2} et une mobilité de l'ordre de $\mu_\tau \sim 2 \times 10^6$ cm^{2}V^{-1}s^{-1}. Les 2DEG sont fabriqués au laboratoire C2N par A. Cavanna et U. Gennser.

1.7.1 Configuration expérimentale

Notre configuration repose sur une paire de boîtes quantiques électrostatiquement définies, utilisées comme émetteur et détecteur résolus en énergie comme illustré dans la Fig. 1.4. Le dispositif est fabriqué au laboratoire C2N par D. Mailly par lithogra-

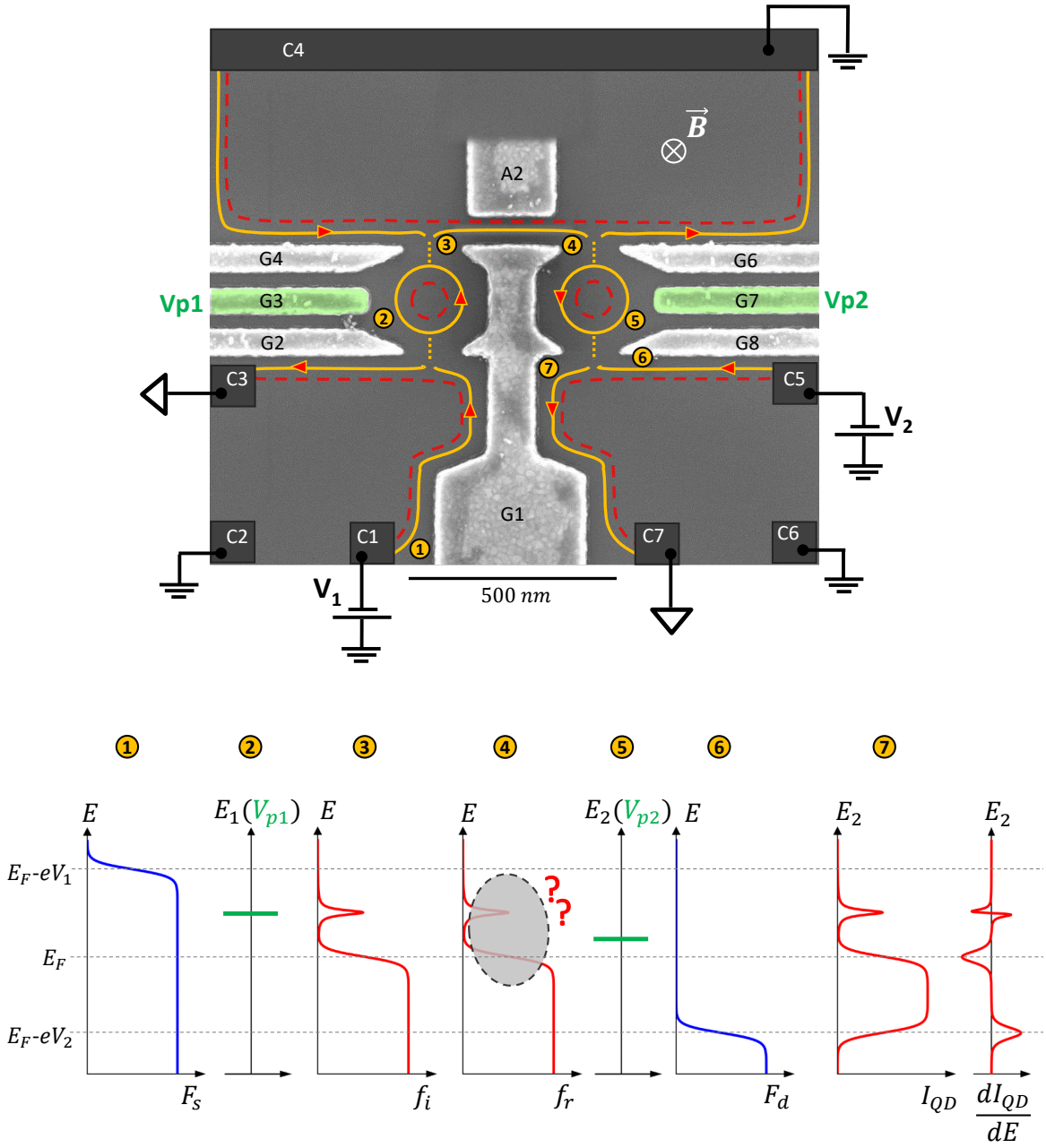

Figure 1.4: **Top:** Micrographie électronique à balayage de l'échantillon ***E33***. Deux boîtes quantiques sont définies électrostatiquement afin d'effectuer une spectroscopie résolue en énergie de la relaxation dans un canal de bord. Les deux QDs sont faiblement couplés uniquement au canal de bord extérieur, tandis que le canal de bord intérieur est entièrement réfléchi par toutes les électrodes qui définissent les deux QDs. Le premier QD (à gauche) injecte des quasiparticules au-dessus de la mer de Fermi dans le canal de bord qui provient du contact $C4$ mis à la masse. Les excitations injectées se propagent dans le canal de bord, de **3** à **4**, jusqu'à ce qu'elles atteignent le deuxième boîte quantique (à droite) qui est implémenté comme un détecteur. **Bottom:** Diagramme des énergies et distribution des particules dans les différentes parties de l'appareil. Le schéma d'injection est représenté par **1**, **2**, **3**. La propagation se produit entre **3** et **4**. Le schéma de détection est représenté par **4**, **5** et **6**. Le signal attendu à être mesuré dans la transconductance à travers la deuxième boîte quantique est représenté par **7**. Voir le texte pour plus des détails (section 6.2). Les dispositifs sont fabriqués au laboratoire C2N où les 2DEG sont produits par A. Cavanna et U. Gennser, tandis que les nanostructures métalliques sont faites par D. Mailly.

phie électronique. Le premier boîte quantique est définie par l'ensemble d'électrodes $\{G1, G2, G3, G4\}$ sur le côté gauche, et le second boîte quantique est définie par l'ensemble d'électrodes $\{G1, G6, G7, G8\}$ sur le côté droit. L'émetteur est obtenu en appliquant une tension drain-source finie V_1 sur la premier boîte quantique (**1**), avec un seul niveau résonant dans la fenêtre de polarisation (**2**). La position du niveau résonant, qui est contrôlée par la tension V_{p1} sur l'électrode $G3$, définit l'énergie E_1 à laquelle les électrons sont émis au-dessus de l'énergie de Fermi E_F du drain (**3**). Par conséquent, la fonction de distribution hors équilibre injectée $f_i(E)$ est constituée de la mer de Fermi en équilibre $F(E)$ et des quasiparticules émises avec une distribution de Lorentz $L(E, E_1)$ centrée à l'énergie E_1 dont l'amplitude $\mathcal{T}_1$ et la largeur à mi-hauteur Γ_1 sont déterminées par les caractéristiques du niveau résonant dans la premier boîte quantique.

$$f_i(E) = F(E, E_F) + L_1(E, E_1) \tag{1.4}$$

Après une longueur de propagation dans l'échelle micrométrique (de **3** à **4**), nous effectuons une spectroscopie résolue en énergie des électrons émis en utilisant le second boîte quantique comme filtre d'énergie (**4**, **5**, **6** et **7**). Pour cette procédure de détection nous suivons la méthode précédemment démontré pour détecter la relaxation de une fonction de distribution avec une forme en double marche (Section 1.6).

1.7.2 Relaxation du pic de quasiparticules

Dans le chapitre 6 nous présentons les données que nous avons obtenues en mettant en ouvre le dispositif de la Fig. 1.4, ce qui constitue la première observation expérimentale d'un pic de quasiparticules au-dessus de la mer de Fermi d'un canal de bord.

Relaxation vs Energie d'Injection

La figure 1.5 montre une mesure effectuée après une courte distance de propagation $L = 0.48\,\mu$m à une température $T_0 = (23.1 \pm 0.6)$mK. La figure montre la mer de Fermi mesurée à l'équilibre et toutes les fonctions de distributions mesurées à différentes énergies d'injection $E_1 \in \{22, 43, 65, 87, 108, 130, 152, 173\}\mu$eV. S'il n'y a pas eu de relaxation, l'amplitude attendue du pic des quasiparticules est $\mathcal{T} \sim 0.3$. Bien que l'on observe une relaxation croissante au fur et à mesure que l'énergie d'injection E_1 augmente, la structure d'un pic a quand même été détectée dans toutes les courbes. Ces observations, obtenues au facteur de remplissage $\nu = 2$ de l'effet Hall quantique, montrent que bien que la propagation sur une distance submicrométrique entraîne un relaxation important du pic injecté, une petite partie des quasiparticules survit à la relaxation, même aux énergies relativement élevées, ici jusqu'à 175μeV.

Comme le montre la figure 1.6, une caractérisation détaillée de l'évolution du pic des quasiparticules en fonction de l'énergie d'injection E_1 montre que le processus de relaxation qui a eu lieu le long de la propagation n'affecte pas l'énergie à laquelle le pic

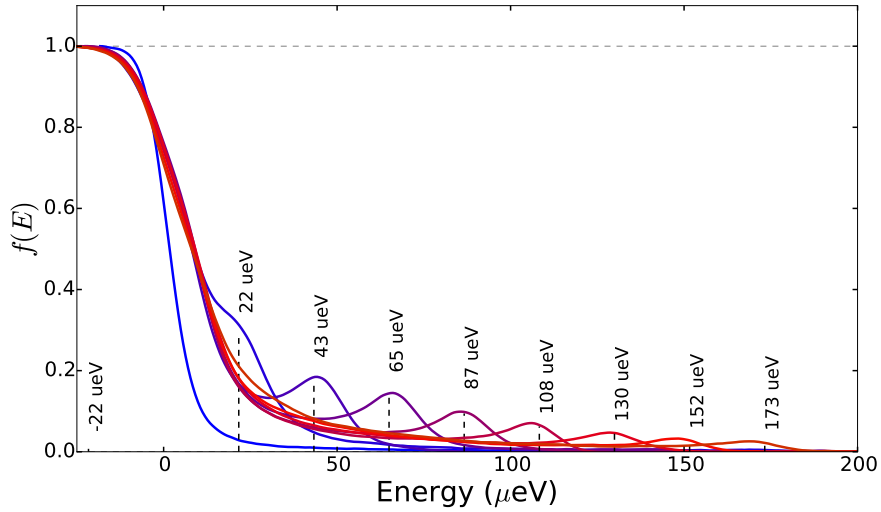

Figure 1.5: ***Spectre R-72.*** Évolution de la fonction de distribution $f(E)$ mesurée après une distance de propagation $L = 0.48\mu$m tout en augmentant l'énergie d'injection E_1, indiquée par les lignes pointillées verticales, autour desquelles est centrée une structure du pic qui est le reste du pic des quasi-particules injecté. La mer de Fermi en équilibre (ligne bleue claire) avec le potentiel électrochimique $E_F \sim 0\mu eV$ a été mesuré quand aucune particule n'a été injectée ($E_1 = -22\mu eV < E_F$).

est centré étant toujours trouvé autour de l'énergie d'injection E_1. De plus, la forme du pic est toujours bien décrite par une fonction de Lorentz dont la largeur Γ_L (FWHM) reste constante et indépendante de l'énergie d'injection. Plus important encore, ces mesures ont montré que l'amplitude du pic de quasiparticules diminue suivant une décroissance exponentielle en fonction de l'énergie d'injection. L'énergie caractéristique E_{decay} de la désintégration exponentielle était de l'ordre de $E_{decay} \sim 60\,\mu$eV pour une distance de propagation $L = 0.48\mu$m à une température $T_0 = 23.1 \pm 0.6$ mK.

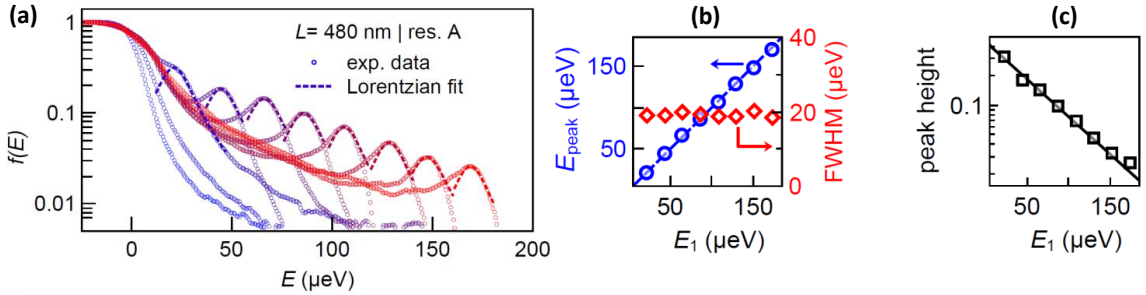

Figure 1.6: **(a)**Fonction de distribution $f(E)$ mesurée et présenté en échelle semi-logarithmique afin de mettre en évidence l'évolution du pic des quasi-particules tout en augmentant l'énergie d'injection E_1. La ligne pointillée correspond à un modèle lorentzien du pic des quasiparticules. **(b)** Centre du pic E_{peak} (cercles bleus) et largeur du pic à mi-hauteur FWHM (diamants rouges) extrait des ajustements de Lorentzian fits en fonction de l'énergie d'injection E_1. La ligne pointillée bleue est une ligne y = x. **(c)** Hauteur de pic (carrés noirs) extraite des ajustements montrés dans **a** versus E_1, en échelle semi-logarithmique. La ligne noire est un ajustement exponentiel du décroissance.

Relaxation vs Distance de Propagation

De plus, nous avons observé que l'énergie caractéristique E_{decay} est fortement affectée par la température électronique T et la distance de propagation L. D'une part, une augmentation de la température électronique de $\Delta T = 150$ mK réduit l'énergie caractéristique E_{decay} par presque un facteur deux. Par contre, une augmentation de la longueur de propagation de $L = 0.48\,\mu$m à $L = 0.75\,\mu$m entraîne une diminution de l'énergie de relaxation de $E_{decay} \sim 60\,\mu eV$ vers $E_{decay} \sim 20\,\mu eV$. L'effet de la distance est illustré dans la figure 1.7b qui montre la fonction de distribution mesurée à chaque distance, pour des différentes énergies d'injection, et la décroissance exponentielle de l'amplitude du pic des quasiparticules obtenue à partir d'eux.

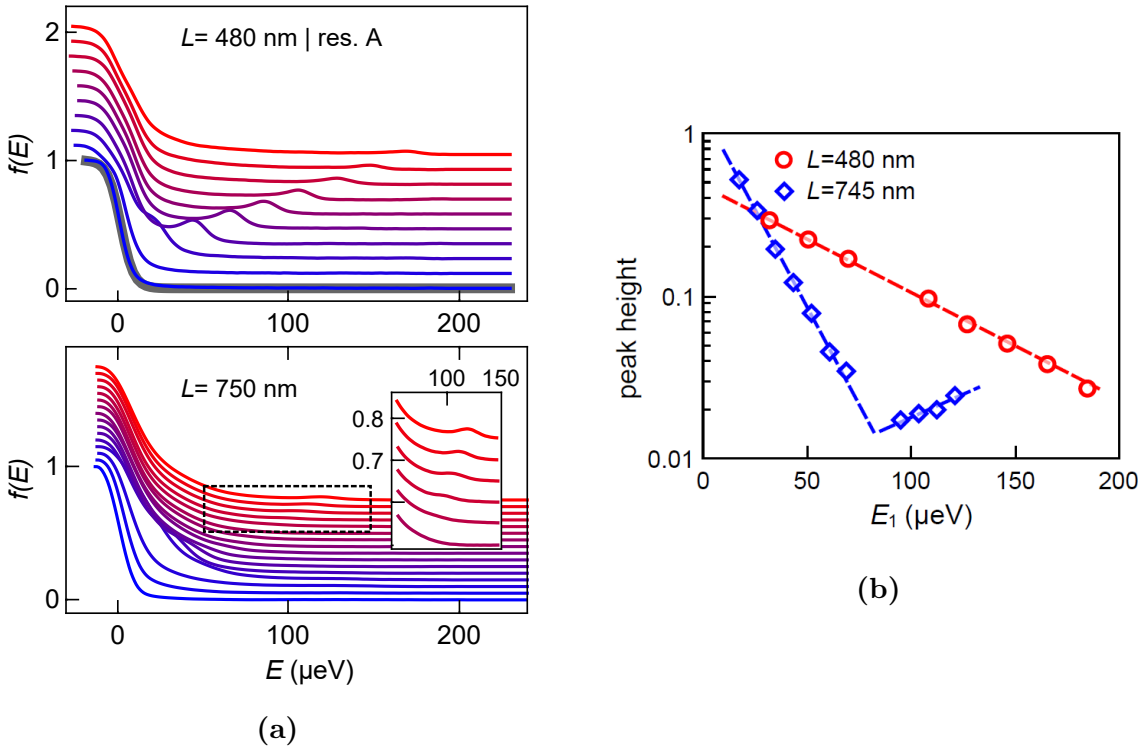

Figure 1.7: **(a)** Fonctions de distribution mesurées après la propagation. Les courbes ont été décalées verticalement pour plus de clarté. **Top:** Spectre mesuré dans l'échantillon ***E33*** pour $L = 0.48\,\mu$m. Chaque courbe correspond à un incrément de l'énergie d'injection $\delta E_1 \approx 21\mu$eV, de $E_1 = -21\mu$eV (bleu) à $E_1 = 173\mu$eV (rouge). La ligne grise épaisse est une fonction de Fermi qui correspond aux données obtenues à $E_1 = -21\mu$eV. **Bottom:** Spectre mesuré dans l'échantillon ***D31*** pour $L = 0.75\,\mu$m. Chaque courbe correspond à un incrément de l'énergie d'injection $\delta E_1 \approx 9\mu$eV, de $E_1 = 9\mu$eV (bleu) à $E_1 = 121\mu$eV (rouge). **(b)** Hauteur de pic extraite des ajustements de une fonction de Lorentz illustrés dans la Fig. 1.6, tracée en l'échelle semi-logarithmique en fonction de l'énergie d'injection E_1 pour les deux longueurs de propagation $L = 480$ nm (cercles rouges) et $L = 750$ nm (diamants bleus) représentées dans **a**. Les lignes pointillées rouges et bleues sont des ajustements exponentiels.

Une comparaison des distributions de particules observées à plusieurs distances pour un pic de quasiparticules injecté approximativement à la même énergie $E_1 \approx 40\,\mu$eV est présentée dans la figure 1.8. Avec l'analyse précédente du comportement du pic

de quasiparticules, cette comparaison permet de décrire comment le mécanisme de relaxation amène le système à l'équilibre. Dans un premier temps, une grande partie des particules injectées perdent de l'énergie et l'amplitude du pic de quasiparticules injecté diminue rapidement sur une distance de propagation sub-micrométrique. Notez qu'aucun relaxation n'a été observé pour les distances sub-micrométriques quand on il a été investigué la propagation d'une fonction de distribution avec une forme en double marche [51]. Une fois que le pic de quasiparticules a presque disparu à une distance d'environ $\sim 1\mu$m, ce qui reste est une distribution différente d'un fonction de Fermi, qui est toujours hors équilibre, qui n'as pas des traits aigus et qu'a une longue queue qui s'étend dans une large gamme d'énergies. Comme on peut le voir qualitativement dans la Fig. 1.8 cette distribution ne change pas beaucoup tant qu'elle se propage jusqu'à 3.4 μm. En fait, à ce stade, il ressemble à un état intermédiaire du processus de relaxation de la distribution avec une forme en double marche, pour la quelle la relaxation totale vers l'équilibre est atteint à de grandes distances ($\sim 10\mu$m).

On peut donc distinguer deux échelles de temps dans le processus de relaxation, qui ont d'abord été mises en évidence dans le modèle théorique décrit dans la Réf. [56]. La première étape du processus de relaxation, qui se produit sur des longueurs sub-micrométriques, rapproche les particules injectées vers la mer de Fermi en décomposant le pic de quasiparticules en une distribution étendue de particules sur une large gamme des énergies. La deuxième étape du processus de relaxation, qui amène la distribution étendue des particules dans une distribution de Fermi, se produit sur plusieurs micromètres de propagation.

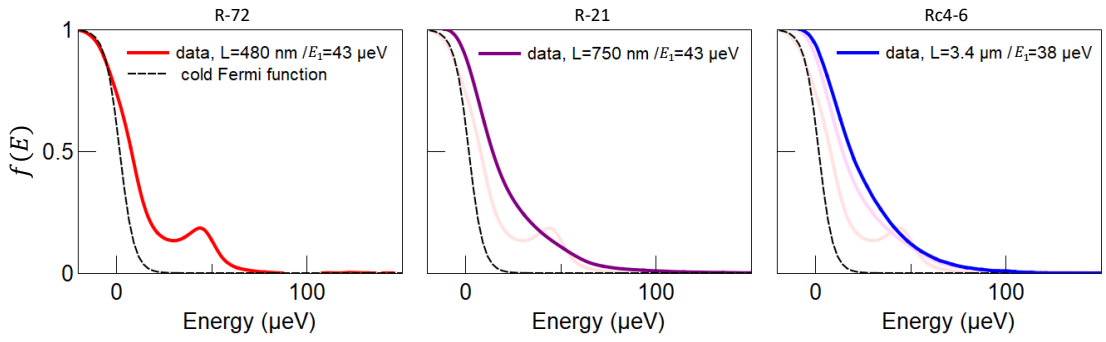

Figure 1.8: Fonction de distribution mesurée (ligne continue) pour une énergie d'injection similaire E_1 à des distances de propagation croissantes: $L = 480$nm (**left**), $L = 750$nm (**middle**) et $L = 3.4\mu$m (**right**). Dans chaque cas, la ligne en pointillés est la mer de Fermi en équilibre mesurée quand aucune particule n'a été injectée.

Signatures de la résurgence du pic de quasiparticules

En plus, pour une distance de propagation $L = 750$ nm et à basse température $T \sim 20$ mK, nous avons observé des signatures d'un résurgence du pic de quasiparticules. Comme on peut le voir dans la Fig. 1.7b l'amplitude du pic de quasiparticules non

seulement s'écarte soudainement de la décroissance exponentielle près de $E_1 \sim 80\,\mu$eV, mais elle augmente à mesure que l'énergie d'injection est incrémenté. Ce comportement a été observé dans plusieurs spectres mesurés en utilisant différentes configurations électrostatiques dans les deux boîtes quantiques, ce qui permet dé exclure des artefacts occasionnés par la présence de possibles états excités ou des instabilités de charge dans les électrodes à proximité. Bien que le modèle théorique proposé dans la Réf. [57] n'explique pas la décroissance exponentielle de l'amplitude du pic de quasiparticules, il prédit un comportement oscillatoire de l'amplitude du pic en fonction de l'énergie d'injection E_1 qui pourrait expliquer nos observations.

1.7.3 Courant de Chaleur

Dans le chapitre 7 nous étudions le courant de chaleur $J(E)$ porté par les excitations électrons-trous créées dans la fonction de distribution injectée $f_i(E)$, ce qui fournit des informations additionnelles sur l'échange d'énergie dans le système grâce au processus de relaxation.

Courant de Chaleur vs Énergie d'Injection

L'injection de quasiparticules avec une distribution de Lorentz $L_1(E, E_1)$ centrée sur l'énergie d'injection E_1 entraîne une augmentation du potentiel électrochimique $\Delta\mu$ donné par:

$$\Delta\mu = \int L_1(E, E_1)dE \tag{1.5}$$

ce qui est lié au courant de charge dans le canal de bord. En plus, l'injection de nouvelles particules entraîne également une augmentation du courant de chaleur ΔJ_i puisque de nouvelles excitations de électron-trou ont été créées sur le système. L'augmentation du courant de chaleur ΔJ_i qui a été injecté devrait suivre un comportement linéaire en fonction de l'énergie d'injection E_1, donnée par:

$$\Delta J_i(E_1) = (E_1 - \mu)\Delta\mu + \frac{1}{2}(\Delta\mu)^2 \tag{1.6}$$

Remarquablement, comme le montre la figure 1.9 pour deux distances de propagation $L = 0.48\mu$m (gauche) et $L = 0.75\mu$m (droite), nous observons une grande différence entre le courant de chaleur injecté ΔJ_i (ligne rouge) et le courant de chaleur détecté ΔJ_r (ligne noire avec symboles) mesuré après propagation. Dans les deux cas, on peut voir qu'à haute énergie d'injection E_1, le courant de chaleur détecté est beaucoup plus petit que ce qui était attendu, indiquant que l'énergie n'est pas conservée sur le canal de bord. Comme l'a clairement démontré H. le Sueur *et al.* [52], l'interaction avec le canal de bord co-propageant induit un échange d'énergie entre les deux canaux de bord, ce qui devrait être, en partie, responsable de l'écart observé sur la figure 1.9a et 1.9b.

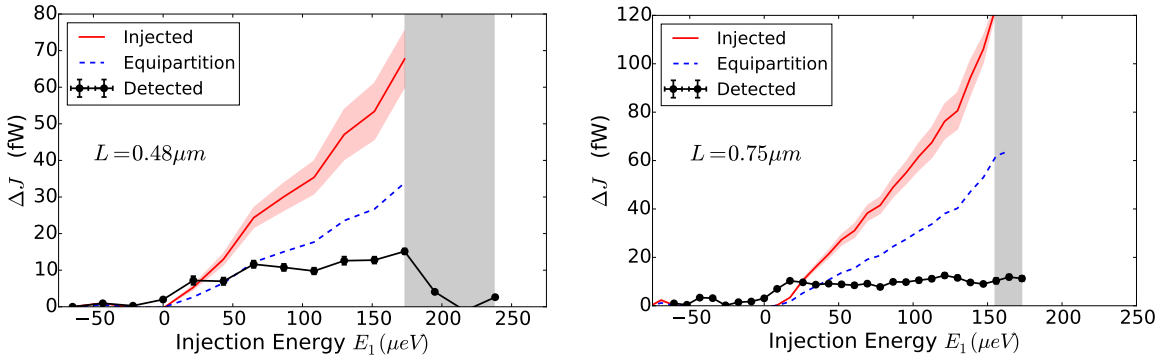

Figure 1.9: Comparaison entre le courant de chaleur en excès ΔJ_i qui a été injecté (ligne rouge) dans le canal de bord et le courant de chaleur en excès ΔJ_r qui a été mesuré après une propagation (symboles noirs). Chaque graphe correspond à la mesure prise après une longueur de propagation $L = 0.48\mu$m (**a**) et $L = 0.75\mu$m (**b**). Dans les deux cas, la ligne pointillée bleue représente la limite inférieure ΔJ_r^{min} qui est prédite par tous les modèles théoriques comme conséquence de l'équipartition d'énergie entre les deux canaux de bord co-propageants. La zone ombrée en gris correspond à la partie finale de la spectroscopie, où l'énergie d'injection atteint sa valeur maximale quand le niveau d'énergie discret dans la premier boîte quantique sort de la fenêtres de biais.

Cependant, les différents modèles théoriques qui décrivent ce système en interaction, soit dans le cadre des fermions chiraux [54] soit dans le cadre de la théorie des liquides de Luttinger qui suggère le développement des excitations de plasmons [58, 55], prévoient que cette interaction mène à une équipartition d'énergie entre les canaux voisins. En conséquence, il y a une limite inférieure ΔJ_r^{min} pour le courant de chaleur restant sur un canal de bord qui devrait être atteint à pleine relaxation. Cette limite inférieure est indiquée par la ligne pointillée bleue pour les mesures présentées sur la Fig. 1.9. On voit clairement que le courant de chaleur en excès qui reste dans le canal mesuré après la propagation est bien en dessous de la limite inférieure. Nous observons qu'il reste jusqu'à 70% moins d'énergie que ΔJ_r^{min} pour une distance de propagation $L = 0.75\mu$m.

Ces mesures montrent qu'il y a une très grande fuite d'énergie qui n'est en accord avec aucun des modèles théoriques actuels qui décrit l'interaction dans le régime de l'effet Hall quantique entier au facteur de remplissage $\nu = 2$. En plus, dans le cas de la relaxation de la fonction de distribution avec une forme en double marche, nous avons observé une fuite d'énergie plus faible, en accord avec les résultats présentés dans la Réf. [52] (Voir Fig. 1.3). Nos mesures dans les deux régimes excluent absolument tout artefact expérimental qui pourrait mener à une fuite d'énergie *apparente*. Alors qu'une fuite d'énergie constante de 25% a été observée sur la relaxation de la fonction de distribution avec une forme en double marche, nous rapportons ici que la relaxation des excitations résolues en énergie conduit à une fuite d'énergie qui dépend fortement de l'énergie d'injection E_1 du pic de quasiparticules. Ainsi, la quantité d'énergie perdue pendant la propagation suggère que les mécanismes de relaxation vers des degrés de liberté externes jouent un rôle important et inattendu dans les expériences d'optique

quantique électronique.

Courant de chaleur vs Longueur de propagation

Nous avons observé qu'une fuite d'énergie importante se développe très rapidement au cours du premier micromètre de propagation. A $L = 2.17\mu$m et au-delà, la fuite d'énergie n'augmente pas beaucoup et semble avoir atteint un comportement stationnaire. Cela coincide avec le fait que le processus de disparition de la structure du pic de quaisparticules se produit à des distances sub-micrométriques. A toutes les distances, nous observons que la fuite d'énergie est plus large à des énergies d'injection plus élevées. Grosso modo, la fraction du courant thermique résiduel $\Delta J_r/\Delta J_i$ suit une dépendance $1/E_1$ en fonction de l'énergie d'injection E_1.

Courant de chaleur vs Température

Tel que décrit précédemment, les mesures de la relaxation après une courte distance de propagation ($L = 0.48\mu$m) ont montré que l'amplitude du pic de quasiparticules diminue environ deux fois plus vite lorsque la température électronique augmente de 150 mK. Cependant, pour le même ensemble de spectres, nous avons mesuré que la température n'a aucun effet sur la quantité de courant de chaleur qui s'échappe du canal du bord.

1.7.4 Réduction de la relaxation

Dans le chapitre 8 nous démontrons que la relaxation du pic de quasiparticules injecté dans le canal de bord extérieur peut être affaibli (jusqu'à cinq fois) en découplant ce canal de bord du canal de bord intérieur voisin. Nous montrons qu'il est possible d'atteindre ce régime simplement en mettant en place une grille de déplétion, sur la surface de l'échantillon, qui est utilisée pour dévier seulement le canal de bord intérieur le long d'un trajet plus long, laissant le canal de bord extérieur se propager seul en suivant le court trajet comme illustré schématiquement sur les panneaux de gauche de la figure 1.10.

Le design de nos échantillons (Fig. 1.4) permet de modifier, in situ, la distance de propagation sur le même dispositif en polarisant une grille métallique de surface: l'électrode ***A2***. Lorsque l'électrode ***A2*** n'est pas négativement polarisé (($V_{A2} \geq 0$V), les deux états de bord se propagent librement sur le court trajet direct entre les deux boîtes quantiques. Inversement, quand il est complètement polarisé à *pinch-off* ($V_{A2} \sim -0.5$V) il pousse les deux canaux de bord à suivre un chemin plus long. De cette façon, il était possible d'augmenter la distance de propagation dans l'échantillon ***D31*** de $L = 0.75\,\mu$m jusqu'à $L = 2.17\,\mu$m. Cependant quand l'électrode ***A2*** est polarisée à une tension intermédiaire, $-0.5V \leq V_{A2} \leq 0.0$ V, nous pouvons accéder à un régime

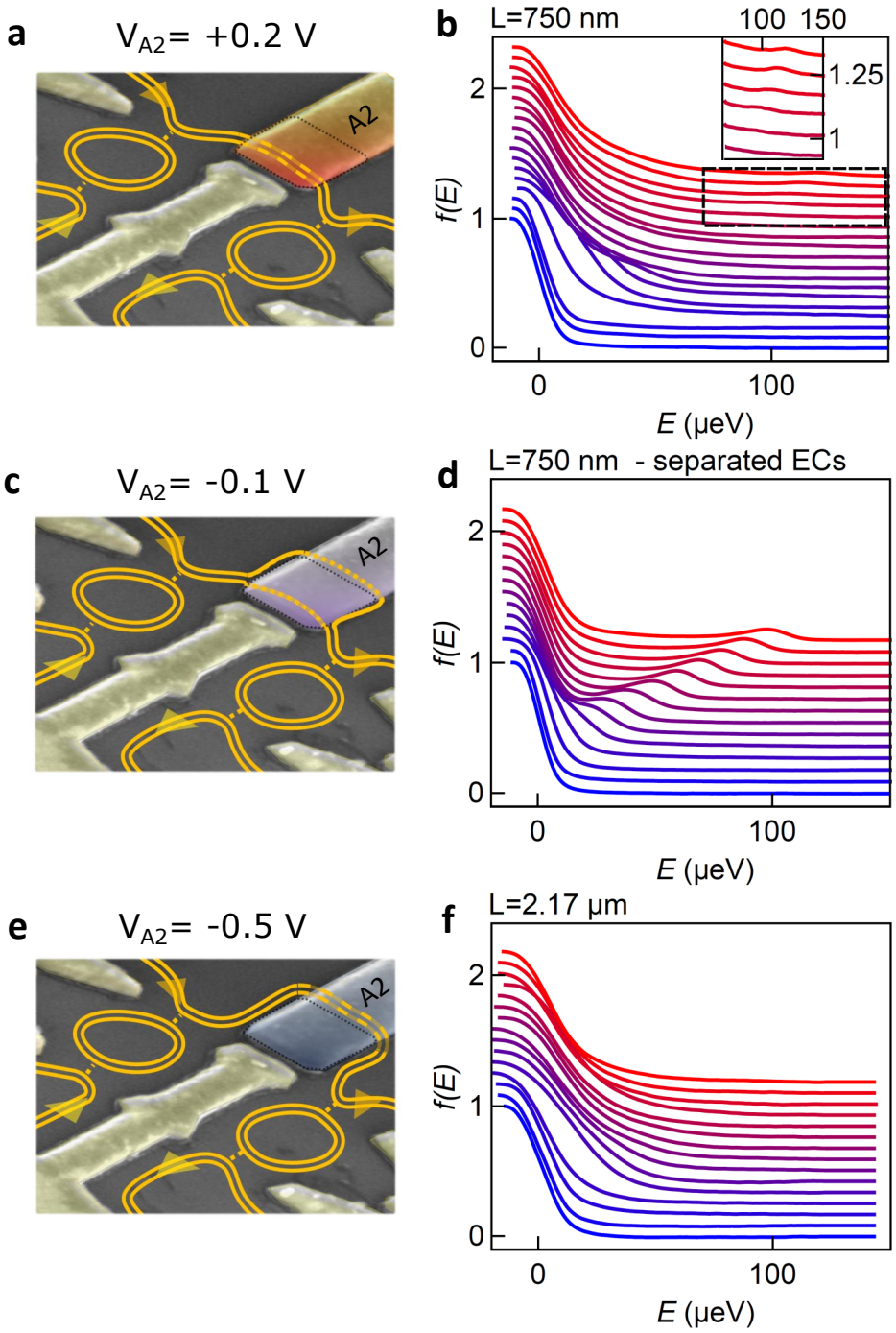

Figure 1.10: **a**, **c**, **e**: Micrographies électroniques à balayage en fausses couleurs d'un échantillon typique, représentant les trajectoires des canaux de bord pour $V_{A2} = 0.2$ V (**a**, ***A2*** grille surlignée en orange), $V_{A2} = -0.1$ V (**c**, ***A2*** grille surlignée en violet), et $V_{A2} = -0.5$ V (**e**, ***A2*** grille surlignée en bleu). Dans **a**, les deux canaux de bord co-propaguent le long d'un chemin court de $L \approx 750$ nm. Dans **c**, les deux canaux de bord sont séparés spatialement (lignes pointillées orange) lorsqu'ils passent sous la grille ***A2***. Dans **e**, les deux canaux de bord co-propaguent le long d'un chemin de $L \approx 2.17\mu$m long. **b**, **d**, **f**: Fonction de distribution $f(E)$ mesuré pour les configurations représentées respectivement dans **a**, **c**, et **e**. Chaque courbe, décalée pour plus de clarté, correspond à un incrément d'énergie d'injection $\delta E_1 \approx 9\mu eV$, de $E_1 \approx -26\mu$eV (bleu) à $E_1 \approx 122\mu$eV (rouge, **b**) et $E_1 \approx 98\mu$eV (rouge, **d** et **f**). L'encart dans **b** est un zoom sur la région délimitée par le carré noir pointillé.

différent sur lequel le couplage entre les deux états de bord co-propageant peut être syntonisé.

Une représentation schématique de ces trois régimes distincts est présentée dans la figure 1.10, ainsi que les fonctions de distribution mesurées après la propagation dans le canal du bord extérieur, où le pic de quasiparticules a été injecté. Dans le régime intermédiaire (Fig. 1.10(d)), le pic résiduel de quasiparticules détecté est remarquablement plus grand que celui mesuré dans la Fig. 1.10(b) pour la même distance de propagation, ce qui suggère que le mécanisme de relaxation habituelle a été considérablement atténué.

Ces observations adressent un aspect central dans le domaine du *electron quantum optics* qui n'a pas été démontré à ce niveau jusqu'à présent: jusqu'à quel point une excitation électronique peut-elle se propager sur le canal de bord avant de se dégrader? Avec ces expériences, nous avons déterminé les limitations imposées par la relaxation dans le régime de l'effet Hall quantique entier, dans des conditions standard, et nous avons démontré comment la relaxation peut être considérablement réduite en prolongeant au moins cinq fois la durée de vie des excitations à énergie finie.

1.7.5 Coexistence de nombreux pics de quasiparticules

Enfin, dans la dernière partie du chapitre 8 nous présentons quelques mesures où de nombreux pics de quasiparticules ont été injectés simultanément dans le canal de bord en implémentant, dans le premier boîte quantique, un niveau résonant avec des états excités.

La figure 1.11a montre les fonctions de distribution $f(E)$ mesurées après une longueur de propagation $L = 0.75\,\mu$m obtenues aux différentes énergies d'injection $E_1(V_{p1})$. Nous pouvons identifier deux pics de quasiparticules principaux situés à proximité l'un de l'autre qui sont détectés autour de l'énergie d'injection E_1. Ils peuvent être facilement vus dans la figure 1.11b qui est un zoom sur les queues des distributions présentées sur la figure 1.11a. Notez qu'il y a un petit troisième pic autour d'une énergie $E = 80\,\mu eV$ qui apparaît sur les trois premières courbes étiquetées avec l'énergie d'injection $E_1 \in \{0, 10, 20\}\mu$eV. Une analyse détaillée de cette mesure permet d'identifier chaque pic avec un état excité dans la structure des niveau d'énergies de la boîte quantique d'injection. Cela est constitué d'un état fondamental, un premier état excité à $21\,\mu$eV et un second état excité à $80\,\mu$eV.

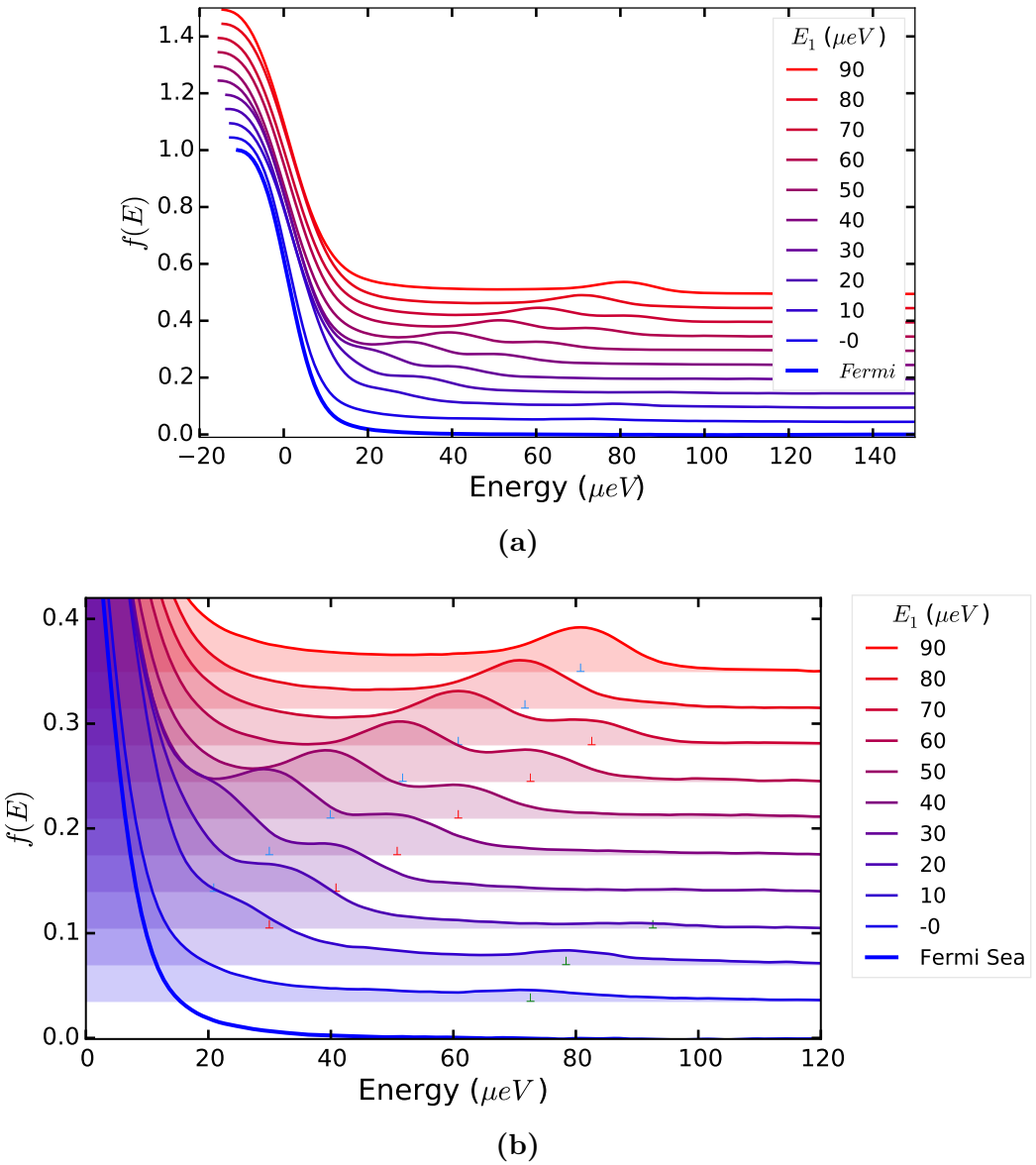

Figure 1.11: **Top:** Fonctions de distribution, à différentes énergies d'injection, mesurées dans l'échantillon ***D31*** avec une tension de polarisation $V_{A2} = -0.1$ V et avec la premier boîte quantique dans une configuration où le niveau résonant présente des états excités. Les courbes ont été décalées verticalement pour plus de clarté par un décalage constant proportionnel à l'augmentation de l'énergie d'injection $\delta E_1 = 10\mu$eV. **Bottom:** Zoom sur les queues de la fonction de distribution présentées dans le panneau supérieur montrant que différents pics de quasiparticules coexistent pendant leur propagation. Trois pics de quasiparticules peuvent être identifiés.

Chapter 2

Introduction

This chapter is a summary of the investigations carried out during this thesis. The first part introduces the general context of the mesoscopic electronic transport. I describe briefly the quantum Hall effect and the properties of the edge channels. It is followed by a discussion about the decoherence and relaxation mechanisms that can take place in this regime and how these processes have been investigated experimentally within the framework of the electron quantum optics. Several unexpected observations on those experiments as well as some open questions at the most fundamental level of different theoretical models have motivated this work. In the following I present the experiment on which we have performed an energy resolved spectroscopy of the relaxation of quasiparticles in a quantum Hall edge channel. Finally I discuss the main results and observations of this experiment on which the quasiparticle peak was directly measured for the first time in a 1-dimensional chiral edge channel.

2.1 Mesoscopic Transport in Semiconductors

Semiconductors have shown to be fascinating systems to investigate electronic transport in condensed matter. One of the reasons is that it is possible to fabricate these materials with a high level of control in the purity and the disorder of the crystalline structure. Therefore several of their intrinsic electronic properties can be designed at demand. Another reason is that there exists already a very mature technology to shape these systems down to the nano-scale where the classical transport theory starts to fail and a quantum description is needed. These degrees of tunability open a path to explore the electronic transport in a wide variety of regimes.

In particular, in 2-dimensional electron gases (2DEG) obtained in semiconductor heterostructures, the density of electrons, typically of the order of $n_s \sim 10^{11}$ cm^{-2}, is low enough such that the interactions can not be effectively screened but sufficiently high to bring those interactions at play, in a non negligible way, inducing strong quantum correlations between the particles. Moreover, the high mobility, typically of the order

of $\mu_\tau \sim 10^6$ cm^2/Vs, obtained on these systems makes possible to design electronic devices with dimensions below some of the characteristic length scales of the electronic transport, such as: the *elastic length* l_e where particles propagate without loosing energy, the *mean free path* $\bar{l}$ where particles propagates free of collisions in a ballistic fashion or even the coherence length l_φ that sets the distance over which the particles keep the phase associated to its wave nature. Consequently, signatures of the quantum character of electronic transport are reflected on measurable macroscopic quantities like the current and the resistance. This regime is better known as the mesoscopic transport regime.

In GaAs/AlGaAs 2DEG many hallmark mesoscopic phenomena have been observed. For example the quantization of the conductance in a ballistic regime [1, 2, 3]; the Coulomb blockade effect in highly confined systems like quantum dots [4, 5]; and quantum interference between particles like in the Aharonov-Bohm effect realized in ring geometries [6, 7] or the weak localization observed in disordered systems [8]. Of particular interest on this thesis is the ***integer quantum Hall effect*** [9] that is observed when a 2DEG is under a strong perpendicular magnetic field and at low enough temperature. This is a striking robust quantum phenomena that radically changes the usual classical laws for describing the electronic transport even in the most simple resistive circuit.

2.2 The Quantum Hall Effect

In the semi-classical theory, charged particles under a magnetic field move in cyclotron orbits as a consequence of the Lorentz force. While the cyclotron frequency ω_c is fixed only by the magnetic field B, the radius of the orbit r_c depends both on the magnetic field and the energy E of the particle:

$$w_c = \frac{eB}{m} \qquad\qquad r_c = \frac{v}{w_c} = \frac{\sqrt{2Em}}{eB} \tag{2.1}$$

Since the particles in a conductor have a maximum energy of the order of the Fermi energy E_F, by increasing the magnetic field the radius can be made so small that it becomes comparable to the *de Broglie* wavelength of the particle. Hence quantization effects of the energy and the orbital radius are expected to arise in the limit of high magnetic fields. In fact the main electronic properties of a 2DEG under a strong perpendicular magnetic field are described by the quantum theory in terms of Landau levels. These are discrete energy levels, separated by $\hbar\omega_c$ as represented in Fig. 2.1a, that result directly from the quantization of the cyclotron motion.

In order to observe the effects of the Landau quantization in the transport properties, two main conditions have to be satisfied: First, the electrons need to be able to perform at least a complete cyclotron orbit before being scattered out, which implies

that $\omega_c\tau = B\mu_\tau \gg 1$; Second, the electronic temperature T needs to be small enough such that only one Landau level is thermally excited at a time $k_bT \ll \hbar\omega_c$.

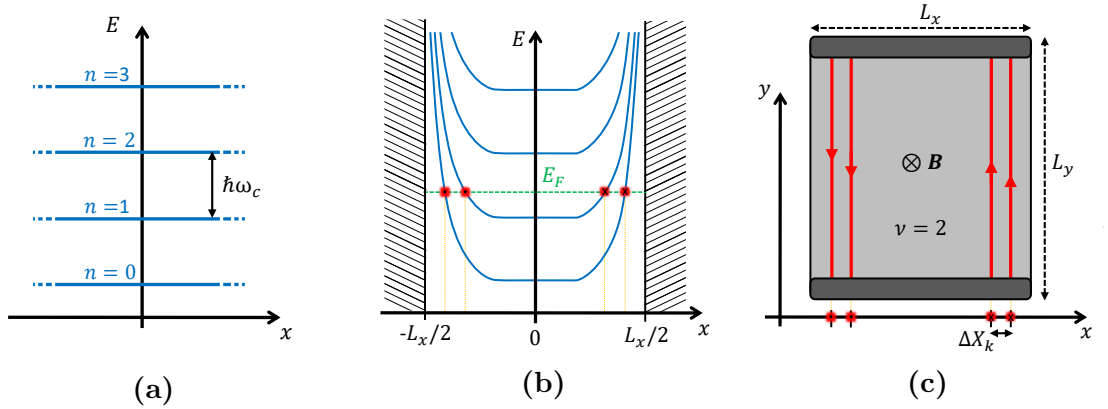

Figure 2.1: **(a)** Flat Landau levels $E_n = \hbar\omega_c(n + 1/2)$ formed in an infinite 2DEG under a uniform magnetic field $\boldsymbol{B}$. **(b)** Landau level formed in a system with finite size L_x along the $\hat{x}$ direction. The confinement potential created at the boundaries (here represented as hard walls) bends up the Landau levels. **(c)** Each time a Landau level crosses the Fermi level E_F in **b**, a chiral edge state develops on the sample located at the position of the crossing. The number of edge states is given the number of filled Landau level at the bulk of the system.

Additionally, when a 2DEG with finite size is considered the Landau levels are modified near the boundaries of the system: they are bent up as a consequence of the confining potential that defines the boundaries (Fig 2.1b). Nevertheless in the bulk, Landau levels remain flat (if there is no disorder) and separated by the cyclotron energy $\hbar\omega_c$.

Furthermore, the energy of the Landau Levels can be tuned with the magnetic field to let the Fermi energy E_F laying in between two bulk levels. In this condition the bulk becomes insulating and the only possible low energy excitations are located near the edges. It means that in this regime the electrons can propagate only along the borders of the system in the so called ***edge states*** [10]. As detailed in Fig 2.1b and 2.1c an edge state is developed each time a Landau levels crosses the Fermi energy and it is located in the system at the position where the crossing takes place. In this simple representation, the number of edge channels is given by the integer part of the filling factor $\nu = n_s h/eB$, which corresponds to the number of bulk landau levels that are below the Fermi level.

The classical chirality imposed by the magnetic field in a cyclotron motion is reflected here by the fact that edge states propagating in opposite directions are located in opposite sides of the system, usually separated by a macroscopic distance. As a consequence, backscattering is suppressed and the propagation of electrons results robust against impurities and disorder. In this regime the transport is said to be chiral and topologically protected: the particles propagate on the edge channels in a ballistic fashion. For these reasons the edge states of the quantum Hall effect have been considered as good candidates of *ideal 1-dimensional quantum wires* where the particles

can propagate coherently and without dissipation.

2.3 Electron Quantum Optics

The peculiar properties of the propagation of electrons in the edge channels of the integer quantum Hall regime has motivated physicist to perform quantum optics-like experiments where electrons are use to mimic propagation of photons in quantum optics experiments. Progress in this direction has lead to the recent development of a field within the mesoscopic transport that is known as *electron quantum optics*.

During the last decades a considerable effort has been done in order to determine how far this analogy can be extended. While the ballistic properties of the edge channels provides the beam like motion of the electrons, it was also demonstrated that electrostatic nanostructures such as quantum point contacts (QPC) and quantum dots (QD) could be efficiently implemented as the electronic analogous of beam spliters and energy filters. Moreover, recently several types of single electron sources have been developed in order to perform these experiments with unique particles [11, 12, 13, 14, 15, 16, 17].

In condensed matter physics, the Fermi character of the electrons as well as the Coulomb interaction are expected to play an important role. Electron quantum optics experiments provide a way to probe the analogy between the coherent propagation of electrons and photons, but also to highlight their differences.

A major aspiration of this field is to investigate and to understand the importance of the electronic interactions in order to be able to manipulate the quantum state of single excitations in quantum Hall edge channels. This would provide a promising platform for the implementation of electronic flying qubits for quantum information [18, 19]. In quantum computation, the flying qubits are needed for the coherent transmission of the information between separated parts of the physical network [20, 21]. The robust chiral propagation of electrons in the quantum Hall effect regime offers great advantages for this purpose since the electron trajectories can be manipulated easily with electrostatic gates. Moreover, electronic flying qubits have been proposed to be implemented, not only to transfer information but to perform logic operations since the information can also be encoded in the trajectories of the electrons [21]. Therefore a fundamental step is to determine how far the electrons can propagate coherently and free of relaxation along the quantum Hall edge channels.

In this thesis we address this question by experimentally investigating the relaxation of quasiparticles emitted at a well defined energy above the Fermi sea of an edge channel in the integer quantum Hall regime at filling factor $\nu = 2$. This experiments probes the strength of the interactions in the IQHE regime which allows the particles to exchange energy and therefore to relax.

2.4 The Role of Interactions

The simple quantization of the cyclotron motion of electrons is good enough to explain many experimental observations of the electronic transport in the integer quantum Hall regime but it is only a non interacting description. Since it does not take into account the interactions, little can be known about the relaxation and decoherence of quasiparticles.

The role of the interaction in electronic systems is a very fundamental question that was originally considered in the Landau theory of Fermi liquids [22, 23, 24]. It describes a Fermi gas where the Coulomb interactions between particles are turned on adiabatically from the non interacting case. This results in a system, the Fermi liquid, whose ground state is still a Fermi Sea and the low energy excitations are still described by long-lived single-particle states that follow a Fermi statistic.

However the *adiabatic hypothesis* does not always hold. A well known example is the case of a superconductor, whose ground state is radically different to a Fermi sea. Consequently it can not be described by this theory. Another case where the adiabatic hypothesis is expected to fail are low dimensional systems because the effects of the interactions are usually enhanced due to the extra confinement, in consequence unusual many body effects have been suggested to occur. The Luttinger liquid theory [25, 26] describes a 1-dimensional interacting Fermi gas and predicts instead that the excitations in this system are better represented by bosonic quasiparticles that consist of collective excitations [27, 28].

In this context, the very nature of quasiparticles propagating in chiral quantum Hall edge channels is still under investigation [29, 30, 31]. Due to its 1-dimensional character, it is not clear to what extent the fundamental low energy excitations can be represented as stable Landau quasiparticles. In the experiments carried out in this thesis we directly probe how far the quasiparticles can propagate before decaying into collective excitations.

2.5 Decoherence in Edge Channels

During the last two decades several experiments were performed to investigate the properties of the edge states in the integer quantum Hall regime, mainly at filling factor $\nu = 2$.

Mach-Zehnder interferometers (MZI) have been implemented to investigate the coherence properties of the edge channel by producing quantum interference reflecting the ballistic and coherent propagation of electrons [32, 33, 34, 35, 36] . Interferences with a visibility as high as 90% were obtained [37] and coherence lengths of the order of $20\,\mu m$ at a temperature of $20\,mK$ were experimentally determined [33]. Later it was also shown that the electrical noise present in the co-propagating edge channel and the

environment was a source of decoherence that could be manipulated [38, 39].

The development of an on-demand single electron source that ensures a good control on the emission time and energy resolution of a wave packet has opened a way to investigate the decoherence at the the single particle level [11, 40]. Two-particle interferences in the Hong-Ou-Mandel configuration were implemented suggesting that the decoherence of single particles results indeed from the emergence of collective excitations induced by Coulomb interaction between the two co-propagating edge channels [41, 42, 43].

Some of these observations were in good agreement with the theoretical model that describe the two co-propagating edge channels coupled by Coulomb interaction in term of the Luttinger liquid theory [44, 45, 46]. However, other recent experiments performed with MZI, where particles were injected above the Fermi sea at a well defined energy, demonstrated a robust quantum coherence at high energy: it was observed that above a threshold energy, the visibility of the interference fringes remain constant and independent of the energy [47]. These results are in strong contradiction with the theoretical models that instead predict a continuous decrease of the visibility as a function of the injection energy.

Explanations for the unexpected observations in interference experiments are still under debate. Moreover, since the interactions provide a way to exchange energy between the particles of the system, the investigation of the relaxation mechanisms in the edge channels can give new insights to better understand the role of the interactions at the most fundamental level.

2.6 Relaxation in Edge Channels

Experiments that investigate the energy relaxation consist basically in bringing the system out of equilibrium, in some controllable way, and then measure *how* it comes back to the equilibrium state. By doing that we can investigate the relaxation mechanism and probe its dependencies with other parameters such as the electronic temperature, the propagation distance or the particular electromagnetic environment. This idea was implemented to investigate the role of the interactions in various mesoscopic systems like metallic diffusive wires [48], carbon nanotubes [49], nanostructures in semiconductor [50] and recently in the edge channels of the IQHE [51, 52] at filling factor $\nu = 2$. Since the propagation in the quantum Hall regime is chiral the evolution of the out-of-equilibrium state can be followed along the edge of the sample: time and distance are related simply by the drift velocity v_d.

In Ref. [51] it was demonstrated that a direct measurement of the distribution function $f_r(E)$ in the edge channel can be obtained from the tunneling current I_{QD} trough a quantum dot that is weakly coupled to the edge channel. This spectroscopy technique relies on the elastic and sequential tunneling of electrons trough a single

discrete level in the quantum dots whose energy E_2 can be electrostatically manipulated to probe the distribution function of the edge channel at different energies. If the edge channel to be investigated is at the source of the quantum dot, then the tunneling current simply reads:

$$I_{QD}(E_2) = I_{max}\Big(f_r(E_2, \mu_r) - F_d(E_2, \mu_d)\Big) \tag{2.2}$$

where I_{max} is a constant determined by the characteristics of the quantum dot and F_d is the Fermi function at the drain reservoir on which a finite bias voltage V_d is applied in order to separate the electrochemical potential of drain (μ_d) and source (μ_r) reservoirs: $|eV_d| = \mu_r - \mu_d$.

As it will be discussed in chapter 5, this method was implemented to measure the relaxation of an out-of-equilibrium state injected on the edge channel which consists of a double step distribution function $f_i(E)$ generated with a quantum point contact set at an intermediate transmission $\tau_{qpc} \sim 0.5$ and biased with a voltage V_1. Thus, the QPC mixes the Fermi distributions[1] $F(E)$ of a grounded ohmic contact with the Fermi distribution $F(E - eV_1)$ of the biased ohmic contact:

$$f_i(E) = \tau_{qpc}F(E - eV_1) + (1 - \tau_{qpc})F(E) \tag{2.3}$$

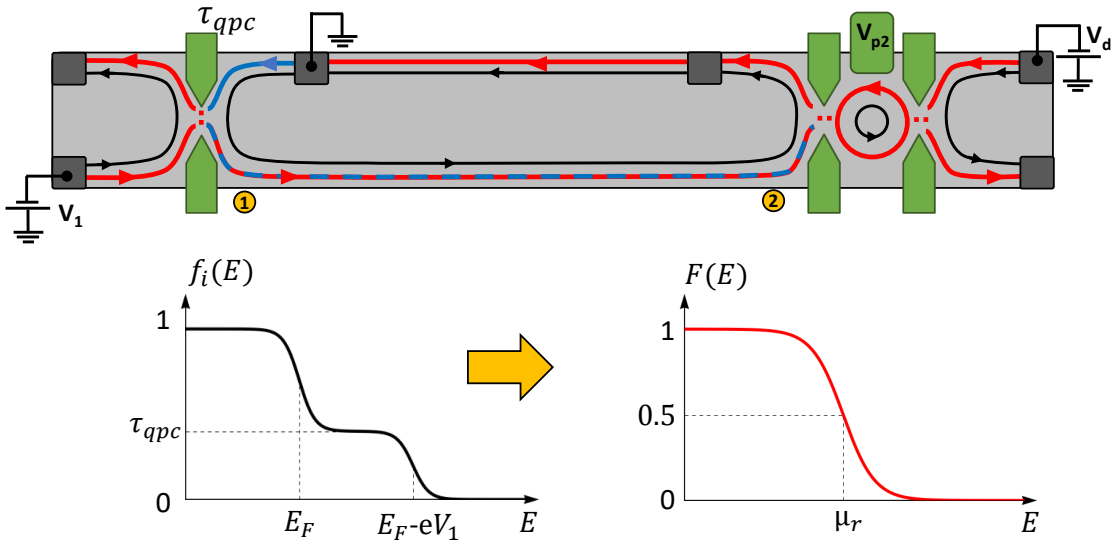

Figure 2.2: Top: Schematic representation of the experimental configuration to investigate the relaxation of a double step distribution function in the IQHE regime at filling factor $\nu = 2$. The biased QPC at intermediate transmission τ_{qpc} creates a double step distribution function f_i in the outer edge channel. After few micrometers of propagation, where relaxation takes place, the resulting distribution f_r is measured with a quantum dot implemented as an energy filter. (**Bottom:**) Initial and final state of the distribution functions before and after the relaxation process.

[1] Fermi functions are represented in capital letter $F(E)$ while other distribution function are represented in small letter $f(E)$.

Fig. 2.2 illustrates the experimental configuration for the investigation of the relaxation of the double step distribution function injected in the outer edge channel obtained in the integer quantum Hall regime at filling factor $\nu = 2$. On these experiments it was demonstrated that after a short distance, of about $0.8\,\mu$m, the injected out-of-equilibrium state does not relax at all. Subsequent experiments showed that the relaxation process takes place progressively while the particles propagates along few micrometers. A full relaxation towards a hot electron regime was measured to be achieved at a distance of $10\,\mu$m [52] and to remain unchanged at large distances, up to $30\,\mu$m.

The Coulomb interaction between the two co-propagating edge channels, that are only capacitively coupled, was identified as the mean source of relaxation. In fact a direct energy exchange was observed between the two edge channels and it was shown that this energy exchange could be prevented by forcing the inner edge channel to form loops. When the inner edge channel forms loops, its density of state becomes discrete as in a quantum dot, thus the outer edge channel is now coupled to a quantized spectrum instead of continuous spectrum. This limits the energies at which they can exchange energy reducing the relaxation of the double step distribution function that was injected in the outer edge channel [53].

Although some of the observations are in good agreement with the scenario of two interacting edge channels capacitively coupled, it was also observed that 25% of the injected heat current leaks out of the system constituted by the two edge channels suggesting that there could be extra degrees of freedom that play an unexpected role in the relaxation mechanism and that were not considered in previous theoretical models [52, 54, 55].

In chapter 5 we present measurements that we have performed in the same regime, to investigate the relaxation of a double step distributions function, which are in agreement with the main results of the experiments originally done in the Phynano team of the C2N(LPN) laboratory [51, 52]. In these experiments we have verified that in our samples, which have a different geometry, we observe the same relaxation rate for the double step distribution function, meaning that the relaxation process is not strongly affected by the particular disorder or the specific geometrical configuration of the metallic electrodes that define the device. Our measurements are in agreement with the fact that the double step distribution function relaxes towards a hot electron regime within the $10\,\mu m$ of propagation.

Furthermore, we observed the same energy leak of $\sim 25\%$ from the whole system constituted by the two interacting edge channels. This is an important verification of the observation done first in Ref. [52] that we quantitatively reproduce for the first time and which suggest that it is in fact an intrinsic characteristic of the relaxation mechanism. This energy leak can be seen in the measured excess temperature T_{exc}, which is proportional to the square root of the heat current in the edge channel, that is

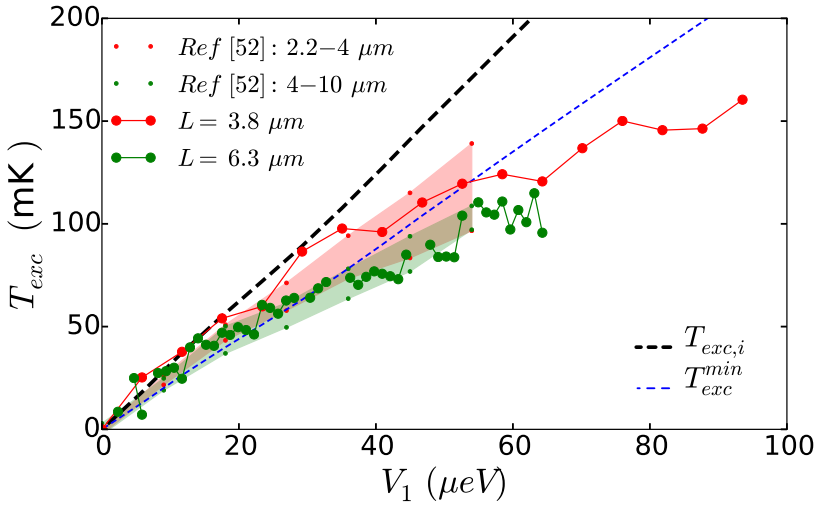

Figure 2.3: Excess temperature measured after the short (long) propagation distance plotted using big red (green) filled symbols as a function of the bias voltage V_1 across the QPC. Our measurements fall within the corresponding expected range represented by the red (green) shaded region for the short (long) distance. These shaded regions were determined using the data presented in Ref. [52] (See chapter 5 for further details). In **a** the *energy conservation on the edge channel* is indicated by the thick black dashed line ($T_{exc,i}$), while *energy conservation in the whole system of two interacting edge channels* is indicated by the thin blue dashed line (T_{exc}^{min}) which is a lower bound predicted by the theory.

presented in Fig 2.3 as a function of the bias voltage V_1 in the QPC for two propagation lengths, $L = 3.8\mu$m (red) and $L = 6.3\mu$m (green). Here, the energy leak manifests as the increasing deviation seen in the measured points at large bias voltage and large distance from the diagonal line T_{exc}^{min} (blue thin dashed line) which is the lower bound predicted by all the theoretical models.

2.7 Finite Energy Relaxation

While the experiments described up to now have clearly demonstrated that the inter-channel interactions at filling factor $\nu = 2$ are the main source of decoherence and relaxation, they also showed that these processes could be controlled and suppressed up to some level. However, the missing energy also suggest that the current understanding of the relaxation mechanism is not complete. Moreover, there remains still fundamental questions that could not be answered from these experiments: ***How a quasiparticle peak, well defined in energy, will relax toward the Fermi sea?*** and ***How far can energy resolved excitations propagate in an edge channel before relaxing?***. These are basic questions originally addressed in the Landau theory of Fermi liquids which are of fundamental importance for the coherent manipulation of quasiparticle in the QHE regime for future applications.

In this thesis we address these questions and provide experimental evidence of the decay of a quasiparticle peak by performing a finite energy spectroscopy of the

relaxation of quasiparticles injected, at a well defined energy, above the Fermi sea in a quantum Hall edge channel. Experiments are performed on a GaAs/AlGaAs based 2DEG with electron densities ranging $n \approx 2.5 \times 10^{11}$ cm^{-2} and mobility of the order of $\mu_\tau \sim 2 \times 10^6$ cm^{2}V^{-1}s^{-1}. The 2DEGs are grown at the C2N laboratory by A. Cavanna and U. Gennser.

2.7.1 Experimental Configuration

Our setup relies on a pair of electrostatically defined quantum dots, used as energy-resolved emitter and detector as illustrated in Fig. 2.4. The device is fabricated at the C2N laboratory by D. Mailly using electron beam lithography. The first quantum dot is defined by the set of gates $\{G1, G2, G3, G4\}$ in the left side, and the second quantum dot is defined by the set of gates $\{G1, G6, G7, G8\}$ in the right side. The emitter is realized by applying a finite drain-source voltage V_1 on the first quantum dot (**1**), with a single resonant level in the bias window (**2**). The position of the resonant level, which is controlled with the plunger gate voltage V_{p1}, sets the energy E_1 at which electrons are emitted above the drain Fermi energy E_F (**3**). Therefore, the injected out-of-equilibrium distribution function $f_i(E)$ consist on the equilibrium Fermi sea $F(E)$ and the emitted quasiparticles with a Lorentz distribution $L(E, E_1)$ centered at the energy E_1 whose amplitude $\mathcal{T}_1$ and width Γ_1 are determined by the characteristics of the resonant level in the first quantum dot.

$$f_i(E) = F(E, E_F) + L_1(E, E_1) \tag{2.4}$$

After a tunable propagation length in the micrometer scale (from **3** to **4**), we perform an energy resolved spectroscopy of the emitted electrons using the second quantum dot as an energy filter (**4**, **5**, **6** and **7**) in a similar way as it was done for the spectroscopy of the double step distribution function (Section 2.6).

2.7.2 Quasiparticle Peak Relaxation

In chapter 6 we present data that we obtained by implementing the device of Fig. 2.4 which constitutes the first experimental observation of a quasiparticle peak above the Fermi sea of an edge channel.

Relaxation vs Injection Energy

The Figure 2.5 shows a measurement performed after a short propagation distance $L = 0.48\,\mu$m at a temperature $T_0 = (23.1 \pm 0.6)$mK. The figure displays the measured Fermi sea at equilibrium and all the measured distributions at different injection energies $E_1 \in \{22, 43, 65, 87, 108, 130, 152, 173\}\mu$eV. If there was no relaxation, the expected amplitude of the quasiparticle peak is $\mathcal{T} \sim 0.3$. Although we observe an increasing

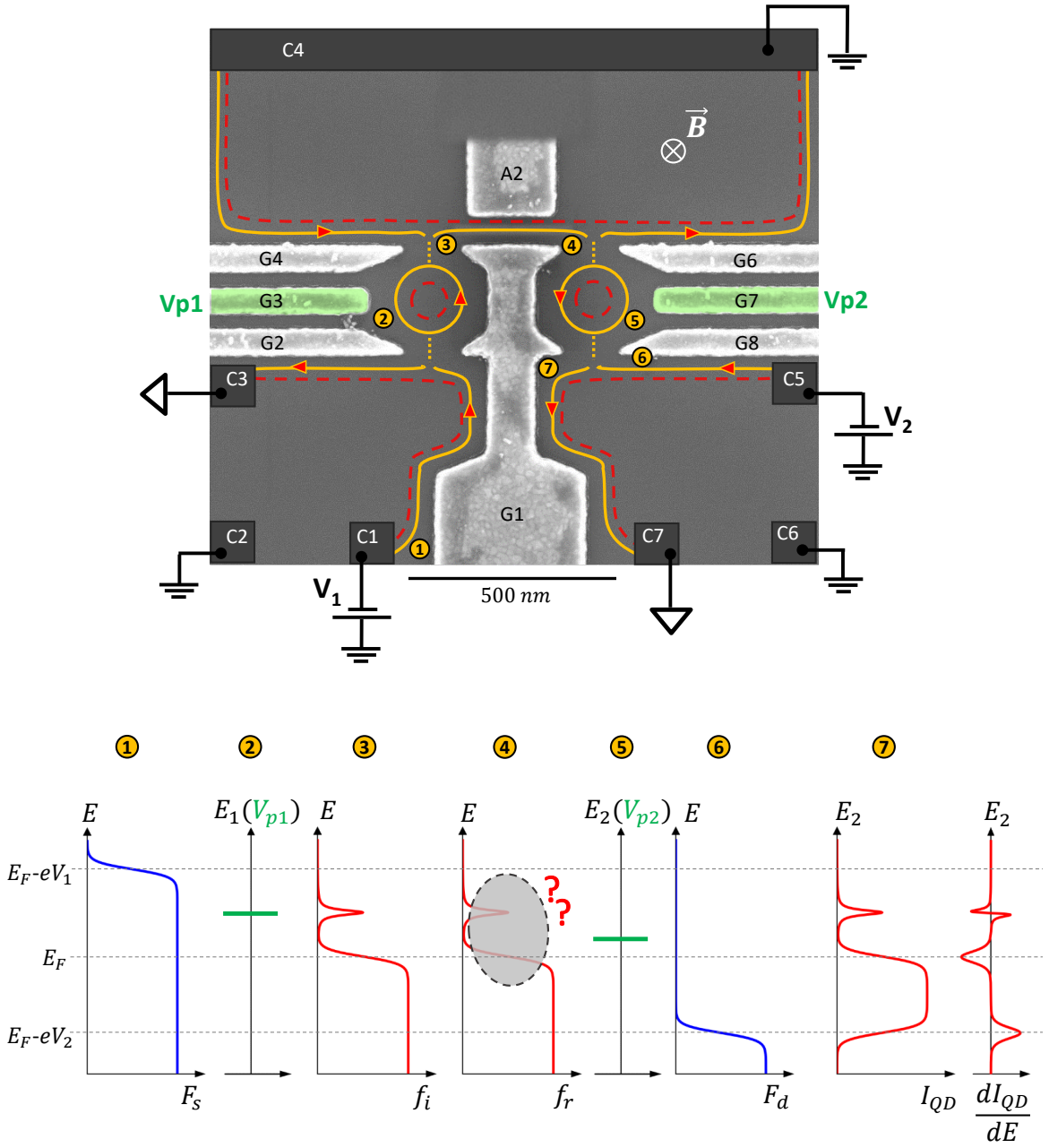

Figure 2.4: **Top:** Scanning electron micrograph of the sample ***E33***. Two quantum dots are electrostatically defined in order to perform an energy resolved spectroscopy of the relaxation in an edge channel. The two QDs are tunnel coupled only to the outter edge channel, while the inner edge channel is fully reflected by all the electrodes that define the two QDs. The first QD (left) injects quasiparticles above the Fermi sea in the edge channel that comes from the grounded contact $C4$. The injected excitations propagates in the edge channel, from **3** to **4**, until they reach the second quantum dot (right) that is implemented as a detector. **Bottom:** Energy diagram and distribution of particles in different parts of the device. The injection scheme is represented by **1**, **2**, **3**. The propagation happens between **3** and **4**. The detection scheme is represented by **4**, **5** and **6**. The expected signal to be measured in the transconductance across the second quantum dots is represented by **7**. See text for further details (section 6.2). The devices are fabricated at the C2N laboratory where the 2DEGs are grown by A. Cavanna and U. Gennser, while the metallic nanostructures are fabricated by D. Mailly.

relaxation as the injection energy E_1 is increased, the peak structure was still detected in all the curves. These observations, obtained at filling factor 2 of the quantum Hall

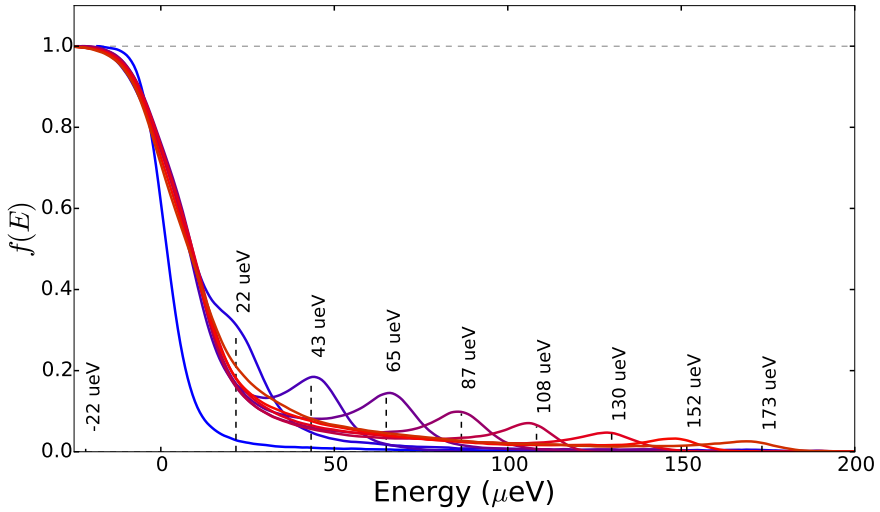

Figure 2.5: ***Spectrum R-72.*** Evolution of the distribution function $f(E)$ measured after a propagation distance $L = 0.48\mu$m while increasing the injection energy E_1, indicated by the vertical dashed lines, around which is centered a peak structure that is the remnant of the injected quasiparticle peak. The equilibrium Fermi sea (the lighter blue line) with electrochemical potential $E_F \sim 0\mu eV$ was measured when no particles were injected ($E_1 = -22\mu eV < E_F$).

effect, shows that although the propagation over a sub-micrometer distance leads to an important relaxation of the injected peak, a small portion of the quasiparticles survives to the relaxation even at relatively high energies, up to 175 μeV.

As presented in Fig. 2.6, a detailed characterization of the evolution of the quasiparticle peak as a function of the injection energy E_1 shows that the relaxation process that took place along the propagation does not affect the energy at which the peak is centered being always found around the injection energy E_1. Additionally the peak shape was found to be still well described by a Lorentz function whose width Γ_L (FWHM) remains constant and independent of the injection energy. More importantly, these measurements showed that the amplitude of the quasiparticle peak decreases following and exponential decay as a function of the injection energy. The characteristic energy E_{decay} of the exponential decay was found to be of the order of $E_{decay} \sim 60\,\mu$eV for a propagation distance $L = 0.48\mu$m at a temperature $T_0 = 23.1 \pm 0.6$ mK.

Relaxation vs Length

Furthermore, we have observed that the characteristic energy E_{decay} is strongly affected by the electronic temperature T and the propagation distance L. On the one hand, an increase in the electronic temperature of $\Delta T = 150$ mK reduces the decay energy E_{decay} by almost a factor two. On the other hand, an increase in the propagation length from $L = 0.48\,\mu$m up to $L = 0.75\,\mu$m leads to a decrease in the decay energy from $E_{decay} \sim 60\,\mu eV$ toward $E_{decay} \sim 20\,\mu eV$. The effect of the distance is shown in the Fig. 2.7b which display the distribution function measured at each distance for different injection energies and the exponential decay of the quasiparticle peak's

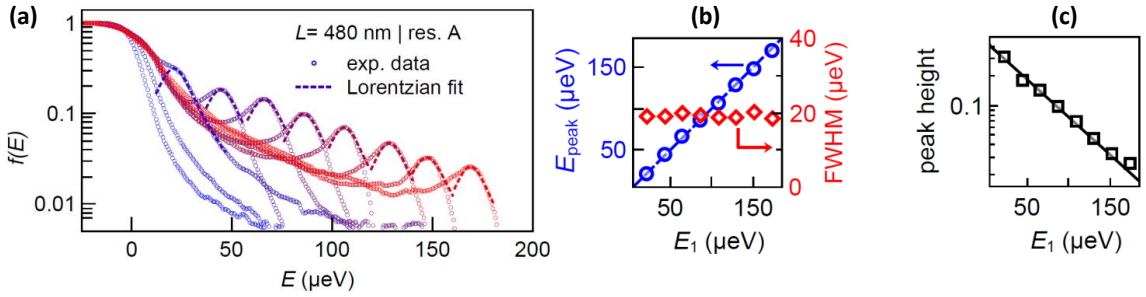

Figure 2.6: **(a)**Measured distribution function $f(E)$ in semi-log scale in order to highlight the evolution of the quasiparticle peak while increasing the injection energy E_1. The dashed line corresponds to Lorentzian fits of the quasiparticle peak. **(b)** Center of the peak E_{peak} (blue circles) and full width at half a maximum FWHM (red diamonds) extracted from the Lorentzian fits plotted versus injection energy E_1. The blue dashed line is a y = x line. **(c)** Peak height (black squares) extracted from the fits shown in **a** versus E_1, in semi-log scale. The black line is an exponential decay fit.

amplitude.

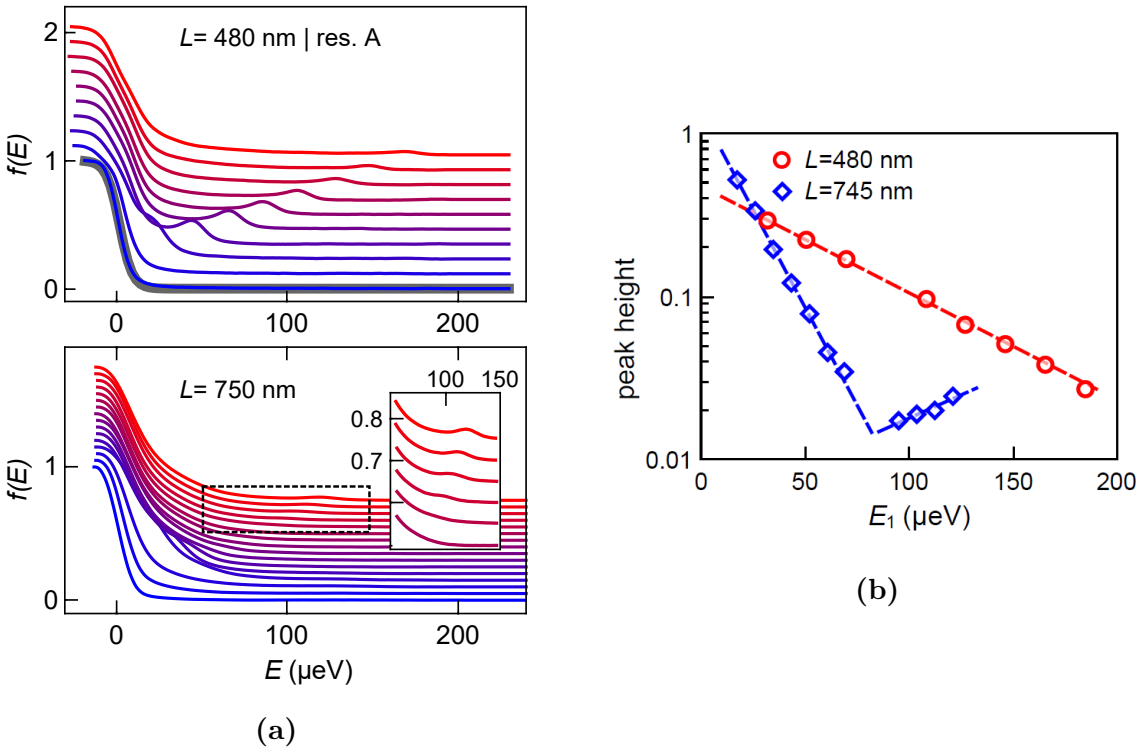

Figure 2.7: **(a)** Distribution functions after the propagation. The curves were vertically shifted for clarity. **Top:** Spectrum measured in sample ***E33*** for $L = 0.48\,\mu$m. Each curve, correspond to an increment of the injection energy $\delta E_1 \approx 21\mu$eV, from $E_1 = -21\mu$eV (blue) to $E_1 = 173\mu$eV (red). The thick grey line is a Fermi function fit of the data at $E_1 = -21\mu$eV. ***Bottom:*** Spectrum measured in sample ***D31*** for $L = 0.75\,\mu$m. Each curve, correspond to an increment of the injection energy $\delta E_1 \approx 9\mu$eV, from $E_1 = 9\mu$eV (blue) to $E_1 = 121\mu$eV (red). **(b)** Peak height extracted from the Lorentzian fits illustrated in Fig. 2.6, plotted in semi-log scale as a function of injection energy E_1 for the two propagation lengths $L = 0.48\,\mu$m (red circles) and $L = 0.75\,\mu$m (blue diamonds) shown in **a**. The red and blue dashed lines are exponential fits.

A comparison of the distributions of particles observed at several distances for a quasiparticle peak injected approximately at the same energy $E_1 \approx 40\,\mu$eV is shown in the figure 2.8. Together with the precedent analysis of the quasiparticle peak behavior this comparison allows to describe how the relaxation mechanism brings the system to equilibrium. At first, a large amount of the injected particles lose energy and the amplitude of the injected quasiparticle peak rapidly decays in a sub-micrometer propagation distance. Notice that no relaxation was observed for sub-micrometer distances when the propagation of a double step distribution function was investigated [51]. Once the quasiparticles peak has almost vanished at a distance of about $\sim 1\mu$m what is left is a non-Fermi distribution, with no sharp features and a long tail that extends in a wide range of energies, which is still out of equilibrium. As can be qualitatively seen in the Fig. 2.8 this distribution does not change much while it propagates up to $3.4\,\mu$m. In fact, at this point it resembles an intermediate state of the relaxation process of the double step distribution which was seen to finally achieve the equilibrium at large distances $\sim 10\mu$m.

Therefore we can distinguish two time scales in the relaxation process, which were first pointed out in the theoretical model described in Ref. [56]. The first step of the relaxation process, that occurs on sub-micrometer lengths, brings the injected particles closer to the Fermi sea decomposing the quasiparticle peak into an extended distribution of particles that spreads over the whole energy range. The second step in the relaxation process, that brings the resulting extended distribution of particles into a Fermi sea, occurs over several micrometers of propagation.

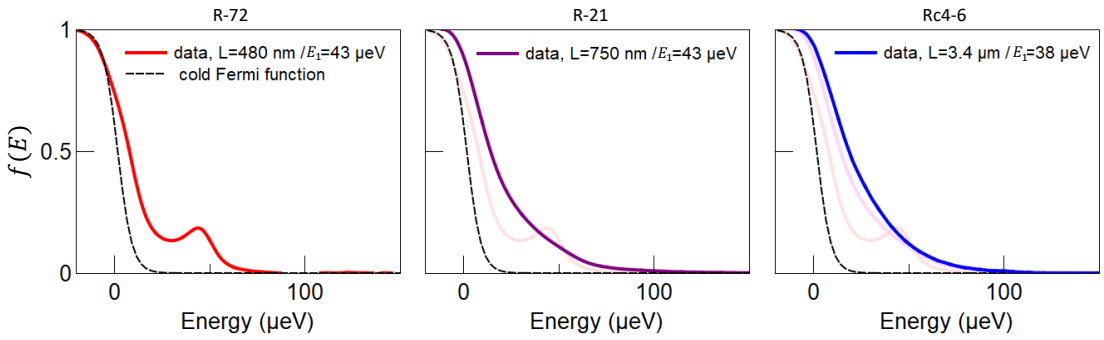

Figure 2.8: Measured distribution function (continuous line) for similar injection energy E_1 at increasing propagation distances: $L = 480$nm (**left**), $L = 750$nm (**middle**) and $L = 3.4\mu$m (**right**). The dashed line is the equilibrium Fermi sea measured in each case when no particles were injected.

Signatures of a Quasiparticle Peak Revival

Additionally, for a propagation distance $L = 750$ nm and at low temperature $T \sim 20$ mK, we have observed signatures of a quasiparticle peak revival. As it can be seen in Fig. 2.7b the amplitude of the quasiparticle peak not only suddenly deviates

from the exponential decay near $E_1 \sim 80\,\mu$eV, but surprisingly it increases as the injection energy increases. This behavior was observed in several spectra measured using different electrostatic configuration in both quantum dots which allows to rule out artifacts caused by possible excited states or charge instabilities in nearby electrodes. Although the theoretical model proposed in Ref. [57] does not explain the exponential decay of the quasiparticle peak's amplitude, it predicts an oscillatory behavior of the peak's amplitude as a function of the injection energy E_1 which could explain our observations.

2.7.3 Heat Current

In chapter 7 we investigate the heat current $J(E)$ carried by the electron-hole excitations created in the injected distribution function $f_i(E)$, which provides direct information about the exchange of energy in the system due to the relaxation process.

Heat Current vs Injection Energy

The injection of quasiparticles with a Lorentz distribution $L_1(E, E_1)$ centered around the injection energy E_1 leads to an increase in the electrochemical potential $\Delta\mu$ given by:

$$\Delta\mu = \int L_1(E, E_1)dE \tag{2.5}$$

which is related to the charge current in the edge channel. Additionally, the injection of new particles also leads to an increase in the heat current ΔJ_i since new electron-hole excitations have been created on the system. The heat current increase ΔJ_i that have been injected is expected to follow a linear behavior as a function of the injection energy E_1, given by:

$$\Delta J_i(E_1) = (E_1 - \mu)\Delta\mu + \frac{1}{2}(\Delta\mu)^2 \tag{2.6}$$

Remarkably, as shown in the Fig. 2.9 for two propagation distances $L = 0.48\mu$m (left) and $L = 0.75\,\mu$m (right), we observe a large discrepancy between the injected heat current ΔJ_i (red line) and the detected heat current ΔJ_r (black line with symbols) measured after the propagation. In both cases, we can see that, at high injection energy E_1, the detected heat current is much smaller than what was expected, indicating that the energy in not conserved on the edge channel. As it was clearly demonstrated by H. le Sueur *et al.* [52], the interaction with the co-propagating edge channel induces an energy exchange between the two edge states, which is expected to be, in part, responsible of the observed discrepancy on Figure 2.9a and 2.9b.

However, the different theoretical models that describes this interacting system, within the framework of chiral fermions [54] or within the framework of the Luttinger liquid theory which suggest the development of plasmon excitations [58, 55], predict that the interaction leads to an energy equipartition between the edge channels. In

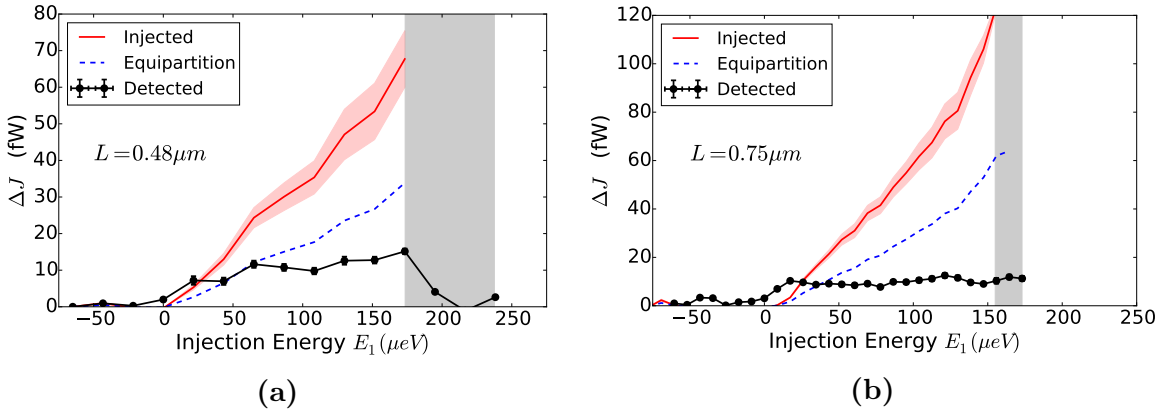

Figure 2.9: Comparison between the excess heat current ΔJ_i that was injected (red line) on the edge channel and the excess heat current ΔJ_r that was measured after a propagation (black symbols). Each plot corresponds to measurement taken after a propagation length $L = 0.48\mu$m (**a**) and $L = 0.75\mu$m (**b**). In the two cases the blue dashed line represent the lower bound ΔJ_r^{min} that is predicted by all the theoretical models as a consequence of the energy equipartition between the two co-propagating edge channels. The area shaded in grey correspond to the final part of the spectroscopy, where the injection energy is reaching its maximum value and the discrete level in the first quantum dot is going out of the bias windows.

consequence there is a lower bound ΔJ_r^{min} for the remaining heat current on the edge channel which is expected to be achieved at full relaxation. This lower bound is indicated by the blue dashed line for the measurements shown on the Fig. 2.9. It is clearly seen that the remaining excess heat current measured after the propagation is well below the lower bound. We observe that there is up to 70% less remaining energy than ΔJ_r^{min} for a propagation distance $L = 0.75\mu$m.

These measurements show that there is a very large energy leak which is not in agreement with any of the current theoretical models that describes the interaction in the integer quantum Hall regime at filling factor $\nu = 2$. Additionally, when the relaxation of the double step distribution function was measured we observed a smaller energy leak, in agreement with the results reported in Ref. [52] (See Fig. 2.3). Our measurements in both regimes absolutely rules out possible experimental artifact that could lead to an *apparent* energy leak. While a constant 25% of energy leak was observed on the relaxation of the double step distribution function, here we report that the relaxation of energy resolve excitations leads to an energy leak that strongly depends on the injection energy E_1 of the quasiparticle peak. Therefore the amount of energy lost during propagation suggests that relaxation mechanisms towards external degrees of freedom play an important and unexpected role in electron quantum optics experiments.

Heat Current vs Length

We have observed that large energy leak develops very fast during the first micrometer of propagation. At $L = 2.17\mu$m and beyond that the energy leak does not increases

much and it seems to have reached a stationary behavior. This is coincident with the fact that the process on which the quasiparticle peak structure vanishes happens in sub-micrometer distances. At all distances, we observe that the energy leak is larger at higher injection energy. Roughly, the fraction of remaining heat current $\Delta J_r/\Delta J_i$ follows a $1/E_1$ dependence as a function of the injection energy E_1.

Heat Current vs Temperature

As described before, measurements at the short propagation distance ($L = 0.48\mu$m) showed that the amplitude of the quasiparticle peak decays approximately two times faster when the electronic temperature is increased by 150 mK. However, for the same set of spectra, we measured that the temperature has no effect on the amount of heat current that leaks out of the edge channel.

2.7.4 Suppression of the Relaxation

In chapter 8 we demonstrate that the relaxation of the quasiparticle peak injected in the outer edge channel can be weakened (up to five times) by decoupling this edge channel of the neighboring inner edge channel. We show that it is possible to achieve this regime simply by implementing a surface depletion gate which is used to divert only the inner edge channel along a longer path, leaving the outer edge channel to propagate alone following the short path as schematically illustrated on the left panels of Fig. 2.10.

The sample design (Fig.2.4) allows to change, in situ, the propagation distance on the same device by polarizing a surface metallic gate: the electrode ***A2***. When the electrode ***A2*** is not polarized ($V_{A2} \geq 0V$), both edge states propagate freely along the short direct path between the two quantum dots. Conversely, when it is fully polarized at *pinch-off* ($V_{A2} \sim -0.5V$) it forces both edge channels to follow a longer path. In this way, it was possible to increase the propagation distance in sample ***D31*** from $L = 0.75\,\mu m$ up to $L = 2.17\,\mu m$. However when the electrode ***A2*** is polarized at an intermediate voltage, $-0.5V \leq V_{A2} \leq 0.0V$, we can access a different regime on which the coupling between the two co-propagating edge states can be tuned.

A schematic representation of these three distinct regimes is shown in the figure 2.10, together with the distribution functions measured after the propagation in the outer edge channel, where the quasiparticle peak was injected. In the intermediate regime (Fig. 2.10(d)), the residual quasiparticle peak that is detected is remarkably larger than what it was measured in Fig. 2.10(b), at the same propagation distance, suggesting that the usual relaxation mechanism was considerable suppressed.

These observations address a central aspect in the field of *electron quantum optics* that has not been demonstrated at this level up to now: how far can an electron excitation propagates on the edge channel before decaying?. With theses experiments,

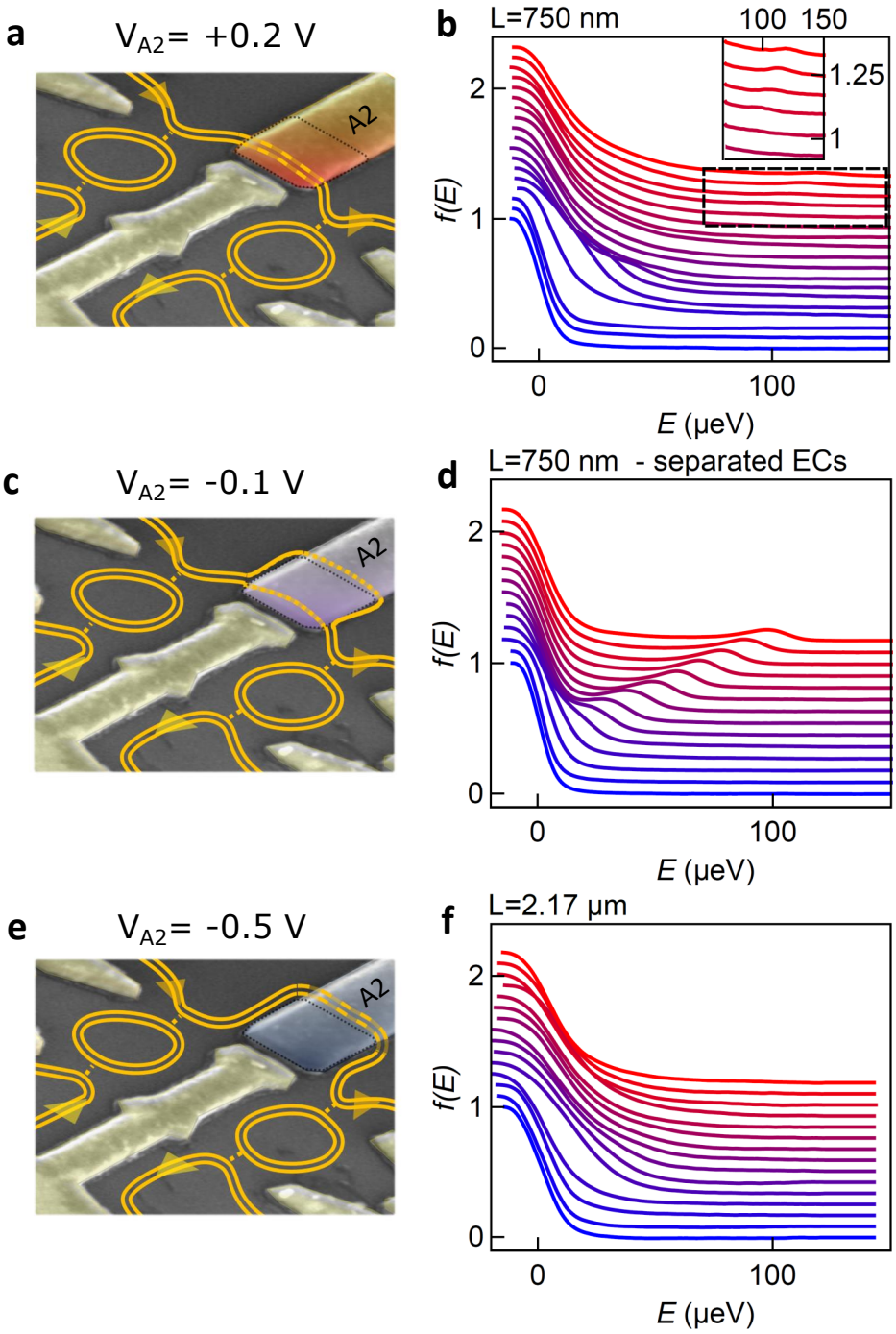

Figure 2.10: **a**, **c**, **e**: False-colour scanning electron micrographs of a typical sample, depicting the trajectories of the edge channels for $V_{A2} = 0.2$ V (**a**, ***A2*** gate highlighted in orange), $V_{A2} = -0.1$ V (**c**, ***A2*** gate highlighted in purple), and $V_{A2} = -0.5$ V (**e**, ***A2*** gate highlighted in blue). In **a**, the two edge channels co-propagate along a $L \approx 750$ nm short path. In **c**, the two edge channels are spatially separated (orange dotted lines) as they flow below the ***A2*** gate. In **e**, the two edge channels co-propagate along a $L \approx 2.17\mu$m long path. **b**, **d**, **f**: Measured $f(E)$ for the configurations depicted in resp. **a**, **c**, and **e**. Each curve, offset for clarity, corresponds to an injection energy increment $\delta E_1 \approx 9\mu eV$, from $E_1 \approx -26\mu eV$ (blue) to $E_1 \approx 122\mu eV$ (red, **b**) and $E_1 \approx 98\mu eV$ (red, **d** and **f**). The inset in **b** is a zoom on the region delimited by the black dashed square.

we determined the limitations imposed by the relaxation in the integer quantum Hall regime, under standard conditions, and we demonstrated how the relaxation can be considerably reduced extending the lifetime of finite energy excitations at least five times.

2.7.5 Coexistence of Multiple Quasiparticle Peaks

Finally, in the last part of chapter 8 we present some measurements were multiple quasiparticle peaks were simultaneously injected in the edge channel by implementing, in the first quantum dot, a resonant level with excited states.

The figure 2.11a shows the distribution functions $f(E)$ measured after a propagation length $L = 0.75\,\mu$m obtained at the different injection energies $E_1(V_{p1})$. We can identify two main quasiparticle peaks in close proximity that are detected around the injection energy E_1. They can be easily seen in the figure 2.11b which is a zoom on the tails of the distributions presented on Fig. 2.11a. Notice that there is a small third peak around an energy $E = 80\,\mu eV$ that appears on the first three curves labeled with the injection energy $E_1 \in \{0, 10, 20\}\mu eV$. A detailed analysis of this measurement allows to identity each quasiparticle peaks with one excited state in the level structure of the quantum dot which consists of a ground state, a first excited state at $21\,\mu eV$ and a second excited state at $80\,\mu eV$.

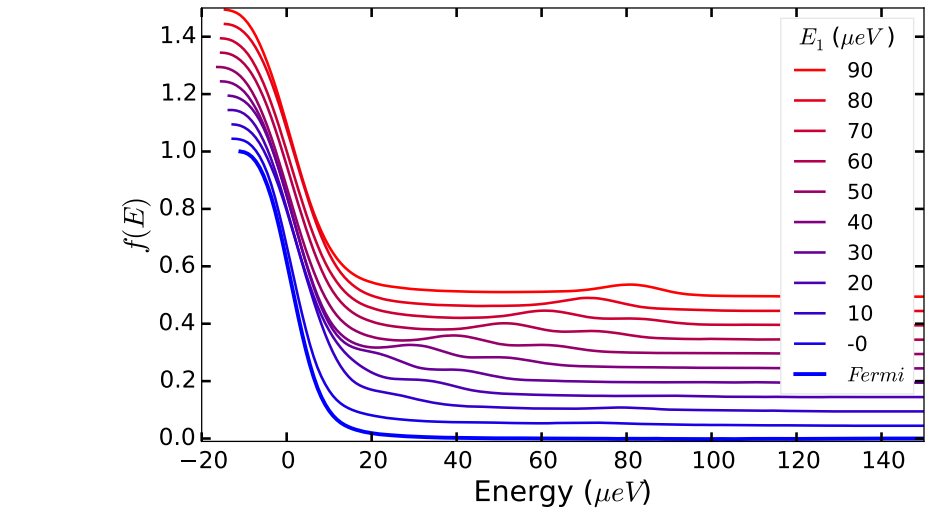

(a)

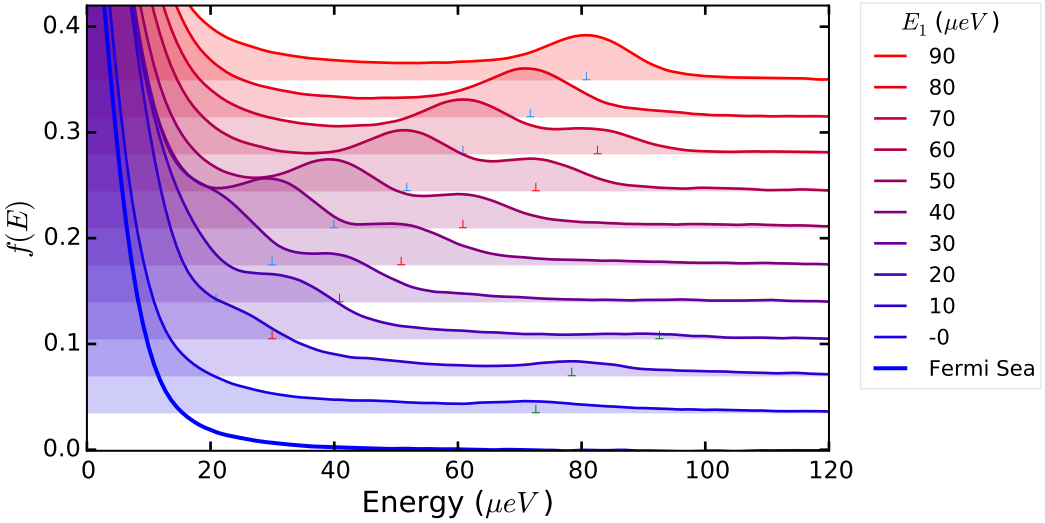

(b)

Figure 2.11: Top: Distribution functions, at different injection energies, measured in sample ***D31*** with a polarization voltage $V_{A2} = -0.1V$ and with the first quantum dots in a configuration where the resonant level presents excited states. The curves were vertically shifted for clarity by a constant offset proportional to the injection energy increase $\delta E_1 = 10\mu eV$. **Bottom:** Zoom on the tails of the distribution function presented in the upper panel showing that different quasiparticle peaks coexist while they propagates. Three quasiparticle peaks could can be identified.

Chapter 3

The Quantum Hall Effect

This chapter describes the basic theory of the integer quantum Hall effect. In the first part I present the main electronic properties of the 2-dimensional electron gas where the quantum Hall effect is induced. Then I describe the dynamics of the electrons of the conduction band when the system is placed under electric and magnetic fields. While a classical theory is enough to explain the properties at low fields, a full quantum description of the electron motion is required to understand the transport properties observed at high magnetic fields. The formation of Landau levels is described within a non interacting picture, neglecting the Coulomb interaction between the electrons, which leads to the formation of fully independent co-propagating edge channels as the eigenstate of transport in the quantum Hall effect. Finally I discus the importance of the disorder for the experimental observation of this phenomena.

3.1 2-Dimensional Electron Gas

2-dimensional electron gases have been observed in a set of different systems: electrons can be trapped in the flat surface of liquid He or they can be found naturally in 2-dimensional materials like Graphene. Furthermore they can be artificially created on heterostructure devices, such as MOSFETs (metal-oxide-semiconductor field effect transistors) or doped GaAs/AlGaAs semiconductors, which are layered systems that combine different materials to engineer the resulting band structure. This means that it is possible to control in some degree the type of carriers, the carrier density, the location of the active layer and the intrinsic resistivity, etc.

3.1.1 GaAs/AlGaAs heterostructure

In GaAs/AlGaAs heterostructure the 2DEG is located at the interface between the GaAs and the AlGaAs layers. The electrons are confined by a triangular potential well that results from the band bending at the interface. The confinement potential is a combination of the repulsive barrier due to the conduction band offset between the

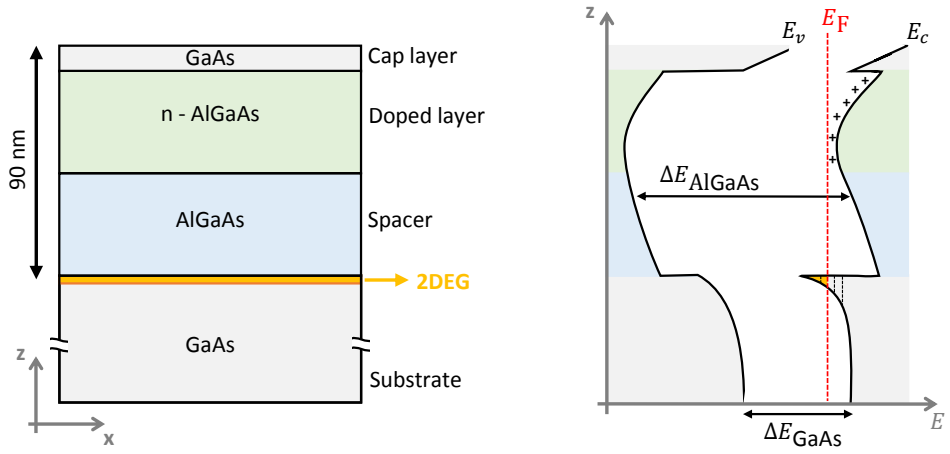

Figure 3.1: ***Left:*** A typical GaAs heterostructure on which a 2-dimensional electron gas, highlighted in yellow, forms at the interface between the AlGaAs and the GaAs layers. ***Right:*** The band bending diagram of the heterostructure: As a result of charge equilibration the conduction band energy along the z direction forms a triangular quantum well, where the electrons are trapped, located approximately 90 nm below the surface.

two semiconductors[1]and the attractive potential due to the positively charged ionized donors left in the AlGaAs side (See Fig 3.1).

The confinement of the electrons results in the quantization of the motion along the direction perpendicular to the interface, defined as $\hat{z}$, generating 2-dimensional subbands $\{E_{xyi}(k)\}$ (Fig. 3.2). Electrons are free to move in the plane of the interface but the transverse kinetic energy E_z takes only discrete values $\{E_{zi}\}$. In GaAs a typical energy separation between subbands is of the order of 10-40 meV. This means that at low temperature, typically below 100K, and low electrons density only the first subband is occupied and the system behaves as an effective 2-dimensional conductor.

GaAs and AlGaAs have very similar crystalline structure, with a lattice constant that differs by less than 0.15% [59], and they can be fabricated by *Molecular Beam Epitaxy* (MBE). In this process the heterostructure is grown layer by layer, with high purity and crystalline order, such that the interface where the 2DEG is hosted can be defined at a perfect crystalline plane. This is important in order to reduce the backscattering due to the roughness at the interface. Additionally, a spacer made of undoped AlGaAs is used to further separate the donors and the 2DEG reducing also the backscattering with the ionized impurities. This is a remarkable advantage with respect of MOSFET devices where these two backscattering sources are a major limitation that can not be overcome easily since the 2DEG is formed directly at the interface between the donor layer and an amorphous oxide.

A direct consequence of the low backscattering rate and a the low effective electron mass in GaAs is that a high mobility can be obtained in this heterostructure which is fundamental for the emergence of quantum phenomena at macroscopic scales.

[1]A conduction band offset is created at the interface since the GaAs and the AlGaAs have different band gap

In this thesis the experiments are performed using GaAs/AlGaAs based 2DEG with electron densities ranging $n \approx 2.5 \times 10^{11}$ cm^{-2} and mobility of the order of $\mu_\tau \sim 2 \times 10^6$ cm^{2}V^{-1}s^{-1}. The 2DEGs are grown at the C2N laboratory by A. Cavanna and U. Gennser.

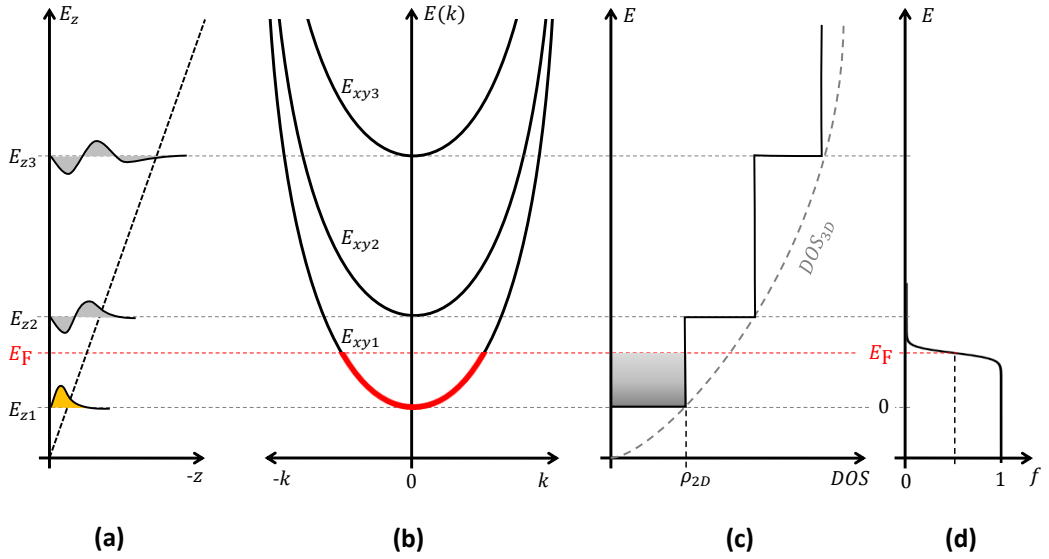

Figure 3.2: (a) The triangular potential well that forms in the GaAs/AlGaAs interface leads to the quantization of the kinetic energy E_z along the vertical direction ($\hat{z}$) in a set discrete values $\{E_{zi}\}$.(b) Electrons are free to move on the $x-y$ plane, hence a parabolic dispersion relation $E_{xy}(k)$ develops from each E_{zi} value.(c) Each 2-dimensional sub-bands contributes to the total density of states with a constant characteristic value ρ_{2D}. (d)The thermal occupation of the states is described by a Fermi function. The low electron density in obtained in GaAs/AlGaAs sets the Fermi level in the first 2D-subband.

3.1.2 Electronic properties

Here we describe several electronic properties of the 2DEG at zero magnetic field and we give some characteristic values estimated for a typical electron density $n_s \approx 2.5 \times 10^{11}$ cm^{-2} unless a different value is specified.

Density of states

Free electrons in 2 dimensions have the simple parabolic dispersion relation $E_{xy}(k)$ describing their kinetic energy, from which a constant density of state $\rho_{2D}(E)$ can be deduced:

$$E_{xy}(k) = \frac{\hbar^2 k^2}{2m} \qquad \rho_{2D}(E) = \frac{g_s m}{2\pi\hbar^2} \tag{3.1}$$

where $g_s = 2$ is the spin degeneracy in GaAs.

Fermi level

The electron density n_s sets the Fermi level E_F at zero temperature simply through the density of states: $n_s = \rho_{2D} E_F$ with the energies measured from the bottom of

the conduction band E_{z1}. Similarly, other related quantities at the Fermi level can be obtained from the electron density, such as the Fermi wave vector k_F which indicates the radius of the circular Fermi surface of the system, the Fermi wavelength λ_F and the Fermi velocity v_F:

$$k_F = \sqrt{\frac{4\pi n_s}{g_s}} \qquad \lambda_F = \frac{2\pi}{k_F} \qquad v_F = \frac{\hbar k_F}{m} \tag{3.2}$$

Fermi wavelength

Due to the low electron density in GaAs/AlGaAs, the Fermi wavelength λ_F can be of the order of 50 nm. In the one hand λ_F is much bigger than the lattice constant, that is of the order of 5.6 Å, which indicates that electrons are well delocalized over many unit cells. Thus they are less sensitive to local defect in the crystalline structure. The residual interaction with the lattice is considered in the effective mass approximation. This is: the effective mass m of the electrons is determined by the curvature of the conduction band, which gives $m = 0.067 \times m_0$, with m_0 the electron mass at rest. In the other hand, at low electron density, λ_F which is similar to the average distance between electrons $a_{ee} = 1/\sqrt{\pi n_s}$ becomes larger than the effective Bohr radius $a_B = 4\pi\hbar^2\epsilon/(me^2) \sim 10$ nm. It indicates that the systems enters a regime where the electrostatic energy of the Coulomb interaction between electron becomes non negligible in comparison to the kinetic energy[2] since $a_{ee}/a_B = E_{int}/E_{kin}$. Additionally, the screening on 2D is less effective than in 3D, as a consequence the electrostatic potentials decay following a $1/r^3$ power law instead of an exponential decrease and no screening length can be well defined. Therefore Coulomb interactions between the electrons is expected to start to play a role in low density 2-dimensional electron gases.

Fermi velocity

Quasiparticles excited above the Fermi level at an energy $\delta E = 300\,\mu eV$, which is the maximum excitation energy that will be investigated along this thesis, propagate at a velocity $v = \sqrt{2(E_F + \delta E)/m}$. A comparison with the Fermi velocity, which is of the order of 2×10^5 m/s for an electron density $n_s \approx 2.5 \times 10^{11}$ cm^{-2}, shows that the relative change in the propagation speed of a single particle states is less than 2%. However when the system is placed under a strong magnetic field and the Coulomb interaction are considered, the behavior can be different from this simple non interacting description of the 2DEG.

[2]The Hamiltonian of N interacting electrons: $H = \sum \frac{-\hbar^2}{2m}\nabla^2 + \sum \frac{e^2}{4\pi\epsilon|\boldsymbol{r}_i - \boldsymbol{r}_j|}$ can be expressed in term of the ration $r_s = a_{ee}/a_B$ by measuring the distances in units of a_{ee} ($\boldsymbol{r} \equiv a_{ee}\boldsymbol{u}$ and $\nabla^2 \equiv \nabla'^2/a_{ee}^2$) and the energies in terms of the Rydberg energy $E_{Ryd} = \frac{me^4}{32\hbar^2\pi^2\epsilon^2}$. This results in: $H' = H/E_{Ryd} = -\frac{1}{r_s^2}\sum\nabla'^2 + \frac{2}{r_s}\sum\frac{1}{|\boldsymbol{u}_i - \boldsymbol{u}_j|}$. Thus at large r_s the interacting term becomes relevant.

Occupation function

At finite temperature not only the density of state but also the occupation function must be taken into account to describe the system. Since the Fermi energy is well above the bottom of the conduction band, at temperatures below $10\,K$ the energy of the thermal excitations is less than 5% of the Fermi energy E_F, then the electronic system behaves as a degenerate system. It means that the Fermi-Dirac quantum statistic $f(E)$, that takes into account the Pauli principle, replaces the classical Boltzmann statistic.

$$f(E) = \frac{1}{\exp(\frac{E-\mu}{k_b T}) + 1} \tag{3.3}$$

In Fermi degenerate systems the electrochemical potential μ and the Fermi energy coincide contrary to classical system where the chemical potential deviates from the E_F as the temperature is increased[3].

Mean free path

The mobility μ_τ is related to the mean scattering time $\bar{\tau}$ which sets the mean free path $\bar{l}_F$ for particles at the Fermi level:

$$\mu_\tau = \frac{e\bar{\tau}}{m} \qquad\qquad \bar{l}_F = v_F\bar{\tau} \tag{3.4}$$

The high mobility obtained in GaAs/AlGaAs 2DEG by reducing the different sources of scattering allows the mean free path to reach values well above of the smallest size of electronic circuits that can be fabricated at the laboratory. Mean free path up $10\,\mu m$ can be obtained [60] at low temperature ($T < 0.35$ K) in 2DEG's with an electron density $n_s = 2.42 \times 10^{11}$ cm^{-2} and a mobility $\mu_\tau = 11.7 \times 10^6$ cm^2/Vs, opening the way for the investigation of the ballistic transport regime.

Conductivity

The intrinsic conductivity σ of the 2DEG is defined by both, the electron density and the mobility. It implies that simple measurement of the resistance, by applying an electric field, will not be enough to determined n_s and μ_τ separately. Instead, electric and magnetic fields will be needed to determine both parameters independently.

$$\sigma = n_s e \mu_\tau \tag{3.5}$$

All these quantities set the relevant energy, length and time scale of the electronic transport in 2DEG.

[3]In general, the electrochemical potential μ is the sum of the chemical potential μ_{ch} and the electrostatic potential μ_{el} that fix the energy of the bottom of the conduction band. In degenerate systems $\mu_{ch} = E_F$.

3.2 Classical Dynamics: Weak Fields

In this section I briefly describe the electron motion under uniform magnetic and electric fields in terms of the solutions of the classical Newton's equation $m\ddot{\mathbf{r}} = \mathbf{F}$. This basic description will help to understand in which conditions the effects of the quantum mechanics will become important and which aspects of the electron motion will be modified.

3.2.1 Motion in an Electric Field: Drude's model

The solution of the classical equation of motion shows that electrons acquire momentum in the same direction of the electric field $\boldsymbol{\mathcal{E}}$ but it also indicates that they can be continuously accelerated by an applied constant electric field.

$$[\dot{\boldsymbol{p}}]_{field} = m\ddot{\boldsymbol{r}} = -e\boldsymbol{\mathcal{E}} \tag{3.6}$$

However even in the cleanest systems there is always a residual disorder that set the stationary regime on which the particles lose momentum, due to the scattering with the defects of the crystalline structure, at the same rate at which they gain momentum due to the field (Fig 3.3a).

$$[\dot{\boldsymbol{p}}]_{scatt} = [\dot{\boldsymbol{p}}]_{field} \qquad \Rightarrow \qquad \frac{m\boldsymbol{v}_D}{\tau} = -e\boldsymbol{\mathcal{E}} \qquad \Rightarrow \qquad \boldsymbol{v}_D = \frac{e\tau}{m}\boldsymbol{\mathcal{E}} \tag{3.7}$$

The characteristic velocity v_D is now constant and proportional to the electric field $\boldsymbol{\mathcal{E}}$. This is described by the Drude model that actually introduces the concept of the mobility as the proportionality constant: $\mu_\tau \doteq v_D/\mathcal{E}$

3.2.2 Motion in a Magnetic Field: Cyclotron motion

Charged particles in a magnetic field are under the action of the Lorentz force:

$$m\ddot{\boldsymbol{r}} = -e\boldsymbol{v} \times \boldsymbol{B} \tag{3.8}$$

Since the motion of electrons on the 2DEG in the z-direction is frozen, only a perpendicular magnetic field $\mathbf{B} = B\hat{z}$ has a relevance. The solution to the equation is a cyclotron motion: the electrons perform circular orbits with a cyclotron frequency ω_c set by the magnetic field and with a cyclotron radius r_c:

$$\omega_c = eB/m \qquad r_c = v/\omega_c \tag{3.9}$$

The radius depends on the initial kinetic energy of the particle but the movement is isochronous: Fast particles move in large orbits and slow particles in small orbits, such

that all of them perform a single orbital trip in the same period of time, returning to their initial position simultaneously (Fig 3.3b). This is an usual property of harmonic oscillators for which the period is independent of the amplitude or, in other words, the initial excitation. In fact, the circular motion can be viewed as the combination of an harmonic oscillation in the $\hat{x}$ direction with another in the $\hat{y}$ direction dephased by $\pi/2$.

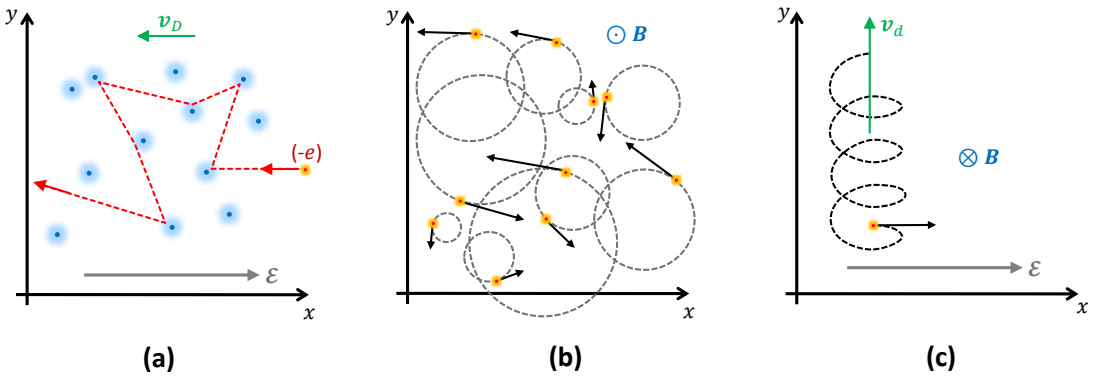

Figure 3.3: (a) Electrons under a uniform electric field $\boldsymbol{\mathcal{E}}$ reach a stationary regime where they propagate at a constant speed v_D due to the random collisions with scattering centers (blue dots) in the crystalline structure.(b) Under a uniform magnetic field $\boldsymbol{B}$ the electrons perform cyclotron orbit with a radius proportional to its kinetic energy but with the same angular frequency ω_c driving an isochronous movement: All particles return to their initial position after the same period of time.(c) A combination of a uniform electric and magnetic fields drives a drift of the cyclotron orbit along a direction perpendicular to the electric field.

3.2.3 Motion in Magnetic and Electric Fields

When both, magnetic and electric fields are considered simultaneously in the equation of motion,

$$m\ddot{\boldsymbol{r}} = -e(\boldsymbol{\mathcal{E}} + \boldsymbol{v} \times \boldsymbol{B}) \tag{3.10}$$

the resulting movement is a combination of a cyclotron motion and a drift motion at a constant speed (Fig 3.3c). Remarkably there is no need of considering the residual disorder in the 2DEG, as in the Drude model, to find a stationary regime. In this case the Drude velocity v_D would be an upper limit for v_d. However the resulting drift velocity is perpendicular to the magnetic field and also it is *perpendicular to the electric field*.

$$\boldsymbol{v}_d = -\frac{\boldsymbol{\mathcal{E}} \times \mathbf{B}}{B^2} \tag{3.11}$$

This behavior is counter-intuitive if we expect that the drift velocity will describe the motion of the center of the cyclotron orbit as a sort of center of mass. It puts in evidence that the dynamics of electrons under electric and magnetic field can results in interesting phenomena due to the non linear character of the Newton equation

introduced by the Lorentz force. In fact we can not simply use the superposition principle to add the solution of the section 3.2.1 and 3.2.2

3.2.4 The Classical Hall Experiment

A well known experiment where the classical motion of electrons in 2 dimensions under electric and magnetic field is in action is the Hall experiment. The 2DEG is shaped in a Hall bar and placed in a perpendicular magnetic field as shown in the Fig 3.4a. Additionally a voltage drop that is applied between the Ohmmic contact **1** and **4** generates an electric field $\boldsymbol{\mathcal{E}}_e$ along the $\hat{x}$ direction. As a result of these two external fields, the injected electrons in contact **1** acquire a drift motion in the $+\hat{y}$ direction while they propagate in a similar way as shown in Fig 3.3c. Consequently, negative charges accumulate in the upper border of the Hall bar generating an internal additional electric field $\boldsymbol{\mathcal{E}}_H = -\mathcal{E}_H\hat{y}$ that is called the Hall field. The following incoming electrons are now under the effect of these three fields:

$$m\ddot{\boldsymbol{r}} = -e(\boldsymbol{\mathcal{E}}_e + \boldsymbol{\mathcal{E}}_H + \boldsymbol{v} \times \mathbf{B}) \tag{3.12}$$

The stationary regime is reached when the accumulation of charges at the border of the sample is sufficiently large such that the force created by the Hall field compensates the Lorentz force in the equation of motion. Then electrons move only along the horizontal direction under the single effective action of the external electric $\boldsymbol{\mathcal{E}}_e$.

The longitudinal resistance R_{xx} measured between the contacts **2** and **3** is related to the conductivity simply through Ohm's law,

$$R_{xx} = \frac{V_{23}}{i_0} \qquad \longrightarrow \qquad R_{xx} = \frac{L}{\sigma W} \tag{3.13}$$

while the Hall resistance, defined as R_{xy}, is related to the density of electrons:

$$R_{xy} = \frac{V_{35}}{i_0} \qquad \longrightarrow \qquad R_{xy} = \frac{B}{en_s} \tag{3.14}$$

Knowing the geometrical factors W and L of the sample, a simple measurement of the resistances R_{xx} and R_{xy} gives access to the electron density n_s and the mobility μ_τ (See Eq. 3.5) which are the two main parameters that characterize a 2DEG. Fig 3.4b is a typical measurement of the Hall resistance in our samples showing the linear dependence with the magnetic field. It also shows the onset of the deviations from this model that arises at high field.

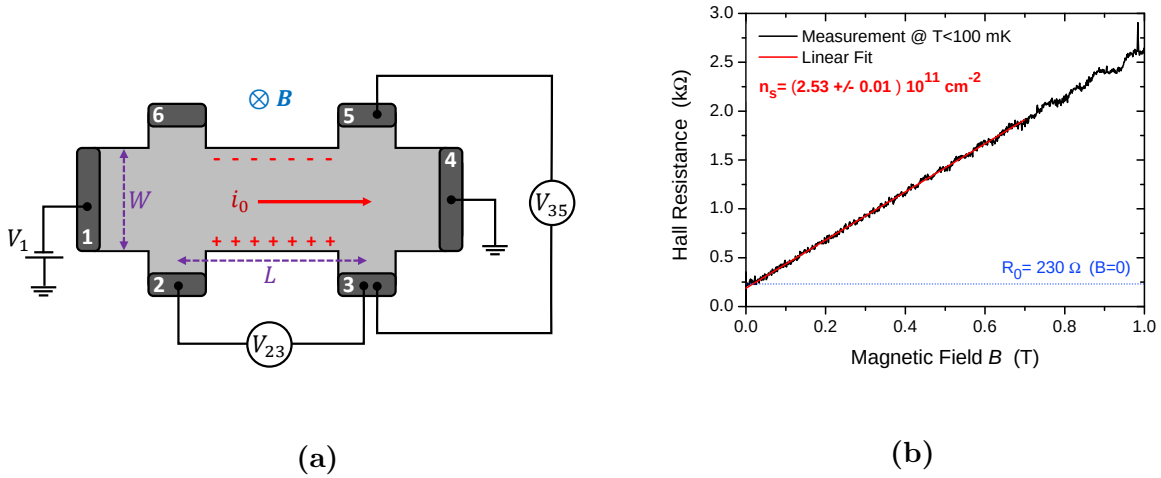

(a) (b)

Figure 3.4: (a)A typical Hall bar configuration from which the electron density n_s and the mobility μ_τ can be measured when electric and magnetic fields are applied inducing the classical Hall effect: a Hall voltage $V_{xy} = V_{35}$ develops in the direction perpendicular to the current due to charge accumulation on the border of the sample. (b) Linear behavior of the Hall Resistance at low magnetic field measured at a temperature $T \sim 100$ mK.

3.3 Quantum Hall Effect: Dynamics in Strong Fields

In the classical description of the electron motion under a perpendicular and homogeneous magnetic field $\boldsymbol{B} = B\hat{z}$, the radius r_c of the cyclotron orbit decreases with the magnitude B but increases with the energy of the particle (See Eq. 3.9). At high enough magnetic field, the orbital length $l_c = 2\pi r_c$ becomes smaller than the elastic length l_e, therefore the electrons can complete at least one tour around the orbit before an scattering event. In this limit, if the temperature is low enough, the quantum wave nature of the particle confined in the orbit emerges in the transport properties. Additionally, in this regime the concept of cyclotron radius loses meaning and a new length scale arises: the magnetic length $l_B = \sqrt{\hbar/eB}$. In the following sections I will present an extensive description of the quantum Hall effect neglecting the coulomb interaction between the electrons of the 2DEG. First, I show that a uniform high magnetic field induces the quantization of the cyclotron motion which results in the formation of Landau levels. Second, I will consider in addition the effect of a uniform electric field, which induces the orbital drift of the quantized circular motion. Finally, I describe these two effects for a system with a finite size which results in the development of edge states.

3.3.1 Observation of the Quantum Hall Effect

Measurements in the Hall configuration shows very peculiar deviations from the classical description at high magnetic fields and low temperatures. First, the longitudinal resistance R_{xx} moves away from its constant value at low $\boldsymbol{B}$ and develops strong oscillations. This is known as the ***Shubnikov-de-Haas effect*** [61] and the minima of

the oscillations occur periodically as a function of $1/B$ with a period:

$$\Delta\left(\frac{1}{B}\right) = \frac{e}{h}\frac{g_s}{n_s} \tag{3.15}$$

Second, at even higher fields the Hall resistance R_{xy}, instead of simply increasing linearly with B, develops wide plateaus while the longitudinal resistance R_{xx} vanishes in the same region as it can be observed in the measurement presented in the figure 3.5. Moreover, the values of R_{xy} at the plateaus are a precise sequence determined by an integer number N and two fundamental constants,

$$R_{xy} = \frac{1}{N}\frac{h}{e^2} \tag{3.16}$$

This is the ***integer quantum Hall effect*** (IQHE) discovered by von Klitzing in 1980 [9]. Remarkably the same quantized values of R_{xy} were observed in systems with different geometries, composition and disorder. The constant $R_K = h/e^2$ can be experimentally determined with a precision of few parts per billion [62] such that nowadays the phenomenon is used to maintain the standard unit of the electrical resistance for the International Unit System (SI) and it also provides an accurate method to measure the fine structure constant[4].

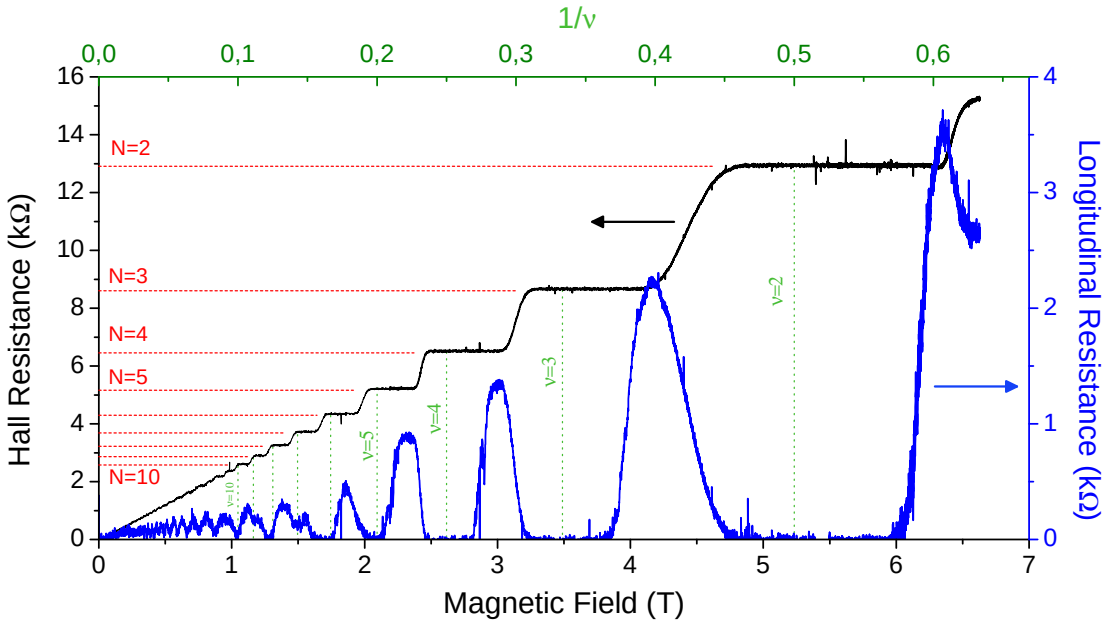

Figure 3.5: At high magnetic field, the Hall resistance R_{xy} (black) displays constant plateaus at the quantized values: R_k/N. Simultaneously the minima of the Shubnikov-de-Haas oscillations observed in the longitudinal resistance R_{xx} (blue) at intermediate magnetic fields ($B \sim 1T$) develops into wide regions where R_{xx} vanishes. Vertical dashes lines shows the magnetic fields at which the filling factor $\nu = n_s\phi_0/B$ reaches integer values.

[4]The fine structure constant α is related to the Quantum Hall effect through: $h/e^2 = Z/2\alpha$ with $Z = \sqrt{\mu_0/\epsilon_0}$ the impedance of the free space.

3.3.2 Orbital Quantization: Landau Levels

In this section I present a quantum description of the electron motion using the wave function $\Psi(x,y)$ and the energy spectrum E_{xy} which are the solutions of the stationary Schrödinger equation:

$$\hat{H}\Psi(x,y) = E_{xy}\Psi(x,y) \tag{3.17}$$

In a first place I describe the system without any gauge choice to represent the magnetic field in order to show that many important properties can be derived from general considerations. A particular gauge will be set only to obtain the functional form of the wave function and it will be specified in each case. Additionally, I describe solutions of the Schrödinger equation for spinless electrons but the spin degree of freedom will be incorporated latter on.

Landau Levels

The Hamiltonian describes the free electrons in the magnetic field $\boldsymbol{B} = \nabla \times \boldsymbol{A}(\boldsymbol{r})$ through the mechanical momentum operator $\hat{\boldsymbol{\pi}}$:

$$\hat{H} = \frac{\hat{\boldsymbol{\pi}}^2}{2m} = \frac{(\hat{\boldsymbol{p}} + e\boldsymbol{A})^2}{2m} \tag{3.18}$$

It is worth to remember that it is the mechanical momentum the one that is related to the velocity $\boldsymbol{\pi} = m\dot{\boldsymbol{r}}$, while the canonical momentum $\boldsymbol{p} = m\dot{\boldsymbol{r}} - e\boldsymbol{A}$ is a gauge dependent quantity.

First, each component of the canonical momentum operator acts on a wave function $\psi(\boldsymbol{r})$ as a derivative $\hat{p}_\alpha = -i\hbar\frac{\delta}{\delta\alpha}$ and they satisfy the usual commutation rule $[\hat{p}_x, \hat{p}_y] = 0$. Second, the vector potential acts on a wave function just as a multiplicative operator and it is related to the magnetic field trough $B = \frac{\delta A_y(\boldsymbol{r})}{\delta x} - \frac{\delta A_x(\boldsymbol{r})}{\delta y}$. With this in mind it is not difficult to show that the components of the mechanical momentum operator satisfy the commutation rule[5]: $[\hat{\pi}_x, \hat{\pi}_y] = i\hbar/l_B^2$

Therefore we can use the components of the mechanical momentum to define others more convenient operators, a and $a^\dagger$, which satisfy the commutation relation $\left[a, a^\dagger\right] = 1$

$$a = \frac{l}{\sqrt{2}\hbar}\left(\pi_x - i\pi_y\right) \qquad a^\dagger = \frac{l_B}{\sqrt{2}\hbar}\left(\pi_x + i\pi_y\right) \tag{3.19}$$

These are the ladder operators, in terms of which the Hamiltonian reduces simply to:

$$H = \hbar\omega_c\left(a^\dagger a + 1/2\right) \tag{3.20}$$

In this representation it is clear that the Hamiltonian describes an harmonic oscillator

[5]We should demonstrate the equality $(\hat{\pi}_x\hat{\pi}_y - \hat{\pi}_y\hat{\pi}_x)\,\psi(\boldsymbol{r}) = (i\hbar/l_B^2)\psi(\boldsymbol{r})$ where each component of the mechanical momentum acts as $\hat{\pi}_\alpha\psi(\boldsymbol{r}) = -i\hbar\delta(\psi(\boldsymbol{r}))/\delta\alpha + eA_\alpha(\boldsymbol{r})\psi(\boldsymbol{r})$ for $\alpha = x, y$.

at a frequency ω_c and whose energy spectrum is a set of discrete energy level

$$E_n = \hbar\omega_c(n + 1/2) \tag{3.21}$$

In the case of a 2DEG under a magnetic fields these are called the ***Landau levels*** which are not just traditional discrete level since they have a high degeneracy. Additionally we must notice that any particular gauge choice was needed in order to find the energy spectrum.

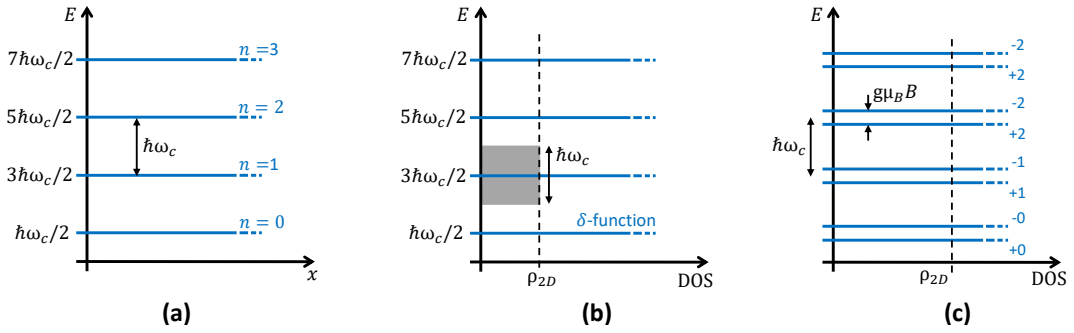

Figure 3.6: **(a)**Flat Landau levels, equally separated, develop as a consequence of the cyclotron quantization. **(b)**The uniform density of states ρ_{2D} of spinless particles ($g_s = 1$ in Eq. 3.1) within an energy range of $\hbar\omega_c$ collapses to form the highly degenerate Landau levels around each energy E_n. **(c)**When the spin degree of freedom is considered, each Landau level splits in two spin polarized levels separated by the Zeeman energy $E_Z = g\mu_B B$ but also the zero field DOS ρ_{2D} duplicates since $g_s = 2$ in Eq. 3.1 for particles with spin 1/2. Therefore each discrete level has the same degeneracy $D_n = 1/2\pi l_B^2$ than in the spinless case. The number label $+n(-n)$ refers to the landau Level n and spin number $+1/2(-1/2)$.

Density of States

The formation of Landau levels leads to a dramatic change on the density of states from the constant value ρ_{2D} characteristic of a 2DEG. A large portion of ρ_{2D} in the energy range $\hbar\omega_c$ around each Landau energy collapses to form a δ-function defining the discrete levels. Therefore the degeneracy of each level is $D_n = \rho_{2D}\hbar\omega_c$ for spinless particles (Fig 3.6a and 3.6b).

The DOS is now periodic with $\hbar\omega_c$, and therefore with B. Since many properties of the electronic transport depends on the DOS at the Fermi level, some of these quantities shows oscillatory behavior at high magnetic field. This is the origin of the ***Shubnikov-de-Haas*** (SdH) oscillations seen in the longitudinal resistance and the ***Haas-van-Alphen*** oscillations that appear in the magnetic susceptibility [61].

As mentioned at the beginning of this section, two main conditions have to be satisfied in order to observe the effects of the Landau quantization in the transport properties. First, the electrons need to be able to perform at least a complete cyclotron orbit before being scattered out, which implies that:

$$\omega_c\tau = B\mu_\tau \gg 1 \tag{3.22}$$

Second, the temperature needs to be small enough such that only one Landau level is thermally occupied at a time:

$$k_b T \ll \hbar\omega_c \tag{3.23}$$

The first condition actually can be used to obtain an estimation of the mobility μ_τ by measuring the magnetic field B_{SdH} at which the first Shubnikov-de-Haas oscillations are observed on the longitudinal resistance[6].

Group velocity

Since the LL's are independent of the momentum $\boldsymbol{k}$, the dispersion relation is flat and the group velocity associated to them is zero. Landau levels describe then states that can not propagate as expected from the classical picture of a cyclotron motion.

$$v_g = \frac{1}{\hbar}\frac{\partial E_n}{\partial k} = 0 \tag{3.24}$$

Wave function

A more complete description of the electronic state is given by the wave function $\Psi(x, y)$ which can be obtained after choosing a particular gauge to represent the magnetic field through the vector potential. Since the magnetic field is homogeneous and it imposes a defined chirality in the rotation of electrons, we can use a symmetric gauge on which $\boldsymbol{A} = \frac{1}{2}\boldsymbol{B} \times \boldsymbol{r} = (-By/2, Bx/2, 0)$ that in cylindrical coordinates reads: $\boldsymbol{A} = -Br/2\,\hat{e}_\theta$. In addition we must remember that the origin of coordinates is arbitrary, thus the same solutions will be found for any other choice of the origin.

Within this gauge the wave function has the form:

$$\Psi_{n,m}(\boldsymbol{r}) = C_{n,m}\left(\frac{r}{l_B}\right)^{|n-m|} exp\left(i(n-m)\theta\right)\, L^{|n-m|}_{min\{n,|m|\}}\left(\frac{r^2}{2l_B^2}\right)\, exp\left(-\frac{r^2}{4l_B^2}\right) \tag{3.25}$$

where $C_{n,m}$ is the normalization constant and L^β_α is the generalized Laguerre polynomial. Wave functions within the same Landau level n are distinguished by a second quantum number, $m > 0$, that is related to the angular momentum $L_z = \hbar(n - m)$.

Semiclassical Interpretation

Even though the notion of cyclotron orbit is meaningless in the quantum limit, it is still worth to have a semi-classical view of the electron motion in terms of trajectories in order to better understand the different terms of the wave function. The Fig. 3.7 represents the density probability of a wave function $\Psi_{n,m}$ at the lowest Landau level

[6] In general, the value of the mobility estimated from the onset of the Shubnikov-de-Haas oscillations can be up to one order of magnitude lower than the actual value of the 2DEG mobility μ_τ at zero field. A more precise estimation of μ_τ can be obtained by a detailed modeling of the complete functional form of the oscillations $R_{xx}(B)$ (See Section 2.7.6 of Ref. [63]).

$(n = 0)$ but with a finite angular momentum[7].

$$\Psi_{0,m}(\boldsymbol{r}) = C_{0,m}\left(\frac{r}{l_B}\right)^m exp\,(-im\theta)\,exp\left(-\frac{r^2}{4l_B^2}\right) \tag{3.26}$$

On the one hand, the wave function is extended on the radial direction with a characteristic width of the order of l_B as it can be see from the Gaussian term, but the maximum of the density probability form a circumference of radius $\sqrt{2m}l_B$ preserving the rotational symmetry. On the other hand, an expression of the cyclotron radius can be obtained following its classical definition in the circular motion. It shows that the magnetic length l_B is the cyclotron radius for all the states in the lowest Landau level, $n = 0$:

$$r_c = v/w_c = \sqrt{2E_n/m}/w_c \quad \rightarrow \quad r_c = \sqrt{2}\,l_B\sqrt{n+1/2} \tag{3.27}$$

Consequently we can interpret to the wave function $\Psi_{0,m}$ like describing a localized state which can be seen as a linear combination of several cyclotron orbits with radius l_B and whose centers are over the circumference of radius $\sqrt{2m}l_B$. The motion of electrons is essentially a cyclotron motion, but a coherent superposition of many of them is needed to form the wave functions that are solutions of the Schrödinger equation (Fig. 3.7).

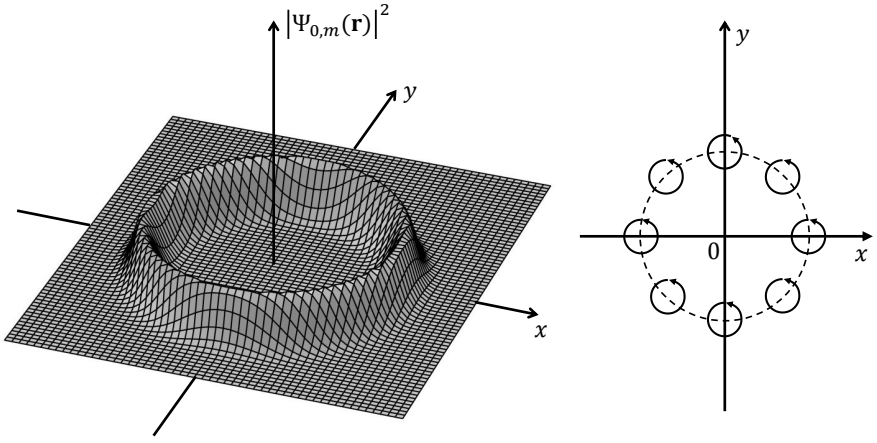

Figure 3.7: Left: Probability density $|\Psi_{0,m}(\boldsymbol{r})|^2$ of a state in the first Landau Level $n = 0$ with a finite angular momentum $L_z = \hbar m$ has a peak on the circumference of radius $\sqrt{2m}l_B$ and a Gaussian dependence on the radial direction with an extension of the order of l_B. **Right**: The complete wave function $\Psi_{0,m}(\boldsymbol{r})$ can be interpreted as a coherent superposition of many classical cyclotron orbits with radius l_B located on the circunference of radius $\sqrt{2m}l_B$. Pictures were adapted from Ref. [64].

Flux quantization.

The density of states ρ_{2D} gives the number of states per unit of energy and area, thus the degeneracy D_n of each LL gives the number of states per unit area that there are in the system when a LL is complete. Since $D_n = 1/2\pi l^2$, it follows that there is

[7]The generalized Laguerre polynomial $L_\beta^\alpha(x)=1\ \forall\alpha\ if\ \beta = 0$

one state per area $2\pi l^2$, which enclosed exactly one flux quanta $\phi_0 = h/e$. Furthermore from 3.27 it can be shown that each successive orbit ($n \to n+1$) incorporates a flux quanta [65]. This flux quantization is a direct consequence of the *Bohr-Sommerfield* quantization condition applied to the cyclotron motion.

Spin.
The spin degree of freedom can be considered in the Hamiltonian (Eq. 3.18) by adding a term $+g\mu_B sB$ where μ_B is the Bohr magneton and g is the coupling constant which in vacuum is $g = 2$ but in GaAs it is renormalized to $g \approx -0.4$ due to the spin-orbit interaction. This sets the Zeeman energy to be ~ 70 times smaller than the cyclotron energy $\hbar\omega_c$. Since $s = \pm 1/2$ the effect of adding the spin degree of freedom in the precedent description is that each Landau Level now split in two but each component still has the degeneracy $D_n = 1/2\pi l^2$ since the density of states at zero field ρ_{2D} also duplicates (Fig. 3.6c). The energy spectrum of the system is simply:

$$E_n s = \hbar\omega_c(n + 1/2) + g\mu_B sB \qquad n = 0, 1, 2, ... \quad s = \pm 1/2 \tag{3.28}$$

It is important to notice that the lowest Landau level, labeled by $n = 0$, now consist of two spin family levels.

Filling factor.
Since the quantum number n does not indicates anymore the number of discrete Landau levels, it is useful to introduce the concept of filling factor ν which accounts for the number of occupied Landau level at the Fermi energy. Therefore the filling factor is related to the total density of electrons trough:

$$n_s = D_n \nu \quad \longrightarrow \quad \nu = n_s \frac{h}{eB} = n_s \frac{\phi_0}{B} \tag{3.29}$$

This expression can be rewritten in terms of the total number of electrons N_e and the total magnetic flux $\phi = BA$ threading the system area A as: $\nu = \frac{N_e}{\phi/\phi_0}$. This shows that the filling factor indicates the number of electrons per flux quanta.

3.3.3 Orbital Drift: Finite Group Velocity

Landau gauge.
Let's consider that in addition to the uniform magnetic field $\boldsymbol{B} = B\hat{z}$ there is a uniform electric field $\boldsymbol{\mathcal{E}} = \mathcal{E}\hat{x}$, which defines a preferential direction, $\hat{y}$, where the momentum is conserved. Thus it is convenient to use in this situation a gauge with a translation symmetry on $\hat{y}$. This is the case of the *Landau gauge*, which is commonly used for its mathematical simplicity, where the vector potential has a single component $\boldsymbol{A} =$

$(0, xB, 0)$ and the wave function takes the form:

$$\Psi_{nk}(x,y) = \frac{1}{\sqrt{L}} e^{ik_y y} \psi_{nk}(x) \tag{3.30}$$

For each k-family on the $\hat{y}$ direction, the $\psi_{nk}(x)$ is the solution of the Schrödinger equation[8]:

$$\begin{aligned} \frac{1}{2m}\left[p_x^2 + (\hbar k_y - eBx)^2 - e\mathcal{E}x\right]\psi_{nk}(x) &= E_{nk}\psi_{nk} \\ \left[\frac{p_x^2}{2m} + \frac{m\omega_c^2}{2}(x - X_k)^2\right]\psi_{nk}(x) &= \left[E_{nk} + e\mathcal{E}X_k - \frac{m}{e}\left(\frac{\mathcal{E}}{B}\right)^2\right]\psi_{nk}(x) \end{aligned} \tag{3.31}$$

The last form makes evident that it is again the equation of an harmonic oscillator at the frequency ω_c but centered at X_k

$$X_k = -k_y l_B^2 + \frac{e\mathcal{E}ml_B^4}{\hbar^2} \tag{3.32}$$

Eigenvalues and group velocity.
The first thing to notice is that the spectrum for the full wave function $\Psi_{nk}(x,y)$ is no longer degenerate since the states are spread in energy through X_k (Fig 3.8a):

$$E_{nk} = \hbar\omega_c\left(n + \frac{1}{2}\right) - e\mathcal{E}X_k + \frac{1}{2}m\left(\frac{\mathcal{E}}{B}\right)^2 \tag{3.33}$$

Thus the group velocity gives:

$$\boldsymbol{v}_g = \frac{1}{\hbar}\nabla_k E_{nk} = \frac{\mathcal{E}}{B}\hat{y} \tag{3.34}$$

which, of course, coincides with the expectation values $\langle\hat{v}_x\rangle = 0$ and $\langle\hat{v}_y\rangle = \mathcal{E}/B$ and with the result of the classical description (Eq. 3.11)

Wavefunctions.
The second thing, is that the ψ_{nk} part of the wave function is similar to that obtained with the symmetric gauge (Section 3.3.2) since there is an oscillatory polynomial modulated by a Gaussian decay along the non symmetric direction:

$$\psi_{nk}(x) = \left(\frac{1}{\pi}\right)^{1/4}\left(\frac{1}{2^n n! l_B}\right)^{1/2} exp\left(-\frac{(x - X_k)^2}{2l_B^2}\right) H_n\left(\frac{x - X_k}{l_B}\right) \tag{3.35}$$

where the H_n is the Hermite polynomial[9].

[8]Notice that, in order to simplify the notation, a simple sub-index k is used to label the solutions $\psi_{nk}(x)$ for a given k_y-family.

[9]The Hermite polynomial of order n is generated by $H_n(x) = (-1)^n exp(x^2)\frac{d^n}{dx^n}exp(-x^2)$

The wave function is fully extended on the $\hat{y}$-direction as a free wave while it spreads along the $\hat{x}$-direction in a length of $\sqrt{2n+1}l_B$, which is in fact the quantized cyclotron radius r_n (Eq. 3.27).

Therefore Ψ_{nk} describes an electron in a cyclotron motion centered in X_k that drifts perpendicular to the electric field following an equipotential line. This can also be seen from the spectrum, where the first term is the energy of the quantized cyclotron motion, the second is the electrostatic potential energy at X_k and the last one is the kinetic energy of the drift motion.

Figure 3.8b shows the probability density along $\hat{x}$ calculated for an state of $n = 4$ as an example. Even though there is an oscillatory finite probability to find the electron inside the cyclotron orbit, the probability is higher at the two outer most peaks located roughly at r_n of the center X_k. This is the remanent of the classical cyclotron orbit.

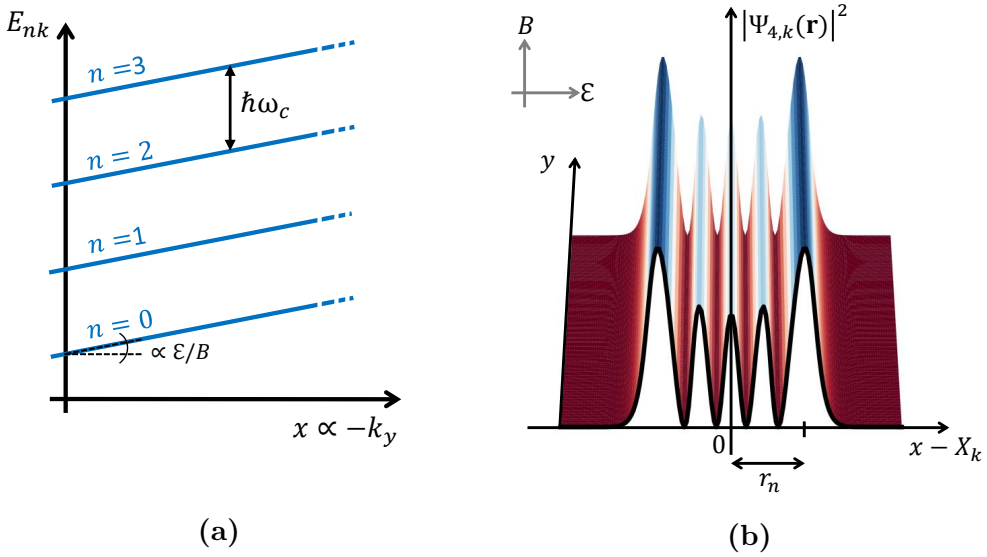

Figure 3.8: **(a)** Landau levels of an infinite 2DEG of spinless particles under a uniform electric field $\boldsymbol{\mathcal{E}}$ acquires a uniform dispersion which sets a finite group velocity $v_g = \mathcal{E}/B$ in the direction perpendicular to the electric field. **(b)** The probability density of an state $\Psi_{n,k}(\boldsymbol{r})$ with $n = 4$ shows that the electron is more likely to be found at a distance r_n from the center of motion. $\Psi_{n,k}(\boldsymbol{r})$ has the same translation symmetry than the Landau gauge along the $\hat{y}$ direction.

3.3.4 Finite Size System: Edge States

In a realistic system with a finite size, the boundaries impose a confining potential $U(\boldsymbol{r})$ that keeps the electrons inside through the electric field that is locally created $\boldsymbol{\mathcal{E}}_b = -\nabla_{\boldsymbol{r}} U(\boldsymbol{r})$.

When $U(\boldsymbol{r})$ is smooth in a range of the order of r_n, the typical extension of a wave function, it can be approximated by a Taylor expansion up to 1st or 2nd order and then analytic solutions of the Schrödinguer equation can be found.

However, despite the particular functional form of the solutions, we can still say that the wave functions will be characterized by a center of motion X_k related to k_y, due to the magnetic field as usual, with a contribution due to the electric field:

$$X_k = -k_y l^2 + \mathcal{F}(\mathcal{E}_b) \tag{3.36}$$

The wave function it will also drift along equipotential lines at a local constant speed $v_g \sim \mathcal{E}_b/B$ and the energy spectrum will have mainly the contributions from the equipotential energy, the kinetic energy of the orbital drift and the quantized cyclotron energy as in Eq 3.33:

$$E_{nk} = \hbar\omega_c \left(n + \frac{1}{2}\right) - eU(X_k) + \frac{1}{2}mv_g^2 \tag{3.37}$$

The figure 3.9b shows the spectrum along $\hat{x}$ for a 2DEG of finite area $S = L_x L_y$ under a magnetic field $\boldsymbol{B} = -B\hat{z}$. The flat Landau levels of the bulk are bent up when they approaches the boundaries. consequently, they describe localized states in the bulk and propagating states at the edges that are known as the ***Edge States***. This description neglects the Coulomb interaction in the electronic gas which will be considered in the next chapter and which gives rise to the edge reconstruction, a mechanism for which the edge states acquires internal degree of freedom. As can be seen on equation 3.37, the spin degree of freedom was also neglected by simplicity, but it can be easily incorporated on this description as explained in section 3.3.2.

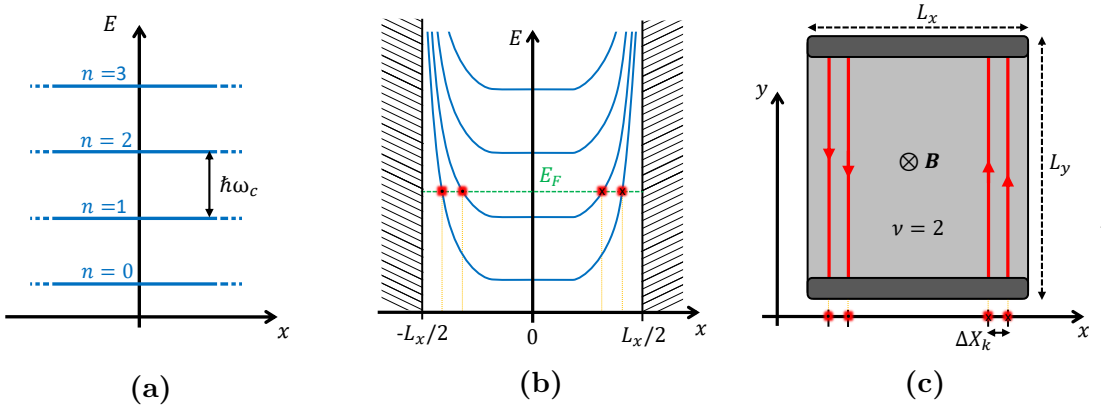

Figure 3.9: ***Formation of edge states for a 2DEG of spinless particles due to confinement impose by the finite size of the system.*** **(a)** Flat Landau levels of an infinite 2DEG under a uniform magnetic field $\boldsymbol{B}$. **(b)** Landau level of a system with finite size L_x along the $\hat{x}$ direction. The electric field $\boldsymbol{\mathcal{E}_b}$ created at the boundaries bends up the Landau levels. **(c)** Each time a Landau level crosses the Fermi level E_F it develops a chiral edge state on the sample located at the position of the crossing. The number of edge states is given by the filling factor $\nu = 2$ which indicates the number of filled Landau level at the bulk of the system. The center of motion of different edge states are spatially separated by ΔX_k which depends on the sharpness of the confinement potential U.

Transport Properties on the Edge States

The group velocity calculated from the spectrum changes sign at opposite sides of the system indicating that the propagation of edge states is ***chiral***:

$$v_g \propto \frac{\delta E_{nk}}{\delta k_y} \propto \frac{\delta U\left(X_k\right)}{\delta X_k} \frac{\delta X_k}{\delta k_y} \tag{3.38}$$

When the Landau levels are filled up to a Fermi energy E_F that is not aligned with a bulk Landau level, the only possible low energy excitations (electron-hole excitations near the Fermi sea) are on the edge states. In the bulk, all the states are below the E_F, so they are fully occupied and they will not contribute to the transport. The number of edge states is determined by the number of fully occupied bulk Landau levels which is given by the filling factor ν. Each edge channel is located in the sample at the position where the LL crosses the Fermi level, which defines its center of motion X_k (Fig 3.9c).

Electrons propagating in one edge state undergo no backscattering, so the motion is ***ballistic***. Despite the impurities an electron with $+\boldsymbol{k}$ momentum can not be backscattered because all the states with $-\boldsymbol{k}$ momentum are located at the other edge of the sample. Therefore the tunneling element that mixes the two state is exponentially small due to the macroscopic distance between both borders $L_x \gg l_B$.

On the one hand, the wave function of co-propagating edge states originated from different Landau levels will be spatially separated on the sample if the distance between their centers of motion $\Delta X_k^{n,n+1}$ is larger than the wave function extension l_B:

$$l_B \ll \Delta X_k^{n,n+1} \quad \Longleftrightarrow \quad l_B e \frac{\partial U(x)}{\partial x} \ll \hbar\omega_c \tag{3.39}$$

This implies that the confinement potential must be smooth enough. As a consequence, the elastic scattering rate $\tau_{el}^{n,n+1}$ between the co-propagating edge states is exponentially suppressed from its value τ_{el} at zero magnetic field [66]:

$$\frac{1}{\tau_{el}^{n,n+1}} = \frac{1}{\tau_{el}} \left(\frac{\Delta X_k^{n,n+1}}{l_B}\right)^{4n+2} exp\left[-\frac{1}{2}\left(\frac{\Delta X_k^{n,n+1}}{l_B}\right)^2\right] \tag{3.40}$$

T. Martin and Shechao Feng [66] showed that the inelastic scattering rate, which can be mediated by acoustic phonons at temperatures of the order of $T \sim 1$ K, also results exponentially suppressed by the same poor wavefunction overlap and the low thermal occupation of the phonon bath.

On the other hand, the wavefunction of edge states with different spin polarization coming from the same Landau level, are well separated if:

$$l_B \ll \Delta X_k^s \quad \Longleftrightarrow \quad l_B e \frac{\partial U(x)}{\partial x} \ll g\mu_B B \tag{3.41}$$

where ΔX_k^s is the separation between their centers of motion. G. Müller *et al.* [67]

reported that while a Landau gap of $3.2\,meV$ induces a spatial separation $\Delta X_k^{n,n+1} \approx$ 780 Å between spin-degenerate edge channels, a Zeeman gap $E_Z = g\mu_B B \sim 90\,\mu eV$ will produce a spatial separation $\Delta X_k^s \approx 20$ Å between spin polarized co-propagating edge channels. Therefore a large overlap is expected since the spatial extent of the wave function $l_B \approx 130$ Å at the same magnetic field.

However, even if the wavefunctions of neighboring edge states overlap, the electrons can not simply tunnel due to spin and momentum conservation. Tunneling of electrons between edge states with different spin polarization requires a spin flip process which can be mediated by the spin-orbit interaction, the nuclear spin polarization (hyperfine interaction) or by magnetic impurities. However the amount of magnetic impurities is expected to be very low in 2DEG fabricated by molecular beam epitaxy due to the high degree of control in the fabrication process.

The tunneling of electrons between the edge states involving spin flip processes mediated by the hyperfine interaction with the nuclear spins was originally investigated by Dovers [68] and Kane [69] with transport measurements. In a subsequent work of Keith R. Wald *et al.* [70] we can see that scattering processes that involves the tunneling of electron between adjacent edge states where the electron spin flips while the nuclei spin of the Ga and As ions flops does not take place if the energy of the electrons is below $200\,\mu eV$.

G. Muller *et al.* [67] showed that the spin-orbit interaction in GaAs heterostructures allows transitions between neighboring spin polarized edge states which is also accompanied by a change in the $k-$momentum. Additionally, the spin-orbit interaction induces an effective magnetic field in the plane of the 2DEG seen from the moving frame of the electrons, which give rise to an enhancement of the Landé g-factor at the edge. As a consequence, long equilibration lengths $l_{eq} \sim 160\,\mu m$ where predicted in agreement with experimental observations.

Due to this property edge states can be considered as independent wave guides for the wave function of electrons. Aditionally, each edge state is characterized by the intrinsic resistance R_K which defines the quantum of conductance $G_0 = 1/R_K = e^2/h$. Within this picture, edge states carry the current acting as parallel *ideal* unidimensional quantum wires.

Edge States in the Hall Configuration

The previous description of the edge states predicts the observed values of the Hall resistance and the vanishing longitudinal resistance measured in Hall bar geometry. In the usual six contact configuration (Fig. 3.10) a voltage difference V_1 is applied between contact **1** and **4** which drives a current through N edge channels, each one of

resistance R_K. The total injected current I_1 at contact **1**, reads:

$$I_1 = I^{(out)} - I^{(in)} = \sum^{N} \frac{V_1}{R_K} - \sum^{N} \frac{V_4}{R_K} = \frac{N(V_1 - V_4)}{R_K} \tag{3.42}$$

Due to the lack of inter-channel scattering, each edge state carry the electrochemical potential μ_i of the reservoir i from which they have emanated and dissipate this energy at the reservoir where they arrive. In this example the contact **1** and **4** are the reservoir while the contacts **2**, **3**, **5** and **6** are voltage proves (floating ohmic contacts) weakly coupled to the 2DEG. Thus $V_1 = V_2 = V_3$ and $V_4 = V_5 = V_6$.

The longitudinal and the Hall resistance are obtained by measuring respectively the voltage difference between the probes **2** & **3** and between the probes **3** & **5**, thus:

$$\begin{aligned} R_{xx} &= \frac{V_2 - V_3}{I_1} \quad \rightarrow \quad R_{xx} = 0 \\ R_{xy} = \frac{V_3 - V_5}{I_1} &= \frac{V_1 - V_4}{I_1} = \frac{R_K}{N} \quad \rightarrow \quad R_{xy} = \frac{R_K}{N} \end{aligned} \tag{3.43}$$

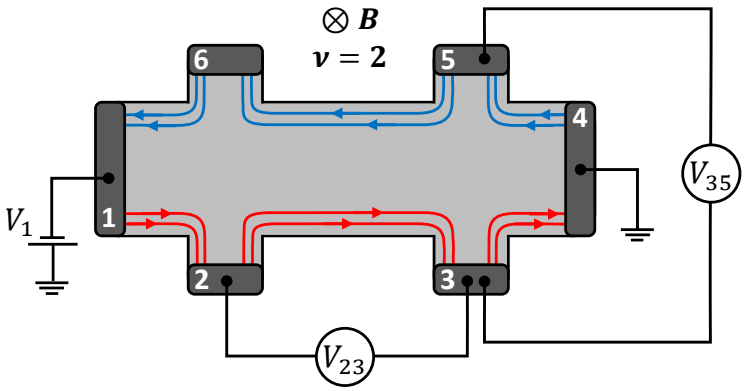

Figure 3.10: Edge states propagation in a Hall bar geometry at filling factor $\nu = 2$.

Semiclassical Interpretation of the Edge States

The chiral propagation of the edge states can be understood from the classical cyclotron motion of an electron in a finite size system with hard walls. While the electrons on the bulk are localized on simple cyclotron orbits, the circular motion of the electrons that are near the edges is interrupted by the walls resulting in skipping orbits (See Fig 3.11). The chirality of the cyclotron motion imposed by the magnetic field directly implies that the skipping orbit are also chiral in the same way the edge states are chiral in the quantum description.

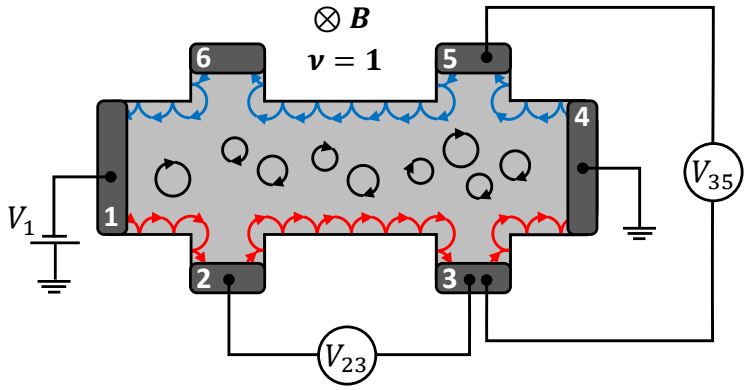

Figure 3.11: Semiclassical interpretation: edge states are the quantum equivalent of the classical skipping trajectories that results when cyclotron orbits are reflected on a hard wall representing the boundaries of the system. The regime of filling factor $\nu = 1$ was represented for simplicity.

3.4 Disorder

Paradoxically, the Quantum Hall effect could not be observed in an ideal system with no disorder, meaning that the quantized values of R_{xy} will only occur at the very precise values of the magnetic field at which the filling factor takes exactly integer values (See Fig. 3.5) and they would not be observed as wide plateaus. It turns out that the disorder is fundamental not only to break the translation symmetry but also because it plays a central role in some processes that make possible a stable conduction through the edge states in wide ranges of the magnetic field. I describe in this section the most relevant of these processes.

3.4.1 Stability of the Fermi Level

In order to observe the IQHE with edge channels carrying the current we made the implicit hypothesis that the Fermi level can be tuned at free will in between two bulk Landau levels. As we will see this is not the case since the Fermi level is unstable on regions of low density of states, meaning that it can easily fluctuate by large amounts, of the order of $\hbar\omega_c$.

The Fermi level, which indicates the energy of the last occupied levels in a system[10], is related to the number of particles to arrange, the number of available states at per energy and the degeneracy of those states. It can be calculated at zero temperature as:

$$n_s = \int_0^{E_F} \rho(E) dE \tag{3.44}$$

Fluctuations on the electron density dn_s are then related to the variations of the Fermi

[10] In a system at equilibrium at finite temperature E_F indicates the energy at which the occupation probability is 50%.

level through the DOS at the Fermi energy:

$$dn_s = \rho(E_F, B)dE_F \tag{3.45}$$

When the magnetic field applied to a 2DEG is changed, the Fermi level will adjust to keep the density of electrons constant ($dn_s = 0$) compensating the variations induced on the density of states ρ due to the change in the quantized cyclotron energy $\hbar\omega_c$ and the degeneracy D_n of each Landau level.

If the Fermi level is in a region of low ρ, small changes on the degeneracy of the Landau levels will produce large changes in E_F. Therefore the Fermi level position is unstable. Conversely, when the Fermi level is in a region of large ρ, the fluctuations of E_F are small and it is stable while particles are reorganized among the many available levels. Consequently, in an ideal system without disorder the Fermi level will always be aligned to a Landau level. Thus if the magnetic field is increased, the Fermi level will jump from one Landau level to another while they are being depopulated. The presence of disorder avoid these jumps by inducing a finite width on the Landau levels, thus increasing the density of state in this region, which helps to stabilize the Fermi level.

The equation 3.45 also shows that for a fixed magnetic field, which fixes $\rho(E, B)$, and at an energy of large density of states the electron density can be largely modified when E_F is changed. Then the 2DEG is called ***compressible***. In other regions, when ρ is small, the density of electrons is constant and insensitive to changes in E_F and the 2DEG is ***incompressible*** (Fig. 3.12).

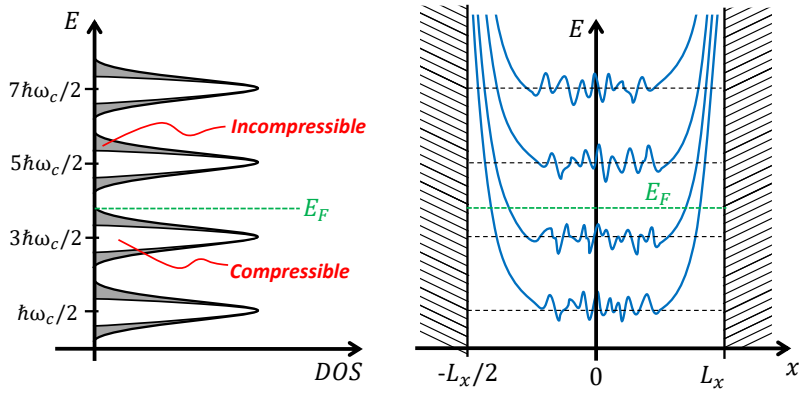

Figure 3.12: The disorder in the electrostatic potential on the 2DEG induces a finite width of the Landau levels. The 2DEG is *compressible* in regions where the DOS is high since the electron density can be tuned with the Fermi level E_F. Conversely, the 2DEG is said to be *incompressible* where the DOS is low.

3.4.2 Pinning of Localized States

The second main reason why the disorder is important is that the bulk localized states, which in a semi-classical interpretation corresponds to the cyclotron orbit that do not interact with the boundaries of the 2DEG, are not really *localized* in an ideal system with no disorder, meaning that they are not pinned and they can flow in response to electric fields (Fig. 3.13a).

In usual transport measurements the applied voltage difference used to drive the current generates an extra electric field which was not considered in the previous description of the electron motion. Therefore there are two electric fields, which are illustrated in the Fig. 3.13b for a two terminal device for simplicity:

1- The electric field $\boldsymbol{\mathcal{E}}_b$, that is naturally created at the boundaries, which drives the center of motion of the cyclotron orbit along the edges defining the edge states. This electric field is much more intense than the external fields but it only exist close to the boundaries.

2- The external electric field $\boldsymbol{\mathcal{E}}_e = \mathcal{E}\hat{y}$ created by the applied voltage difference which dominates in the bulk. In response to this field, the cyclotron orbits in the bulk will drift along the $\hat{x}$-direction connecting counter propagating edge channels. This would break the description of the Hall bar experiment given in section 3.3.4 that successfully explained the observation of the quantized Hall resistance and the vanishing longitudinal resistance.

In fact, when the disorder is considered the description in terms of chiral propagating edge channels separated by an insulating bulk holds perfectly. The disorder generates on the bulk a random potential landscape with hills and valleys which widen the Landau levels. Moreover, the local variation of this potential on the scale of l_B creates a local electric field that induces a drift of the cyclotron orbits in the bulk. However the equipotential around hill and valleys are close paths, hence the cyclotron orbits are pinned and effectively localized as shown in Fig. 3.13c.

3.4.3 Percolation

The random potential created by the disorder also explains the occurrence of plateaus in R_{xy} and the transitions between them. When the magnetic fields increases, the LL's are raised in energy but at the same time they are being depopulated. It means that the Fermi energy E_F falls within a LL exploring different spatial electrostatic landscapes.

Fig. 3.14 shows this situation, zooming in the second LL, while it is aligned with the Fermi level (Top left panel). The rest of the left panels in Fig. 3.14 shows the equipotentials $U = E_F$ in a particular region of the sample while the LL is being depopulated from the stage labeled as **1** down to **5**.

The typical size of the closed equipotential grow when the Fermi energy is close to the center of the Landau energy which corresponds to the peak in the DOS. At this

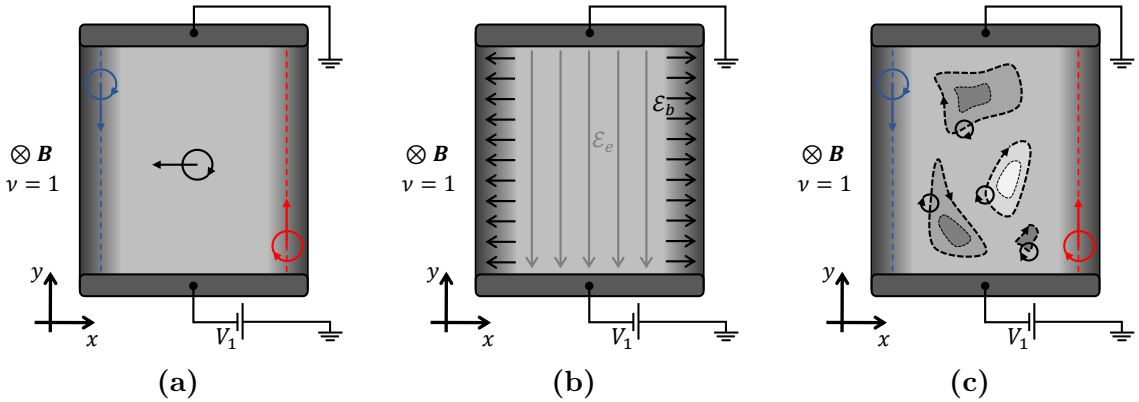

Figure 3.13: **(a)**In absence of disorder the cyclotron orbits in the bulk are not pinned and the can move in response to electric fields, thus the bulk is not insulating. **(b)** In a usual transport measurement, the external electric fields $\boldsymbol{\mathcal{E}}_e$ induces the drift of the unpinned cyclotron orbit in the bulk connecting counter propagating edge channels, leading to a non vanishing longitudinal resistance in opposition to the experimental observations. **(c)** The disorder generates a random potential landscape which traps the cyclotron orbit on the bulk along closed equipotential lines, therefore a vanishing longitudinal resistance and a quantized Hall resistance are attainable.

condition, a finite thermal energy can induce the electrons to tunnel from one edge channel to the counter-propagating through several equipotential paddles in the bulk. Therefore the bulk conduction is allowed, thus the longitudinal resistance R_{xx} shows a peak and the Hall resistance R_{xy} moves away from the quantized plateaus.

This effect defines two regimes in the DOS (Top right panel in Fig. 3.14). One around the center of the peak, when the equipotential $U = E_F$ are large and percolation is possible through the bulk. This regime consist of ***bulk extended states***. The second regime consists of the regions located away from the peak, where equipotentials are small and are isolated. These region defines the ***bulk localized states***[11].

In consequence the plateaus on R_{xy} are observed in ranges of the magnetic field between two LL's where the bulk consists of localized states. The transitions between plateaus occurs within the region of extended states of each LL.

[11]Note that these regions defined on the DOS are not necessarily the same that defines the compressibility of the 2DEG seen in Section 3.4.1.

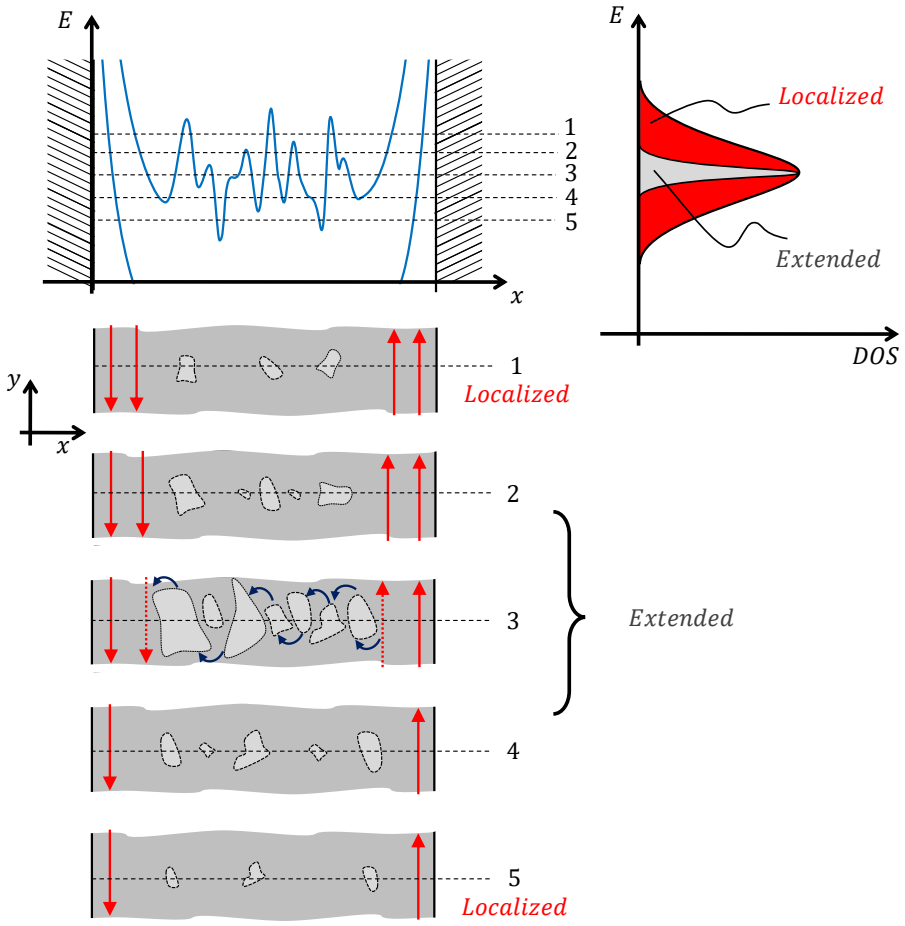

Figure 3.14: Left: Zoom in the second Landau level which reflects the disordered electrostatic potential presented in the bulk of the 2DEG. When changing the magnetic field or the Fermi level it is possible to explore different electrostatic configurations. By increasing the magnetic the Landau level is being depopulated from from **1** to **5**. The equipotential lines resulting in the bulk of the sample for this five configurations are shown below. When the puddles are big enough the electrons can tunnel through the bulk which consist of extended states. **Right:** Extended and localized states in the DOS.

Chapter 4

Electron Quantum Optics

This chapter addresses the general concepts of the electron quantum optic field and how the role of the interactions in the Quantum Hall regime can be investigated in this field. The first part presents the fundamental nanoestructures that are usually implemented in order to perform quantum optics-like experiments with electrons in the quantum Hall effect regime. These nanostructures provides the electronic analogous of particle sources, waveguides, beam splitters, etc. In particular we focus on the description of quantum dots and show how they can be implemented as energy filters, which are the main element that we use in our experiments. The second part of the chapter presents two main framework that incorporate the Coulomb interaction in the description of the quantum Hall effect. Firts we discuss *the electrostatic description*, which predicts the edge reconstruction for smooth confinements and the development of an internal structure in the edge channel. Finally we present *the Luttinger liquid theory* which predicts the decay of the Landau quasiparticles in the 1D chiral edge channel.

4.1 Optic with Electrons

As seen in the previous chapter, in the integer quantum Hall effect regime the electrons propagate in a chiral and ballistic fashion along the edge states. Thus edge states behave as ***wave-guides*** that can be used to manipulate the beam like motion of electrons in a similar way as optic fibers are used to manipulate photons in optics. Indeed, this analogy has motivated scientist to perform quantum optics-like experiments in 2D materials using electrons to mimic the photons.

The investigations in the field of ***photon quantum optics*** have demonstrated that it is possible to produce, characterize and manipulate the quantum states of the electromagnetic field which allows to implement those states to perform quantum computation algorithms. One of the objectives of the emerging field of ***electron quantum optics*** is to achieve such a degree of control on the quantum state of electrons in solid state systems. Besides the potential applications in future technologies there is also a

fundamental interest in the phenomena that could result from the different nature of electrons and photons.

One the one hand, photons are bosonic particles whose quantum statistic, which determines the equilibrium properties of an ensemble of particles, is described by the Bose-Einstein distribution. On the other hand, electrons are fermions and they obey the Pauli principle, thus their quantum statistic is described by the Fermi-Dirac distribution. Furthermore, the exclusion principle leads to the formation of the Fermi sea, which is a many body state, as the ground state of an electronic system. Therefore, unlike photons that can propagate through an electromagnetic vacuum, the electrons are always in presence of a Fermi sea when they propagate in a conductor.

Another major difference is that since electrons are charged particles they can easily interact with the surrounding charges in the heterostructure, the electromagnetic environment or even with the particles that constitute the Fermi sea. In fact, it has been predicted that these interactions can induce decoherence and relaxation. Since the electron quantum optic experiments are sensitive to the phase coherence, they provide a variety of versatile tools to investigate the decoherence and relaxation mechanism.

Nowadays a lot of effort is devoted to the manipulation of the quantum state of electrons at the single particle level. In that direction many types of single electron sources have been develop based on elementary nanostructures. Among the single electron sources that have been demonstrated in GaAs system are: the ***mesoscopic capacitor*** realized with an AC driven quantum dot [11], the single ***electron pump*** based on dynamic quantum dots [12, 13], the ***leviton pulse*** emitted by an Ohmic contact driven by a high frequency voltage [14, 15] and the transfer of electrons by ***surface acoustic waves*** along electrostatically defined quantum wires [16, 17].

Therefore, in the next sections, after a brief introduction to the Landuer-Buttiker formalism, I will describe some of the basic nanostructures that are commonly used to perform electron quantum optics experiments where one coherently manipulates the quantum state of the electrons and its propagation across the system. These nanostructures can be implemented to realise the electronic analogous of the usual optic components such as particle sources, beam splitters, energy filters, interferometers, etc. In particular, apart from the ac-sources mentioned before I will describe how a simple ohmic contact can be considered both as a dc-source of particles and as an effective local source of relaxation and decoherence. I will continue the discussion by describing a quantum point contact and how it can be implemented has a beam splitter and as a heat source. Finally, I will focus on the description of quantum dots that are used as **energy filters** and which are the main components that we implement during this thesis to perform an energy resolved spectroscopy of the relaxation of electrons in quantum Hall edge channels.

4.1.1 Landauer Description

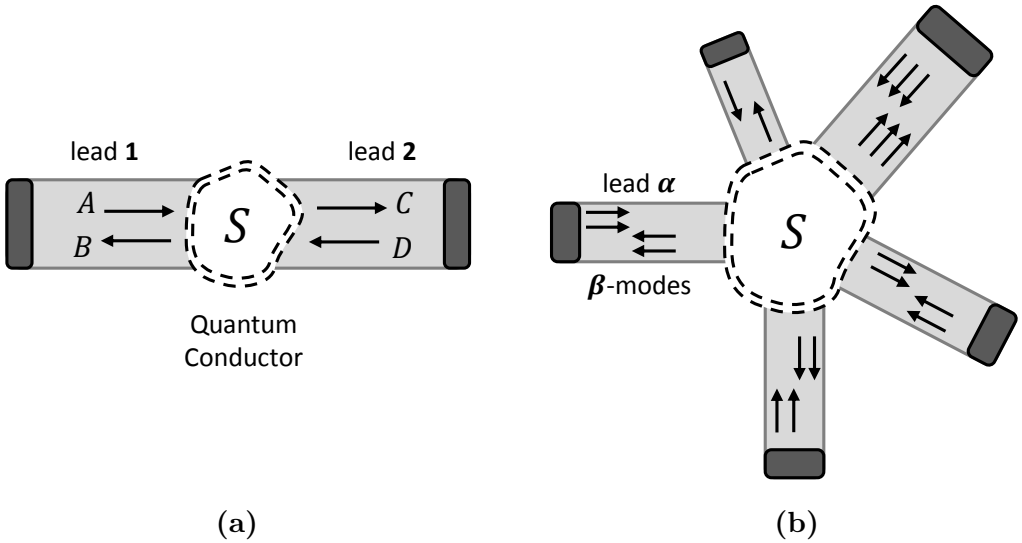

Figure 4.1: **(a)** Two terminal device with a single conduction channel: The quantum conductor is represented in the Landauer-Büttiker formalism as a scattering center S connected with ideal lead to the particle reservoirs. **(b)**. Representation of a multiterminal device with many modes in each lead. The scattering matrix S relates the incoming state in each mode of every lead with all the outgoing states in every mode of every lead.

In classical transport, usually in a diffusive regime, the Ohm's law relates two macroscopic observables, the current I and the voltage drop V_{sd} through the resistance R of the conductor, which is a coefficient that characterizes the whole system: $V_{sd} = IR$. Although the resistance is an extensive property it can be linked to the resistivity ρ_e, which is an intrinsic quantity that characterized the microscopic details of the system, through geometrical factor such has the length L along the direction of the current and the transversal area S. The conductance $G = 1/R$ and the conductivity $\sigma = 1/\rho_e$ are consequently related by the same factors:

$$R = \frac{\rho L}{S} \quad \longleftrightarrow \quad G = \frac{\sigma S}{L} \tag{4.1}$$

In the ballistic or coherent transport regime, when the size of the system is comparable or smaller than the elastic length l_e or the coherence length l_φ, the conductivity can not be well defined as a local quantity because the transport depends on the properties of the whole system. Thus the conductance G is the most convenient and well defined coefficient to describe the relation between the current and the voltage: $I = GV_{sd}$. In the general case of non linear transport, the differential conductance $G = dI/dV_{sd}$ is instead most convenient.

Furthermore, the conductance can be still related to the intrinsic properties of the electronic system within the Landauer-Büttiker formalism [71, 72, 73] which describes the electron propagation in a quantum conductor as the scattering of electronic waves.

The quantum conductor is represented as a scattering center, characterized by a scattering matrix S, where incoming electron waves are scattered in outgoing waves. For the simplest case of a two terminal device, with a single conduction channel, incoming waves with amplitudes A and D result in outgoing waves with amplitudes B and C (See Fig 4.1a), given by:

$$\begin{bmatrix} B \\ C \end{bmatrix} = S \begin{bmatrix} A \\ D \end{bmatrix} \qquad with \qquad S = \begin{bmatrix} r & t' \\ t & r' \end{bmatrix} \tag{4.2}$$

The diagonal elements of the scattering matrix are simply the complex reflection amplitudes of the wave at each side, while the off-diagonal elements are the complex transmission amplitudes from one side to the other. The reflection and transmission probabilities for the current of particles are: $R = |r|^2$ and $\mathcal{T} = |t|^2$, which are real numbers. Due to current conservation the scattering matrix is unitary[1], which implies that $R+\mathcal{T}=1$.

In consequence, for a two terminal device with a single conduction channel this formalism gives the conductance G in terms of the transmission $\mathcal{T}$ of the channel and the electric conductance quantum $G_0 = e^2/h$:

$$G = \frac{e^2}{h}\mathcal{T} \tag{4.3}$$

This is known as the Landauer formula and it can be generalized to other cases. If the same system has a spin 1/2 degeneracy, there are two independent states per energy that contribute to the conduction, thus the conductance of a two terminal device doubles:

$$G = \frac{2e^2}{h}\mathcal{T} \tag{4.4}$$

In fact each spin family acts as an independent conduction channel that contributes equally to the global conductance. The Landauer formula can be extended to the case where there are N conduction channels, each one characterized by a transmission $\mathcal{T}_n$ such that the conductance of a two terminal device is given by:

$$G = \frac{e^2}{h}\sum_n^N \mathcal{T}_n \tag{4.5}$$

Furthermore this description can be generalized to describe a system with multiple conduction channels, with different transmission and in a multiprobe geometry [73, 74, 75]. In such a case the scattering matrix relates the incoming state in each mode of every lead with all the outgoing states in every mode of every lead (See Fig. 4.1b).

[1] A unitary matrix satisfy $S^\dagger S = \mathbf{1}$ where $S^\dagger$ denotes the Hermitian conjugate and $\mathbf{1}$ the unity matrix

4.1.2 Ohmic Contacts

Ohmic contacts implemented either as current leads or as voltage probes are particle and energy *reservoirs* at a thermal equilibrium characterized by a local electrochemical potential μ and a temperature T. They absorb all the incoming particles and emits particles with a Fermi distribution $f(E, \mu, T)$ and random wave function phases.

A steady DC source of particles.

Figure 4.2(a) represents a two terminal device with $N = 2$ edge channels. Each lead, labeled as **1** and **2**, is set at a different voltage. The lead **1** is biased at a voltage V_1 and emits particles from the bottom of the conduction band up to the electrochemical potential $\mu_1 = E_F - eV_1$ with a Fermi distribution f_1. As an ideal lead, it emits the same distribution of particles in each *outgoing* edge channel. In a similar way the lead **2**, connected to the ground ($V_2 = 0$), emits particles up to the Fermi level $\mu_2 = E_F$ with a distribution f_2 in each edge channel.

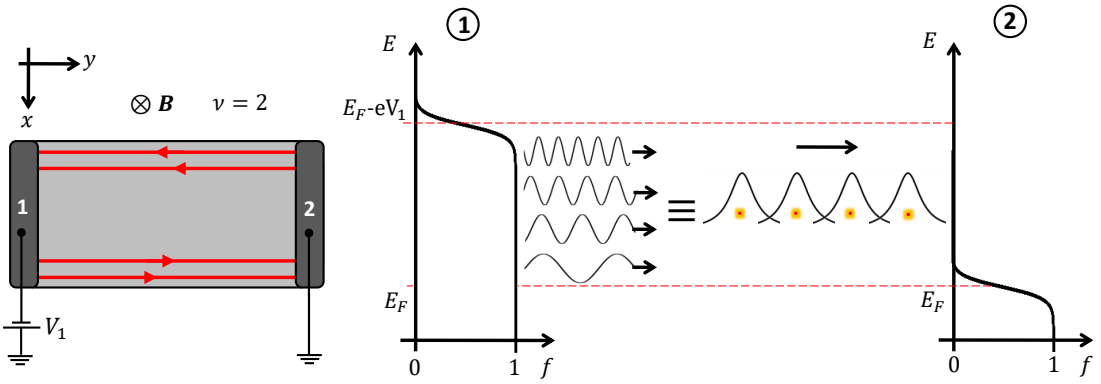

Figure 4.2: A biased Ohmic contact injects a net current in the system emitting free electrons in the bias energy windows eV_1. The free waves can be combined to build a representation in terms of sequentially emitted and single occupied orthogonal wave packets [76].

The *net current* I injected by the biased lead **1** takes into account the incoming and outgoing distribution of particles at all energies in each of the N edge channels:

$$I = I^{out} - I^{in} = N \int dE\, e\, v(E)\, \rho(E)\, [f_1(E, \mu_1, T) - f_2(E, \mu_2, T)] \tag{4.6}$$

In the 1-dimensional edge channel the velocity $v(E)$ perfectly compensates the energy dependence of the density of state $\rho(E)$ up to a constant: $v(E)\rho(E) = 1/h$. This perfect cancellation in 1-dimension leads to the quantization of the conductance for N channels as seen before:

$$I = \frac{e}{h} N \int dE\, [f_1(E, \mu_1, T) - f_2(E, \mu_2, T)] = \frac{e}{h} N(\mu_1 - \mu_2) = \frac{e^2}{h} N(V_1 - V_2) \tag{4.7}$$

Therefore a biased ohmic contact can be seen as a steady source of particles (a dc source) that emits free electrons in the bias energy windows $(\mu_1 - \mu_2)$. Furthermore, the emitted waves can be combined to construct orthogonal wave packets that the ohmic emits, with single occupation, in each edge channel separated by a time $e(V_1 - V_2)/h$. This representation, shown in Fig 4.2, only relies on the Pauli and the Heisenberg Principles as described in Ref. [76].

A Model for Inelastic and Incoherent Scattering.

In the Landauer-Büttiker formalism the scattering matrix only describes elastic processes while inelastic scattering can take place only inside the ohmic contacts. Electrons that are absorbed by a voltage probe (a floating ohmic contact) lose their phase coherence and relax to the equilibrium state defined in the reservoirs, then they are re-emitted or replaced by other electrons such that the current is conserved on the whole quantum conductor (Fig. 4.3). Büttiker [77] pointed out that in fact voltage probes can be used to mimic the effects of phase-randomizing inelastic scattering events on quantum transport.

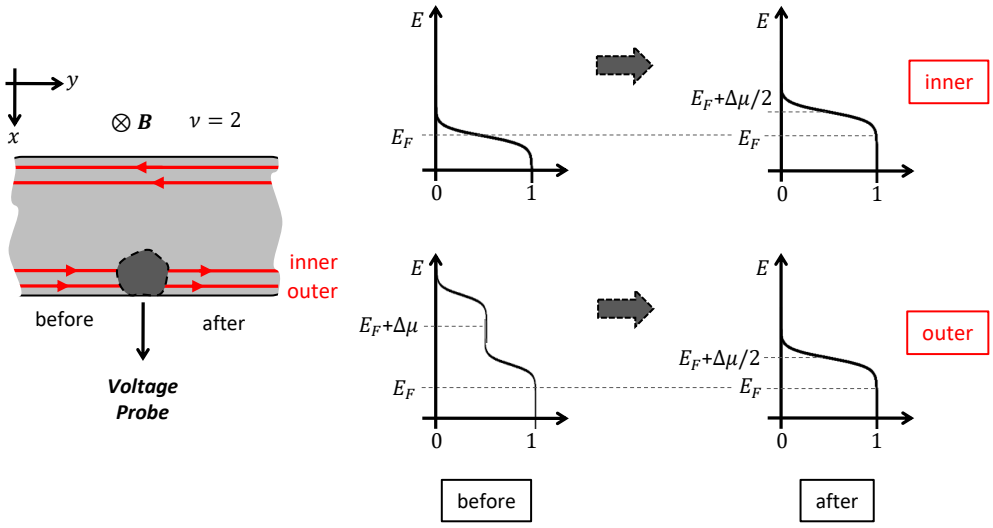

Figure 4.3: Left: A voltage probe is a floating Ohmic contact that can be implemented to introduce relaxation and decoherence in the system. When considering the electronic transport in the quantum Hall effect regime, a voltage probe will introduce equilibration among the co-propagating edge channels. **Right:** As an example, an out-of-equilibrium state injected in the outer edge channel before the voltage probe is brought to an equilibrium distribution after the voltage probe with the particles redistributed in both edge channels.

At first D. Sprinzak *et al.* implemented a voltage probe to quench the phase coherence in an entangled interferometer-detector system realized in the IQHE [78]. Later, S.Oberholzer *et al.* used a voltage probe to induce inter edge channel equilibration and redistribution of the current fluctuations in two co-porpagating edge channels [79].

However a first quantitative and systematic experimental demonstration of the dephasing properties of a voltage probe in a quantum conductor was done by P. Roulleau *et al.* in 2009 [80]. They implemented a Mach-Zehnder interferometer (MZI) with one of the arms connected to a small floating ohmic contact through a quantum point contact. The quantum point contact allows to control the transmission probability $\mathcal{T}_p$ for a particle to be absorbed by the voltage probe. They observed that the visibility of the quantum interferences decreases when particles have a higher probability to be absorbed by the voltage probe with a $\sqrt{1-\mathcal{T}_p}$ dependence.

Additionally, C. Altimiras *et al.* used a voltage probe to progressively induce a faster relaxation of an out-of-equilibrium state created on an edge channel in the integer quantum Hall effect regime [53].

Therefore voltage probes serve as a simple model to include relaxation and decoherence in quantum transport. The importance of this approach resides on the simplicity of the model to include the effects of rather complicated processes in theoretical calculations or in experiments. There exists as well more sophisticated models that generalize the Büttiker approach in order to describe phase breaking and inelastic scattering in a more distributed way [81, 82, 83].

4.1.3 Quantum Point Contact

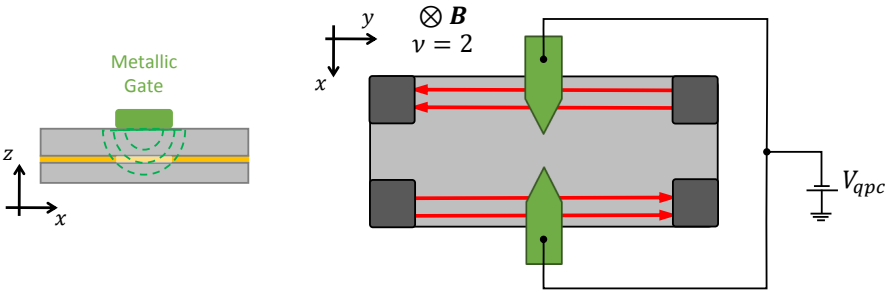

Figure 4.4: A quantum point contact nanostructure formed by two metallic finger placed on the surface of the GaAs heterostructure, which is only capacitively coupled to the 2DEG creating an electrostatic barrier for the electrons.

A quantum point contact (QPC) can be realized with a metallic nanostructure as shown in Fig. 4.4 which consists of two electrodes placed on the surface of the GaAs heterostructure defining a small gap. The metallic gates are only capacitively coupled to the 2DEG which is at about ~ 90 nm under the surface. When the electrodes are polarized with a negative voltage V_{qpc} they create an electrostatic barrier generating a smooth constriction in the electrostatic landscape where the edge states propagate.

The constriction brings closer counter propagating edge states corresponding to the same Landau level. Therefore the QPC allows the edge channel to have finite proba-

bility of being backscattered or transmitted through the region. Since the edge states developed from higher Landau levels are located closer to the bulk, the edge states can be successively reflected by the QPC. The outer edge channel, which corresponds to the lowest Landau level ($n = 0$ and spin polarization $s = +1/2$) is always the last edge state to be reflected.

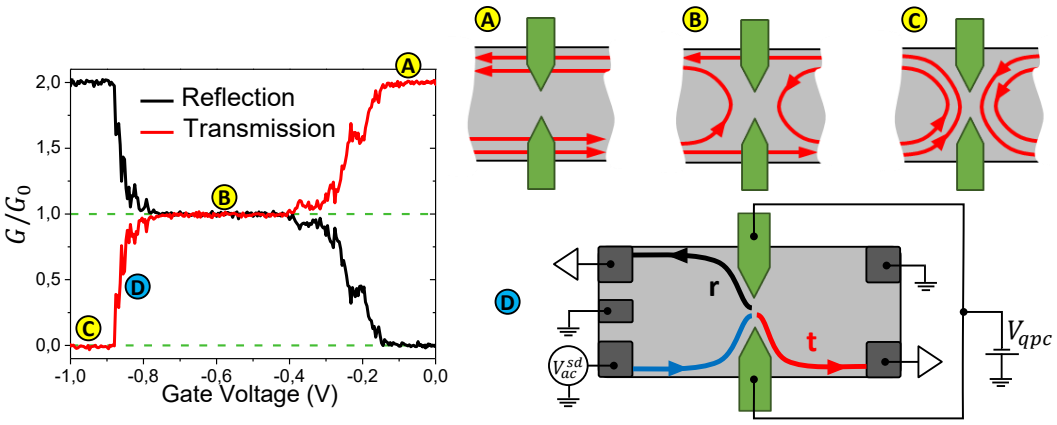

Figure 4.5: Measurement of the differential conductance G of a QPC as a function of the polarization voltage V_{qpc}. The QPC can be used to control the number of edge channels that are transmitted from ones side to the other (Insets: **a**,**b**,**c**). In the transition region between the large quantized plateaus, the QPC works as a *beam splitter* for one edge channel (Inset **d**). A schematic representation of the measurement circuit is shown in inset **d** where we only depict the partitioned edge channel that is driven by a small ac-signal for a lock-in detection.

The Fig. 4.5 shows the transmission and reflection probability of a QPC as a function of the polarization voltage V_{qpc} measured in the integer quantum Hall effect at filling factor $\nu = 2$. The reflection and transmission coefficients are obtained by measuring the differential conductance G of the QPC at the two outputs by using a standard lock-in technique. As seen in the measurements, the QPC is an electrostatic gate that can be operated to control the number of edge channels that are transmitted from one side of the system to the other side (Fig. 4.5 (a)-(c)). The large plateaus indicates the quantization of the conductance on each edge state as predicted by the Landauer-Büttiker theory as integer multiples of the electric conductance quantum G_0. In the vertical transition regions between the plateaus there is an edge channel that is partially transmitted and partially reflected. Thus the QPC works as a ***beam splitter*** for that edge state, while the other is completely reflected or transmitted.

Furthermore, a QPC can be implemented as well as a ***heat source*** when a finite bias voltage V_{sd} is applied while the transmission of the QPC is set to an intermediate value $0 < \tau_{qpc} < 1$ for a single edge channel (See Fig. 4.6). In such conditions the QPC mixes the two incoming distribution such that at the right output of the QPC the distribution of particles is a double step function[2].

[2]At the other output we find the complementary distribution:

$$f_{out/left}(E) = (1 - \tau_{qpc}) f_F(E - eV_{ds}) + \tau_{qpc} f_F(E)$$

$$f_{out}(E) = \tau_{qpc} f_F(E - eV_{ds}) + (1 - \tau_{qpc}) f_F(E) \tag{4.8}$$

This is an out-of-equilibrium state that carries a heat current due to the electron-hole excitations that have been created on the edge channel. The relaxation of such distribution of particles along the edge channel was experimentally measured by H. le Sueur *et al.* [52] in order to investigate the role of interactions in the IQHE regime. I will discus some of their observation in the next chapter in connection with the measurements performed in this thesis in the same regime.

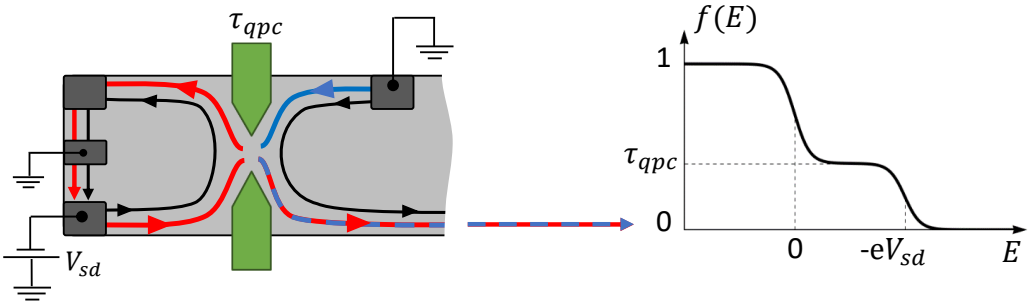

Figure 4.6: The biased QPC, set at an intermediate transmission τ_{qpc}, mixes the incoming distributions from a grounded contact (up right) and the biased contact (down left) at V_sd. At the right output a double step distribution function is created only on the partitioned edge channel. This out-of-equilibrium distribution carries a charge and a heat current. The Fermi level E_F defines the zero in the energy scale.

4.2 Quantum Dot

A metallic nanostructure as shown in figure 4.7, that is only capacitively coupled to the 2DEG, can be used to confine the electrons in a small region defining a quantum dot (QD). A suficiently large negative polarization of the set of electrodes deplete the 2DEG underneath but also trap some electrons in the central region of the structure.

The pair of electrodes ***G1-G2*** (***G1-G4***) defines a QPC that allows to control the coupling strength between the confined electrons and the source (drain) reservoir, hence the transmission probability $\mathcal{T}_s$ ($\mathcal{T}_d$). The plunger gate or electrode ***G3*** is used to add an electrostatic energy to the ensemble of electrons in the QD which will be used to control the electrochemical potential of the QD.

Electrostatically defined QD's in GaAs heterostructures shows remarkable characteristic behaviors of a zero dimensional many body system such energy and charge quantization and strong electron-electron correlations that results in the Coulomb blockade phenomena. In the following sections I will describe the basic notions of these effects in order to shows how a quantum dot can be implemented as an tunable energy filter.

In absence of interactions the distribution of particle in the inner edge channel is not affected since it is completely reflected at the QPC.

All the measurements were performed in the systems where we will perform the energy resolved spectroscopy of the relaxation.

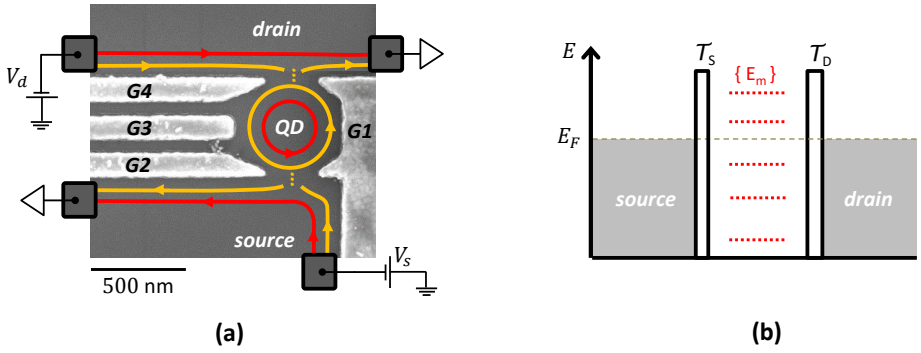

Figure 4.7: **(a)** Scanning electron micrograph of a typical quantum dot implemented during this thesis. The schematic circuit allow to characterize the quantum dot by measuring the either the reflected or the transmitted current. **(b)** Energy diagram showing the discrete energy levels of the QD developed due to the spacial confinement. The electrostatic barriers, characterized by transmission probabilities $\mathcal{T}_s$ and $\mathcal{T}_d$, defines the coupling of the QD with the source and drain reservoirs which have a continuum of states at thermal equilibrium. Notice that only the outter edge channel is coupled to the reservoir while the inner edge channel which also forms a QD is completely isolated from the reservoirs, thus it does not contributes to the transport trough the structure.

4.2.1 Charge quantization

In the weak coupling regime the electrons are well localized in the central region of the structure and therefore the total charge in the QD can only be an integer number of e,

$$Q_N = -Ne \qquad N \in \mathbb{N} \tag{4.9}$$

This means that the quantum fluctuations in the particle number N is small under the condition that the tunnel resistance of each QPC is large enough:

$$R_t > \frac{h}{e^2} \quad \longleftrightarrow \quad \frac{G_{qpc}}{G_0} < 1 \quad \longleftrightarrow \quad \mathcal{T}_{s,d} < 1 \tag{4.10}$$

We must notice that such a charge quantization is not guaranteed in a normal conductor like any of the electrodes that define the QD. When these electrodes are polarized the induced charge Q_g that appears is due to the rearrangement of the electron gas inside of the metal with respect to the positive background ions. Thus Q_g can change continuously between any values. In the metal electrode the polarization charge is related to the applied voltage V_g through the geometrical capacitance C_g,

$$Q_g = C_g V_g \tag{4.11}$$

Recently S. Jezouin *et al.* [84] experimentally demonstrated how the quantization of the charge in a metallic QD was progressively destroyed while reducing the strength of the tunneling barriers. A full control of the quantum fluctuations allows them to explore the whole regime from the tunnel barrier to the ballistic regime.

4.2.2 Energy quantization

The extreme spatial confinement leads to the *full* quantization of the energy spectrum of the electrons in the QD, pretty much as the text book problem of a particle in a box in quantum mechanics (Fig 4.7)b. Of course, the particular energy spectrum $\{E_m\}$ depends on the details of the confinement potential and the sample geometry. In any case, beside possible degeneracies, the energy levels are single particle levels that at zero temperature must be occupied one by one following the Pauli exclusion principle like in the atomic model. For this reason QDs are also known as artificial atoms.

As it will be described in the next section (4.2.3), in small QDs the electron-electron interaction is not negligible and it will introduce an extra energy scale that modifies the energy level separation between the last occupied level and the next empty level.

Occupation at finite temperature

At finite temperature the occupation of the energy level of the QD can not be simply described by a Fermi-Dirac distribution since the system is highly interacting and it is almost isolated from the reservoirs causing the total energy of the system to be strongly dependent on the number of particles. At equilibrium the thermal occupation of a set of discrete energy levels is better described by the Gibbs distribution which can be calculated in the grand canonical ensemble in statistical mechanics [85, 63]. When the thermal energy is comparable to the level spacing the Gibbs distribution can be radically different from the Fermi function [86].

Intrinsic Lineshape

The QD can be understood as well as an effective Fabry-Perot interferometer where the edge channel interferes with itself due to the multiple internal reflections.

The intrinsic lineshape $L(E, E_1)$ of a particular energy level E_1, calculated either with this simple model or with the scattering theory, is Lorentzian:

$$L(E, E_1) = \mathcal{T}_1 \frac{(\Gamma_1/2)^2}{(E - E_1)^2 + (\Gamma_1/2)^2} \tag{4.12}$$

with an amplitude $\mathcal{T}_1$ and a width Γ_1 (FWHM) that depends on the transmission probability $\mathcal{T}_s$ ($\mathcal{T}_d$) between the QD and the source (drain) reservoir, the propagation speed v_d and the size of the QD through the variable a that is the total propagation

length between two successive reflection in the same barrier:

$$\mathcal{T}_1 = \frac{4\mathcal{T}_s\mathcal{T}_d}{(\mathcal{T}_s+\mathcal{T}_d)^2} \qquad \Gamma_1 = \frac{\hbar v_d}{2a}(\mathcal{T}_s+\mathcal{T}_d) \tag{4.13}$$

A simple model of a circular QD with a radius $r = 250$nm, which set $a = \pi r$, at the tunneling regime $\mathcal{T}_s \approx \mathcal{T}_d \approx 0.005$ and assuming a propagation speed $v_d = 2\times10^5$ m/s gives an estimation for the linewidth $\Gamma_1 = 5\mu$eV expected for a QD defined by a structure as the one shown in Fig. 4.7.

The amplitude $\mathcal{T}_1$ gives the transmission probability through a single resonant level. In the case of symmetric barriers $\mathcal{T}_s = \mathcal{T}_d$ the discrete level has a perfect transmission $\mathcal{T}_1 = 1$ and the electrons that have the same energy can tunnel the QD without reflection even if each QPC is tuned almost at pinch-off ($\mathcal{T}_s{=}\mathcal{T}_d \ll 1$).

4.2.3 Charging effects

The effects of the residual Coulomb interaction in the 2DEG is enhanced in the QD since the electrons are not free to rearrange themselves to minimize the electrostatic energy. Therefore electron-electron interactions strongly affects the tunneling process in the QD and the addition of an extra electron raises the total energy of the QD not only due to the new single particle level that is occupied but also due to the Coulomb repulsion between the electrons.

The constant interaction model describes the Coulomb interaction, as a mean field theory, assigning a finite capacitance C_{eq} to the QD [87, 88]. This capacitance can be understood as the total geometrical capacitance between the small QD area and the surrounding electrodes (C_g), the source (C_s) and the drain reservoir (C_d) (See Fig 4.8a for the equivalent circuit representation).

$$C_{eq} = C_s + C_d + \Sigma_{gates} C_g \tag{4.14}$$

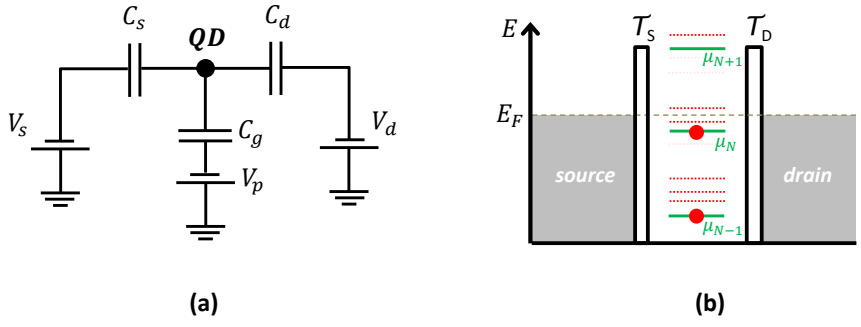

Figure 4.8: **(a)** Equivalent circuit of a QD in the *constant interaction* model. **(b)** Energy diagram of the quantum dot showing the electrochemical potential μ_N corresponding to states with different number of charge N (green) and the discrete single particle energy levels (red).

The total ground state energy $U(N)$ of the QD containing N electrons is the sum of all the single particle energies and the electrostatic energy stored in the capacitance[3] C_{eq} due to the charge imbalance between the quantized charge in the Dot and the continuous induced charge on the leads and the metal electrodes. Here we consider only the induced charge Q_g by the plunger gate voltage V_p applied in the electrode $G3$, since the other electrodes are usually polarized to a fix value to form the QD and will only contribute with a constant offset to the energy. Then the total energy reads:

$$U(N) = \sum_{n=1}^{N} E_n + \frac{(-eN + Q_g)^2}{2C_{eq}} \tag{4.15}$$

The electrochemical potential $\mu_D(N) = U(N) - U(N-1)$ that indicates the minimum energy that was necessary to add the N^{th} electron is:

$$\mu_D(N) = E_N + \frac{e^2}{C_{eq}}\left(N - \frac{1}{2}\right) - e\frac{C_g}{C_{eq}}V_p \tag{4.16}$$

which shows that the electrochemical potential of the dot can be linearly controlled with the plunger gate voltage V_p through its lever arm defined as $\alpha_p = C_g/C_{eq}$.

At zero bias voltage $V_{sd} = V_s - V_d$, if $\mu_D(N)$ is aligned with the electrochemical potential of the leads (resonant condition), the electrons can tunnel through the QD while the charge fluctuates between the two values $N \leftrightarrow N-1$. Conversely, if $\mu_D(N)$ is put below the electrochemical potential of the leads, the state with N charges stabilizes and there is no current until the next alignment between $\mu_D(N+1)$ and the electrochemical potential of the leads. The period in the gate voltage ΔV_g between two successive resonant conditions is

$$\Delta V_g = \frac{1}{e\alpha_p}\left((E_{N+1} - E_N) + \frac{e^2}{C_{eq}}\right) \tag{4.17}$$

At fix plunger gate voltage V_p, the change in electrochemical potential $\Delta\mu_D = \mu_D(N+1) - \mu_D(N)$ between the state with $N+1$ charges and the state with and N charges results:

$$\Delta\mu_D = e^2\left(\frac{1}{C_Q} + \frac{1}{C_{eq}}\right) = dE_{N+1} + E_c \tag{4.18}$$

where $C_Q = \rho_{1D}e^2$ is the quantum capacitance of the QD from the zero dimensional density of states $\rho_{1D} = 1/dE_{N+1}$. We can identify the two contribution to $\Delta\mu_D$: An increase of the *chemical potential* due to the increase in the number of particles (C_Q term) and an increase of the *electrotatic potential* due to the Coulomb interaction (C_{eq} term). The latter defines the charging energy $E_c = e^2/C_{eq}$.

[3] Assuming that the QD's capacitance is constant and that the set of single particle energy levels $\{E_N\}$ is not essentially modified by the Coulomb interaction

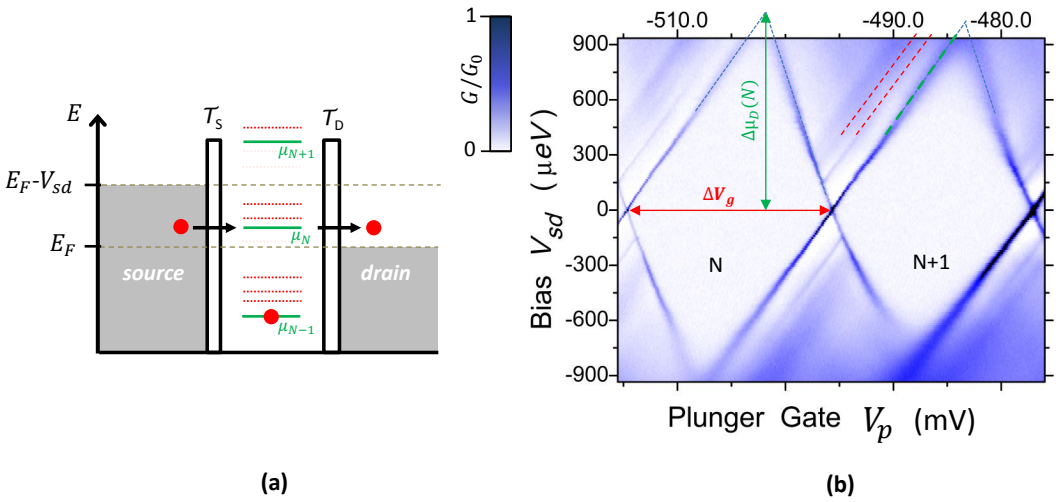

Figure 4.9: **(a)** Energy diagram of the QD and the reservoirs at finite bias V_{sd}. The ground state of the quantum dots with different number of particles N is represented in green and the excited states in red. **(b)** Measurement of the differential conductance as a function of the bias voltage V_{sd} and the plunger gate voltage V_p. Two Coulomb diamonds are observed, where the transport is suppressed, which correspond to the charge states with N and $N+1$ electrons. In between the Coulomb diamonds sequential transport is allowed but the charge fluctuates only by $\pm e$. The excited states appear as additional faint lines, highlighted by the red dashed lines, in between adjacent Coulomb diamonds.

4.2.4 Coulomb Blockade

The interplay between the spatial confinement and the charging effects can be clearly seen by measuring the differential conductance $G = dI/dV_{sd}$ of the QD as a function of the source-drain bias voltage V_{sd} and the plunger gate voltage V_p in the regime in which the thermal energy is smaller than the charging energy and the level spacing $\{E_c, dE_m\} \gg k_b T$ (Fig. 4.9b).

The large rhomboidal regions are called Coulomb Diamonds and correspond to situations where the current through the QD is suppressed due to the charging effects. This is known as the Coulomb blockade regime. Essentially it occurs because the electrochemical potential of the QD is outside of the bias energy windows and hence tunneling can't take place. Thus the total charge of the QD is stable and well defined.

Outside of these regions, the current can flow through the QD but the tunneling remains sequential as a collateral consequence of the charging effects. If the bias energy window is $|eV_{sd}| < \Delta\mu_D$, then only one discrete level can be occupied at a time and the charge of the QD fluctuates by $1e$. If the bias energy window is $\Delta\mu_D < |eV_{sd}| < 2\Delta\mu_D$, then the level of μ_N and μ_{n+1} can be simultaneously inside of the bias window and two states cna be occupied at a time , thus the charge of the dot fluctuates by $2e$. Increasing the bias, increases the number of discrete levels that can simultaneously contribute to the current across the quantum dot, which gives rise to the Coulomb staircase. During the experiments carried out along this thesis, we remains in the low bias regime such that the transport is sequential through a single energy level.

A comparison between the vertical and the horizontal elongation of the Coulomb diamonds provides an accurate determination of the lever arm α_p of the plunger gate as well as a good estimation of the charging energy and the level spacing of the quantized energy levels.

4.2.5 QD thermometry

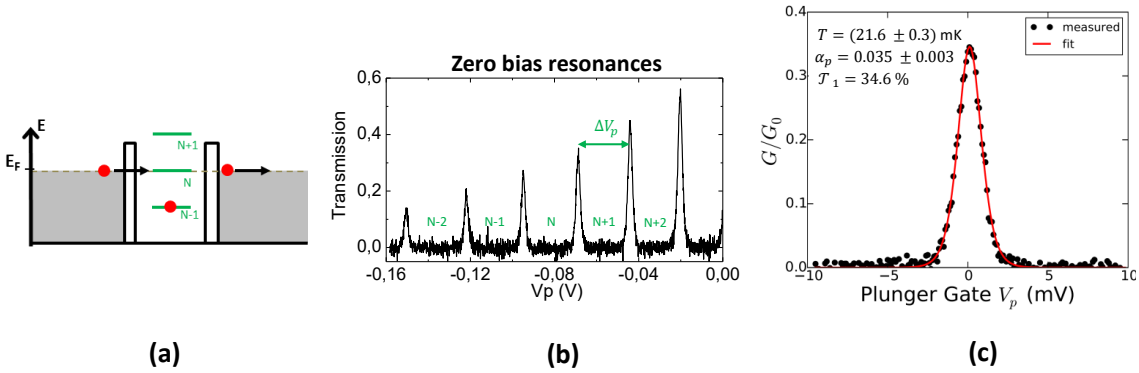

Figure 4.10: **(a)** At zero bias voltage, a discrete level of in the QD is at a resonance condition when it is aligned to the electrochemical potential of the leads. **(b)** A measurement of the differential conductance G or the transmission $\mathcal{T}_1 = G/G_0$ as a function of the plunger gate voltage shows a peak each time the QD is at a resonant condition. **(c)** Fit of the thermal broadened Coulomb resonance using Eq. 4.19, from which the electronic temperature $T = 21.5$ mK can be extracted while the phonon temperature was about ~ 18 mK.

The Fig. 4.10b shows a measurement of the differential conductance dI/dV_{sd} at zero bias as a function V_p showing the equidistant Coulomb peaks characteristic of successive resonant conditions in the QD 4.10a.

When the thermal energy k_bT of the electrons in the leads is larger than the intrinsic width Γ_1 of the discrete levels in the QD, the Coulomb resonances measured in the differential conductance does not reflect the intrinsic lineshape of the resonant levels. Instead, Beenakker [86] calculated that in this regime, the line shape of the peaks measured in the differential conductance $G(V_p)$ becomes:

$$G(V_g) = G_{max}\left[cosh\left(\frac{\alpha_p e(V_p^{(i)} - V_p)}{2k_bT}\right)\right]^{-2} \tag{4.19}$$

In this regime the QD level is probing the thermal broadening of the Fermi sea at the leads. Therefore QD's are used as local thermometers that are directly coupled to the electronic system. The fig. 4.10c shows a fit of a single Coulomb resonance using equation 4.19 from with we obtain an electronic temperature of $(21.5 \pm 0.3)\,mK$ while the base temperature of the fridge was $(18 \pm 0.3)\,mK$.

4.2.6 QD as an energy filter

Let's consider the transport through the QD in the coherent resonant tunneling regime ($E_c > k_bT > \Gamma_1$) where elastic tunneling events are the first order processes that can take place. At finite bias V_{sd} the QD can be implemented as a ***tunable energy filter*** as long as there is a single active level within the bias energy window as represented in Fig. 4.11a. Such condition is obtained close to the vertex between two adjacent Coulomb diamonds, the charge degeneracy point, at low bias $|eV_{sd}| < \Delta\mu_D$ such that the transport remains sequential. The Fig. 4.11b shows a measurement on which only the boundaries of the Coulomb diamonds are observed and no other extra features are seen indicating that indeed transport occurs through a single active level.

Although a detailed and quantitative description will be discussed in section 6.2, let us explain here the basic ideas by which a quantum dots can be implemented as an energy filter to inject or detect particles. Briefly, such implementation is possible since the tunneling through the QD is sequential and elastic. As shown in the Fig. 4.11a when the electrochemical potential μ_N of the QD is within the bias energy window $\mu_s - \mu_d = eV_{sd}$, only the electron in the source reservoir that has the same energy than μ_N can tunnel into the QD. Electrons in the source reservoir at higher or lower energies than μ_N can not tunnel since there are no available states on the dot at those energies. The electron in the QD has a lifetime τ_N given by the intrinsic width[4] Γ_1 of the resonant level $\tau_N = h/\Gamma_1$ after which it will be emitted in the drain reservoir since $\mu_N > \mu_d$. The emitted electron is released at an energy $E_1(Vp) = \mu_N(V_p) - \mu_d$ above the electrochemical potential of the lead. Of course the selected energy E_1 is a linear function of the plunger gate voltage V_p, thus the QD behaves as a tunable energy filter.

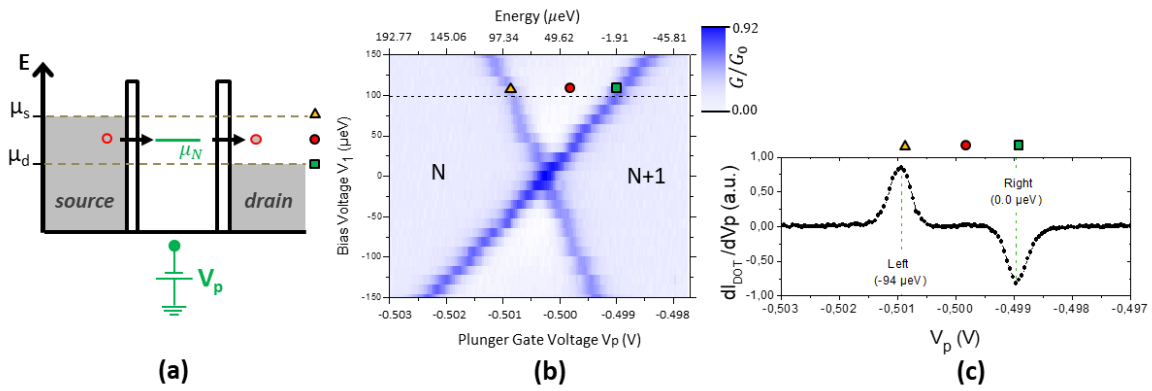

Figure 4.11: **(a)** Energy diagram of the quantum dot with a single active level on the bias windows. **(b)** Differential conductance measurement in a regime of sequential transport through a single resonant level. No signatures of excited states are seen in between adjacent Coulomb diamonds. **(c)** Transconductance measurement at a finite bias $eVsd = \mu_s - \mu_d = 94\mu$ eV.

[4]Notice that the the intrinsic width Γ_1 is determined by the transmission, $\mathcal{T}_s$ and $\mathcal{T}_d$, of the two barriers that form the quantum dot as explained in section 4.2.2.

This is a clear example on which the QD can be implemented as an energy filter to select the energy at which the electron are injected over the Fermi sea of the drain lead. However one can imagine that if the distribution of particles in the source lead is unknown, the QD in the same configuration, can be implemented as an energy resolved detector to measure the unknown distribution. This can be done by measuring the transmitted current $I(E_1)$ as a function of the resonant energy E_1. In order to access to the absolute value of the transmitted current $I(E_1)$ it is more convenient to measure the ***transconductance*** $dI/dV_p(V_p)$ than the usual *differential conductance* $dI/dV_{sd}(V_p)$. A typical transconductance measurement is shown in Fig. 4.11c which is detected by a standard low frequency lock-in technique with a small ac-excitation dV_p on the plunger gate in addition to its finite dc-value V_p. Then the transmitted current $I(E_1)$ (Fig. 4.12a) is obtained simply by integrating the transconductance measurement (Fig. 4.11c).

The transmitted current as a function of the resonant energy is expected to follow from the convolution of the bias energy windows $(f_s - f_d)$ and the lineshape $L(E, E_1)$ of the detector described by equation 4.12:

$$I(E_1) = \frac{e}{h} \int L(E, E_1) \left[f_s(E, \mu_s) - f_d(E, \mu_d) \right] dE \tag{4.20}$$

When the Fermi energy of both leads are well separated ($eV_{sd} \gg k_b T$) there are three regions that can be distinguished in the measured $I(E_1)$ (Fig. 4.12a). The transmitted current for each one of these regions reads:

$$\begin{aligned}
&(i) \qquad I_i(E_1) = \frac{e}{h} \int L(E, E_1) \left[1 - f_d(E, \mu_d) \right] dE \\
&(ii) \qquad I_{ii}(E_1) = \frac{e}{h} \int L(E, E_1) dE \qquad \longrightarrow \qquad I_{max} = \frac{e}{h} \frac{\pi}{2} \Gamma_1 \mathcal{T}_1 \\
&(iii) \qquad I_{iii}(E_1) = \frac{e}{h} \int L(E, E_1) \left[f_s(E, \mu_s) \right] dE
\end{aligned} \tag{4.21}$$

Equation 4.21(ii) defines the maximum transmitted current I_{max} when the discrete level is well inside the bias windows. The small wiggle of the current in this region reflects the variations of the transmission $\mathcal{T}_1$ or the intrinsic width Γ_1 as a function of the plunger gate voltage V_p. Additionally in 4.21(iii) the QD is probing the Fermi sea of the source lead and, in fact, if $\Gamma_1 \ll k_b T$ it provides a direct measurement of the Fermi sea since the lineshape can be approximated by a normalized delta function $L(E, E_1) \to (\pi \Gamma_1 \mathcal{T}_1 / 2) \times \delta(E - E_1)$:

$$I_{iii}(E_1) = I_{max} \times f_s(E_1, \mu_s) \tag{4.22}$$

The Figure 4.12(b) shows the measured Fermi Sea of the edge channel in the source lead at equilibrium. We see that it is well described by a Fermi function with an

effective temperature $T = 68$ mK. Deviations from a Fermi distribution appears at the tails of the Fermi Sea as a consequence of the finite width of the discrete level. Further details of the effect of the convolution will be presented in section 6.3.

Quantum dots were already identified to function as energy filters in double quantum dots configurations [89] and they were also implemented in magnetic focusing experiments [90]. More recently C. Altimiras *et al.* experimentally demonstrated that indeed the same approach can be use to extract the full energy distribution $f(E)$ of the particles in an edge channel in the IQHE regime as discussed above [51].

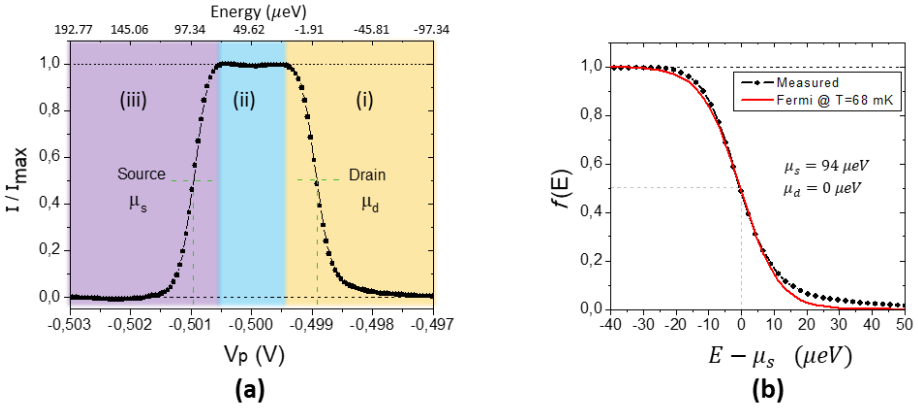

Figure 4.12: **(a)** Transmitted current at finite bias $I(E_1)$ normalized by the maximum current I_{max}. **(b)** Measured Fermi distribution from the source lead (region (iii)). The red line is a fit with a Fermi function at an electronic temperature $T = 68$ mK. Deviations between the measured points and the fit at the tails of the distributions arise from the finite width Γ_1 of the discrete level in the QD.

4.2.7 Excited states

Excited states in a QD arises when there are there are multiple energy levels that allow to change the charge state from N to $N + 1$.

When many excited states are available within the bias window the transport remains sequential, since the charging energy prevents electrons to tunnel simultaneously, but they act as alternative channels for the tunneling current. The intrinsic transmission of a discrete level in a QD depends on the extension of the associated wave function and its overlap with the wave function of the electrons in the leads, hence different excited states can have different transmission probabilities. Therefore excited states affect the global transmission of the QD and the mean escaping time of the electrons, thus the effective linewidth of the QD. They can also leads to regions of negative differential conductance (NDC) and no monotonous behavior of the temperature dependence of the Coulomb peaks' amplitude at zero bias.

Excited states can be detected in different ways. They can be seen as extra lines between Coulomb diamonds in measurements of the differential conductance or the transconductance as a function of bias and gate voltage (See Fig. 4.9). The extra lines

are usually parallel to the boundaries of the Coulomb diamonds since the excited states change the global transmission when they enter or leave the bias window. The excited states can be seen as well in the precise determination of the lever arm of the QD or as an effective increase in the electronic temperature extracted from the measurement of the Fermi distribution of the source and/or drain reservoir.

In the constant interaction model, excited states are just the single particle levels $\{E_m\}$ due to the spatial confinement for a fixed number of electrons. However in real QDs excited states can be originated from more complex processes such as collective excitation [91]. In addition asymmetric coupling to the leads can cause some of the excited states to be suppressed in some regions between Coulomb diamonds and or produce shifts in the Coulomb peaks positions as investigated by E. Bonet. *et al.* [92].

In order to perform the energy resolved spectroscopy by implementing quantum dots as energy filter we will avoid electrostatic configurations that lead to the presence of excited states in the quantum dots. This can be achieved by tuning the polarization voltages in the four electrodes that defines the QD in order to change its size or position until the conditions are found.

4.3 Interactions in 1D

As mentioned before, electron quantum optics experiments provide a way to investigate the role of the interactions in the electronic transport in the quantum Hall effect regimen. Beyond the standard dc charge transport, measurements of the coherence of quantum states, the energy transport or time resolved propagation of charges allows to unveil and characterize the different interaction mechanisms. In this section I present a description of some of those mechanisms that have been so far identified to affect the propagation of electrons along quantum Hall edge channels. In this thesis we explore the consequences of the interactions by looking at the energy transport associated to the propagation of charges.

4.3.1 Edge Reconstruction

The competition between the confinement potential, that tends to push the edge channels together, and the repulsive Coulomb interaction between neighboring edge channels can leads to a completely new spatial reorganization of the edge states. This is known as edge reconstruction which take place for smooth enough confinements.

If the confinement is *sharp* (hard wall) the repulsive interaction between edge channels can be neglected. Thus they are well described by the non interacting picture as represented in Fig. 4.13a (See Eq. 3.39).

For *smooth* confinements, the non interacting picture predicts well separated edge states in comparison with their widths $r_n \sim l_B$. However this implies that the local

density of electron has a sharp transition when an edge state crosses the Fermi level as shown in Fig. 4.13a. This spatial profile on the density of electrons is unstable and it will be modified due to the Coulomb interaction between particles.

The self-consistent solution indicates that the confined 2DEG splits into a series of regions consisting of ***compressible edge channels*** and ***incompressible bulk strips***, which corresponds to the regions indicated, respectively by the red and the blue arrows in the figure 4.13(b) [93]. The compressible edge state strips are flattened Landau levels at the Fermi energy that are partially filled. Thus, like in a metal, electrons can screen the original confinement potential to keep the compressible region as an equipotential while the density of electrons varies across it, resulting in a self-consistent confinement potential that is also flat. Now, between the edge channels there are incompressible bulk stripes, which can not screen the external potential and where the density of electrons remains constant (See Fig. 4.13(b)). The number of compressible edge strips remains equal to the filling factor, preserving the correspondence with the number of expected edge states. The existence of these type of structures have been experimentally investigated in Ref. [94, 95, 96].

Position and width of the strips

The position and width of the incompressible bulk strips can be estimated within this electrostatic model in terms of the depletion length L_D [93]. Let see this description in order to have an estimation of the characteristic width of a reconstructed edge channel and its separation to the neighboring co-propagating edge channels.

Metal gates that are capacitively coupled to the 2DEG deplete the 2DEG underneath when a negative potential V_g is applied on them. It means that the density of electrons is reduced to zero over a distance L_D from the electrode. Beyond the depletion length, the electrons screen the potential which give rise to a smooth density profile $n(x)$. At zero magnetic field, the depletion length and the density profile reads,

$$L_D = \frac{2V_g\epsilon}{e\pi n_s} \tag{4.23}$$

$$n(x) = \left(\frac{x - L_D}{x + L_D}\right)^{1/2} n_s\Theta(x - L_D) \tag{4.24}$$

where $\Theta(x)$ is the step function. For a typical electron density $n_s = 2 \times 10^{15} m^{-2}$ and a polarization voltage $V_g = 1V$, the depletion length[5]is $L_D = 225$ nm.

At filling factor ν_L, the location x_i and the width a_i of the incompressible bulk strip i coming from to the Landau level $n = i$ can be evaluated from:

$$x_i = L_D\frac{\nu_L^2 + i^2}{\nu_L^2 - i^2} \tag{4.25}$$

[5]Using the dielectric constant in GaAs $\epsilon = 12.8\epsilon_0$.

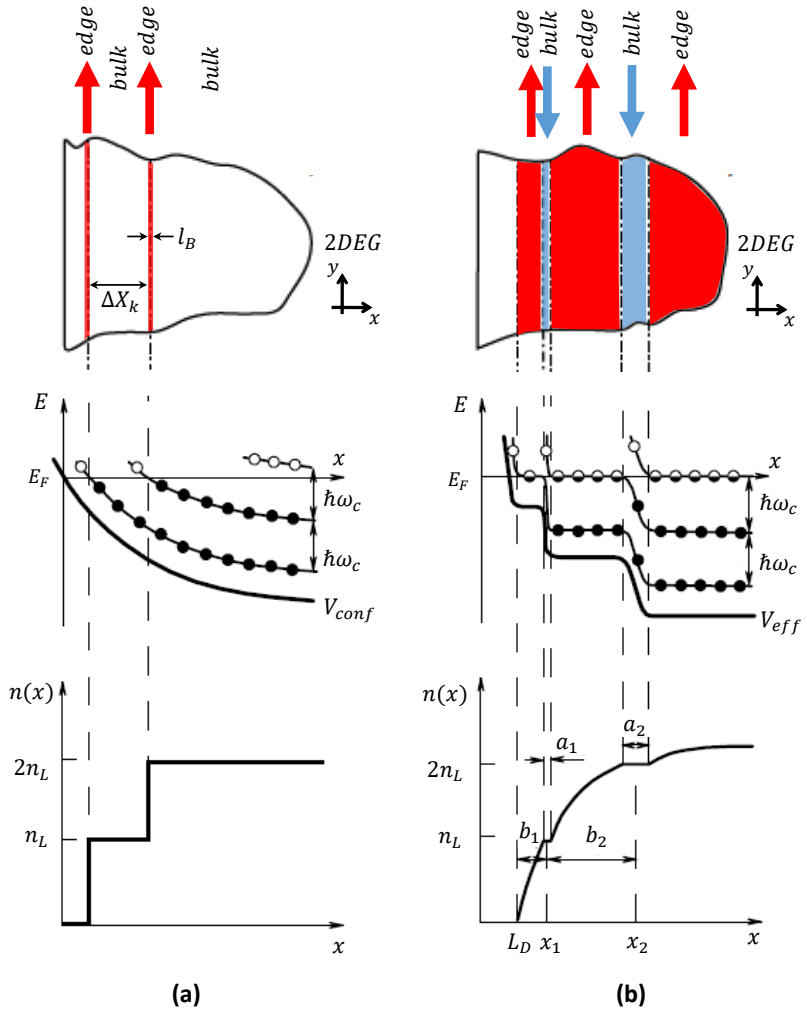

Figure 4.13: Bottom panels: electron density profile $n(x)$ as a function of the spatial coordinate x. Middle panels: the electrostatic potential $V(x)$ and the dispersion induced in the Landau levels. Filled circles indicate fully occupied states (*incompressible* 2DEG), half-filled circles indicate partially occupied states (*compressible* 2DEG) and open circles indicate empty states above the Fermi level E_F. Upper panels: spatial distribution of the edge states (highlighted in red) that are developed parallel to the y direction of the system. The top arrows indicate the direction of propagation of the current for a magnetic field $\boldsymbol{B} = +B\hat{z}$. ***(a)-Left:*** In the non interacting picture discussed in section 3.3.4 an edge channel is develop each time a Landau level crosses the Fermi level and at this position the electron density has a sharp increase. The edge states have a characteristic width of the order of the magnetic length $l_B \sim 10$ nm (at $B = 5$ T) and neighboring edges channels are separated by ΔX_k which depends on the profile of the confining potential V_{conf}. ***(a)-Right:*** Interacting model - Edge Reconstruction: The coulomb interaction in the 2DEG leads to a reorganization of the charges resulting in a smooth increase of the electron density profile $n(x)$. This process leads to self consistent confining potential V_{eff} that flattens the Landau levels in regions where the edge states are developed (half filled circles). Consequently the edge states acquire a finite width of the order of ~ 100 nm separated by thinner incompressible bulk stripes where the electron density remains constant. Notice the anti-parallel and alternating pattern form by the slope of the potential V_{eff} and the density profile $n(x)$ causing that edge and bulk stripes can carry a current but in opposite directions. Adapted picture from Ref. [93]

$$a_i = \sqrt{\frac{8a_B L_D}{\pi}} \frac{\nu_L i^{1/2}}{\nu_L^2 - i^2} \tag{4.26}$$

where $a_B = \frac{4\pi\epsilon\hbar^2}{me^2}$ is the Bohr radius in the 2DEG which gives $a_B \sim 10nm$. The ratio $a_1/x_1 \sim \sqrt{a_B/L_D} \ll 1$ indicates that in general the incompressible bulk strips are separated by much more wider compressible edge stripes. The width b_1 of the outer edge strip can then be estimated as:

$$b_1 = x_1 - L_D = \frac{2L_D}{\nu_L^2 - 1} \tag{4.27}$$

At filling factor $\nu_L = 2$ and for the estimated depletion length $L_D \sim 225$ nm, this gives a width for the outer edge strip of $b_1 \sim 150$ nm which is separated from the inner edge channel by a bulk strip of width $a_1 \sim 50$ nm.

Currents Distribution

A remarkable consequence of this model is that both type of strips can transport a current but they do it in opposite directions [97]. The ***incompressible bulk strips*** carry a density current j_{bulk} due to the finite slope of the dispersion relation $\nabla V_{eff}(x)$, while the ***compressible edge strips*** now carry a density current j_{edge} due to the finite gradient in the density of electrons $\nabla n(x)$:

$$j_{bulk} \propto \nabla V_{eff}(x) \tag{4.28}$$

$$j_{edge} \propto \nabla n(x) \tag{4.29}$$

We can see that these two contributions have opposite directions because the confinement potential profile and the electron density profile are anti-parallel defining an alternating pattern along the edge of the system (Fig. 4.13). At equilibrium, both contributions exactly cancels. However when a finite bias is applied to the edge of the system increasing the electrochemical potential by $\Delta\mu$, the width of compressible edge strip decreases while the incompressible region become wider giving rise to the *excess current* [98]. Despite the presence of this alternating pattern of strips with counter-propagating currents, Thouless [98, 99] demonstrated that the Büttiker formalism is still valid even when it was built based on a completely different model.

Edge Magnetoplasmons

Furthermore, in this model additional excitations can appear across the finite width of the *compressible* edge strip which are known as *edge magnetoplasmons* [100]. These excitations are density oscillations across the stripe width that can propagate. The infinite number of modes allowed can be labeled by the number of nodes j that they create inside of the strip as represented in the figure 4.14. An hydrodynamic description

[100] gives the dispersion relation for each mode[6] j:

$$\begin{aligned} E(k)_{j=0} &= ln\left(\frac{e^{-\gamma}}{2|ka|}\right)\frac{2\bar{n}e^2}{4\pi\epsilon\omega_c}k \\ E(k)_{j>0} &= \frac{2\bar{n}e^2}{4\pi\epsilon\omega_c}\frac{k}{j} \end{aligned} \tag{4.30}$$

from where we can see that they are gapless excitations that propagates with different drift velocities $v_d^{(j)} \propto \partial E(k)_j/\partial k$. Usually the $j=0$ mode is called the ***charge mode*** because it consist of a density modulation of charge along the axis of the compressible edge stripe, while the other modes are known has ***neutral modes*** since the charge modulation is transversal to the stripe as represented in Fig. 4.14. However since the electron density is not constant along the strip width, this modes can also propagate a finite charge.

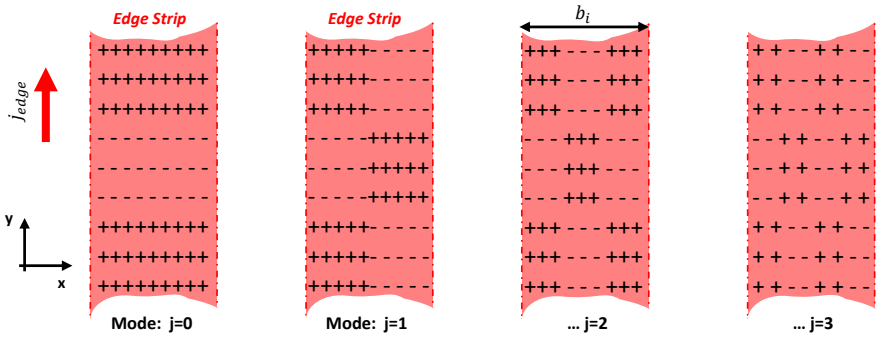

Figure 4.14: Representation of different acoustic modes which can exist since the compressible edge stripe has a finite width b_i that the result from the edge reconstruction process. The charge mode ($j=0$) corresponds to a density modulation along the direction $\hat{y}$ of the propagation of the edge state strip. Conversely, the neutral modes ($j>0$) are modulation of the electron density across the width in the transverse direction $\hat{x}$.

These acoustic branches of edge excitations can be seen as additional internal degrees of freedom of the edge states but they can not be detected in usual dc-charge transport measurements since this approach averages the detected signal in time. However the acoustic excitations can be investigated in *Time of Flight* experiments due to the different drift velocities of the excitations. Time resolved experiments of this type have been carried out to detect the charge mode and the additional acoustic excitations [101, 102, 103] and additionally it was demonstrated that the drift velocities could be tuned by screening the Coulomb interaction on the edge channel with nearby electrode [104].

However only from the observations of time of flight experiments it is not possible to definitely conclude that the reconstructed edge states can host an infinite internal excitations since there exist an alternative theory, based in a completely different treatment of the interactions, which also leads to the development of plasmonic excitations

[6] γ is the Euler constant.

that propagates at different velocities. In the next section, I will describe this second approach and its implication in the relaxation of particles in edge channels.

4.3.2 Luttinger Liquid Theory

The interaction between particles in a Fermi system is a very fundamental question that was originally considered by Landau in the theory of Fermi liquids [22, 23, 24]. However this is a perturbative theory that fails to describe Fermi systems on which the ground state is radically different from a Fermi sea, like the case of superconductors. Fermi liquid theory also fails to describe a simple metallic state in low dimensions, since the Fermi sea becomes unstable in 1D against any small perturbation. The interacting many fermion system in 1D is described by the Tomonaga-Luttinger liquid theory [25, 26].

Fermi Liquid

It describes an interacting Fermi gas, the Fermi liquid, where the interactions are adiabatically turned ON such that they do not drive any phase transition or symmetry breaking in the process. As a consequence, there is a $1:1$ correspondence between the excitations of the Fermi liquid to those of the Fermi gas and the following general properties are preserved:

1. The ground state of the Fermi liquid is still a Fermi Sea.
2. The low energy excitations, called *quasiparticles*, follow a Fermi statistic.
3. The transport is still described by the Boltzmann equation.
4. The correlation between particles are weak even if the interactions are strong.

The mean difference with the Fermi gas is that now the *quasiparticles* have a finite lifetime. In fact if we excite a quasi-electron at a state $|\tilde{e}_k\rangle$ with momentum k, it decays into two quasi-electrons and one quasi-hole. Three quasiparticles are needed due to the charge, momentum and energy conservation,

$$|\tilde{e}_k\rangle \quad \longrightarrow \quad |\tilde{e}_{k'}\rangle + |\tilde{e}_{k''}\rangle + |\tilde{h}_{k'''}\rangle \tag{4.31}$$

When the electron is close to the Fermi Sea, there are less available states for the decaying process and the quasiparticle becomes longlived. Moreover the lifetime at low energy, which scales as $\tau \sim \hbar/(E-E_F)^2$, is longer than the inverse of excitation energy $\hbar/(E-E_F)$ indicating that in fact the quasiparticle is well defined at low energy ([105] and ref. therein).

The Fermi liquid theory works well for most of the electronic systems in 3D and 2D since even if the interaction is strong, it only opens a gap in a relatively small part

of the Fermi surface and therefore the system can be considered as a very dilute gas of interacting quasiparticles. This implies that the interactions can be treated with a perturbation theory.

Luttinger Liquid

When the dimensionality of the Fermi gas is reduced the phase space at the Fermi surface does it as well. In the extreme case of a 1-dimensional Fermi gas, the Fermi surface consists only of two singular point: $\pm k_F$. As a consequence, any interaction that couples the states at the Fermi level opens a gap that completely destroys the whole Fermi surface of the system. It does not matter how small the interaction are, they can not be turned ON adiabatically or described by a perturbation theory. The free-electron like metal state in 1 dimension is not stable.

This is where it comes the Luttinger liquid theory which describes the interacting Fermi gas within a non perturbative approach leading to the formation of the Luttinger liquid state where:

1. The elementary excitations are collective modes that follows a Bose-Einstein statistics.

2. The correlation between the particles are always strong.

3. Spin and charge excitations are gapless and have a linear dispersion relation.

An effective linearization of the dispersion relation of a given system can be obtained by the ***bosonization*** approach which allows to compute exact solutions of the interacting many fermions problem. All the physical properties can be calculated in term of only two parameter per degree of freedom α: The speed of propagation of the excitation v_α and the renormalization coupling constant K_α. In general terms, a non interacting system with free electrons has $K_\alpha = 1$; if $K_\alpha > 1$ the effective interaction in the system are atractive but if $K_\alpha < 1$ the interaction are repulsive. Properties such as the specific heat, the susceptibility, the electronic compressibility and conductance depend on these parameters. Moreover they dictate the power-law behavior in all the correlation functions [30, 29].

The bosonization approach that was initially applied and improved by Haldane, Mattis and Lieb [28, 106] predicts some peculiar and interesting phenomena:

1. Charge-spin separation: charge and spin excitations have different propagation velocities, v_c and v_s respectively. For repulsive interaction they satisfy that $v_s < v_F < v_c$ where v_F is the Fermi velocity.

2. Charge fractionalization: An injected wavepacket of charge q breaks up into several fractionalized charge wavepackets.

3. A renormalization of the quantum of conductance: $G = G_0 K_c$

Several systems have been identified to behave as Luttinger liquids such as: semiconductor 1D-wires [107, 108, 109], quasi-1D organic crystals [110], Carbon nanotubes [111] and the edge states of the fractional quantum Hall effect [112].

4.3.3 A Chiral Luttinger Liquid in the IQHE

A important generalization of the Luttinger Liquid theory was originally investigated by Wen [31, 113] to describe the dynamics of excitation in the edge channels of the fractional quantum Hall effect where the propagation is chiral. As a result, the bosonization approach in the Luttinger liquid theory can be still used to describe the Coulomb interaction between the particles along the 1-dimensional chiral edge channels. Moreover, the same approach can be implemented to describe the electrostatic interaction between two co-propagating edge channels in the integer quantum Hall effect regime.

Within this framework, the Hamiltonian of a single non interacting edge channel can be expressed in terms of the local density operator $\hat{\rho}(x)$ and the drift velocity v_d of the particles,

$$H_0 = \pi\hbar v_d \int \hat{\rho}^2(x)dx \tag{4.32}$$

Intra-channel Interactions.
In a similar way the interaction between the particles propagating in the same edge channel can be described as a local density-density interaction characterized by a coupling strength g,

$$H_0' = H_0 + H_{intra} = (\pi\hbar v_d + g) \int \hat{\rho}^2(x)dx \tag{4.33}$$

which simply leads to a renormalization of the drift velocity $v = v_d + g/\pi\hbar$.

Inter-channel Interactions.
At filling factor $\nu = 2$ the co-propagating edge channels are capacitively coupled resulting in a finite inter-channel interaction. Additionally, since they are located at different positions they can have different degree of screening on the internal interactions[7]resulting in different drift velocities v_1 and v_2. Therefore the Hamiltonian of the system at filling factor $\nu = 2$ describes each edge channel $i = 1, 2$ with its own drift velocity v_i and its density operator ρ_i, while the mutual interaction is characterized by the coupling constant g_{12},

$$H = H_0' + H_{inter} = \pi\hbar \int \left(v_1\hat{\rho}_1^2(x) + v_2\hat{\rho}_2^2(x) + \frac{g_{12}}{\pi\hbar}\hat{\rho}_1(x)\hat{\rho}_2(x) \right) dx \tag{4.34}$$

The interacting problem can be diagonalized performing a rotation transformation of

[7]The degree of screening can be adjusted with the proximity to metallic electrodes [104]

the density operators characterized by an angle θ, which result in

$$H = \pi\hbar v_c \int \hat{\rho}_c^2(x)dx + \pi\hbar v_s \int \hat{\rho}_s^2(x)dx \tag{4.35}$$

This gives rise to the development of two new orthogonal eigenmodes, ρ_c and ρ_s, which are a combination of the two independent edge channel and that are characterized by the drift velocities, v_c and v_s, respectively:

$$\rho_c = cos(\theta)\rho_1 + sin(\theta)\rho_2 \quad \text{with} \quad v_c = \frac{v_1+v_2}{2} + \sqrt{\left(\frac{g_{12}}{\pi\hbar}\right)^2 + \left(\frac{v_1-v_2}{2}\right)^2} \tag{4.36}$$

$$\rho_s = sin(\theta)\rho_1 - cos(\theta)\rho_2 \quad \text{with} \quad v_s = \frac{v_1+v_2}{2} - \sqrt{\left(\frac{g_{12}}{\pi\hbar}\right)^2 + \left(\frac{v_1-v_2}{2}\right)^2} \tag{4.37}$$

The hybridization of the edge channel depends on the angle θ of the transformation which defines the so called *mixing angle* $\varphi = 2\theta$ that is more commonly used in the literature and which is determined by the coupling constant:

$$tan(\varphi) = \frac{g_{12}/(\pi\hbar)}{v_1 - v_2} \tag{4.38}$$

A remarkable consequence of the hybridization is that the a wavepacket carrying a charge q_0 injected in one edge channel will fractionalize into the two presented modes, ρ_c and ρ_s, with each one carrying a non trivial charge, q_c and q_s respectively, given by:

$$q_c = \alpha q_0 + \beta q_0 \qquad q_s = (1-\alpha)q_0 - \beta q_0 \tag{4.39}$$

with the coefficients defined as

$$\alpha = \frac{1+cos(\varphi)}{2} \qquad \beta = \frac{sin(\varphi)}{2} \tag{4.40}$$

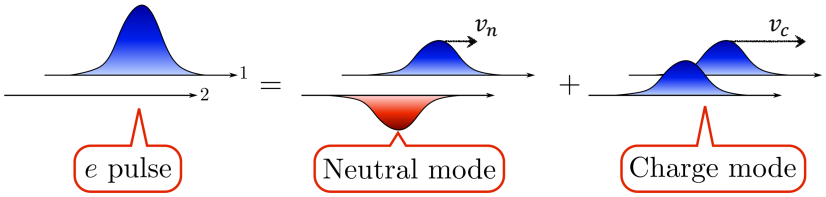

Figure 4.15: A wave packet injected in one edge channel fractionalizes into two modes: the slow neutral mode that propagates at a speed v_n and fast charge mode that propagates at a speed v_c. Picture adapted from Ref. [114].

Strong Coupling Regime

In the strong coupling regime $g_{12} \gg (v_1 - v_2)$, which gives a mixing angle $\varphi = \pi/2$ (or $\theta = \pi/4$) there is the maximum hybridization.

$$\rho_c = \frac{1}{\sqrt{2}}(\rho_1 + \rho_2) \qquad \text{with} \qquad v_c = \frac{v_1 + v_2}{2} + \frac{g_{12}}{\pi\hbar} \tag{4.41}$$

$$\rho_s = \frac{1}{\sqrt{2}}(\rho_1 - \rho_2) \qquad \text{with} \qquad v_s = \frac{v_1 + v_2}{2} - \frac{g_{12}}{\pi\hbar} \tag{4.42}$$

In this case ρ_c defines a symmetric distribution of charge, called the *charge mode* that has no net spin, while ρ_s describes a dipolar distribution of charge that is neutral but that carries a spin. Since they have different propagation speeds $v_s < v_c$ it results in the *spin-charge separation* phenomena.

Relaxation of Landau quasiparticles

The emergence of the new eigenmodes must be seen as the development of collective excitation that challenge the idea of well defined and longlived Landau quasiparticles as the low energy excitations in the edge channel of the integer quantum Hall effect.

P. Degiovanni *et al.* modeled the relaxation of quasiparticles injected at a well defined energy E_0 above the Fermi sea of an edge channel in the integer quantum Hall regime at filling factor $\nu = 2$[115]. The interaction with the co-propagating edge channel and the electrons in the Fermi sea were described as a scattering region of length L, through which the particles pass, using the plasmon scattering approach. The 2x2 unitary plasmon scattering matrix $S(\omega, L)$ in frequency domain is given by the mixing angle $\varphi = 2\theta$ that characterize the strength of the interactions

$$S(\omega, L) = e^{i\omega L/v_0} e^{-i(\omega L/v)(cos(\varphi)\sigma_z + sin(\varphi)\sigma_x)} \tag{4.43}$$

where v_0 and v are velocities such that the velocity of the spin (s) and charge (c) eigenmodes are: $v_{c,s}^{-1} = v_0^{-1} \pm v^{-1}$, while σ_z and σ_x are the Pauli matrices [55].

This approach allows to compute the probability Z of a particle injected at an energy E_0 above the Fermi sea to propagate across the interaction region without losing energy. In Ref. [55] the elastic scattering probability $Z(E)$ for a single electron excitation was explicitly determined[8]in the strong coupling regime ($\varphi = \pi/2$) to be given by:

$$Z(E_0) = (J_0(E_0 L/\hbar v))^2 \tag{4.44}$$

This indicates that the quasiparticle decays over a distance of $L_{in} = \hbar v/E_0$. For a injection energy of $E_0 \sim 100\mu eV$ and a velocity parameter of the order of the typical drift velocity $v \sim 0.5 \times 10^5$ m/s we get $L_{in} \sim 1.3\mu m$. We will therefore experimentally investigate the relaxation of a quasiparticles within this distance.

[8] $J_0(x)$ is the first kind Bessel function which roughly decays as $1/\sqrt{x}$

Numerical calculation of the elastic scattering probability $Z(E_0)$ were obtained also for different coupling parameters φ displaying an oscillatory behavior as shown in Fig. 4.16.

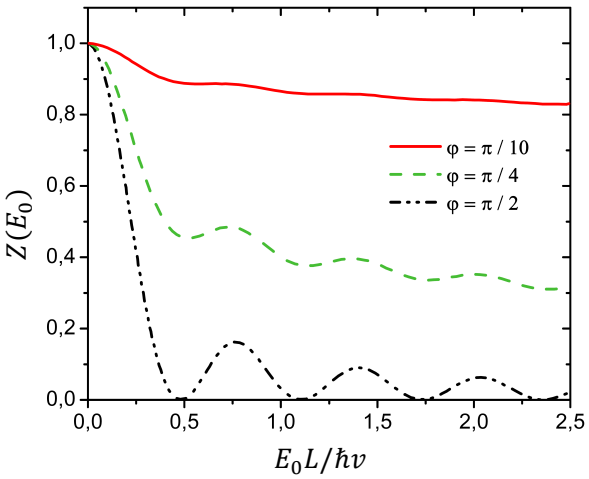

Figure 4.16: Elastic scattering probability $Z(E_0)$ for a single electronic excitation, injected at a well defined energy E_0 above the Fermi Sea of an edge channel in the integer quantum Hall regime at filling factor $\nu = 2$, after a propagation length L calculated by C. Grenier *et al.* [116, 115]. The calculations were performed at different coupling regimes given by the mixing angle φ.

Furthermore a full visualization of the relaxation scenario of Landau quasiparticles well resolved in energy $\Gamma_0 \ll E_0$ was computed by D. Ferraro *et al.* using the Wigner function representation [56]. This approach allows to have access to the time evolution of the wavepacket and the energy distribution function. On these calculations, they pointed out that the decaying process of the wavepacket involve two time scales. First, the energy resolved excitation relax towards the Fermi Sea after a time of flight $\tau_{rel} \sim \hbar/E_0$. Then, after a time of flight given by the wavepacket extension $\tau_{dec} \sim \hbar/\Gamma_0$ it splits in two components which are the slow and fast modes expected to produce the spin charge separation.

Finite frequency admittance and noise measurements have demonstrated the spin charge separation [117, 118] in the quantum Hall effect. Moreover, the same mechanism was also proposed to explain the unexpected lobe-type structure observed in the visibility of MZI at finite voltage [44]. The same phenomena is thought to be also responsible for the decoherence observed in MZI as well as in HOM interferometers [43] since the information of a quantum state produced in one edge channel is lost in the decaying process.

H. le Sueur *et al.* performed the first attempts to experimentally investigate the energy relaxation mechanism on the edge channels [52]. However, due to their experimental configuration, they were only able to investigate the relaxation of an state that was already close to the Fermi sea and that was not resolved in energy. Their observations would correspond to the final phase of the relaxation process, during the

second time scale τ_{dec}, illustrated in Fig. 4.17 insets (d),(e) and (f). These experiments provided the first accurate measurements of a part of the relaxation process which could be compared with the theoretical models.

Some deviation provided the first clue that the theoretical model based on two interacting edge channel is not complete. On this thesis we experimentally address the primordial relaxation of Landau quasiparticles, injected at a well defined energy, that takes place during the first time scale τ_{rel}, illustrated in Fig. 4.17 insets (a),(b) and (c). We will observe, in other words, Landau quasiparticles *splashing down* on the Fermi Sea.

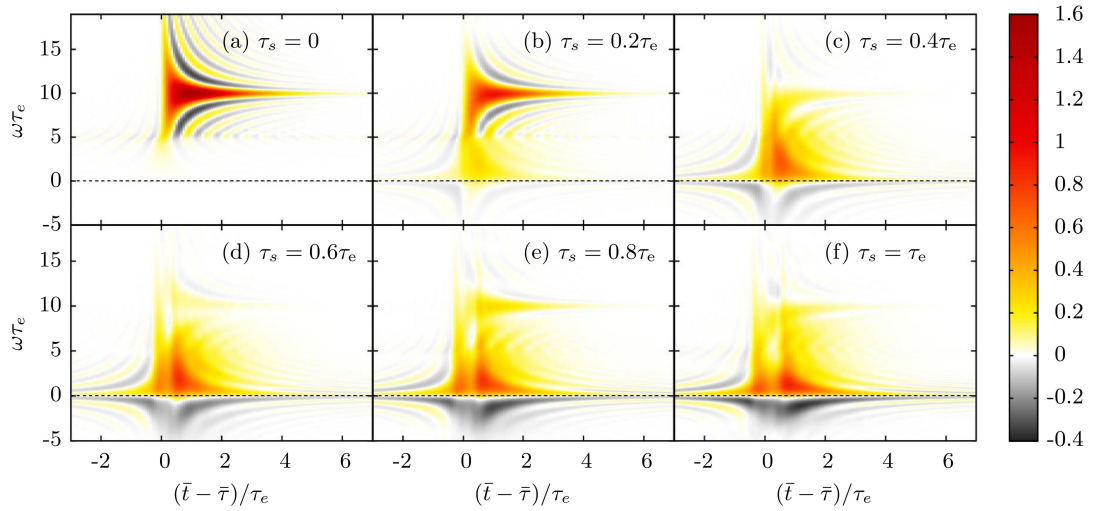

Figure 4.17: Relaxation scenario computed with the Wigner function representation by D. Ferraro *et al.*. Panels (a) to (f) represent the time evolution of the Wigner function along the propagation. First, the Landau quasiparticle, injected at an energy $E_0 = \hbar\omega_e = 10\hbar\tau_e^{-1}$ relaxes toward the Fermi sea indicated by the horizontal dashed line at $\omega = 0$ (Panel a, b and c). In the second part, Wigner function splits in two parts: the slow and fast mode (inset d, e and f). Picture taken from [56].

Chapter 5

Relaxation of a double step distribution function

In this chapter I describe the experiments carried out in the Phynano team, at the C2N(LPN) laboratory, which constitutes the first attempt to experimentally investigate the energy relaxation mechanism in the integer quantum Hall effect at filling factor $\nu = 2$ [51, 52]. I present measurements that we did in the same regime which are in agreement with their main observations and which allow us to draw some important conclusions about our system. Our measurement contribute to consolidate the reproducibility and replicability of such important observations by obtaining the same quantitative results in a different laboratory using different devices. Moreover these experiments are an important benchmark that provides us a solid basis from which we can move forwards to perform the energy resolved spectroscopy.

5.1 Description of the experiment

Experiments are performed in the integer quantum Hall regime at filling factor $\nu = 2$ where two chiral edge channels co-propagate along the edges of the system. The experiments are carried out at low temperature $T_{base} \sim 20$ mK where each edge channel is fully spin polarized.

In this experiment we investigate the relaxation of an out-of-equilibrium state created near the Fermi sea using a biased QPC set at an intermediate transmission $0 < \tau_{qpc} < 1$ for a single edge channel, as depicted in Fig 5.1, while the other edge channel is completely reflected. As explained in section 4.1.3 in these conditions the QPC creates a double step distribution of particles $f_i(E)$ at the left output which then propagates along the edge channel. For an applied bias voltage V_1 at the source of the QPC, the injected distribution reads

$$f_i(E) = \tau_{qpc}\, F(E - eV_1) + (1 - \tau_{qpc})F(E) \tag{5.1}$$

where the capital letter F denotes that the distribution is a Fermi function. The derivative of $f_i(E)$ consists of a double dip structure whose relative amplitude is set by the transmission of the QPC:

$$\frac{df_i}{dE}(E) = \tau_{qpc}\frac{dF}{dE}(E - eV_1) + (1 - \tau_{qpc})\frac{dF}{dE}(E) \tag{5.2}$$

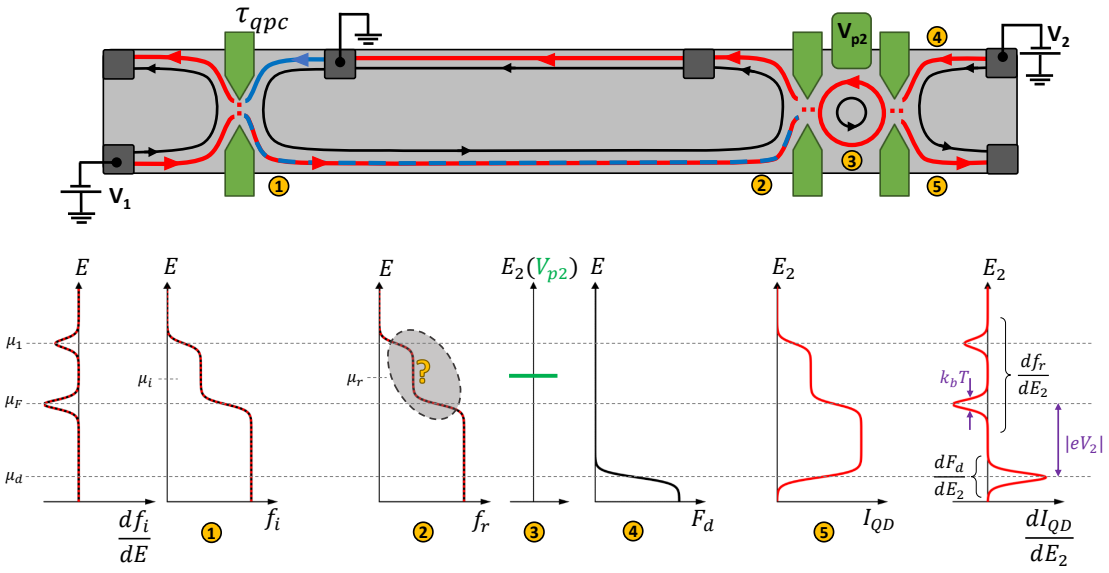

Figure 5.1: Top: Schematic representation of the experimental configuration to investigate the relaxation in the IQHE regime at filling factor $\nu = 2$. The biased QPC at transmission τ_{qpc} creates a double step distribution function f_i (with electrochemicl potential μ_i) in the outer edge channel. After few micrometers of propagation, where relaxation takes place, the resulting distribution f_r (with electrochemicl potential μ_r) is measured with a quantum dot implemented as an energy filter. The horizontal dashed lines denotes the electrochemical potential μ_1, μ_F and μ_d of the equilibrium distribution functions respectively emitted by the ohmic contact biased at voltage V_1, the grounded contact and the ohmic contact biased at voltage V_2.

After a tunable propagation length L of several micrometers on which the energy is redistributed among the particles, the resulting distribution f_r is measured using a quantum dot with a single active level at a tunable energy E_2. The quantum dot is then implemented as an energy filter allowing to directly extract the unknown distribution function f_r, at its source lead, from the transmitted current $I_{QD}(E)$ as explained in section 4.2.6. A constant bias voltage V_2 is also applied at the drain lead of the QD such that the transmitted current results:

$$I_{QD}(E_2) = I_{max}\Big(f_r(E_2, \mu_r) - F_d(E_2, \mu_d)\Big) \tag{5.3}$$

which is obtained after integration of the measured transconductance signal $\frac{dI_{QD}}{dE_2}$:

$$\frac{dI_{QD}}{dE_2}(E_2) = I_{max}\left(\frac{df_r}{dE_2}(E_2, \mu_r) - \frac{dF_d}{dE_2}(E_2, \mu_d)\right) \tag{5.4}$$

where I_{max} is a constant which only depends on the characteristics of the detector quantum dot[1]. We can see that a large enough voltage V_2 allows to decouple both derivative signals, df_r/dE and dF_d/dE, when $|\mu_r - \mu_d| \gtrsim |eV_2| \gg k_bT$.

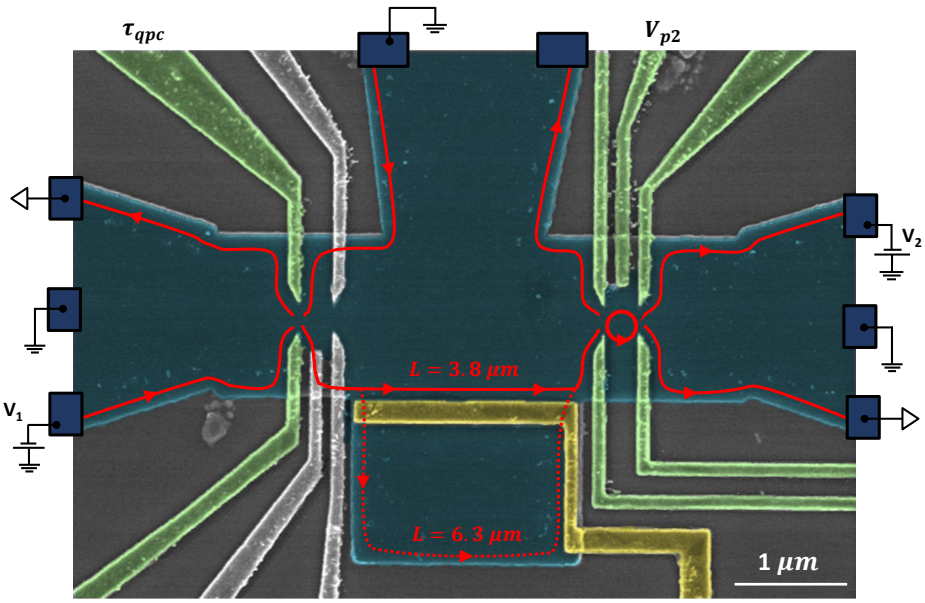

Figure 5.2: Colored scanning electron micrograph of the sample (C4) with the 2DEG mesa highlighted as the blue cross-shaped region. The electrodes colored in green are used to define the QPC, which injects the double step distribution function in the edge channel, and the QD that is used as a detector. In red is represented the path followed by the outer edge channel. The yellow electrodes is used either completely polarized to define a short path, or completely unpolarized in order to let the edge channel to follow the longer path indicated by the red dotted line along the edge mesa. The inner edge channel is not shown for simplicity but it is completely reflected by all the gates that defines the QPC and the QD, however in the central region the inner edge channel is reflected by the path selector gate in the same way as the outer edge channel. The gray electrodes near the QPC are not used and they remain unpolarized.

5.2 Distribution Functions Partially Relaxed

First, the injected distribution f_i and the resulting distribution f_r are compared in order to describe the relaxation process. C. Altimiras *et al.* [51] observed that within a distance $0.8\,\mu m$ there is no relaxation: a double step distribution function was measured which corresponds to the injected distribution (Eq. 5.1). Subsequently, H. le Sueur *et al.* [52] measured that a full relaxation towards a hot Fermi sea is reached after a propagation length of $10\,\mu m$. The hot Fermi sea, characterized by a temperature $T =$ 80 mK, was found to remain stationary for longer distances (up to $30\,\mu m$). Therefore

[1]Following the discussion of section 4.2.6 the constant I_{max} depends on the intrinsic linewidth Γ_2 of the resonance at the quantum dot and its transmission $\mathcal{T}_2$, resulting in: $I_{max} = e\pi\Gamma_2\mathcal{T}_2/2h$.

it was established that the whole relaxation mechanism takes place between $0.8\,\mu m$ and $10\,\mu m$ after the injection point.

We have performed the same type of measurement at two propagation distances, $L = 6.3\mu m$ and $L = 3.8\mu m$. A scanning electron micrograph of our sample is shown in figure 5.2 displaying a schematic representation of the path followed by the outer edge channel. The propagation distance L between the QPC at the left and the QD at the right can be tuned in situ between the two values by using the central electrode highlighted in yellow.

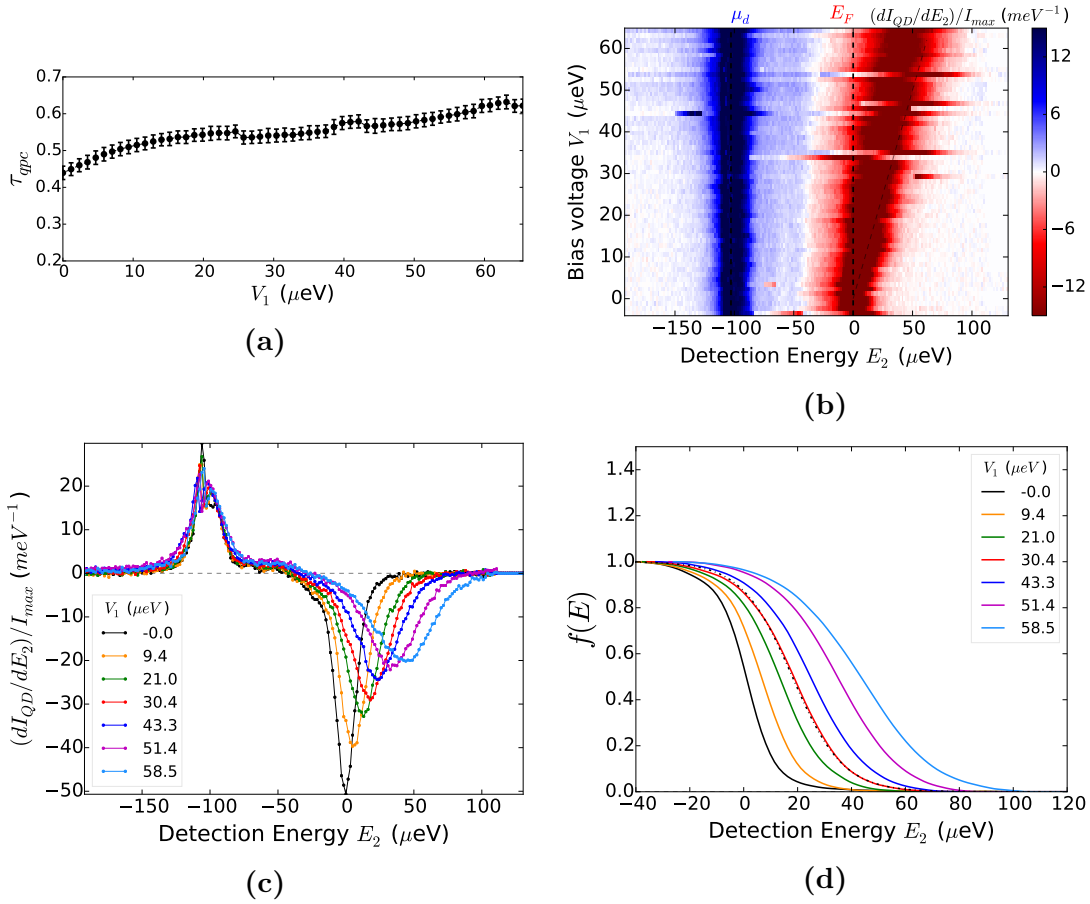

Figure 5.3: Measurements at the long propagation distance $L = 6.3\mu m$. **(a)** The operating points of the injector QPC are characterized by measuring the transmission as a function of the bias voltage. **(b)** 2D-plot of the transconductance signal measured as a function of the detection energy E_2 of the QD and the bias voltage V_1 across the QPC. The energy E_F corresponds to the electrochemical potential measured from the equilibrium distribution function emitted by a grounded ohmic contact when $V_1 = 0$. **(c)** Some horizontal traces taken from the 2D plot at fixed V_1. When the voltage V_1 is increased, the dip in the transconductance signal moves towards positive energies while the peak remains relatively unchanged. **(d)** The distribution functions obtained from the integration of the dip are approximately well described by Fermi functions. A Fermi function is plotted in black dotted line for the distribution measured at $V_1 = 30.4\mu$eV

Long Propagation Distance.

For the longer propagation distance $L = 6.3\mu m$, Figure 5.3b shows a 2D plot of the measured transconductance dI_{QD}/dE_2 as a function of the energy E_2 along the x-axis

for different bias voltages V_1 across the QPC (y-axis).

Figure 5.3c shows some horizontal traces measured at the fixed bias values $V_1 \in \{0.0, 9.4, 21.0, 30.4, 43.3, 51.4, 58.4\}\,\mu eV$. The left peak located around $E_2 = \mu_d = -103\mu eV$ corresponds to the derivative $\frac{dF_d}{dE_2}$ in eq. 5.4 which is taken as a fixed point where all the curves are aligned. The right dip located at positive energies corresponds to the derivative $\frac{df_r}{dE_2}$ of the distribution functions measured after the propagation.

We observe that while the voltage V_1 is increased, the dip moves towards more positive energies, its amplitude decreases, its width increases but the dip remains relatively symmetric. Moreover, as expected the changes observed on the dip are significantly larger than the small changes seen on the peak.

The figure 5.3d shows the distributions functions $f_r(E_2)$ obtained after integration of the dip signals. The distributions are similar to Fermi functions which is not surprising since a full relaxation is expected at $10\mu m$. At increasing bias voltage V_1 the measured distributions can be fitted with Fermi function which show increasing electronic temperatures following $T \in \{60, 78, 98, 110, 121, 136, 160\}$ mK respectively for the curves measured at bias $V_1 \in \{0, 9.4, 21, 30.4, 43.3, 51.4, 58.5\}\,\mu$eV. As an example, the Fermi fit of the distribution measured at $V_1 = 30.4\,\mu$eV is plotted in black dotted line in Fig. 5.3d.

Short Propagation Distance.

At a shorter propagation distance $L = 3.8\,\mu m$, similar measurements are shown in Figure 5.4. At $V_1 = 0$ the distribution is a Fermi function with a temperature $T = (43 \pm 1)$ mK which is simply the equilibrium Fermi sea of the edge channel. However, at finite bias the distributions $f_r(E_2)$ deviates from a Fermi function. This can be more easily noticed when looking at the dip in the transconductance signal of Fig.5.4(b) which displays a double dip structure, even though the two components are not well separated. This structure is a remnant of the injected double step distribution function $f_i(E_2)$ which is partially relaxed at this distance. A very similar transconductance signal was measured for a propagation distance of $L = 4\mu m$ in Ref [52].

Therefore, we observe that in our samples the relaxation of a double step distribution function takes place within the same range of propagation distance measured by the other group. This suggests that the relaxation process is not very much dependent of the particular disorder of the sample or the specific geometrical arrangement of the electrodes used to define the QPC and the QD.

Additionally, we can clearly see that although the largest changes are seen principally in the dip structure, the peak located around $E_2 = -80\mu eV$ also shows an evolution with the bias voltage V_1. These changes in the peak most probably arise from the charge noise generated in the measured edge channel. In principle, the shot

noise spectrum density in this edge channel is simply related to the bias V_1 through,

$$S_I = 2eG_0V_1\tau_{qpc}(1-\tau_{qpc}) \tag{5.5}$$

To assess the voltage fluctuations one has to estimate an effective bandwidth on which integrating these fluctuations. Fluctuations at too high frequencies average to zero along the part of the edge channel interacting with the dot. A maximum frequency is also set by the voltage itself, thus $\Delta f = eV_1/h$. For the shorter propagation, case one clearly sees that the width of the peak increases with the bias. This is associated with the increase of these charge fluctuations. A simple estimation of the voltage fluctuations $\Delta V^2 = S_I R_K^2 \Delta f/2$ for a bias voltage $V_1 = 100\mu eV$ and a transmission $\tau_{qpc} = 0.5$, gives $\Delta V \approx 35\mu$eV which is of the order of the width increase that we observe.

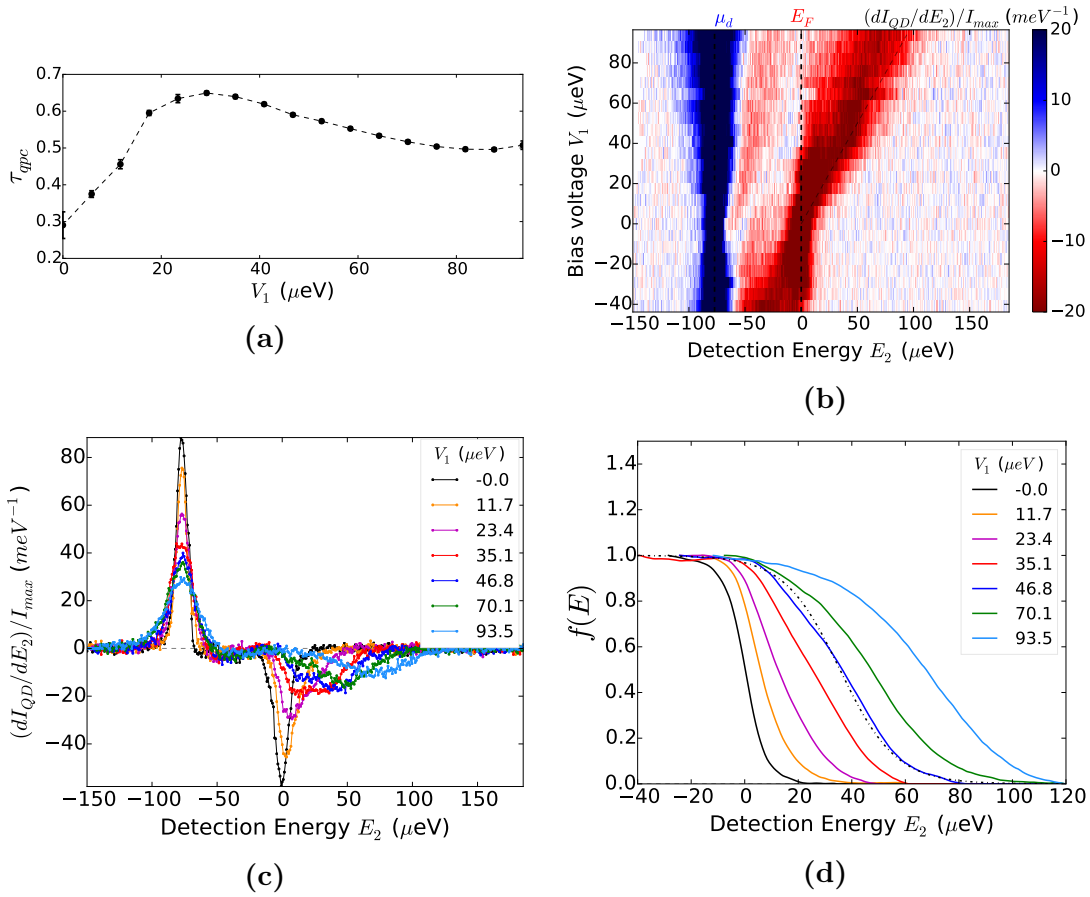

Figure 5.4: Measurements at the short propagation distance $L = 3.8\mu m$. **(a)** The operating points of the injector QPC are characterized by measuring the transmission as a function of the bias voltage. **(b)** 2D-plot of the transconductance signal as a function of the bias voltage V_1 across the QPC and the detection energy E_2 of the discrete level at the detector. **(c)** Some traces from the 2D plot at fix and positive V_1. They shows the development of a double dip structure as the voltage V_1 is increased. **(d)** Distribution function obtained from the integration of the dip observed in the transconductance traces. The distributions correspond to the injected double step distribution function that is partially relaxed, which can be better appreciated from the double dip structure in **c**.

5.3 The Electrochemical Potential

The electrochemical potential μ of a distribution of particles indicates the highest energy states that are occupied at zero temperature following the Pauli's exclusion principle and therefore it reflects the number of particles in the system trough the density of states. In a Fermi distribution at finite temperature, the electrochemical potential indicates the energy of the states that have a probability of 50% to be occupied by thermal excitation. Furthermore, the electrochemical potential is not restricted to characterize Fermi functions, but it can be defined for any arbitrary distribution of particles $f(E)$ as follow [51]:

$$\mu = E_A + \int_{E_A}^{E_B} f(E)dE \tag{5.6}$$

where E_A and E_B are such that $f(E) = 1\ \forall E \leq E_A$ and $f(E) = 0\ \forall E \geq E_B$. This determination gives the electrochemical potential up to an arbitrary constant, E_A, but this is not an problem since only the changes in the electrochemical potential $\Delta\mu$ will be relevant.

On the one hand, the increase in the electrochemical potential $\Delta\mu_i$ that is expected can be calculated from the injected distribution function $f_i(E)$ and the equilibrium Fermi sea $F(E)$ as follows:

$$\Delta\mu_i = \mu_i(V_1) - \mu_0 = \tau_{qpc} e V_1 \tag{5.7}$$

On the other hand, the increase in the electrochemical potential $\Delta\mu_r$ that is measured after the propagation can be calculated from the detected distribution f_r at bias V_1 and the detected Fermi sea with the QPC at zero bias:

$$\Delta\mu_r(V_1) = \mu_r(V_1) - \mu_r(V_1 = 0) \tag{5.8}$$

Figure 5.5 shows a comparison where we see that the measured increase in the electrochemical potential $\Delta\mu_r$ follows the linear behavior that is expected in coincidence with the injected quantity $\Delta\mu_i$. A reasonably good agreement is found within the experimental errors, which indicates the important fact that the injected particles are not tunneling out of the edge channel while they propagate for distances up to $6.3\,\mu m$. This verification is in agreement with the observed much longer particle equilibration distance $l_{eq} \sim 160\mu$m between co-propagating edge channel [67].

Therefore the number of particles injected on the edge channels is preserved during the relaxation mechanism. This is a characteristic behavior that is expected if the relaxation is driven by intra-channel interactions or by the interaction with an effective environment that is only capacitively coupled to the injected particles in the outer edge channel. These type of processes will be further described in the next section.

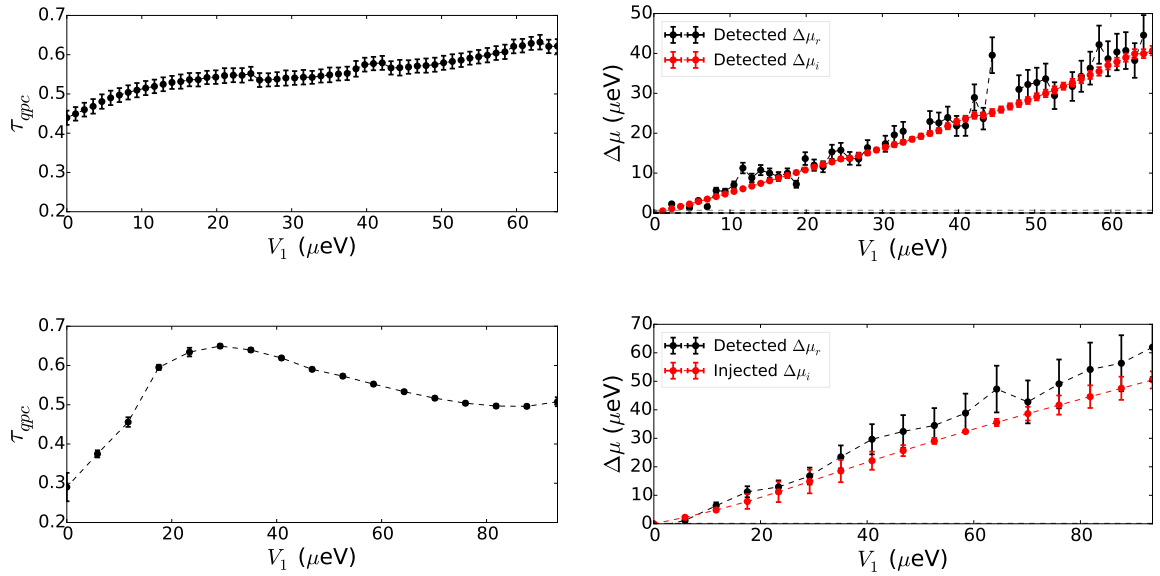

Figure 5.5: Left: Measured bias dependent transmission $\tau_{qpc}(V_1)$ of the QPC. **Right:** Comparison between the electrochemical potential increase $\Delta\mu_r$ measured after the propagation (black) and the same quantity estimated at the injection point $\Delta\mu_i$ (red). The two plots at the upper part were measured with the long propagation distance $L = 6.3\mu$m and the bottom plots at the short propagation distance $L = 3.8\mu$m.

5.4 The Quasiparticle Energy

The heat current J carried by an arbitrary distribution of particles is the total energy stored in the system by creating electron-hole excitations on the distribution. In 1D the heat current can be exactly calculated from the distribution of particles $f(E,\mu)$ due to the exact energy dependence cancellation: $\rho_{1D}(E)v(E) = 1/h$

$$J = \int_{E_A}^{E_B} \rho_{1D}(E)v(E)(E-\mu)\left[f(E,\mu) - \Theta(\mu - E)\right] dE \tag{5.9}$$

$$J = \frac{1}{h}\int_{E_A}^{E_B} (E-\mu)\left[f(E,\mu) - \Theta(\mu - E)\right] dE \tag{5.10}$$

where $\Theta(x)$ is the Heaviside step function, thus $\Theta(\mu - E)$ represents a Fermi function of electrochemical potential μ at zero temperature. Applying this equation, the injected double step distribution (Eq. 5.1) carries a heat current J_i given by:

$$J_i = \frac{\pi^2}{6h}(k_b T)^2 + \frac{\tau_{qpc}(1-\tau_{qpc})}{2h}(eV_1)^2 \tag{5.11}$$

Following Ref [51, 52] we can identify the first term as the ***equilibrium heat current*** J_{eq} that is due to the thermal excitation of the Fermi sea, and the second term as the ***excess heat current*** J_{exc} which is due to the additional electron-holes excitations created by the QPC.

It is convenient to define the ***quasiparticle temperature*** T_{qp} and the ***excess temperature*** T_{exc} as the effective temperature that would be needed for a Fermi distribution to carry a purely thermal heat current equals to J_i or J_{exc} respectively:

$$J_i = \frac{\pi^2}{6h}(k_b T_{qp})^2 \tag{5.12}$$

$$J_{exc} = \frac{\pi^2}{6h}(k_b T_{exc})^2 \tag{5.13}$$

which implies the relation $T_{exc}^2 = T_{qp}^2 - T^2$. These effective temperatures are a convenient way to look at the heat current since they provide an energy scale, through the Boltzman constant, which can then be easily compared with other energy scales involved in the relaxation process. On the one hand, for the injected distribution function $f_i(E)$, the excess temperature $T_{exc,i}$ depends linearly on the bias voltage V_1 at the QPC:

$$T_{exc,i} = \frac{\sqrt{3\tau_{qpc}(1-\tau_{qpc})}}{\pi k_b} eV_1 \tag{5.14}$$

In a similar way, from the detected distribution f_r, measured after the propagation, we can compute the excess current $J_{exc,r} = J_r(V_1) - J_r(V_1 = 0)$ and its associated excess temperature $T_{exc,r}$ in order to compare them with the values obtained from the injected distribution.

If the relaxation mechanism is dominated only by intra-channel interactions that redistribute the energy among the kinetic degree of freedom of the particles within the same edge channel, then it is expected that the injected excess heat current $J_{exc,i}$ will be conserved during the propagation, $J_{exc,i} = J_{exc,r}$, thus we expect to find the same excess temperatures: $T_{exc,i}(V_1) = T_{exc,r}(V_1)$. Figure 5.6a shows the excess temperature $T_{exc,r}$ measured after the propagation (plotted as big red and green symbols) for the two distances on which we have performed this experiment. The estimation of the excess temperature $T_{exc,i}$ in the injected distribution with a transmission $\tau_{qpc} = 0.5$ is plotted as a thick black dashed line. In our experiments, the measured bias dependent transmission varies within the range $\tau_{qpc}(V_1) \in [0.35; 0.65]$ as can be seen on the left panels of Fig. 5.5. Although they substantially differ from the exact value $\tau_{qpc} = 0.5$ it will only modify the slope of the dashed line in Fig. 5.6a by less than 5% due to the square root factor in Eq 5.14. Thus the slope of the $T_{exc}(V_1)$ function does not depend strongly on the transmission around $\tau_{qpc} \sim 0.5$.

The comparison between the excess temperature $T_{exc,i}$ at the injection and the $T_{exc,r}$ after the relaxation shows that the energy is not conserved inside the edge channel among the kinetic degrees of freedom of the charge particles. We observe that the discrepancy increases at a larger propagation distance and a large bias. However this energy loss is in the expected ranges, the red and green regions that are defined for each propagation distance by the measurements presented in Ref. [52] for similar

distances. The current understanding of the relaxation mechanism suggests that part of this energy was transferred towards the co-propagating edge channel, which was directly measured in Ref. [52].

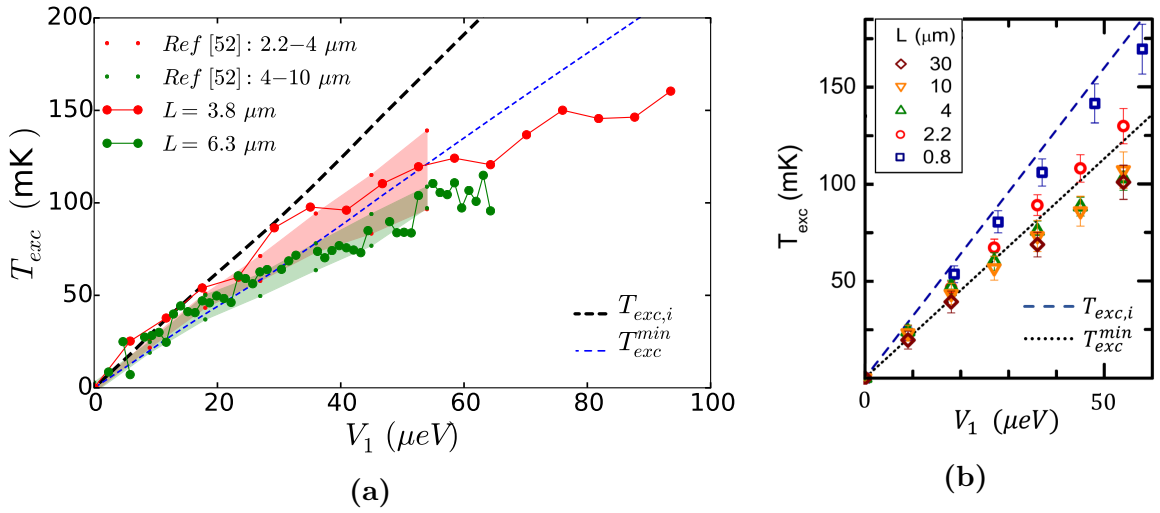

Figure 5.6: **a)** Excess temperature measured after the short (long) propagation distance plotted in big red (green) filled symbols as a function of the bias voltage V_1 across the QPC. Our measurements fall within the expected range represented by the red (green) shaded region for the short (long) distance. These shaded regions were determined from the data measured at Ref. [52]. In **a** the *energy conservation on the edge channel* is indicated by the thick black dashed line ($T_{exc,i}$), while *energy conservation in the whole system of two interacting edge channels* is indicated by the thin blue dashed line (T_{exc}^{min}) which is a lower bound predicted by the theory. **b)** Simplified figure taken from Ref.[52]. The data presented in this reference was used to determine the red and green shaded region displayed in **a**.

Nevertheless if the energy is redistributed only among the charged particles now in the two co-propagating edge channels, still there is a minimum value for T_{exc} that is expected to remain in each edge channel. This lower bound, plotted as thin blue dash line, arises from the heat current equipartition at equilibrium which sets $T_{exc}^{min} = T_{exc,i}/\sqrt{2}$. However we observe that the measured $T_{exc,r}$ (symbols) is smaller than that lower value, which is particularly pronounced at large bias voltage V_1, indicating that the energy redistribution implies extra degrees of freedom which are not related with the charge transport along the two edge channel. This observation also confirms the measurements done in Ref [52], where an energy leak of the two interacting edge channels system was identified in a similar way. They measured that up to 20% of the injected energy was leaking out of the system of two interacting edge channels at larger distances ($\sim 30\mu m$).

It is important to stress that the development of the neutral and the charge mode predicted to arise between two interacting edge channels, presented in section 4.3.3, sets the same lower bound $T_{exc,i}/\sqrt{2}$. Therefore the observation of an energy leak beyond that limit means that this model is not complete. Additionally, in a later experiment [53] it was demonstrated that the energy exchange between co-propagating edge channels could be *frozen* by forcing the inner edge channel to form closed loops.

By doing that, the density of states of the inner edge channel is modified, forcing it to develop discrete energy levels. This limits the energy at which the inner edge channel can be coupled to the outer edge channel where the quasiparticles are injected. In this regime, it was shown that the relaxation of the out-of-equilibrium state injected in the outer edge channel does not excite internal modes in the same edge channel. However it was pointed out that this observation does not rule out the existence of internal neutral modes in the co-propagating edge channel (the inner edge channel) to which the energy could be transferred.

5.5 Transmission Dependence

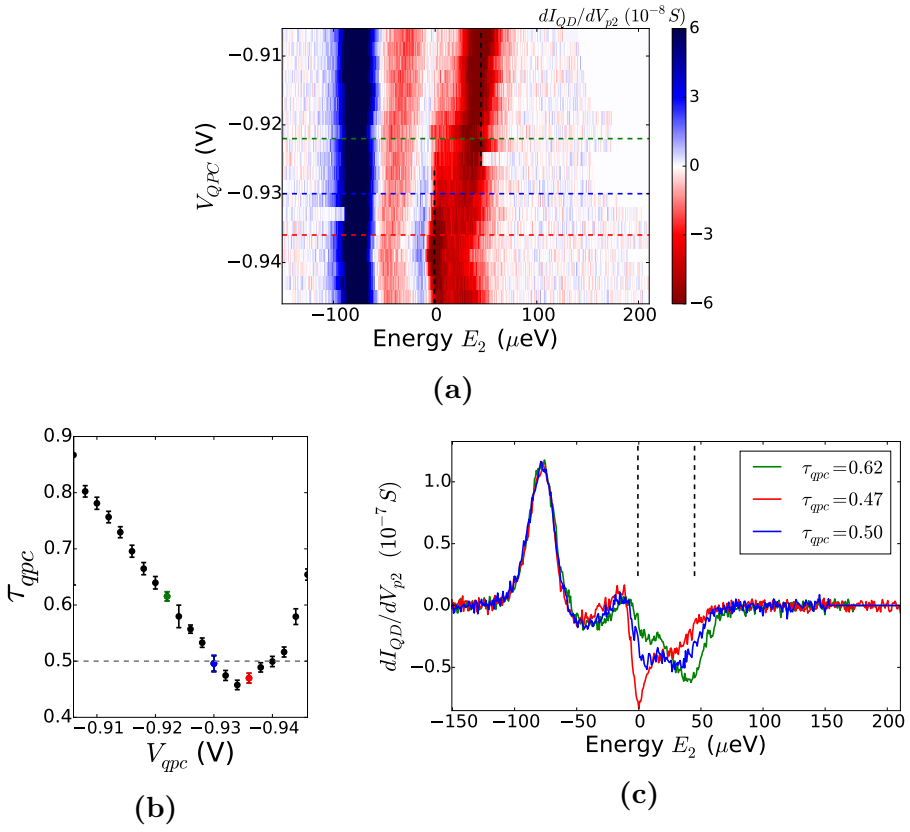

Figure 5.7: Measurements of the partially relaxed distribution function at the propagation length $L = 3.8\,\mu m$ at fixed bias voltage $V_1 = 58.4\,\mu eV$: **(a)** 2D plot of the transconducntance signal as a function of the energy of the detector and the polarization gate voltage of the QPC. The red signal to the right is proportional to the derivative df_r/dE. **(b)** Transmission of the QPC measured as a function of the polarization gate voltage applied in the electrodes that define the QPC. **(c)** Traces taken from the 2D plot on which we can see that the relative amplitude of the two components of df_r/dE are modulated by τ_{qpc}.

At the short propagation distance the two components of the derivative df_i/dE, which leads to the dips in the transconductance measurement in Fig. 5.4, were identified but they were not well resolved since the measured distribution f_r is already partially relaxed. Nevertheless we can test more accurately that there are in fact two

different components by investigating their dependence on the transmission τ_{qpc} of the QPC.

At a fixed bias voltage across the QPC, $V_1 = 58\mu eV$, we measured the $\frac{df_r}{dE}(E)$ while the transmission of the QPC was varied in the range $\tau_{qpc} \in [0.45; 0.8]$ non monotonously (Fig. 5.7b). The measurements of the transconductance at the different values of τ_{qpc} is shown in the 2D plot presented in Fig. 5.7a and some particular traces are shown in Fig. 5.7c. The main result is that the relative amplitude between the two components is modulated by τ_{qpc}, with the component at higher energy being more intense when $\tau_{qpc} > 0.5$ as predicted by eq. 5.2. This observation further confirms that at the distance of $3.8\,\mu m$ we have measured a partially relaxed double step distribution function.

5.6 Conclusions

In this chapter we have investigated the relaxation of an out-of-equilibrium state generated close to the Fermi sea by a biased QPC. We have presented measurements that quantitatively reproduce the experiments originally done in the Phynano team of the C2N(LPN) laboratory [51, 52] which helps to consolidate the scientific evidence of the relaxation mechanism.

We have observed the same relaxation rate of the injected double step distribution in our samples which have a different geometrical configuration of the metallic electrodes that define the device. Our measurements are in agreement with the fact that the double step distribution function relaxes towards a hot electron regime within the $10\,\mu m$ of propagation.

Since we observe that the electrochemical of the injected distribution is preserved ($\mu_i = \mu_r$), we can confirm that in our system the injected particles do not tunnel out of the edge channel while the energy relaxation takes place, at least below the $6.3\,\mu m$ of propagation. This distance is of the order of the relevant length scale of the relaxation meachanism previously observed [51, 52]. Therefore this rules out the inter-channel scattering as the relaxation mechanism or tunneling towards other nearby compressible regions.

Additionally, we observed a non conservation of the energy on the edge channel where the particles were injected. The energy loss increases at longer propagation distance and it was found to be of the same order as reported in Ref. [52] for similar lengths. Moreover we observed as well the same leak of energy from the whole system constituted by the two interacting edge channels. This is an important observation done first in Ref. [52] that we quantitatively reproduce and which indicates that it is an intrinsic characteristic of the relaxation mechanism. This result provides the first signatures that suggest that the description presented in terms of the Luttinger liquid theory (Section 4.3.3) is not complete although many of its prediction, such as the charge fractionalization and the development of the spin-charge modes, have been

experimentally tested.

Last but not least, we have performed these measurements in a configuration where part of the longer propagation path was defined by a chemical etched defined boundary of the 2DEG (See Fig. 5.2) indicating that the type of edge confinement does not radically change the energy relaxation process.

To conclude, the experiments presented in this chapter indicate that our experimental setup and approach are good, which is important for the experiment that will be presented in the next chapter.

Chapter 6

Relaxation of a Quasiparticle Peak

In this chapter we experimentally investigate the energy relaxation of electrons emitted at a well-defined energy in a quantum Hall edge channel, in presence of a second edge channel co-propagating along the former. In the first part we describe our setup which relies on a pair of electrostatically defined quantum dots, used as energy-resolved emitter and detector. In a second part, we present our measurements of the quasiparticle peak obtained after short propagation lengths in the sub-micrometer scale and at low temperature. Then, we investigate the relaxation process as a function of several parameters such the energy at which the particles are injected, the electronic temperature and the propagation distance. Finally, in the last part we discuss data showing signatures of a quasiparticle peak revival which was observed several times under different conditions.

6.1 Motivation

As seen in the previous chapter, the relaxation of a double step distribution function, created with a biased QPC, starts to take place at a distance of $0.8\,\mu$m and ends at a distance of $10\,\mu$m. Therefore a characteristic length scale L_{in} for the relaxation process is expected to be of the order of few micrometers. Assuming an exponential decay for the excess temperature: $T_{exc}(L) \propto exp(-L/L_{in})$, an experimental value of $L_{in} = (2.5 \pm 0.4)\,\mu m$ was determined in Ref. [52]. Notice that this characteristic length L_{in} does not determine the distance over which a full relaxation is achieved, which occurs at $10\,\mu$m. Instead, L_{in} is the characteristic propagation length over which the injected out-of-equilibrium distribution is only "*partially*" relaxed, meaning that indeed energy exchange between the particles has already started but the relaxation still is not complete and the distribution of particles is not a Fermi function yet. Notice as well that this length L_{in} has a similar magnitude to the propagation length $L_{HOM} \approx 3\,\mu m$ on which the spin-charge mode separation was resolved in the same system using a Hong-Ou-Mandel interferometer [43]. Therefore it is possible that in the experiments

described in the previous chapter we were probing the relaxation of the injected out-of-equilibrium state, generated near the Fermi sea, during the same time scale on which the spin-charge separation takes place. This is the second time scale, τ_{dec}, of the two scales that were described in D. Ferraro's work [56] about the relaxation in this same system.

In this chapter we want to experimentally address the previous time scale: the first elementary step of the relaxation process of quasiparticles injected at a well defined energy above the Fermi sea. During this early step the energy resolved excitations get close to the Fermi sea within a characteristic time τ_{rel} defined in Ref. [56] as described at the end of section 4.3.3. In order to investigate this process we implement an energy resolved injection and detection scheme that allows us to perform an energy resolved spectroscopy of the relaxation in the edge channel. Additionally we investigate the relaxation process on sub-micrometer propagation distances, where a priori the double step distribution function discussed before has not relaxed at all [51].

6.2 Experimental description

As before, we investigate the energy relaxation in the integer quantum Hall regime at filling factor $\nu = 2$, for which a magnetic field $B \sim 5$T is applied to the sample and the experiments are carried out at low temperatures $T \sim 20$ mK.

Our experimental setup to perform an energy resolved spectroscopy on the edge channel is based on two electrostatically defined quantum dots that are implemented as energy filters as shown in Fig. 6.1. The surface of the 2DEG mesa appears as dark grey and its chemically etched boundaries are hundreds of micrometers away from the central region where the two QD's are defined. The black boxes $\{C1, C2, C3, C4, C5, C6, C7\}$ are large ohmic contacts also connected to the 2DEG far away from the central region. Finally, the light grey and green strips are surface metallic electrodes, capacitively coupled to the 2DEG.

The set of electrodes $\{G1, G2, G3, G4\}$ are used to define the first quantum dot (QD1), ***the injector***, at the left side, while the set of electrodes $\{G1, G6, G7, G8\}$ defines the second quantum dot (QD2), ***the detector***, at the right side. Both QD's are tunnel coupled only to the outer edge channel depicted as an yellow line. The inner edge channel, depicted in red dashed line, is totally reflected by all the electrodes that define the two QD's.

The applied perpendicular magnetic field going into the plane of the figure set the chirality (anti-clockwise) on the propagation of the edge channels. Thus the edge state moves from the first QD toward the second QD following the boundaries of the deplete electrode $G1$. The surface electrode $A2$ is used to select the propagation path between the two QD's. When $A2$ is not polarized, both edge channels move freely along the short path depicted in Fig. 6.1. The electrode $A2$, seen in Fig. 6.1 as an island labeled

$A2$, is connected to a bonding pad located far away (not shown), through a bridge (not shown). Therefore when $A2$ is completely polarized at *pinch-off*, the small gap between $A2$ and $G1$ is closed and both edge channels are forced to take a longer path going all around the perimeter defined by island labeled $A2$ in Fig. 6.1. This defines a long propagation path that is about three times longer than the short path.

The Injection (QD1)

A negative bias voltage V_1 is applied at the ohmic contact $C1$, which sets the electrochemical potential μ_s of the edge channels in the source of QD1 to the value $\mu_s = E_F - eV_1$. Thus μ_s is above the Fermi level of the edge channel at the drain of QD1, this is, the edge channel that is emitted by the cold ground $C4$.

The QD1 is set to have a single active level within the bias window $[E_F; \mu_s]$ as shown in Fig. 4.11. The energy E_1 of the discrete level, measured from the Fermi level[1], is tuned with the plunger gate voltage V_{p1} applied on the electrode $G3$. As explained in section 4.2.3 (Eq. 4.16) there is a linear relation between them defined by the lever arm now denoted as α_1:

$$E_1 = -e\,\alpha_1 V_{p1} \tag{6.1}$$

The QD1 injects particles at an energy E_1 above a cold Fermi Sea defined by the grounded ohmic contact $C4$. The quasiparticles are injected at a rate given by the transmission $\mathcal{T}_1$ of the resonant level and within a bandwidth $[E_1 - \Gamma_1/2; E_1 + \Gamma_1/2]$ defined by the intrinsic width Γ_1 of the discrete level. In this configuration the particles can be injected at a maximum energy $E_{1,max} = -eV_1$.

Therefore, when the discrete level is fixed at an energy E_1 well inside of the range $[E_F; \mu_s]$, the QD1 generates on the edge channel a distribution of particles $f_i(E)$ given by:

$$f_i(E) = F(E, E_F) + L_1(E, E_1) \tag{6.2}$$

where $F(E, E_F)$ is the equilibrium Fermi sea at the electrochemical potential E_F and $L(E, E_1)$ is a Lorentz peak centered around E_1, which reproduces the lineshape of the discrete level.

Then the energy resolved quasiparticles peak generated above the Fermi sea in the injected distribution $f_i(E)$ propagates for a short distance where the interaction can induce relaxation. The resulting distribution $f_r(E)$ after the propagation is detected with the other quantum dot: QD2.

The Detection (QD2)

The second QD is implemented as a detector in the same way as it was done

[1]We chose the Fermi level E_F as the zero of the energy scales. Thus an energy $E_1 = 0$ means that the discrete level is aligned with the Fermi level. A positive (negative) energy E_1 indicates that the discrete energy level is above (below) the Fermi level. During all our experiments, the Fermi level corresponds to the electrochemical potential of an ohmic contact connected to a cold ground, here $C4$, at base temperature.

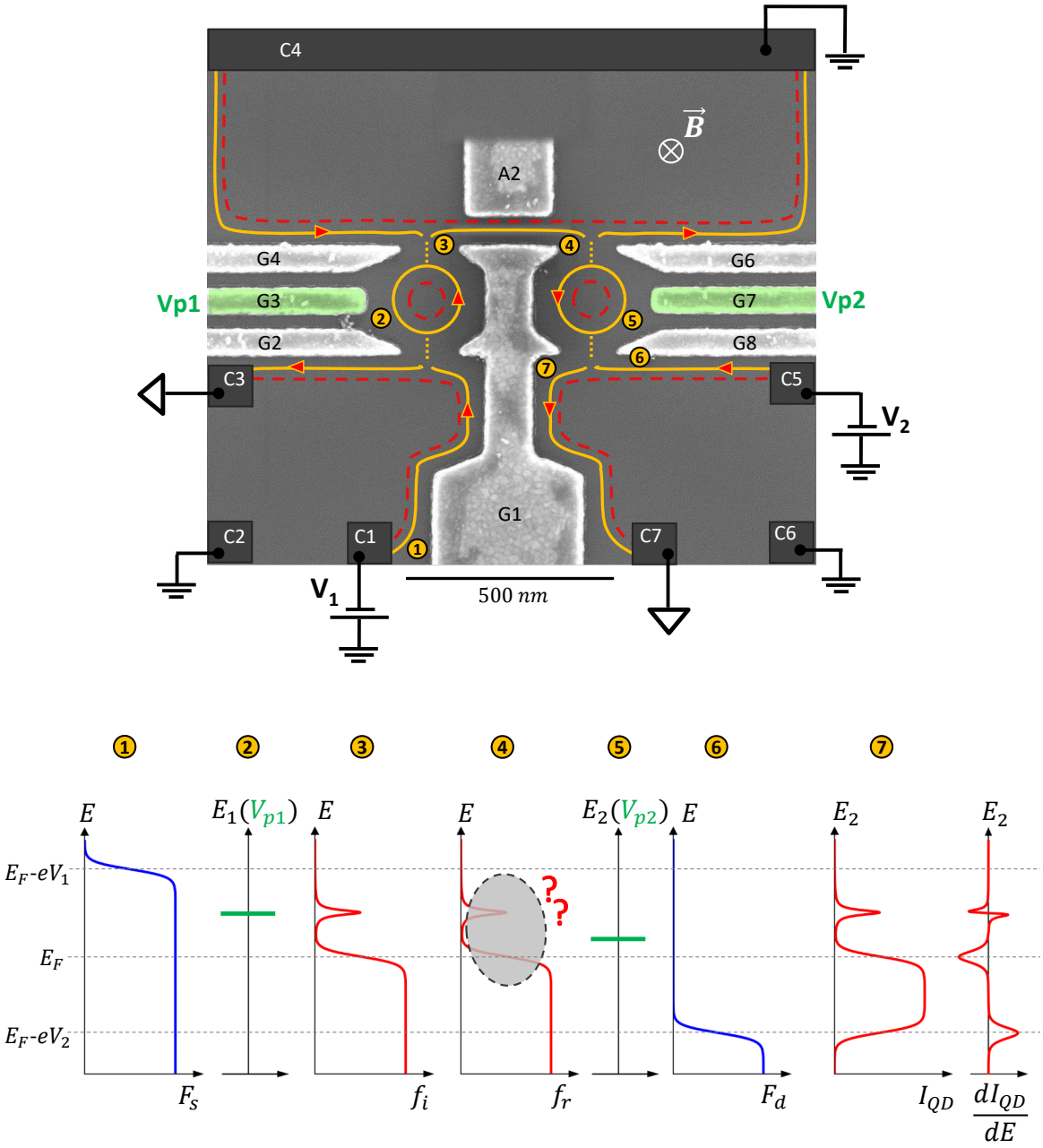

Figure 6.1: Top: Scanning electron micrograph of the sample ***E33***. Two quantum dots are electrostatically defined in order to perform an energy resolved spectroscopy of the relaxation in an edge channel. The two QDs are tunnel coupled only to the outer edge channel, while the inner edge channel is fully reflected by all the electrodes that define the two QDs. The first QD (left) injects quasiparticles above the Fermi sea in the edge channel that comes from the grounded contact $C4$. The injected excitations propagates in the edge channel, from **3** to **4**, until they reach the second quantum dot (right) that is implemented as a detector. **Bottom:** Energy diagram and distribution of particles in different parts of the device. The injection scheme is represented by **1**, **2**, **3**. The propagation happens between **3** and **4**. The detection scheme is represented by **4**, **5** and **6**. The expected signal to be measured in the transconductance across the second quantum dots is represented by **7**. See text for further details (section 6.2). The devices are fabricated at the C2N laboratory where the 2DEGs are grown by A. Cavanna and U. Gennser, while the metallic nanostructures are fabricated by D. Mailly.

for the experiment discussed in the previous chapter. A large positive bias voltage $V_2 \gg k_b T/e$ is applied in contact $C5$ at the drain of QD2 in order to separate the

Fermi level E_F of the edge channel that is being investigated and the electrochemical potential $\mu_d = E_F - eV_2$ of the Fermi function $F_d(E, \mu_d)$ at the drain lead. This is exactly the same type of tuning of the detector QD that was implemented in the experiments described in chapter 5.

The detector is set to have a single discrete level in the energy range $[E_F - \mu_d; E_F - \mu_s]$. The discrete level can be set at an energy E_2, measured from the Fermi level, which is controlled by the plunger gate voltage V_{p2} applied on the electrode $G7$. The lever arm α_2 sets the linear relation:

$$E_2 = -e\,\alpha_2 V_{p2} \tag{6.3}$$

The distribution of particles $f_r(E)$ that arrives at the detector after the propagation is measured through the tunneling current across the QD2 obtained from the transconductance signal that is measured on contact $C7$. Following equation 4.20, the transmitted current $I_2(E_2)$ reads:

$$I_2(E_2) = \frac{e}{h}\int L_2(E, E_2)\,[f_r(E, \mu_r) - F_d(E, \mu_d)]\,dE \tag{6.4}$$

where $L_2(E, E_2)$ is the Lorentzian lineshape of the detector's resonance centered at the tunable energy E_2 and characterized by the transmission $\mathcal{T}_2$ and the intrinsic width Γ_2.

If the resonance at the detector is sharp enough $\Gamma_2 \ll \{k_bT; \Gamma_1\}$, it can be approximated by a normalized delta function $L_2(E, E_2) \to (\pi\Gamma_2\mathcal{T}_2/2) \times \delta(E - E_2)$ such that the transmitted current $I_2(E_2)$ and the transconductance signal dI_2/dE_2 reads:

$$I_2(E_2) = I_{2,max}\,(f_r(E_2, \mu_r) - F_d(E_2, \mu_d)) \tag{6.5}$$

$$\frac{dI_2}{dE_2}(E_2) = I_{2,max}\left(\frac{df_r}{dE_2}(E_2, \mu_r) - \frac{dF_d}{dE_2}(E_2, \mu_d)\right) \tag{6.6}$$

where $I_{2,max} = e\pi\Gamma_2\mathcal{T}_2/2h$. Therefore the distribution function $f_r(E_2, \mu_r)$ after the propagation can be directly measured.

6.3 Finite bandwidth emission and detection

In many cases the condition $\Gamma_2 \ll \{k_bT; \Gamma_1\}$ cannot be well satisfied. Usually we find resonances on the quantum dots with similar widths $\Gamma_2 \sim \Gamma_1$. This means that the detector is not perfect and deviations from equations 6.5 and 6.6 will occur on the measurements. In this section I numerically compute the expected signal $I_2(E_2)$ for a measurement of a Fermi sea and a Lorentz peak performed with a non-ideal detector with a finite linewidth $\Gamma_2 \sim \Gamma_1$. These effects will be seen in the experimental data presented in the following section.

Detection of a Fermi Sea

First let's consider that the QD1 at the injection is set out of resonance with the discrete level below the Fermi level ($E_1 < 0$) or above the electrochemical potential μ_s of the source lead ($E_1 > -eV_1$). In such a case, no particles are injected on the edge channel thus the injected distribution and the distribution after the propagation are equal to the equilibrium Fermi sea at the electronic temperature T_0:

$$f_i(E) = f_r(E) = F(E, E_F, T_0) \tag{6.7}$$

The detected distribution $f_{r,c}(E)$ from the transmitted current across the QD2 is the convolution of the signal to be detected $f_r(E)$ and the Lorentz lineshape of the detector $L_2(E, E_2)$. It can be numerically computed from:

$$f_{r,c}(E) = \frac{I_2(E)}{I_{2,max}} = \int L_2(E, E_2) f_r(E) dE_2 \tag{6.8}$$

The figure 6.2a shows calculations of the convoluted distribution using various linewidth Γ_2 for the detector. We observe that the convoluted signal looks like a hot Fermi sea when Γ_2 is increased. Therefore the electronic temperature $T_{0,c}$ extracted from the convoluted signal differs from the real electronic temperature T_0. The particular dependence of $T_{0,c}$ with the linewidth of the detector is shown in the figure 6.2b which can be exploited to have an estimation of Γ_2 during the experiments.

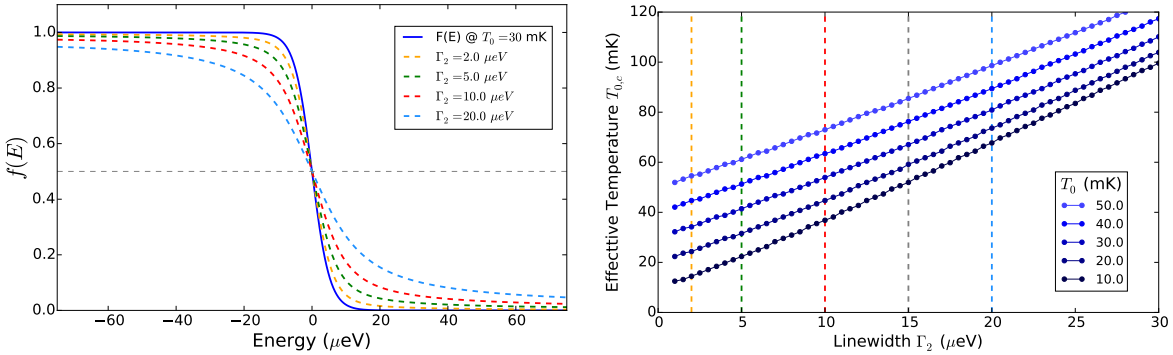

(a) **(b)**

Figure 6.2: **(a)** A Fermi function $F(E)$ with an electronic temperature $T_0 = 30$ mK is plotted in continuous blue line. The convoluted function $f_{r,c}(E)$ (Eq. 6.8) that is measured when the quantum dot, used as a detector, has a non negligible linewidth $\Gamma_2 \sim k_b T_0$, is plotted in dash line for different values of Γ_2. **(b)**As a result of the non ideal detection, the detected Fermi sea $f_{r,c}(E)$ looks hotter than the real Fermi sea $F(E)$. For a given electronic temperature T_0, the effective temperature $T_{0,c}$ measured from the convoluted function $f_{r,c}(E)$ increases with the linewidth of the detector. Knowing T_0 and $T_{0,c}$ this plot allows to extract an estimation of Γ_2.

Moreover, the convoluted distribution shows also some deviation from an actual Fermi function. This can be seen as the long tail that develops on the distribution in figure 6.3(a). We find that, instead of using a Fermi fit, the convoluted distribution is

better described by a function of the form:

$$f_{r,c}(E) \approx \frac{1}{2} - \frac{1}{\pi} \arctan\left(\frac{E - E_F}{k_b T_{0,c}}\right) \tag{6.9}$$

This particular observation concerns experiments where quantum dots are implemented as energy filters to perform an energy resolved spectroscopy. Following the experiments described in chapter 5 about the relaxation of a double step distribution function, it was subsequently predicted that the relaxation process of this type of distribution is expected to go trough a metastable state, under certain conditions, before reaching the final equilibrium [58]. Namely, when the double step distribution function is created using a low transmission τ_{qpc} in the biased QPC, the injected distribution evolves into a metastable state $f_{atn}(E)$ described by:

$$f_{atn}(E) \approx \frac{1}{2} - \frac{1}{\pi} \arctan\left(\frac{E - E_F}{\Gamma_{atn}}\right) \tag{6.10}$$

whit $\Gamma_{atn} = 2e\tau_{qpc}V_1/\pi$ a characteristic width and V_1 the bias voltage across the QPC. This metastable state is expected to arise after a propagation distance $L_{ex} = \hbar v_s/eV_1$ as a consequence of the emergence of the charge and spin modes which propagate respectively at velocities v_c and v_s [58].

A recent experiment has implemented a quantum dot to perform the spectroscopy of the relaxation in this regime in order to elucidate the metastable state [119]. However, the effects of a non-ideal detection were not considered. A non ideal detection of a simple Fermi sea will produce in fact the same functional form as the predicted metastable state (Eq. 6.9 and Eq. 6.10). Since the metastable state is obtained at low QPC transmission, both effects can be comparable in magnitude. Thus, we suggest that these effects should be taken into account to accurately investigate the relaxation process with this system. Moreover, the observation of similar distribution functions with the arctangent dependence under conditions where it is not expected to develop could be explained simply by the convolution of the Fermi sea with the lineshape of the detector without invoking more complicated processes (See Ref. [119]).

Additionally, quantum dots can display a many body effect, the Fermi edge singularity [120], which is also observed in some measurements of Ref. [119]. This many body effect, which was recently observed in laterally defined quantum dots [121], induce a distribution function with a tail which has the same functional form as the mestastable state and as the convoluted Fermi sea that would be measured with a non ideal detector quantum dot.

Therefore, the effects of the non-ideal detection obtained with a quantum dot can have an important impact in the interpretation of these recent experimental results [119, 121]. As we will see in the next section, it will also affect, in a non-trivial way, the observation of a quasiparticle peak injected above the Fermi sea.

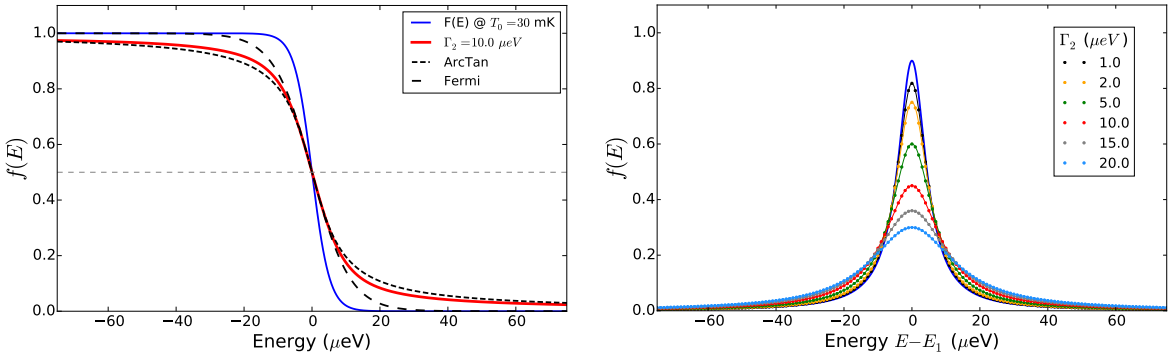

(a) **(b)**

Figure 6.3: **(a)** The Fermi sea with an electronic temperature $T_0 = 30$ mK and the detected function $f_{0,c}$ that results from the convolution with the detector's lineshape with a linewidth $\Gamma_2 = 10\mu eV$ are plotted in continuous blue and red line, respectively. The convoluted function $f_{0,c}$ is better fitted with an arctangent function (short dash), following Eq. 6.9, than with a Fermi function (long dash). **(b)** When a Lorentz peak of amplitude $\mathcal{T}_1 = 0.9$, width $\Gamma_1 = 10\mu eV$ centered at E_1 is convoluted with a second Lorentz peak of different width Γ_2, it results in a Lorentz peak with reduced amplitude $\mathcal{T}_{1,c}$ and larger width $\Gamma_{1,c}$ (Eq. 6.12 and 6.13).

Detection of a Lorentzian Peak

When the first quantum dot is set at resonance, with the discrete level well inside of the bias windows ($0 \ll E_1 \ll -eV_1$), it injects quasiparticles above the Fermi sea with a Lorentz peak distribution $L_1(E, E_1)$. The amplitude $\mathcal{T}_1$ of the Lorentz peak is the transmission of the resonance and its width Γ_1 is the intrinsic width of the resonance which sets the lifetime of the electrons in the discrete level.

If we consider the ideal case where no relaxation occurs along the propagation, the same injected distribution arrives to the detector. If the detector is non ideal, $\Gamma_1 \sim \Gamma_2$, then the detected signal $L_{1c}(E, E_1)$ will correspond to the convolution of the injected peak $L_1(E, E_1)$ with the lineshape $L_2(E, E_2)$ of the detector QD2:

$$L_{1,c}(E, E_1) = \int L_2(E, E_2) L_1(E, E_1) dE_2 \tag{6.11}$$

This can be analytically solved and as a result we obtain that the convoluted signal is also a Lorentz peak centered in E_1, with an effective amplitude $\mathcal{T}_{1,c}$ and a total width $\Gamma_{1,c}$ given by:

$$\mathcal{T}_{1,c} = \mathcal{T}_1 \frac{\Gamma_1}{\Gamma_1 + \Gamma_2} \tag{6.12}$$

$$\Gamma_{1,c} = \Gamma_1 + \Gamma_2 \tag{6.13}$$

Figure 6.3(b) shows the injected peak in blue line and how this peak is observed with a detector for different linewidth Γ_2. The points are the numerical calculation of eq. 6.11 and the solid lines are the analytic solutions using eq. 6.12 and 6.13 in terms of the initial parameters. However, despite these changes, the area under the peak is

conserved: $\frac{\pi}{2}\Gamma_{1,c}\mathcal{T}_{1,c} = \frac{\pi}{2}\Gamma_1\mathcal{T}_1$.

The importance of this observation is that it indicates that even if there is no relaxation along the propagation distance the detected quasiparticle peak will have a smaller amplitude $\mathcal{T}_{1,c}$ than the expected value from the transmission $\mathcal{T}_1$ of the injector quantum dots. This effective reduction on the amplitude of the peak is only a consequence of a non ideal detection, but it can be taken into account in order to access to the actual relaxation when needed. In general we will use this effect only in order to estimate the expected amplitude of the quasiparticle peak in the different measurements.

When the quasiparticle peak is injected close to the limits of the bias windows ($E_1 \sim 0$ or $E_1 \sim -eV_1$) additional deviations can arises since the injected peak is not a perfect Lorentz peak. In a general case, the injected peak is modulated by the bias windows in the first QD:

$$L_{inj}(E, E_1) = L_1(E, E_1) \times [F_s(E, \mu_s, T_0) - F(E, E, T_0)] \tag{6.14}$$

When the resonant level is well inside of the bias windows $L_{inj}(E, E_1)$ reduces to $L_1(E, E_1)$. In other cases, $L_{inj}(E, E_1)$ is an asymmetric peak as shown in Figure 6.4(a).

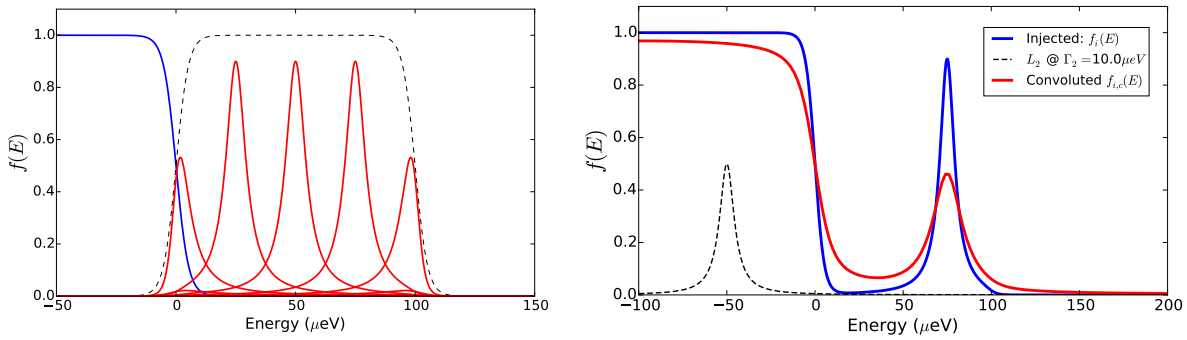

(a) **(b)**

Figure 6.4: **(a)**The equilibrium Fermi sea of the edge channel (blue) over which it is represented the injected peak (red) for various energies E_1 within the bias windows of QD1 indicated in dash gray line. The injected peak deviates from a Lorentz function when it is close to the limits fo the bias window: $E_1 \sim 0\mu eV$ or $E_1 \sim -eV_1 = 100\mu eV$. **(b)** The injected distribution (blue) becomes rounded (red) when it is convoluted with the lineshape (black dash) of the detector. Moreover the injected peak will be detected with a reduced amplitude and larger width even if there was no relaxation just as a consequence of the non ideal detection.

Detection of the Injected Distribution

The Figure 6.4(b) shows, in blue, the injected distribution function $f_i(E)$ where there is a quasiparticle peak of amplitude $\mathcal{T}_1 = 0.9$ and width $\Gamma_1 = 10\mu$eV at an energy $E_1 = 75\mu$eV above a cold Fermi sea at the equilibrium temperature $T_0 = 30$ mK. It is also depicted, in red, how this same distribution will be seen as a convoluted signal

$f_{i,c}(E)$ detected with a QD2 whose resonance (black dash line) has a width $\Gamma_2 = \Gamma_1$ in the case where there is no relaxation. When, in addition, relaxation takes place along the propagation the detected signal $f_{r,c}(E)$ will differ from $f_{i,c}(E)$.

In the previous discussion nothing was said about the transmission $\mathcal{T}_2$ of the resonance at the detector. This is because it does not play an important role since it only determines the normalization constant $I_{2,max}$ in equation 6.8.

6.4 Measured Quasiparticle Peak at Short Distance

In the following I present measured data of the relaxation of a quasiparticle peak, injected above the Fermi sea, after a short propagation length $L = (0.48 \pm 0.05)\mu m$. The quasiparticle peak is generally injected at an energy E_1 in the range $[\,0\,;200]\,\mu eV$ above the Fermi level.

The left panel of Fig. 6.5a presents a typical spectrum where the transconductance dI_2/dE_2 is measured as a function of the detection energy E_2 (x-axis) for several injection energies E_1 (y-axis). Each horizontal sweep is measured several times, between 4 and 10, in order to avoid artifacts arising from possible charge fluctuations on the QD's and averaged to increase the signal-to noise ratio. This is shown in the left panels of Fig 6.5b and 6.5c for two conditions, respectively: when no particles are injected ($E_1 = -53\mu eV < 0$) and when particles are injected at $E_1 = 79\,\mu eV$.

The large peaks in the left panels of Fig. 6.5b and 6.5c correspond to the vertical blue line in the spectrum which is the derivative dF_d/dE_2 of equation 6.6. The large dip and the rest of the signal at positive energies on these plots correspond to the derivative df_r/dE_2 of the injected distribution after propagation (Eq. 6.6). The transconductance signal between the large peak and the large dip, roughly in the energy range $[-80, -20]\,\mu$eV in this particular measurement, is expected to be flat and equals to zero. However as discussed in Ref. [121], the Fermi edge singularity[2] can lead to an effective energy dependent transmission $\mathcal{T}(E)$ of the quantum dot. A reminiscent of this phenomenon on the quantum dot QD2 can then give rise to the small wiggle seen in our transconductance measurements between the large peak and the large dip.

The part of the signal related to the derivative df_r/dE_2 has two components: the large dip located around $E_2 \sim 0$ which is the red vertical line in the spectrum, and the additional small peak-dip structure that corresponds to the diagonal line on the spectrum. These two components are the most important part of the transconductance signal that we want to investigate. In order to get the distribution function $f_r(E)$ we have to integrate this part of the signal. To do so, we proceed to numerically integrate the transconductance signal (dI_2/dE_2) starting from the most positive energy E_{max}

[2]The Fermi edge singularity is due to the Coulomb interaction between a localized electron in the QD with the continuum of the Fermi sea in leads of the QD [121].

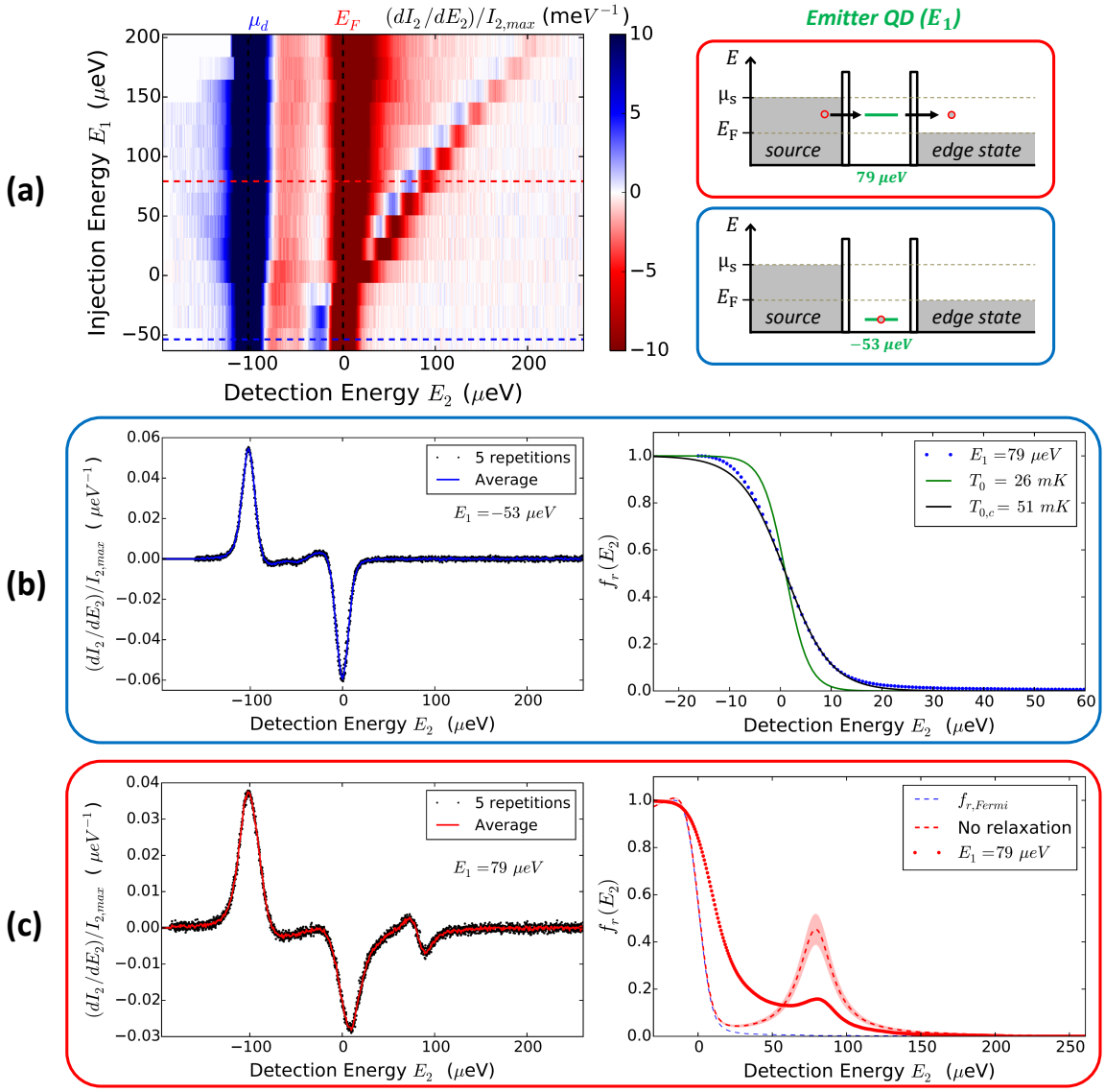

Figure 6.5: ***Spectrum R-107:*** **(a)** 2D-plot of a typical transconductance measurement (dI_2/dE_2), normalized by the constant $I_{2,max}(E_1)$ following equation 6.6, as a function of the detection energy E_2 in the detector QD (x-axis) for different injection energy E_1 in the first QD (y-axis) with a propagation length $L = 0.48\mu$m. Two injection configurations in the first QD are represented in the right part: when no particles are injected ($E_1 = -53\mu eV < E_F$) and when the particles are injected at $E_1 = 79\mu eV$. **(b)** A trace, taken from the 2D-plot, when no particles were injected (left plot) shows a large peak which corresponds to the derivative dF_d/dE_2 and a large dip that corresponds to the derivative df_r/dE_2 (See eq. 6.6). The integration of the later gives the distribution function (blue dots) on the edge channel that we are investigating, which looks like a Fermi sea at temperature $T_{0,c}$ higher than the electronic temperature T_0. **(c)** Same type of plots than (b) but in a configuration when particles were injected at $E_1 = 79\mu eV$. The injected quasiparticle peak is seen in the diagonal line in the 2D-plot in (a) and as small dip-peak structures in the transconductance trace (left-c). After integration, the measured distribution (red dots) shows a quasiparticle peak that is smaller than expected as a consequence of the relaxation undergone along the propagation. The red dashed line is the estimation in the case when there is no relaxation but the signal is measured with the non ideal detector used for the spectroscopy.

towards the negative energy side. We perform the integration in this sense in order to reduce the accumulated error, due to the numerical integration of a noisy signal, in the part of the resulting function $I_2(E_2)$ that is related to df_r/dE_2. Then we multiply the resulting function by (-1) to compensate the inverted integration sense. Notice that we want to obtain a function $I_2(E_2)$ and not the single value of the overall analytic area under the whole transconductance signal. This is:

$$I_2(E_2) = \int_{E_{max}}^{E_2} \frac{dI_2}{dE}(E)dE \tag{6.15}$$

As indicated by equation 6.5, $I_2(E_2)$ is proportional to df_r/dE_2 through the constant $I_{2,max}$. We determine this constant by assuming that $I_2(E_2)/I_{2,max}$ must equals 1 when it gets *flat* at energies below $E_2 = 0$. When the obtained function $I_2(E_2)$ after the integration does not get perfectly flat below $E_2 = 0$, usually due to the small wiggle between the large peak and the large dip in the transconductance signal (See left panels in Fig. 6.5b and Fig. 6.5c), the normalization constant $I_{2,max}$ is determined assuming that $I_2(E_2)/I_{2,max}$ must not be larger than 1 in order to provide a good representation of a distribution function. In practice, in this case we normalize to 1 the first maximum that we find below $E_2 = 0$ in the obtained function $I_2(E_2)$.

In summary, after the described integration and normalization procedure of the dI_2/dE_2 signal we obtain the measured distribution function $f_r(E_2)$ which is shown in the right panels of the figures 6.5b and 6.5c for the two horizontal sweeps indicated on the spectrum. In the first case, no particles were injected, and so it displays the measurement of the equilibrium Fermi sea on the edge channel. The measurement is well described by a Fermi function, besides the discrepancies at the tails, with an effective electronic temperature $T_{0,c} = (51.0 \pm 0.5)mK$. The actual electronic temperature $T_0 = (26,2 \pm 0.9)mK$ of the 2DEG was measured before the spectrum employing another much thinner resonance on the QD's which usually can not be used to perform the spectroscopy due to the low signal-to-noise ratio[3]. The measured $T_{0,c}$ gives an estimation of the linewidth Γ_2 of the detector using the type of plot presented in Fig. 6.2b but calculated for the actual temperature T_0. This procedure gives $\Gamma_2 = (10.0 \pm 0.5)\mu eV$ for the detector. Following a similar procedure during a characterization of the injector QD we estimate $\Gamma_1 = (16.9 \pm 0.5)\mu eV$

In the second case, Fig 6.5c, the quasiparticles were injected at the energy $E_1 = 79\,\mu eV$ with an amplitude $\mathcal{T}_1 = (0.62 \pm 0.03)$ which was also extracted from the characterization of QD1. In the picture we observe a comparison of the ***calculated*** distribution $f_{i,c}$ if there was no relaxation at all and the ***measured*** distribution $f_{r,c}$. We can see that already for this short propagation distance, the quasiparticles peak has gone

[3]Although the signal-to-noise ration can be improved by increasing the number of repetition of each measurements, more than 10 repetition extent the acquisition time of the whole spectrum above 12 hours.

through an important relaxation process, but still a remanent of the injected peak is detected. Although in a previous experiment [50] a peak of particles above the Fermi level of a 2DEG at *zero magnetic field* was detected using a similar technique, our measurements provides the first observation of a quasiparticle peak above the Fermi sea of a 1-dimensional chiral quantum Hall edge channel at high magnetic field. In the following sections I will describe the measured relaxation as a function of several parameters that we can experimentally tune like the injection energy, the electronic temperature and the propagation distance.

An additional feature can be seen in the 2D-plot of Fig 6.5a. When particles are injected, there is a broadening of the vertical blue line which corresponds to the signal of the derivative dF_d/dE of the Fermi sea at the drain of the QD detector. This Fermi sea is not connected to the edge channel where the particles are injected because it comes directly from the biased ohmic contact $C5$ in Fig. 6.1. The broadening that we observe could be caused by the charge noise generated in the edge channel into which the particles are injected, in a similar way as discussed in the last part of section 5.2. In this case the current noise spectrum would be related to the current trough the quantum dot: $S_I = 2eI \times \frac{1}{2}$, but in this case we observe that the broadening is independent of the injection energy.

6.5 Relaxation vs Injection Energy

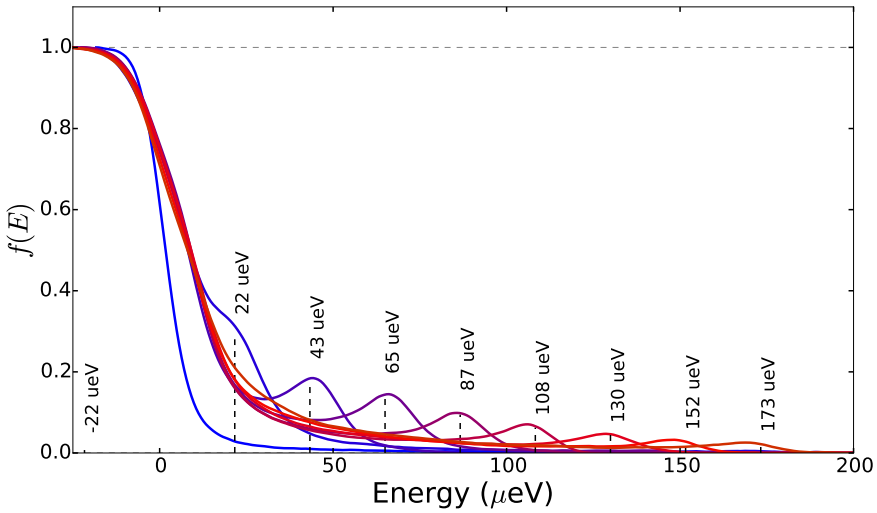

Figure 6.6: ***Spectrum R-72.*** Evolution of the distribution function measured after a propagation distance $L = 0.48\mu$m while increasing the injection energy E_1, indicated by the vertical dashed lines, around which is centered a peak structure that is the remanent of the injected quasiparticle peak. The equilibrium Fermi sea (light blue) with electrochemical potential $E_F \sim 0\mu eV$ was measured when no particles were injected ($E_1 = -22\mu eV < E_F$).

Figure 6.6 shows data corresponding to another realization of the spectroscopy at the short distance using a different set of resonances in both QD's. For this case the

equilibrium electronic temperature was $T_0 = (23.1 \pm 0.6)$ mK and we estimated that $\Gamma_1 = (12.8 \pm 0.4)\,\mu$eV, $\mathcal{T}_1 = (0.44 \pm 0.04)$ and $\Gamma_2 = (5.9 \pm 0.9)\,\mu$eV.

The figure displays the measured Fermi sea at equilibrium and all the measured distributions at different injection energies $E_1 \in \{22, 43, 65, 87, 108, 130, 152, 173\}\mu$eV. The expected amplitude of the quasiparticle peak if there was no relaxation is $\mathcal{T}_{1,c} \sim 0.3$. Although we observe an increasing relaxation as the energy of the quasiparticle peak is increased, the peak structure was still detected at relatively high energies ($\sim 173\,\mu$eV). This is more than 80 times higher that the energy $k_b T_0$ of the thermal excitation at the Fermi sea and the phonon bath (at $T_{ph} \sim 18.5$) mK which constitutes the environment of the system.

Qualitatively we can distinguish three components on the measured distribution $f_{r,c}$. As shown in Fig. 6.7(left) we find an underlying hot Fermi sea (dashed blue) over which there is an *extended* population of particles (dashed red) that give rise to a non Fermi contribution which spreads on the whole energy range below E_1. The third component is the residual peaked distribution located around the injection energy E_1. Alternatively, as it was extensively analyzed in the theoretical work presented in the PhD thesis of C. Grenier [57], the relaxation can be described in term of three components on the electron-hole excitation distribution: The electron-hole pairs created around the Fermi level (representing the heating of the Fermi sea), the relaxation tail at intermediate energies (representing the on going relaxation process) and the residual quasiparticle peak which subsists to the relaxation. The Figure 6.7(right) shows these components on the measured electron-holes pair distribution obtained as: $f_{r,c}(E_2, \mu) - \theta(\mu - E_2)$, where $\theta(x)$ is the step function.

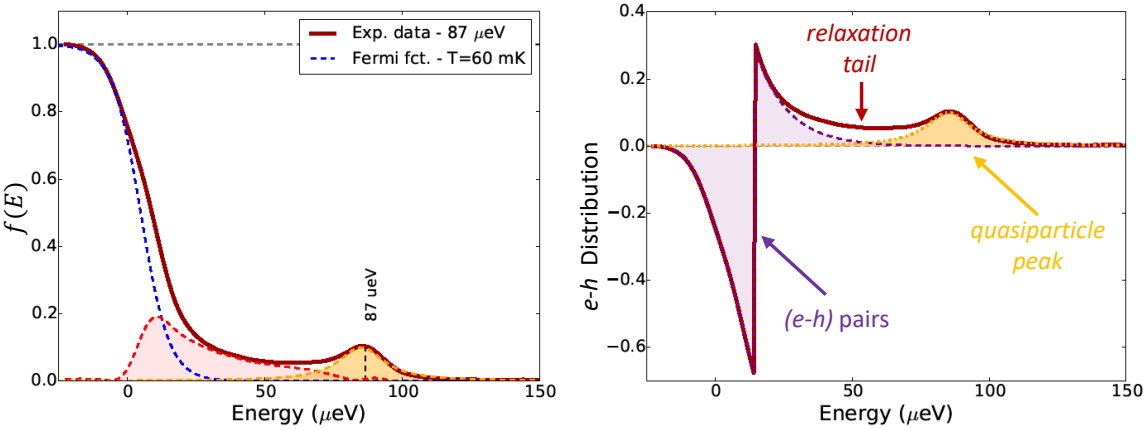

Figure 6.7: ***Left:*** Partially Relaxed distribution function (red continuous line) measured after a propagation distance $L = 0.48\mu$m. Three components can be distinguished: an underlying hot Fermi sea (dash blue), a distribution of particles extended between the Fermi level $E_F = 0\mu eV$ and the injection energy $E_1 = 87\mu eV$, and a remanent quasiparticle peak centered at the injection energy E_1. ***Right:*** Alternatively, three components can be identified in the electron-hole distribution which coincide with the components described in the theoretical investigation presented in the PhD thesis of C. Grenier [57]. These components are a distribution of electron-hole pairs around the Fermi level, a relaxation tail and the remanent quasiparticle peak.

The Figure 6.8 presents the same set of distributions shown in Fig. 6.6 but plotted on a semi-log scale in order to highlight the quasiparticle peak. The circles are the experimental data while the dashed lines are fits using a Lorentz function as suggested by the the intrinsic lineshape of the energy level on the QD's. The Lorentz fit is centered at an energy E_{peak} that coincides with the injection energy E_1 within the experimental errors (Fig. 6.8(b)) which stresses the fact that the peak structure that is measured in the distribution function corresponds to a remanent of the injected quasiparticle peak at the tunable energy E_1. The fitted full width at half a maximum (FWHM) Γ_L remains constant and close to the expected value for a non-ideal detection (Eq. 6.13): $\Gamma_{1,c} = \Gamma_1 + \Gamma_2 = (18.7 \pm 0.7)\mu$eV.

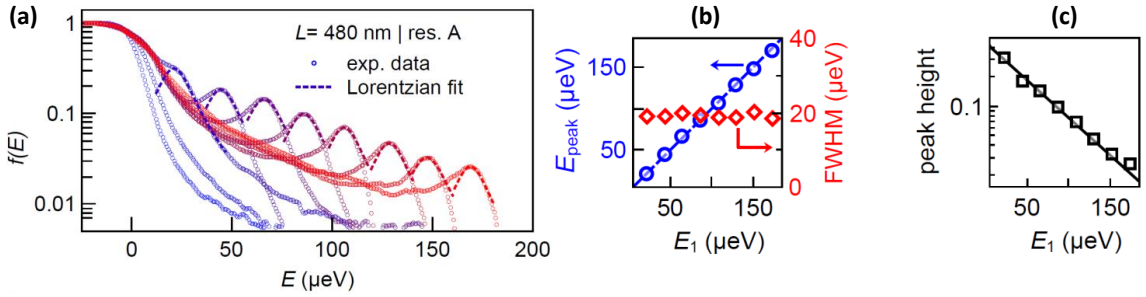

Figure 6.8: **(a)**Measured distribution function $f_{r,c}(E)$ in semi-log scale in order to highlight the evolution of the quasiparticle peak while increasing the injection energy E_1. The dashed line corresponds to Lorentzian fits of the quasiparticle peak. **(b)** Center of the peak E_{peak} (blue circles) and full width at half a maximum FWHM (red diamonds) extracted from the Lorentzian fits plotted versus injection energy E_1. The blue dashed line is a y = x line. **(c)** Peak height extracted from the fits shown in a (black squares) versus E1, in semi-log scale. The black line is an exponential decay fit.

Additionally and most importantly we observe that the amplitude of the measured quasiparticle peak follows an exponential decay with a rather large characteristic energy $E_{decay} \approx 57\,\mu$eV:

$$\mathcal{T}_{1,c} = \mathcal{T}_{1,0}\ \exp\left(-\frac{E_1}{E_{decay}}\right) \tag{6.16}$$

In the theoretical model investigated by C. Grenier *et al.* [116, 115] the relative amplitude decay $\mathcal{T}_{1,c}/\mathcal{T}_{1,0}$ represents the probability for a particle to remain at the injected energy after the propagation across an interacting region. However this quantity, called the *elastic scattering probability* (ESP), does not follow an exponential decay in the theoretical model, instead it follows an oscillatory behavior as presented in Fig. 4.16. Nevertheless, one could think to link the characteristic decay energy that we measured E_{decay} to characteristic energy $E_0 = \hbar v/L$ of the theoretical model at strong coupling parameter ($\varphi = \pi/2$). This would provide, for the short propagation length $L = 0.48\,\mu$m, a characteristic velocity $v \sim 4.2 \times 10^4$ m/s.

The obtained velocity is in the range of drift velocities $v \in [5, 50] \times 10^4$ m/s that have been reported for 2DEGs measured in the IQHE regime at filling factor $\nu = 2$ in devices where the edges where electrostatically defined as recapitulated in Ref. [52].

Moreover the obtained velocity v is also similar to the velocity $v_{sc} = v_c v_s/(v_c - v_s)$ which have been observed to be in the range $v_{sc} \in [2.7, 8.7] \times 10^4$ m/s as discussed in Ref. [119] (see also references therein) using a different analysis of the data presented in ref. [52]. This velocity v_{sc} sets the distance l_{sc} over which the spin and charge modes, that propagates respectively with velocities v_s and v_c, are well separated assuming they have a comparable spatial wave packet extension. The similarity between the obtained v and v_{sc} provides an insight that the spin charge mode separation could be at play during the relaxation process. In appendix-**B** I present a detailed discussion about the propagation speed of the excitations and the relation with other velocity parameters of the theoretical model, which set the energy, time and length scales in different recent experiments.

6.6 Relaxation vs Temperature

Here we investigate the relaxation process as a function of the electronic temperature in the range $T \in [23; 170]$ mK. In particular we focus on the behavior of the quasiparticle peak. In the following we perform the spectroscopy using the same set of resonances that was used to measure the distributions presented in Fig. 6.5 . The resonances are labeled as: *res-C* for the injector QD1 and *res-E* for the detector QD2. At the lowest electronic temperature $T = (23.1 \pm 0.6)$ mK we estimate that $\Gamma_1 = (18.7 \pm 0.7)\mu$eV, $\mathcal{T}_1 = (0.60 \pm 0.05)$ and $\Gamma_2 = (11.2 \pm 0.8)\mu$eV.

For each stationary value of the phonon temperature T_{ph} (this is the fridge temperature measured with a calibrated thermometer), the electronic temperature T is determined using the sharpest available resonance for QD1 to which we refer as *res-1D*. The electronic temperature was obtained by fitting the Coulomb peak measured at zero bias, which is thermally broadened, using equation 4.19. For comparison we also measure the effective electronic temperatures, T_{resC} and T_{resE}, from the Coulomb peaks at zero bias once the QDs are tuned in the resonances chosen for the spectroscopy. These measurements are shown in figure 6.9 on which we observe that the measured electronic temperature T (red dots) closely follows the phonon temperature (black line) down to the lowest value $T = (23.1 \pm 0.6)\, mK$ obtained for a base phonon temperature of $T_{ph} = (18.1 \pm 0.1)\, mK$. In this regime, the effective temperatures, T_{resC} and T_{resE}, are higher than T_{ph} which manifests the underlying non negligible finite width of those resonances [122]. Additional discrepancies are seen also at higher temperatures where surprisingly we obtained values below T_{ph}. There are few artifacts and/or mechanisms that could lead to this observation as I will briefly describe in the following paragraphs.

Quantum dots are sensitive to charge instabilities which can depend on proximity to surrounding metallic electrodes or gates, the detailed electrostatic landscape, the materials of the semiconductor heterostructure or the presence of fluctuating external electromagnetic fields. Charge instabilities lead to random fluctuations of the energy

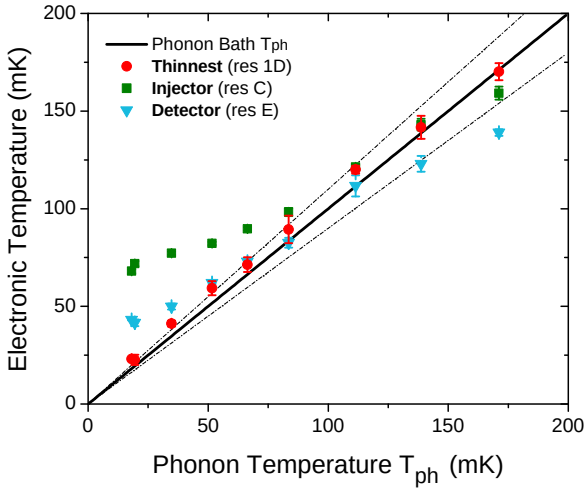

Figure 6.9: Comparison between the phonon temperature T_{ph} and the electronic temperature T (circles) extracted from the thinnest Coulomb peak in the differential conductance of the QD at zero bias. The black line is the $T = T_{ph}$ function, while the dashed line represent deviations of 10%. Additionally, square and triangle symbols, are the effective electronic temperatures extracted from the resonances implemented in each dot to perform the spectroscopy at different temperatures.

of the active level in the QD, usually seen as telegraphic noise in the transmitted current. Charge instabilities can cause both: an effective narrowing or a broadening of the Coulomb peak during a usual differential conductance measurement. As a consequence of this artifact, fictitious fluctuation of the electronic temperature can be detected when comparing individual measurements taken under the same conditions. In order to avoid this effect, several measurements of the same Coulomb peak, under the same experimental conditions, are necessary to obtain a statistical mean value of the electronic temperature. The effective temperatures shown in Fig 6.9 have been determined only from few repetitions (< 4) hampering the determination of a proper representative mean value and the correct standard deviation. This could explain the fact that some measured values are below the phonon temperature, but it is not enough to explain why this effect is more pronounced at higher phonon temperature as seen in the data.

Moreover we notice that similar deviations below the phonon temperature, and beyond the error bars, are seen in other experiments that use quantum dots as thermometers [51, 123]. Furthermore, quantum dots in a similar configuration that we have in our sample have been implemented to purposely lower the electronic temperature in a 2DEG below the fridge temperature by several tens of mili-Kelvins when being implemented as *quantum dots refrigerators* [124, 125, 126].

Let's see now what happens to the relaxation process at different temperatures. Figure 6.10 shows the excess distribution of particles $\Delta f_{r,c}(E)$ which we obtain by subtracting from each distribution $f_{r,c}$ the *measured* Fermi Sea $f_{r,Fermi}$. Here $f_{r,Fermi}$

is the measured distribution when no particles were injected.

$$\Delta f_{r,c}(E) = f_{r,c}(E) - f_{r,Fermi}(E) \tag{6.17}$$

These are all the particles that we have injected initially as a single peak which are now distributed all over from the Fermi level up to the injection energy E_1. The Figure 6.10 shows the evolution of the excess distributions as we increase the energy E_1 for three electronic temperatures $T \in \{39; 120; 170\}$ mK. In each plot the curves were vertically shifted by a constant proportional to the increment in injection energy $\delta E_1 \approx 20\mu$eV, from $E_1 \approx 5\mu$eV (blue) up to $E_1 \approx 160\mu$eV (red).

As the temperature is increased we observe that the component of particles that is close to the Fermi level gets broader which might be a manifestation of the interaction between these particles and the hotter underlying Fermi sea. In consequence, the quasiparticle peak disappears in the tail of that component at high temperatures.

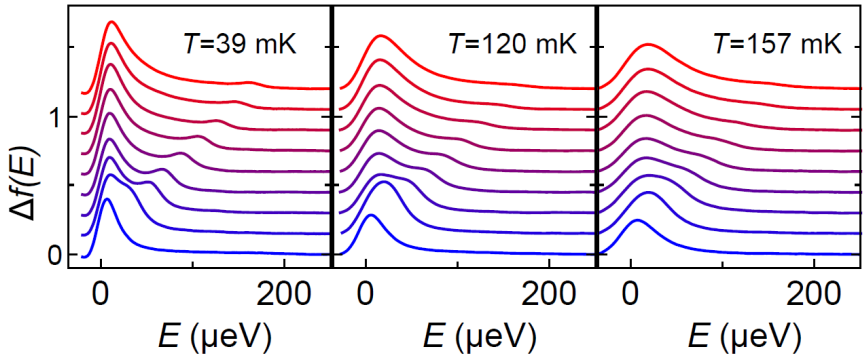

Figure 6.10: Excess particle distribution function $\Delta f_{r,c}(E)$ measured after a propagation length $L = 0.48\mu$m at temperature $T = 39$ (left),120 (center) and 157 mK (right). Each curve, offset for clarity, corresponds to a increment of the injection energy $E_1 = 20\mu eV$, from $E_1 = 5\mu eV$ (blue), to $E_1 = 160\mu eV$ (red).

In a similar way as before we obtain for each temperature the characteristic decaying energy E_{decay} and the width of the quasiparticle peak Γ_L (FWHM) by using a Lorentz model. The behavior of these two parameters as a function of the electronic temperature is plotted in Fig. 6.11a. The E_{decay}, plotted in blue, shows that the amplitude of the quasiparticle peak decays faster at higher temperature, roughly with a decaying energy following $E_{decay} = 75\mu\text{eV} - 2.5k_bT$. This behavior implies that the decaying energy decreases almost by a factor two when the system is warmed by $\Delta T \approx 150$ mK. Such an increase in the temperature, increases the energy of the thermal excitations in the electronic environment only by $k_b\Delta T \approx 13\mu$eV and yet it affects the relaxation of the quasiparticles at much higher energies $E_{1,max} \approx 160\mu$eV. Thus, this behavior suggests that the injected electrons indeed interact with thermalized excitations at much lower energies such as the particles on the Fermi sea in the same edge channel or the particles in the effective environment (quasiparticles in the co-propagating edge channel, charges in nearby electrodes, etc).

Additionally we measured the width Γ_L of the quasiparticle peak as a function of the temperature plotted in red in Fig. 6.11b. We have seen before that at low temperature the width of the measured quasiparticle peak was independent of the injection energy and it was given by the intrinsic linewidth of the discrete levels in the injector and the detector quantum dots, which is also the case on these measurements: $\Gamma_L \approx \Gamma_1 + \Gamma_2 \approx 30\,\mu$eV. The Intrinsic width of a discrete QD level is not thermally broadened, instead it only depends on the transmission of the barriers that defines the QD. Therefore, from the point of view of the simple model that describes the QD's we do not expect any temperature dependence on the width of the quasiparticle peak. The measurements shows that although there is a systematic increase of Γ_L with the temperature, it does not follows the thermal broadening of the Fermi Sea as presented in Fig. 6.11b in the form of the absolute width increase relative to the measurements at $T_{ph} \sim 20$ mK.

Moreover, ballistic and elastic charge transfer between two quantum dots separated by a distance of $\sim 2\mu$m was performed in GaAs at zero magnetic field by Rossler *et al.* [50]. The experimental configuration is similar to our case in that single energy levels on quantum dots are used as energy filter to emit and detect particles. A peak of particles associated to the elastic transfer of electrons was detected, which is the equivalent of the quasiparticle peak, and its evolution with the temperature was investigated. They observed a similar dependence of the increase in the width of the peak. This behavior of the quasiparticle peak at zero magnetic field in a 2-dimensional system is plotted (green data) as a comparison to our data in Fig 6.11b.

A widening of the quasiparticle peak which increases with the electronic temperature can also be related to the charge noise generated in the edge channel. In this case the current noise is directly related to the thermal excitation following a typical $\sqrt{T}$ dependence.

6.7 Relaxation vs Length

We investigate now the evolution of the injected distribution as a function of the propagation distance from the sub-micrometer regime up to few micrometers at low temperature $T \sim 20$ mK. Although in each sample we could change the propagation distance with the electrode G5 in Fig. 6.1, it allows us to chose only between two values. Therefore we compare here data from three different samples where the direct short path was designed to have different lengths. The data shown in the previous sections of this chapter corresponds to the sample ***E33*** for which the short path has the smallest length that we have investigated $L = (0.48 \pm 0.05)\mu m$ and the long path is $L = (1.44 \pm 0.05)\mu m$. The other two samples are: sample ***D31*** with distances $L = (0.74 \pm 0.05)\mu m$ and $L = (2.17 \pm 0.05)\mu m$; and sample ***C4*** with a single path of $L = (3.4 \pm 0.1)\mu m$. All distances were measured from the scanning electron micrographs.

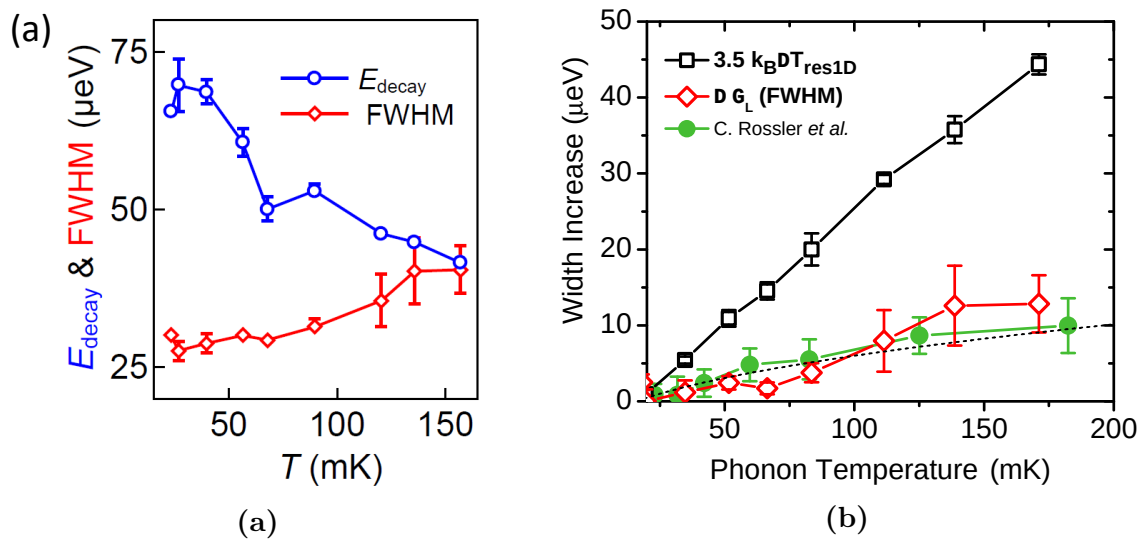

Figure 6.11: **(a)** Characteristic energy E_{decay} (blue circles) of the exponential decay of the quasiparticle peak height and the width Γ_L of the quasiparticle peak (red diamonds), both extracted from the Lorentzian fits as illustrated in Fig. 6.8, plotted versus temperature. **(b)** The width increase versus temperature for the Coulomb resonance (*res-1D*) in the differential conductance of the first quantum dot (empty black square), the measured quasiparticle peak (empty red diamonds) and the quasiparticle peak at zero magnetic field (full green circles) measured in Ref. [50]. The black dotted line is a $\sqrt{T}$ increase from the value at the lowest electronic temperature.

For each sample we verified that the main features, which will be described in the following part, of the measured distribution are consistent when the spectroscopy is performed using different sets of resonances on both QD's, when the QD's are formed under different strength of the confining potential or, sometimes, in different cooling cycles.

In the left panels of figure 6.12 we observe the measured transconductance signal $dI_2(E_2)/dE_2$ as a function of the detection energy E_2 and the injection energies E_1 for three propagation distances. The right panel of Fig. 6.12 show some distribution functions obtained after integration at particular injection energies. As before the curves are vertically shifted, for clarity, by a constant proportional to the increase on the injection energy δE_1 from curve to curve (See caption for the energies E_1 at each curve).

On the table 6.1 it is summarized for each spectrum the values of the intrinsic linewidth Γ_1 of the injection QD1, its transmission T_1 and the intrinsic linewidth of the detector Γ_2 which we use to estimated the amplitude $T_{1,c}$ of the detected peak once it is convoluted with the detector if no relaxation occurs (Eq. 6.12).

Notice that although the resonances used in both quantum dots for the spectrum measured at the propagation distance $L = 0.48\mu$m and $L = 0.75\mu$m are different, they lead to that same expected amplitude $T_{1,c}$ for the quasiparticle peak that would be detected in the case when there is no relaxation. However, the measurements of the quasiparticle peak detected after a propagation length $L = 0.75\mu$m is strongly different from the measurement done at $L = 0.48\mu$m. In the spectrum taken at $L = 0.48\mu$m

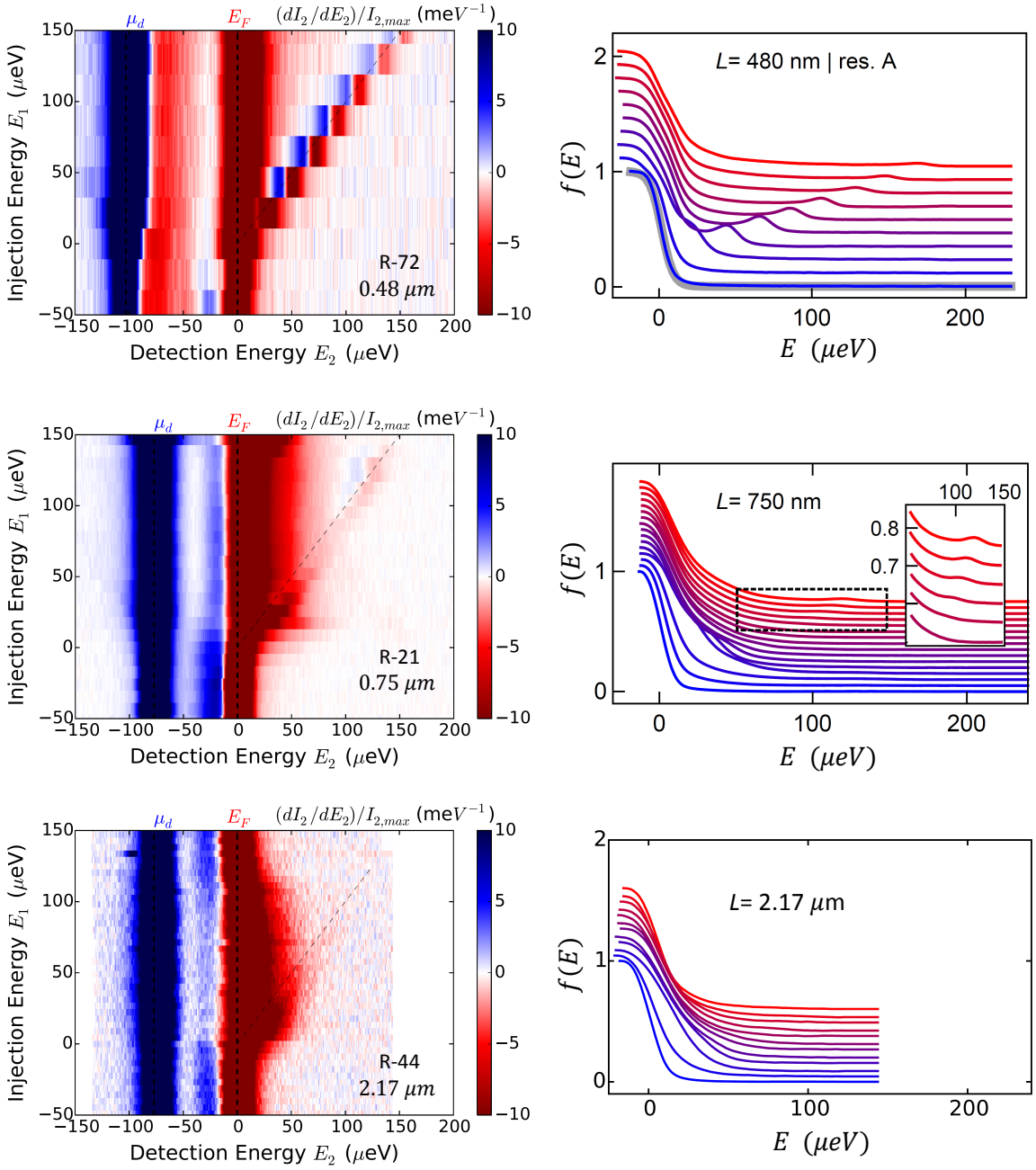

Figure 6.12: The left panels are the measured spectra of the normalized transconductance as a function of the detection energy E_2 (x-axis) and the injection energy E_1 (y-axis) for different propagation distances L. The right panels shows the distribution functions obtained from the spectra where the curves were vertically shifted for clarity. **Top:** Spectrum measured in sample ***E33*** for $L = 0.48\mu$m. Each curve, correspond to an increment of the injection energy $\delta E_1 \approx 21\mu eV$, from $E_1 = -21\mu eV$ (blue) to $E_1 = 173\mu eV$ (red). the thick grey line is a Fermi function fit of the data at $E_1 = -21\mu eV$. ***Middle:*** Spectrum measured in sample ***D31*** for $L = 0.75\mu$m. Each curve, correspond to an increment of the injection energy $\delta E_1 \approx 9\mu eV$, from $E_1 = 9\mu eV$ (blue) to $E_1 = 121\mu eV$ (red). The inset is a zoom on the region delimited by the black dotted square. ***Bottom:*** Spectrum measured in sample ***E33*** for $L = 2.17\mu$m. Each curve, correspond to an increment of the injection energy that alternates between $\delta E_1 \approx 8.9\mu eV$ and $\delta E_1 \approx 13.4\mu eV$, from $E_1 = 0.0\mu eV$ (blue) to $E_1 = 111.5\mu eV$ (red).In all the panels, the vertical offset is equal to $5.5 \times 10^{-3}\delta E_1$.

Length (μm)	Γ_1 (μeV)	T_1 (%)	Γ_2 (μm)	$T_{1,c}$ (%)
0.48	(12.8 ± 0.4)	(44 ± 4)	(5.9 ± 0.9)	(30 ± 8)
0.75	(16.3 ± 0.7)	(54 ± 4)	(9.6 ± 0.9)	(34 ± 7)
2.17	(17.0 ± 0.5)	(43 ± 4)	(15.3 ± 1.0)	(23 ± 4)

Table 6.1: Intrinsic linewidth Γ_1 and transmission T_1 of the resonance in the first quantum dot and intrinsic linewidth Γ_2 of the resonance in the detector quantum dot. From equation 6.13, we estimated the expected amplitude $T_{1,c}$ of the quasiparticle peak to be detected in the case when there is no relaxation.

the quasiparticle peak is clearly seen, but when the propagation distance is increased by almost a factor two, the quasiparticle peak becomes very small, however it can still be identified when zooming on the tails of the measured distributions (Inset in right panel of Fig. 6.12-Medium). Therefore, this demonstrates that the increase in the propagation distance strongly affects the quasiparticle peak. Finally the spectrum taken at a distance $L = 2.17\mu$m shows almost no signatures of the injected quasiparticle peak which was also verified at the longest distance $L = 3.4\mu$m. Only a non equilibrium distribution near the Fermi sea is observed after the propagation.

On the two shortest distances we observe that the amplitude of the quasiparticle peak decays exponentially with increasing injection energy. The Figure 6.13 shows that the decaying energy E_{decay} decreases at longer propagation distance demonstrating that relaxation becomes stronger. In section 6.8 we will address the peculiar behavior at high energy observed on the spectrum measured at $L = 0.75\mu$m.

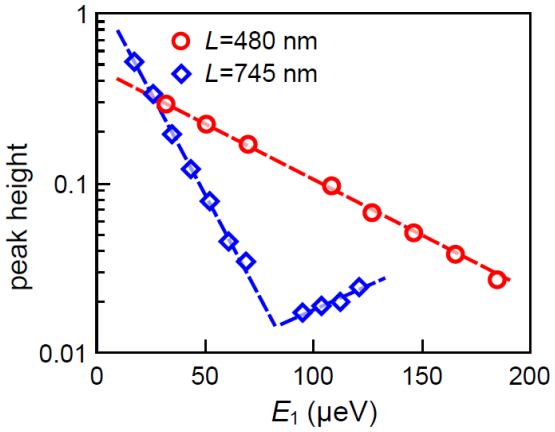

Figure 6.13: Peak height extracted from the Lorentzian fits illustrated in Fig. 6.8, plotted in semi-log scale as a function of injection energy E_1 for two propagation lengths $L = 480$ nm (red circles) and $L = 750$ nm (blue diamonds). The red and blue dashed lines are exponential fits. The particular behavior of the measurements at $L = 750$ nm around $E_1 \sim 100\,\mu$eV will be discussed in section 6.8.

A comparison of the whole distributions of particles observed at several distances for a quasiparticle peak injected approximately at the same energy $E_1 \approx 40\mu eV$ is

shown in the figure 6.14. Together with the preceding analysis of the quasiparticle peak behavior we can describe how the relaxation mechanism brings the system to equilibrium. At first, a large amount of the injected particles lose energy and the amplitude of the injected quasiparticle peak rapidly decays in a sub-micrometer propagation distance. Notice that no relaxation was observed for sub-micrometer distances when the propagation of a double step distribution function was investigated [51]. Once the quasiparticles peak has almost vanished at a distance of about $\sim 1\mu m$ what is left is a non-Fermi distribution, with no sharp features and a long tail that extends in a wide range of energies, which is still out of equilibrium. As can be seen in the Fig. 6.14 this distribution does not change much while it propagates up to $3.4\,\mu m$. In fact, at this point it resembles an intermediate state of the relaxation process of the double step distribution which was seen to finally achieve the equilibrium at large distances $\sim 10\mu m$ (See Fig. 5.4 and section 5.2).

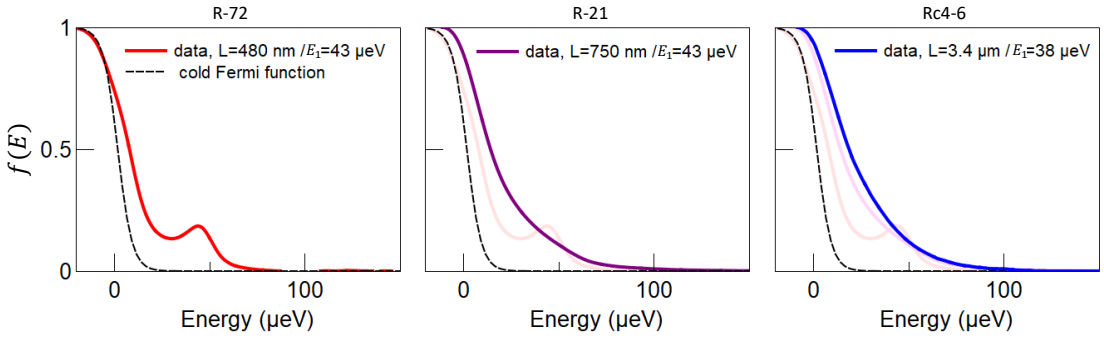

Figure 6.14: Measured distribution function (continuous line) for similar injection energy E_1 at increasing propagation distances: $L = 480$nm (left), $L = 750$nm (middle) and $L = 3.4\mu$m (right). The dashed line is the equilibrium Fermi sea measured in each case when no particles were injected.

In chapter 5 we have verified that in our systems we observe the same relaxation rate for a double step distribution function as reported in Ref. [52]. Therefore, these observations demonstrate that the first part of the relaxation we have described here, which takes place in the sub-micrometer scale, is a genuine phase of the decaying process of the Landau quasiparticles that has not been observed before.

These experimental observations provide an answer for a very fundamental question that was formulated as a central objective of this thesis work: ***How*** *do quasiparticles emitted in a narrow energy window relax during propagation?*. As schematically represented in the figure 6.15 our observation shows that the quasiparticle peak does not drop toward the Fermi sea nor does it broaden, as one may simply think as a first guess. On the contrary, the relaxation process preserves the quasiparticle peak position E_1 and width Γ_L but its amplitude decreases while particles are transferred to lower energies.

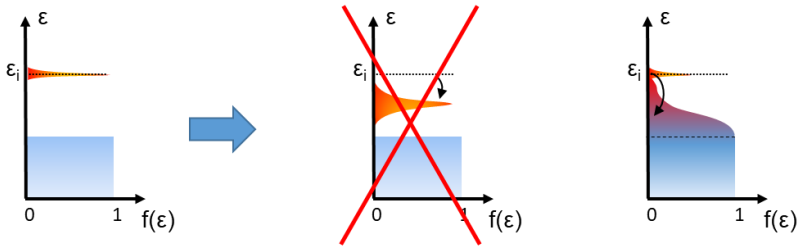

Figure 6.15: Schematic representation of the relaxation process observed in our measurements.

6.8 Signatures of a Quasiparticle Peak Revival

As mentioned in the previous section we have observed a peculiar behavior of the quasiparticle peak at high energy on the spectrum measured at the propagation distance $L \approx 0.75\,\mu m$ (Fig. 6.13). The amplitude of the quasiparticle peak not only suddenly deviates from the exponential decay, but surprisingly it increases as the injection energy increases.

The Figure 6.16 shows a zoom on the tail of the distributions from another realization of the spectrum which was measured using the same set of QD's resonances and under the same experimental conditions than the spectrum presented in the middle panel of Fig. 6.12. Here we can see that the quasiparticle peak literally disappears in the energy range $E_{drop} \sim (75 \pm 15)\mu eV$ following the exponential decay and afterwards it re-appears at higher energies as a small but well defined peaked structure which follows the injection energy E_1. This can be seen either in the transconductance signal or the distribution function.

In the spectrum presented in middle panel of Fig. 6.12 each horizontal sweep was repeated 10 times, which were then averaged, in order to rule out drifts and switching effects on both quantum dots due to possible random charge fluctuations. Additionally, the whole spectrum was measured 5 times, using the same set of resonances on both dots and changing only the bias energy windows applied to each dot. In all of them the peak was found to have the same behaviour around the same energy E_{drop} which shows that it is not caused neither by a particular electrostatic configuration of the leads around the dots.

We have also performed the spectroscopy using two different resonances on the quantum dot at the injection and two different resonances on the quantum dots at the detection: a total of 4 different spectra. Since the same feature was observed we can infer that it is not generated by a particular level structure on the energy levels of the QD's which could be argued since the amplitude of the measured quasiparticle peak $T_{1,c}$ depends on Γ_1, Γ_2 and on the transmission of the first quantum dots which can be energy dependent $T_1(E)$ in some cases. In particular, $T_1(E)$ shows only smooth variations which cannot account for the quasiparticle peak resurgence.

As a final test, the magnetic field was turned off, all the electrodes and Ohmic

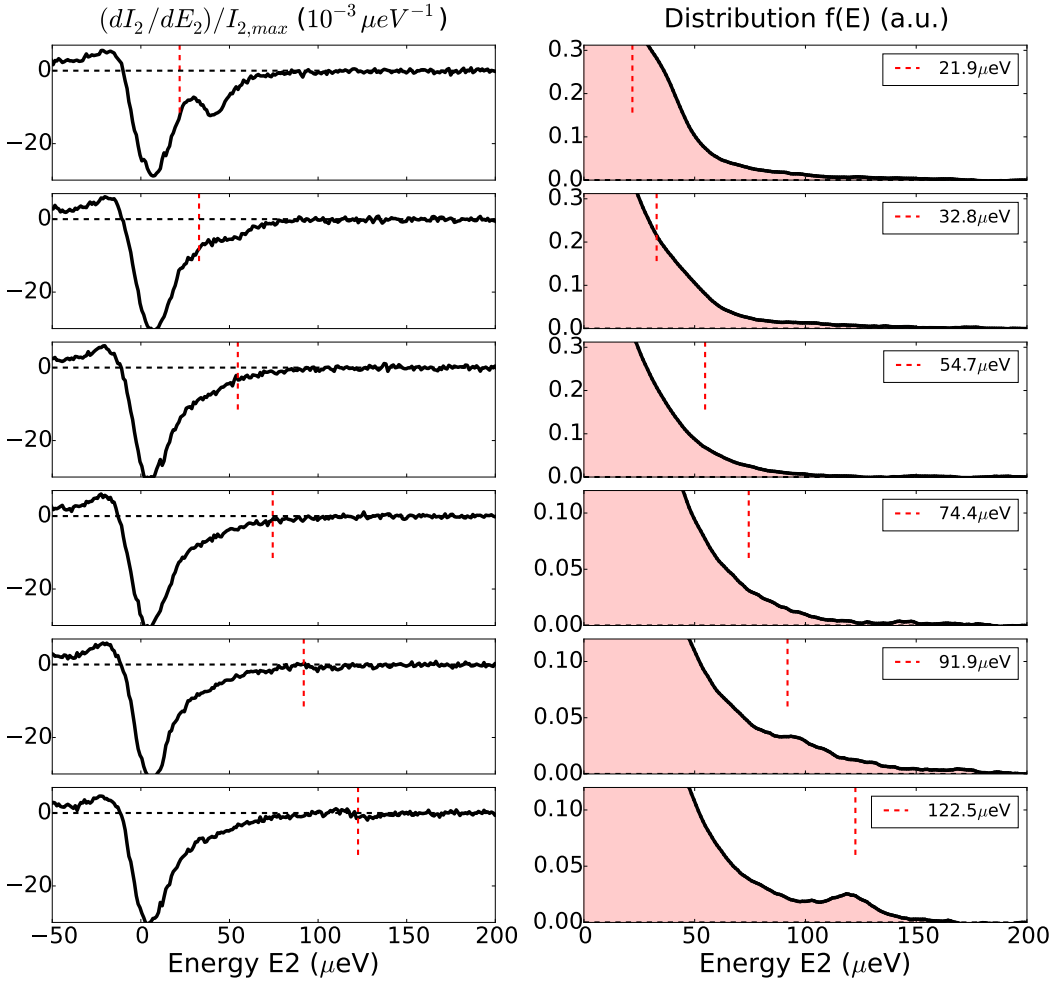

Figure 6.16: ***Quasiparticle peak revival observed in Spectrum R-20.*** **Left:** Zoom in the dip structure associated to the derivative $df_{r,c}/dE$ usually observed in the transconductance measurement. The large dip corresponds to the derivative of the distribtuion function near the Fermi level, while the additional signal that follows the vertical dashed line corresponds to the remanent quasiparticle peak. **Right**: Zoom in the tail of the distributions obtained after integration of the signal presented in the left panels. The legend of each plot indicates the injection energy E_1.

contacts on the 2DEG were connected to the ground and the sample was warmed up to room temperature. Then a new cooling cycle was initiated and the quantum dots were re-defined in completely different electrostatic configurations with which the spectrum was measured at the same propagation length. As a result, the same striking feature was observed in the same energy range.

We can therefore conclude that the revival of the quasiparticle peak that we have presented is a robust observation, measured here in more than ten spectra where different parameters were varied showing no dependence with any of them. Four of these spectra that represent the different conditions that were discussed are presented in Fig 6.17.

Additionally the Coulomb diamonds measured for the set of resonances that we used to obtain these spectra did not show the presence of excited states in the energy

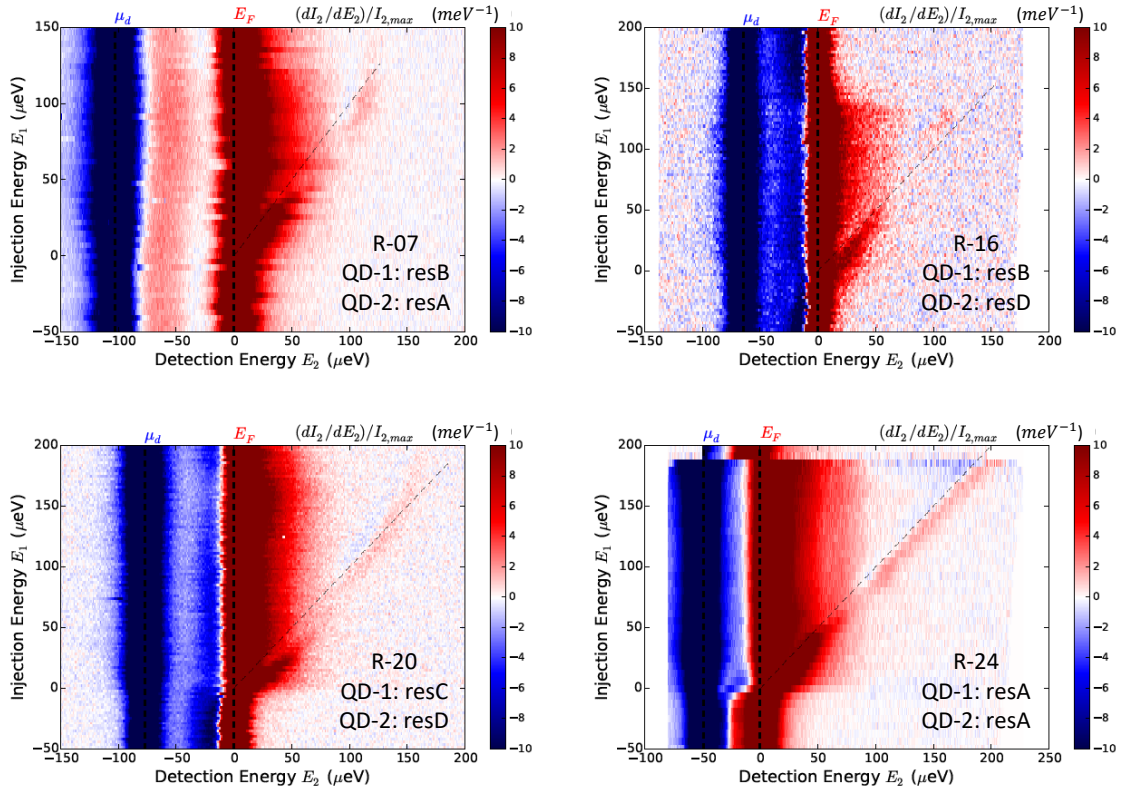

Figure 6.17: Four different spectra measured in sample ***D31*** for a propagation length $L = 0.75\mu m$ and al low temperature $T \sim 20$ mK. The spectra **R-07**, **R-16**, **R-20** where measured using different resonances and bias conditions on the injector QD-1 and the detector QD-2. The spectrum **R-24** was measured in a different cooling cycle and each horizontal sweep is the average of 7 consecutive measurements. In all these different conditions we observe that the quasiparticle peak signal vanishes around $E_{drop} = (75 \pm 15)\mu eV$ and reappears at higher energies.

range where the quantum dots were tuned.

Although the exponential decay is not described by the current theoretical models for the relaxation of quasiparticles in quantum Hall edge channels, the approach considered by C. Grenier *et al.* indicates that the amplitude of the quasiparticle peak decays non monotonously: it shows an oscillatory behaviour. This theoretical model predicts that the injected quasiparticles relax by decomposing onto the plasmon modes. Since the charge mode is expected to propagate with a large velocity than the spin mode, a charge-like plasmon can catch up and recombine with a downstream spin-like plasmon leading to a revival of the quasiparticle excitation and thus of the quasiparticle peak amplitude, which is the reason for the oscillatory behavior. Thus, one possibility is that the increase in the amplitude we have measured could be the onset of these oscillations. The energies at which are located the minima observed in the oscillations in the theory do not strongly depend on the coupling constant as seen in the figure 4.16. Therefore the first minima occurs at the energy $E_{J0} = 2.4\,\hbar v/L$ which is given by the first zero of the Bessel function[4]that describe the strong coupling regime $\varphi = \pi/2$

(Eq: 4.44) If we take the energy E_{drop} at which the measured amplitude starts to grow, deviating from the exponential decay, to be equal to E_{J0} we can estimate the characteristic velocity v. Using the value of the propagation distance $L \approx 0.75\,\mu$m, we find $v \approx (3.5 \pm 0.7)\,10^4$ m/s which is of the same order of magnitude than the value $v \approx 4.2 \times 10^4$ m/s determined previously from the exponential decay (Section 6.5).

Therefore although this theory does not describe well the decaying functionality of the measured amplitude, it provides a framework that supports the evidence of the observation of a quasiparticle revival with a reasonable parameter v.

6.9 Conclusions

In this chapter we have investigated the relaxation of a quasiparticle peak emitted at a well defined energy over the Fermi sea of an edge channel in the integer quantum Hall effect regime at filling factor $\nu = 2$. These experiments constitutes the first observation of a quasiparticle peak above the Fermi sea of an edge channel.

We observed that after a short propagation distance in the sub-micrometer scale, a considerable amount of the injected particles lose their energy and relax toward the Fermi sea. However, although the propagation over submicron lengths leads to sizable energy relaxation, a small portion of quasiparticles are not affected by energy relaxation even at relatively high energies, up to 150μeV. Therefore we were able to measure the a components of particles that has relaxed, a component of particles that were in the process of relaxation and a component of particles that survives to the relaxation.

We measured that while the relaxation takes place, the injection energy E_1 around which the quasiparticle peak is centered was preserved as well as its width Γ_L. However, the amplitude of the measured quasiparticle peak shows an exponential decay as a function of the injection energy E_1 which was not predicted by any theoretical model up to our knowledge.

Moreover, we have observed that the characteristic energy E_{decay} of the exponential decay of the quasiparticle peak's amplitude as a function of the injection energy E_1 is strongly affected by the propagation distance and the electronic temperature. On the one hand, an increase in the propagation distance from $L = 480$ nm up to $L = 750$ nm leads to a decrease in the decay energy from $E_{decay} \sim 60\,\mu$eV to $E_{decay} \sim 20\,\mu$eV. On the other hand, an increase in the electronic temperature of $\Delta T = 150$ mK reduces the decay energy by almost a factor of two.

Furthermore, the comparison of our measurements taken at increasing propagation distance in the range $L \in [0.48; 3.4]\,\mu$m allows to distinguish two time scales in the relaxation process, which were first pointed out in the theoretical model presented in Ref. [56]. The first part of the relaxation process, that takes place in sub-micrometer

[4]The Bessel function $J_0(x)$ of the first kind has the first positive zero at $x = 2.4048$.

lengths, brings the injected particles closer to the Fermi sea decomposing the quasiparticle peak into an extended distribution of particles that spreads over the whole energy range from the Fermi level up to the injection energy. The second part in the relaxation process that brings the resulting extended distribution of particles into a Fermi sea takes places along several micrometers of propagation. In fact, this last part of the relaxation process is presumably the same that is involved in the relaxation of a double step distribution function as investigated in Ref. [52] and in chapter 4.

The sub-micrometer length over which we observe that the quasiparticle peak decays challenges the interpretation of recent experiments of electron interferences with quasiparticles propagating in the outer edge channel of the integer quantum Hall effect at filling factor $\nu = 2$. On the one hand, in Ref. [47] a quantum dot was used to inject quasiparticles at a well defined energy into a Mach-Zehnder interferometer (MZI) that was subsequently used to measure the quantum coherence of the quasiparticle excitation. Surprisingly, for energies greater than $20\,\mu$eV, the visibility of the interferences was shown to remain almost constant instead of decreasing as expected. However, the separation between the emitter quantum dot and the input of the MZI was of $2.7\,\mu$m. Our measurements indicate that, over this distance, the emitted quasiparticle should have gone through an important energy relaxation before entering the interferometer. On the other hand, in Ref. [43] a Hong-Ou-Mandel (HOM) interferometry was implemented in order to measure the decoherence of single electron wave packets propagating in the edge channel. The single occupied wave packets were emitted, at an energy of $E_1 \sim 60\,\mu$eV above the Fermi sea, by ac-driven quantum dots which were previously demonstrated to work as tunable single particle sources [11]. Each quantum dot is located at one input of a QPC, such that the emitted quasiparticle collide when they synchronously arrive to the QPC, which is the interferometer. Although the distance between the quantum dots and the interferometer was about $3\,\mu$m, this experiment has shown that after this propagation length there is a collision of quasiparticles partially coherent. Our measurements suggest that very little of the quasiparticle peak should have remained after the propagation.

Additionally, for a propagation distance $L = 750$ nm and at low temperature $T \sim 20$ mK, we have observed signatures of a quasiparticle peak revival in several spectra measured using different electrostatic configuration in both quantum dot which allows to rules out artifacts caused by possible excited states or charge instabilities in nearby electrodes. Although the theoretical model proposed in Ref. [57] does not explain the exponential decay of the quasiparticle peak's amplitude, it predicts an oscillatory behavior which could partially explain our observations.

To conclude, we have presented robust experimental observations of the relaxation of a quasiparticle peak which are in agreement with the previous investigations of the energy relaxation in quantum Hall edge channels [52] but which strongly defy the current theoretical models that address this question [57, 56] challenging the usual

representation of excitations in the quantum Hall effect.

Chapter 7

Charge and Heat Current

In this chapter we investigate two important quantities that can be obtained from the distribution function $f_{r,c}$ that we measure after the propagation. In the first part we focus on the increase in the electrochemical potential $\Delta\mu$, which gives information about the current of particles injected into the edge channel. Then we consider the heat current $J(E)$ carried by the electron-hole excitations, which provides direct information about the exchange of energy in the system due to the relaxation process.

7.1 The electrochemical potential

The electrochemical potential μ of any distribution function $f(E)$ is obtained by measuring the area under the distribution from an energy E_A, at which $f(E)=1\ \forall E \leq E_A$, up to the energy E_B at which $f(E)=0\ \forall E \geq E_B$:

$$\mu = E_A + \int_{E_A}^{E_B} f(E)\, dE \tag{7.1}$$

In consequence when new particles are added to the system, occupying empty states, there is an increase in the electrochemical potential $\Delta\mu$. Thus, in our experiment, $\Delta\mu$ provides a measurements of the amount of injected particles that carry the current and the energy. Tunneling of particles into the edge channel or out of the edge channel along the propagation length can then be detected.

Injected $\Delta\mu_i$ Before Propagation

As usual, an electrochemical potential increase $\Delta\mu$ in a distribution of particles can be related to a voltage difference ΔV through: $\Delta\mu = e\Delta V$. Our experimental setup allows us to measure the injected current $I_1(E_1)$ as a function of the injection energy E_1 from the reflected signal on the first quantum dot at the ohmic contact $C3$ (Fig. 6.1). Thus the expected increase of the electrochemical potential on the outer edge channel where the current is injected can also be obtained as a function of the injection energy

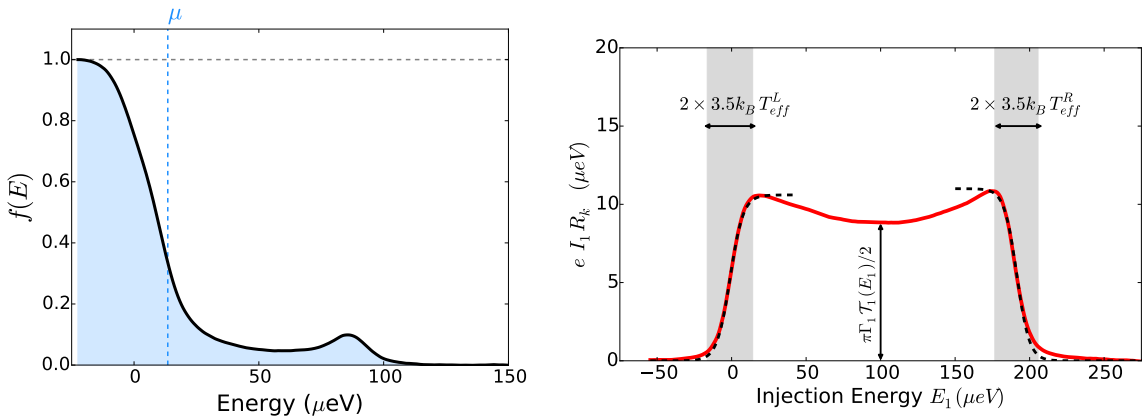

(a) **(b)**

Figure 7.1: **(a)** Illustration of an arbitrary distribution function $f(E)$ and its electrochemical potential μ (blue vertical dashed line) obtained using equation 7.1. **(b)** Electrochemical potential increase $\Delta\mu_i$ (red line) measured from the injected current I_1 as a function of the injection energy E_1. The left and right current flanks are respectively fitted with the functions $1 - F_L(E)$ and $F_R(E)$ (dash line), where $F_L(E)$ and $F_R(E)$ are Fermi function with effective electronic temperatures T^L_{eff} and T^R_{eff} respectively.

E_1:

$$\Delta\mu_i(E_1) = eI_1(E_1)R_k \tag{7.2}$$

From this measurement we can also characterize the resonant level that we use to inject the particles as shown in figure 7.1b. The two steps on the current are described by Fermi functions, as explained in section 4.2.6 (eq. 4.21), with effective temperatures T^L_{eff} and T^R_{eff}. A comparison with the electronic temperature T_{2DEG} of the 2DEG using the type of plot presented on figure 6.2b gives a mean value of the intrinsic width Γ_1 of the resonant level.

The amplitude of the current step is given by $\frac{e\pi}{2h}\Gamma_1\mathcal{T}_1$, from which we can obtain the energy dependent transmission $\mathcal{T}_1(E_1)$ that describe the smooth variations of the current along the step.

The incertitude on the determination of $\Delta\mu_i$ comes from the calibration of our experimental setup ($\sim 3\%$) and from the lever arm incertitude ($\leq 5\%$).

Measured $\Delta\mu_r$ After Propagation

The measured Fermi sea $F_r(E)$ at equilibrium (before the injection of particles) is characterized by an electrochemical potential μ_0 which is close to the Fermi level E_F that was chosen as the zero energy point in the energy scale. In general we measure that $\mu_0 \sim 2\mu eV > E_F$ which is just a constant offset generated as a consequence of the non-ideal detection.

The increase in the electrochemical potential $\Delta\mu_r(E_1)$ measured after the propagation is obtained as the difference between the electrochemical potential μ_r, measured

on the detected distribution $f_{r,c}$, and the one of the Fermi sea:

$$\Delta\mu_r(E_1) = \mu_r(E_1) - \mu_0 \tag{7.3}$$

The errors in the measurement of $\Delta\mu_r$ come from the incertitude on the lever arm ($\leq 5\%$) and from the incertitude on the normalization point of the distribution functions given by the variation of $\mathcal{T}_2(E_2)$ which can go from 10% up to 20% in some cases on which there are signatures of the Fermi edge singularity which leads to a strong increase of $\mathcal{T}_2(E)$ near the Fermi level [121, 120]. In general we perform the spectroscopy when this effect is not pronounced.

Additionally, it can be shown that the measured $\Delta\mu_r$ is independent of the intrinsic width of the resonance in the detector. A non-ideal detection only adds the same small offset for all the measured μ_r which is also accounted for μ_0.

Comparison: $\Delta\mu_i$ vs $\Delta\mu_r$

The figure 7.1 shows a comparison between the ***expected*** electrochemical potential increase $\Delta\mu_i$ and the electrochemical potential increase $\Delta\mu_r$ that is ***measured*** after the propagation along a distance $L = 0.48\,\mu m$ and $L = 2.17\,\mu m$.

Within experimental error we observe an agreement between both quantities which indicates that no particles are tunneling out of the edge channel during the relaxation process within the propagation distances that were investigated. Although sometimes there is a small difference, being $\Delta\mu_i < \Delta\mu_r$, it is unlikely that particles tunnel from the incompressible bulk or from the co-propagating edge channel whose electrochemical potential is at the equilibrium value $\mu_0 < \mu_r$.

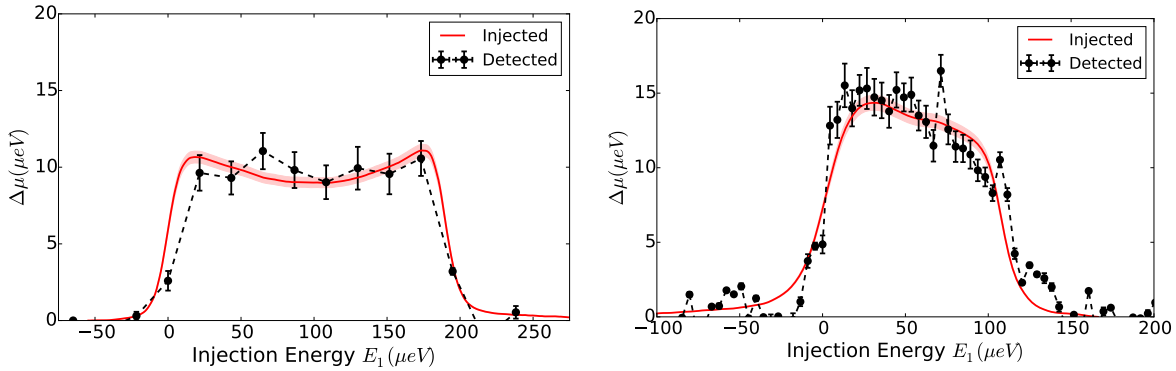

(a) **(b)**

Figure 7.2: Comparison between the electrochemical potential increase $\Delta\mu_i$ (red line) at the injection point, obtained from the measured injected current I_1, and the electrochemical potential increase $\Delta\mu_r$ (black symbols) measured after the propagation, obtained from the detected distribution functions, as a function of the injection energy E_1. The area shaded in red represents the incertitude in the measurement of $\Delta\mu_i$. Two comparisons are shown, for a measurement performed after a propagation distance $L = 0.48\mu$m (**a**) and for $L = 0.48\mu$m (**b**), which indicates that the current of particles is preserved on the edge channel.

7.2 The Heat Current

The heat current J is the energy carried by the electron and hole excitations existing on the distribution function, which can be calculated from the integration:

$$J = \frac{1}{h} \int_{E_A}^{E_B} (E - \mu) \left[f(E, \mu) - \Theta(\mu - E) \right] dE \tag{7.4}$$

Where E_A and E_B are defined as for the electrochemical potential (Eq. 7.1) and $\Theta(x)$ is the step function.

A Fermi sea with electrochemical potential μ_0 at zero temperature carries no heat current simply because there are no electron or hole excitations. Notice that the concept of ***electron excitation*** and ***hole excitation*** are defined as deviations from this zero temperature ground state but that the carriers are always electron particles. In this context, a *hole excitation* means that there is an empty state below the electrochemical potential μ and an *electron excitation* means that there is an occupied state above μ.

Furthermore the amount of hole excitations $\Delta\mu_h$ and electron excitations $\Delta\mu_e$ contained in any distribution function, which are illustrated as an example on figure 7.3a, can be measured by:

$$\Delta\mu_h = \int_{E_A}^{\mu} \left[1 - f(E) \right] dE \tag{7.5}$$

$$\Delta\mu_e = \int_{\mu}^{E_B} f(E)\, dE \tag{7.6}$$

This is similar to the way in which the electrochemical potential μ is used to measure the number of particles by counting the occupied states. The number of electron and hole excitation is not a conserved quantity as it is the number of electron particles, thus they can be created or destroyed as the energy of the system changes.

As explained in section 5.4, a Fermi distribution at temperature T_0 carries the equilibrium heat current $J_0 = \frac{\pi^2}{6h}(k_b T_0)^2$ due to the thermal excitations. When additional hole and electron excitations are created, an excess heat current ΔJ can be defined as: $\Delta J = J - J_0$. The measurement of the excess heat current while relaxation takes place on the edge channel provides a view of the energy flow in the system between the interacting parts, including the environment.

Injected Before Propagation

When new particles are added to the system, changing the electrochemical potential from μ_0 to μ, the additional hole excitations and electron excitations that are created have different contribution to the excess heat current depending at which energy the new particles have been injected. When a quasiparticle peak is injected on the edge channel, the excess heat current ΔJ_i can be analytically calculated in terms of the

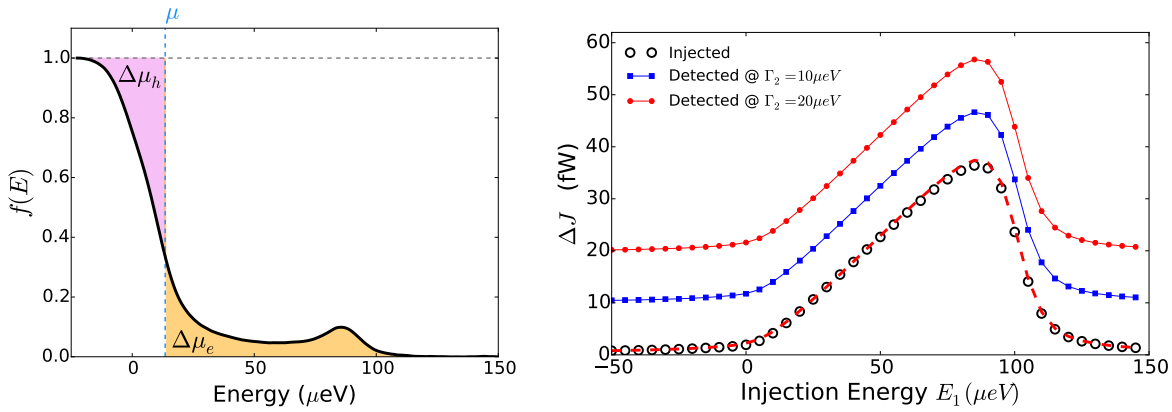

(a) **(b)**

Figure 7.3: **(a)** Illustration of the *hole excitations* $\Delta\mu_h$ and the *electron excitations* $\Delta\mu_e$ that exists in an arbitrary distribution function $f(E)$. **(b)** Numerical calculations of the excess heat current $\Delta J_i = J_i(E_1) - J_0$ carried by a distribution function $f(E)$ using equation 7.4. Empty circles correspond to the calculation from a distribution function that consists of a Fermi sea and a quasiparticle peak injected at the injection energy E_1: $f_i(E) = F(E) + L_1(E, E_1)$. Blue squares (red circles) correspond to the calculation from the distribution function $f_{i,c}(E)$, which is the distribution function $f_i(E)$ measured with a non ideal detector with linewidth $\Gamma_2 = 10\mu eV$ ($\Gamma_2 = 20\mu eV$). The red dashed line is the same data plotted in the red circles but shifted down by a constant offset showing that a non ideal detection only adds and offset to the measure excess heat current.

parameters that characterize the injected distribution such as the injection energy E_1 around which the quasiparticle peak is centered, its amplitude $\mathcal{T}_1$ and its width Γ_1,

$$\Delta J_i(E_1) = (E_1 - \mu)\frac{\pi}{2}\Gamma_1\mathcal{T}_1 + \frac{1}{2}\left(\frac{\pi}{2}\Gamma_1\mathcal{T}_1\right)^2 \tag{7.7}$$

Since the electrochemical potential increase in this case is $\Delta\mu = \mu - \mu_0 = \frac{\pi}{2}\Gamma_1\mathcal{T}_1$, which accounts simply for the area under the quasiparticle peak, we can express the the excess heat current as follow:

$$\Delta J_i(E_1) = (E_1 - \mu)\Delta\mu + \frac{1}{2}(\Delta\mu)^2 \tag{7.8}$$

It can be demonstrated from the definition (Eq. 7.4) that actually this is a very general way to express the excess heat current generated by the injection of new particles to the system, which is independent of the specific shape of the quasiparticle peak and of the low energy excitations on the distribution function (See Appendix A). In a general case when new particles are injected in the system with a distribution $P_1(E)$ the increase in the electrochemical potential is given by $\Delta\mu = \int P_1(E)dE$ and the energy E_1 in equation 7.8 is simply the characteristic energy of the states on which the particles have been injected :

$$E_1 = \frac{\int EP_1(E)dE}{\int P_1(E)dE} \tag{7.9}$$

When all the particles are injected at an energy above μ, the first term on Eq. 7.8

describes the contribution ΔJ_{qp} associated to the excitations injected as a quasiparticle peak $\Delta\mu_q p = \Delta\mu$ centered around the characteristic energy E_1. Additionally, the injection of new particles to the system creates new electron-hole excitations $\Delta\mu_{eh} = \Delta\mu$ located near the electrochemical potential μ, which therefore have a characteristic energy of $\mu \pm \Delta\mu/2$ that is independent of the injection energy E_1 of the quasiparticle peak. In consequence, the second term on Eq. 7.8 describes the contribution ΔJ_{eh} associated to these low energy excitations. It must be stressed that it is due to the quasiparticle peak contribution that the total excess heat current $\Delta J_i(E_1) = \Delta J_{qp}(E_1) + \Delta J_{eh}$ increases linearly with the injection energy E_1.

$$\Delta J_{qp}(E_1) = (E_1 - \mu)\Delta\mu_{qp} \tag{7.10}$$

$$\Delta J_{eh}(E_1) = \frac{1}{2}\left(\Delta\mu_{eh}\right)^2 \tag{7.11}$$

Notice that the equation 7.8 allows to use the measured increase in the electrochemical potential $\Delta\mu_r$ to compute the excess energy that has been injected without relying on the estimations of the parameters that characterizes the quasiparticle peak $\{\Gamma_1, \mathcal{T}_1\}$. By doing that we actually estimate the injected excess heat current as if all the detected particles had been injected as a peak around the energy E_1. In consequence, rather than using equation 7.7 this is a more accurate way of calculating the injected excess heat current that in fact also takes into account the small experimental shifts, coming from charge instabilities, which can occur during the measurements of a distribution function and which give rise to the random fluctuations on the measured $\Delta\mu_r$.

The error on the estimation of ΔJ_i comes from the errors in $\Delta\mu_r$ $(10\% - 20\%)$ and from the lever arm incertitude $(\leq 5\%)$.

Measured After Propagation

The total excess heat current $J_r(E_1)$ when particles were injected at energy E_1 is obtained from the detected distribution f_r, after the propagation, using the integral formula (Eq. 7.4). Then, the excess heat current ΔJ_r is obtained by subtracting the total excess current $J_{r,0}$ calculated in the same way from the measured Fermi sea when no particle were injected:

$$\Delta J_r(E_1) = J_r(E_1) - J_{r,0} \tag{7.12}$$

The incertitude on these measurement arises from the calibration of the energy axis which is set by the lever arm $(\sim 3\%)$ and from the incertitude on the normalization point of the distribution functions which can go from 10% up to 20% in a similar way as for the electrochemical potential.

Importantly, the excess heat current measured in this way does not depends on the width Γ_2 of the detector. We numerically show on picture 7.3b that the non ideal

detection only adds the same constant offset to J_r and $J_{r,0}$. Therefore, although the detector is not ideal, we have access to the exact heat current carried in the edge channel after the propagation.

Heat Current Comparison: ΔJ_i vs ΔJ_r

On the figure 7.4a we show a comparison of the ***injected*** excess heat current $\Delta J_i(E_1)$ and the ***detected*** excess heat current $\Delta J_r(E_1)$ measured after the propagation as a function of the injection energy E_1 for a propagation length $L = 0.48\,\mu m$. The figure 7.4b shows the same comparison for a larger propagation length $L = 0.75\,\mu m$.

Remarkably, we observe a very large discrepancy between the injected heat current and what we have detected, which is beyond the incertitude of both measurements. We can see that, at high injection energy E_1, the detected heat current is much smaller than what was expected, indicating that the energy in not conserved on the edge channel. As it was clearly demonstrated by H. le Sueur *et al.* [52], the interaction with the co-propagating edge channel induces an energy exchange between the two edge states, which is expected to be, in part, responsible of the observed discrepancy on Figure 7.4a and 7.4b.

An alternative way to see this *non conservation of the energy on the edge channel* is shown on the figures 7.4c and 7.4d where we have plot the ratio between the excess heat current ΔJ_r measured after propagation and the injected amount ΔJ_i. If the relaxation mechanism distributes the energy only between the charged excitations within the edge channel, then we expect the ratio $\Delta J_r(E_1)/\Delta J_i(E_1)$ to be constant and equal to one. On the contrary, we observe that the proportion of remaining energy on the edge channel is smaller as we increase the injection energy E_1 of the quasiparticle peak.

On chapter 6 we demonstrated that the injected particles relaxes exponentially faster as the injection energy is increased, which is seen from the amplitude of the residual quasiparticle peak. In addition, the measurements of the heat current indicates that when particles relaxes from a state of higher energy, the process takes more energy out of the edge state. Therefore, ***the faster the relaxation process happens, the more energy is leaking out from the edge channel***.

As we mentioned, part of the energy must have been transferred toward the co-propagating edge channel due to their mutual interaction. However, the theoretical models that describes this interacting system, within the framework of chiral fermions [54] or within the framework of the Luttinger liquid theory which suggest the development of plasmons excitations [58, 55], predict that the interaction leads to an energy equipartition between the edge channels. In consequence there is a lower bound ΔJ_r^{min} for the remaining heat current on the edge channel which is expected to be achieved at full relaxation. This lower bound is plotted in blue dashed line for the measurements shown on the Fig. 7.4.

It is clearly seen that the remaining excess heat current measured after the prop-

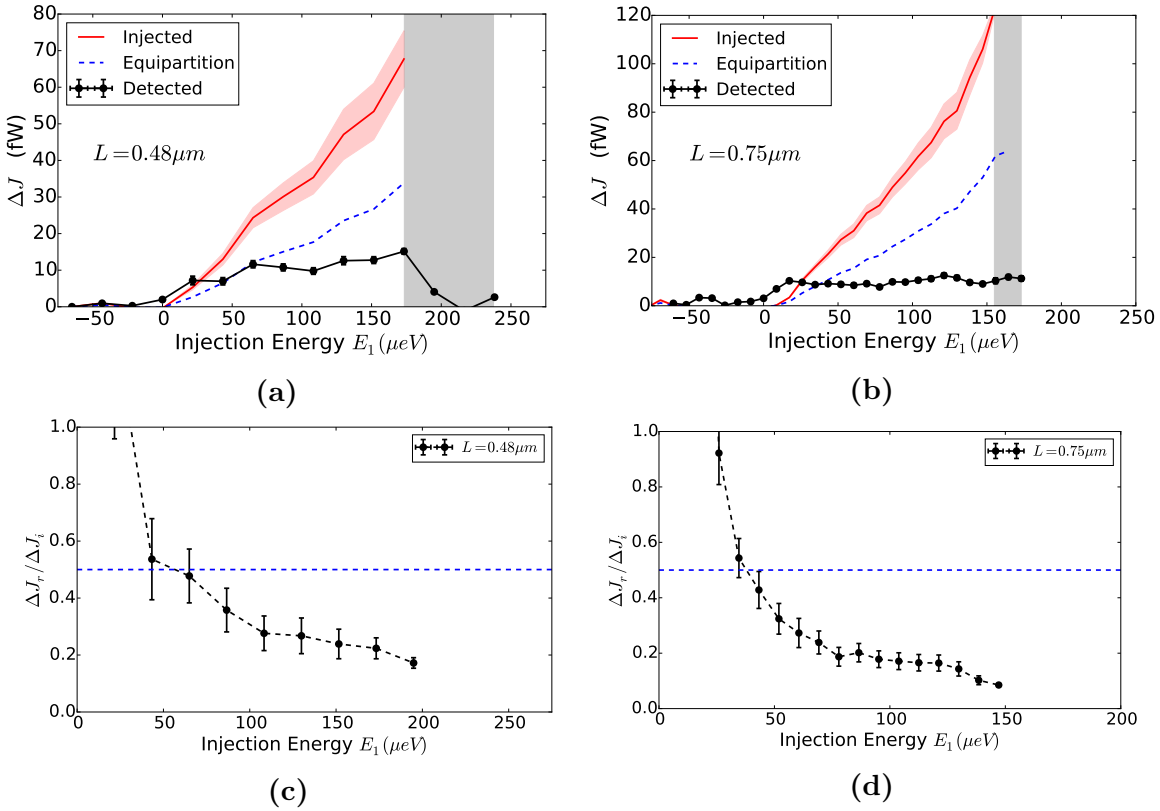

Figure 7.4: **Top:** Comparison between the excess heat current ΔJ_i that was injected (red line) on the edge channel and the excess heat current ΔJ_r that was measured after a propagation (black symbols). The area shaded in grey correspond to the final part of the spectroscopy, where the injection energy E_1 is reaching its maximum value and the discrete level in the first quantum dots is going out of the bias windows. This implies that beyond that energy the number of injected particles starts to drop towards zero and therefore the excess heat current decreases too. **Bottom:** Fraction of the excess heat current $\Delta J_r/\Delta J_i$ that remains on the edge channel after the propagation as a function of the injection energy E_1. The two panels to the left (**a** and **c**) correspond to a measurement taken after a propagation length $L = 0.48\mu$m, while the two panels to the right (**b** and **d**) correspond to a measurement taken after a propagation length $L = 0.75\mu$m. In the four cases the blue dashed line represent the lower bound ΔJ_r^{min} that is predicted by all the models as a consequence of the energy equipartition between the two co-propagating edge channels.

agation goes well below the lower bound. We observe that there is up to 70% less remaining energy than ΔJ_r^{min}. During the experiment described in Ref. [52] a missing energy was also observed: The detected excess heat current was about 25% less than the lower bound and no particular dependence on the bias voltage on the QPC was pointed out. Here we observe that the energy leaking the system of the two interacting edge channels is not constant but instead it increases with the injection energy E_1 of the quasiparticle peak. This suggest that ***the mechanism that induces the relaxation of the injected quasiparticles is not exclusively due to the interaction between the two edge channels***.

Since our experimental scheme only relies on the detection of charged particles, the increasing energy leak of the whole system that we observe could suggest that there are additional degrees of freedom which do not directly participate in the charge transport

but which can be excited during the relaxation mechanism as initially suggested in Ref. [52].

It is important to notice that the development of the slow (neutral) and the fast (charged) modes that arises from the interaction between the two edge channel can not explain the missing energy. This mechanism is exactly what sets the lower bound ΔJ_r^{min} within the Luttinger liquid theory approach [58].

Additional neutral internal degrees of freedom in each edge channel are expected to arise due to the edge reconstruction as described in section 4.3.1. Although in our experiment we can not conclusively determine if this mechanism also participates on the relaxation, this scenario could be *a priori* compatible with such a large energy leak since there are many neutral internal excitations that could capture the missing energy.

As pointed out in Ref [58] the integral equation that we use to compute the heat current (Eq. 7.4) only accounts for the single-particle energy of free electrons. Moreover it was shown that this equation does not provides the actual total heat flux if the plasmon modes, considered within the Luttinger liquid theory, have a non linear dispersion. Therefore, the discrepancy was proposed to explain the missing energy observed on Ref. [52] and it was suggested that it could be found experimentally by investigating its bias dependence and the plasmon spectrum. However, they also showed that a non linear spectrum of charge plasmons arising from the screened Coulomb interaction, the same that gives rise to the edge reconstruction [100], is still a small effect and could not account for the 25 % of energy loss. Other possible dispersion spectra still remain to be theoretically investigated.

For the relaxation of the double step distribution (Chapter 5) P. Degiovanni *et al.* [55] also modeled the inter-edge channel interaction within the plasmon scattering formalism, neglecting the additional modes associated to the internal structure of the edge channel [100]. Within this approach it was possible to reproduce the non linear dependence seen between the measured excess heat current J_{exc}^{QPC} and the bias voltage on the QPC by assuming a drift velocity $v_d \approx 10^5$ m/s. However it was necessary to assume *ad hoc* that a constant 25 % of the heat current is transferred to other degrees of freedom not captured by the model.

Finally, A. M. Lunde *et al.* [54], inspired by the weak relaxation seen at submicrometer distances on Ref. [52, 51], proposed to describe the interaction between coupled edge states in a *perturbative* approach. This model uses the scattering approach to describe the interaction in terms of a two-body collision within the chiral fermion theory including non-momentum conservation scattering processes. In this work the 25 % missing energy was quantitatively explained by considering that equipartition occurs among three relaxation channels instead of two. They suggested that the additional relaxation channel could be related to bulk excitations which can be coupled via long range Coulomb interaction to both edge channels. However the higher 70 % missing energy that we observe seems not compatible with this scenario and it disproves

the central hypothesis that the interactions can be taken into account in a perturbative approach.

7.3 Heat Current vs Electrochemical Potential

As seen before, the measured heat current does not follows the expected behavior as a function of the injection energy E_1 given by equation 7.8. However we observe that there is a particular relation between the ***measured*** excess heat current ΔJ_r and the ***measured*** increase in the electrochemical potential $\Delta\mu_r$.

The non linear curve of the measured heat current ΔJ_r (black points in Fig. 7.4a and 7.4b) can be reproduced with an empiric formula with only two free dimensionless parameters, γ_{qp} and γ_{eh}, following:

$$\Delta J_i(E_1) = \gamma_{qp}(E_1 - \mu_r)\Delta\mu_r + \gamma_{eh}\frac{1}{2}\left(\Delta\mu_r\right)^2 \tag{7.13}$$

$$\Delta J_i(E_1) = \gamma_{qp}\Delta J_{qp}^{(in)}(E_1) + \gamma_{eh}\Delta J_{eh}^{(in)}$$

Importantly, notice that this establishes a relation between two measured quantities from the same distribution functions $f_{r,c}$ detected after the propagation at different injection energies E_1.

The figure 7.5 shows the measured increase in the electrochemical potential $\Delta\mu_r(E_1)$ as a function of the injection energy E_1 in the left panels, while in the right panels it displays the measured excess heat current $\Delta J_r(E_1)$ (black symbols) and the fit (red line) obtained using the equation 7.13, both as a function of the injection energy E_1. From top to bottom the plots correspond to data measured at increasing propagation length $L = \{0.48, 0.75, 2.17\}\mu m$ which shows a variety of cases demonstrating that the measurements can be well described by the empiric formula.

Although the measured excess heat current ΔJ_r does not follows the expected linear dependence with the injection energy E_1, the fairly good description provided by the empiric formula indicates that the relaxation mechanism preserves the dependence with the number of particles. This can be seen in detail by noticing that the same smooth variations measured in $\Delta\mu_r(E_1)$ are also found in the excess heat current $\Delta J_r(E_1)$, namely: when $\Delta\mu_r$ increases (decreases), ΔJ_r increases (decreases). In other terms the relaxation mechanism is independent of the number of injected particles which is proportional to $\mathcal{T}_1 \times \Gamma_1$.

The empiric equation 7.13 allows to quantitatively characterize the energy leak in terms of the two coefficients γ_{qp} and γ_{eh}. Importantly, the two parameters are unique to describe the whole energy range for a given configuration of the experiment: they do not depend on the injection energy E_1 of the quasiparticle peak. Therefore if we obtain both parameters by measuring the residual heat current within an initial energy

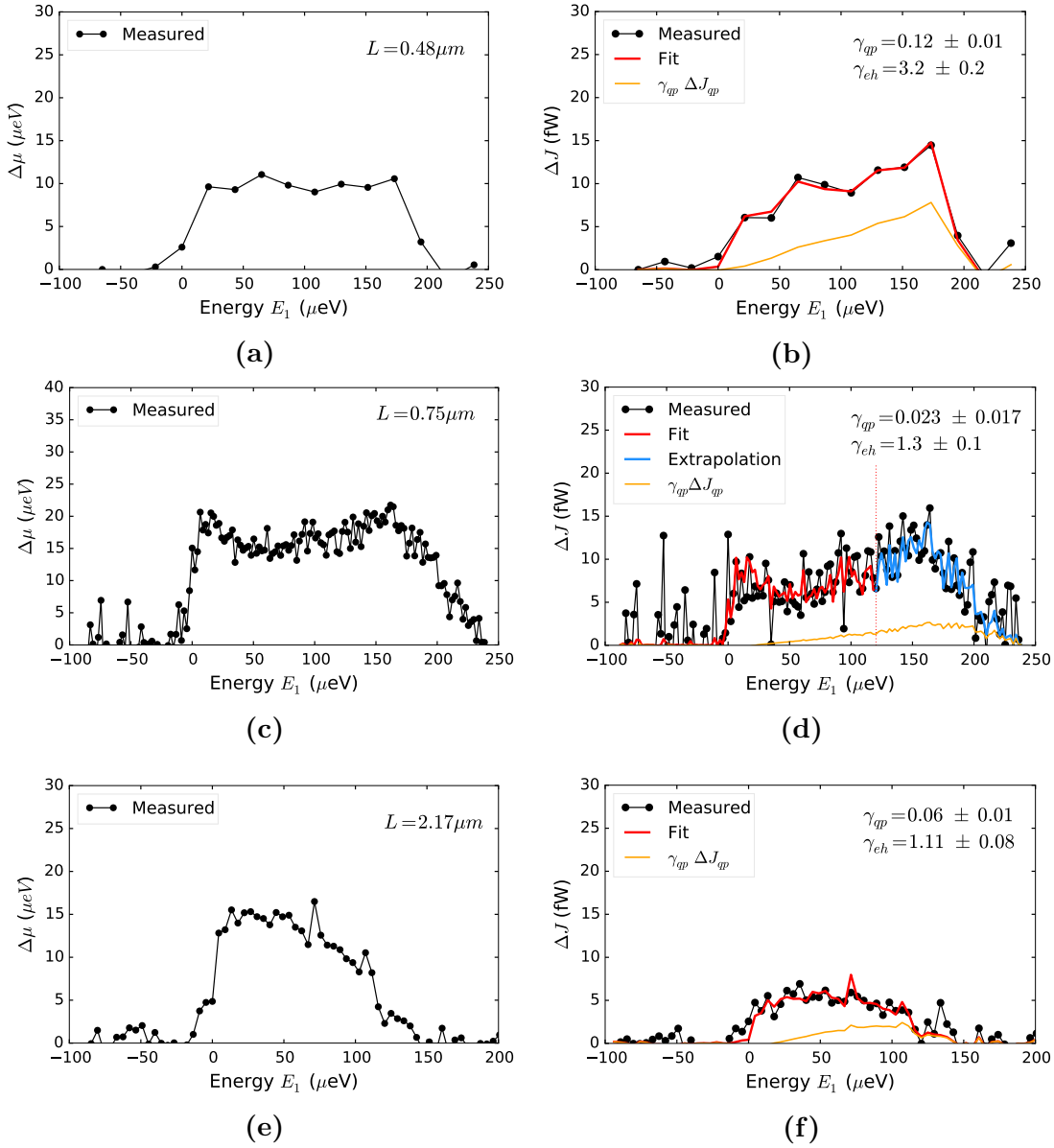

Figure 7.5: Left: Electrochemical potential increase $\Delta\mu_r$ measured after the propagation as a function of the injection energy E_1. **Right:** Excess heat current ΔJ_r (black symbols) measured after the propagation from the same spectrum from which the electrochemical potential increase $\Delta\mu_r$, plotted in the corresponding panel to the left, was obtained. The red line corresponds to a fit using the empiric formula 7.13 with the coefficients γ_{qp} and γ_{eh} shown in the upper right corner. The orange line corresponds to the quasiparticle peak contribution $\gamma_{qp}\Delta J_{qp}^{(in)}(E_1)$ using the coefficient γ_{qp} obtained from the fit. From top to bottom, each pair of panels is a measurement taken for a propagation length $L = 0.48\mu$m (**a** and **b**), $L = 0.75\mu$m (**c** and **d**) and $L = 2.17\mu$m (**e** and **f**)

range, then we can predict how much energy will be lost when a quasiparticle peak with different amplitude $\mathcal{T}_1$ and width Γ_1 is injected at a different energy E_1' outside of the initial known range. This is shown in the figure 7.5d where the parameters γ_{qp} and γ_{eh} have been obtained by fitting the data at energies $E_1 < 120\mu eV$ which is indicated by the vertical dotted line. Using these parameter we can then predict which will be remaining heat current when the quasiparticle peak is injected at higher energies

$120\mu eV < E_1 < 240\mu eV$ even when the amplitude of the quasiparticles peak changes non monotonously. The predicted curve is plotted as light blue line and it describes well by the measured points in this high energy range with the parameter obtained in the low energy range.

In figure 7.6 we show the values of the two coefficients γ_{qp} and γ_{eh} measured from different spectra obtained in different conditions as a function of the transmission $\mathcal{T}_1$ and the intrinsic width Γ_1 of the resonance in the first quantum dot which was implemented to inject the quasiparticle peak. As expected, no clear dependence is seen of either of the fitting parameters with $\mathcal{T}_1$ or Γ_1.

However we can see that for the ensemble of data these parameters have a characteristic mean value $\gamma_{qp} = (0.065 \pm 0.040)$ and $\gamma_{eh} = (1.5 \pm 0.6)$ which characterizes the dispersion of points. Since $\gamma_{eh} \sim 1$, it indicates that the electron-hole excitation contribution to the heat current (Eq. 7.11) remains almost unchanged after the relaxation. This is consistent with the fact that these excitations, created close to the electrochemical potential μ, are out of equilibrium quasiparticles near the Fermi sea, and then it is expected that they will equilibrate on longer distances (between ~ 1 to $10\mu m$ [52]). Additionally, since these excitations are close to the electrochemical potential, their characteristic energy is usually smaller than the characteristic energy E_1 of the quasiparticle peak, thus their contribution to the total injected heat current is actually small in comparison with the contribution of the quasiparticle peak as can be seen from equation 7.8 for $E_1 \gg \mu$. In consequence, most of the injected heat current, which was injected as a quasiparticle peak, is lost from the edge channel after the propagation since $\gamma_{qp} \ll \gamma_{eh}$.

Therefore, we can say that while electron particles relaxes to occupy the empty states near the Fermi level, they release their energy into the system but most of it leaks out of the edge channel instead of being integrally transferred towards the Fermi sea increasing its temperature.

7.4 The heat current vs Distance

Using equation 7.4 we can compute and compare the heat current from the detected distribution function f_r even at large distances when there is no well defined quasiparticle peak. The same applies to the injected heat current which is calculated using the equation 7.8 from the measured $\Delta\mu_r$.

The figure 7.7a shows the ratio between the measured excess heat current ΔJ_r and the injected excess heat current ΔJ_i obtained from multiple spectra measured at different propagation lengths L. We observe a well separated trend between the data of spectra measured at $L = 0.48\mu m$ and at $L = 0.75\mu m$. At $L = 2.17\mu$m and beyond the ratio $\Delta J_r/\Delta J_i$ does not change much and seems to have reached a baseline that describes a stationary behavior which depends on the injection energy E_1. This is

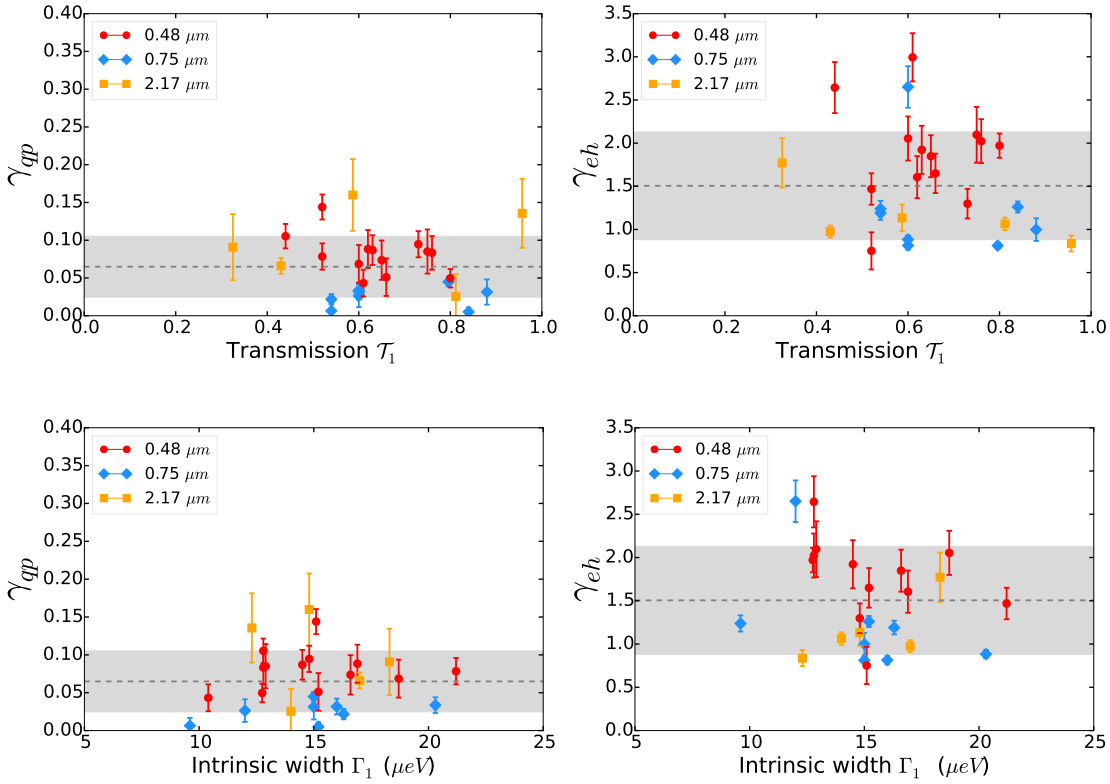

Figure 7.6: The parameters γ_{qp} (left panels) and γ_{eh} (right panels), obtained from the fit of the measured excess heat current Δ_r using the empiric equation 7.13 for the ensemble of spectra measured under different configuration of the experiment, plotted as a function of the transmission $\mathcal{T}_1$ (upper panels) or as a function of the intrinsic width Γ_1 (lower panels) of the resonant level in the first quantum dot. The horizontal dashed line centered in the area shaded in grey, represents the mean value of the parameter and its standard deviation obtained from the ensemble of points in each plot.

coincident with the fact that the process on which the quasiparticle peak structure vanishes happens in sub-micrometer distances.

Though only at a qualitative level, this can also be seen in the evolution of the γ_{eh} coefficient obtained for each spectrum as a function of the propagation distance which is shown in the figure 7.7b. The γ_{eh} coefficient, which represents the major contribution to the measured excess heat current ΔJ_r, follows a more convergent evolution as a function of the distance in comparison with the behavior of the γ_{qp} coefficient.

7.5 The heat current vs Temperature

In section 6.6 we have seen that, at the short propagation distance ($L = 0.48\mu$m), the amplitude of the quasiparticle peak decays roughly two times faster when the electronic temperature is increased by 150 mK. However in this section we show that, for the same set of spectra, ***the temperature has no effect on the amount of heat current that leaks out of the edge channel***.

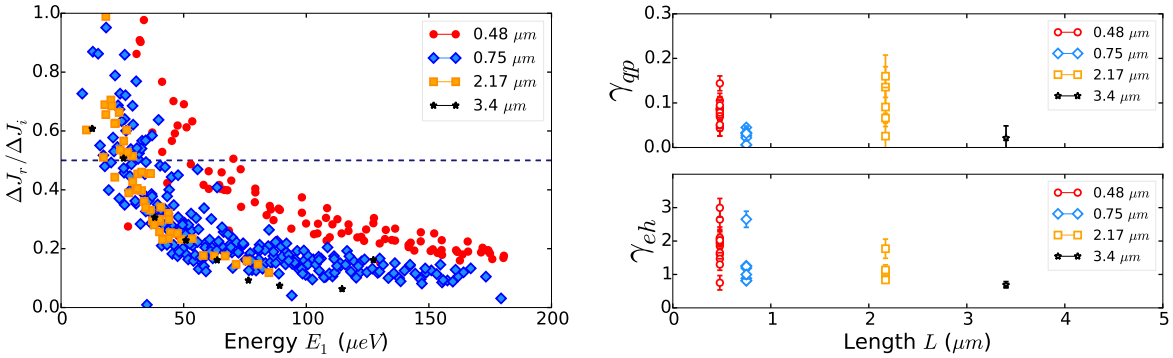

(a) (b)

Figure 7.7: **(a)** Fraction of the excess heat current $\Delta J_r/\Delta J_i$ that remains on the edge channel after the propagation as a function of the injection energy E_1 measured in several spectra taken at different propagation distances: $L = 0.48\mu$m (red circles), $L = 2.17\mu$m (blue diamonds), $L = 0.48\mu$m (orange squares) and $L = 3.4\mu$m (black stars). **(b)** The parameters γ_{qp} (top) and γ_{eh} (bottom), obtained from the fit of the measured excess heat current Δ_r using the empiric equation 7.13 for the ensemble of spectra measured under different configuration of the experiment, plotted as a function of propagation length L.

First, the figure 7.8a shows that although the electronic temperature increases from 23 mK up to 170 mK, the amount of injected particles does not change which can be seen from the unchanged increase in the electrochemical potential $\Delta\mu_r$ that is measured after the propagation. This confirms that the product of the transmission $\mathcal{T}_1$ and the intrinsic width Γ_1 of the resonant level in the first quantum dot does not depend on the electronic temperature as predicted by the simple model of the electrostatic confinement on the quantum dot presented in section 4.2.

The Figure 7.8b shows the ratio $\Delta J_r/\Delta J_i$ between the measured and the injected excess heat current. As it can be seen, all the curves follow the same behavior and no clear dependence on the temperature is observed within the experimental accuracy. Although each point is obtained after performing a statistical average of several measurements under the same conditions, the dispersion of the points is limited by the electrostatic stability of the sample.

Therefore we can conclude from these measurements that an increase in the electronic temperature leads to a stronger relaxation of the quasiparticle peak; however it does not affect the final amount of energy that is lost from the edge channel in the process.

7.6 Conclusions

First, we have shown that a comparison of the increase in the electrochemical potential $\Delta\mu_i$ measured at the injection point and $\Delta\mu_r$ measured after the propagation demonstrate that there is no particle exchange between the edge channel while the relaxation takes place. Thus, this measurement verifies that the particle current is conserved on

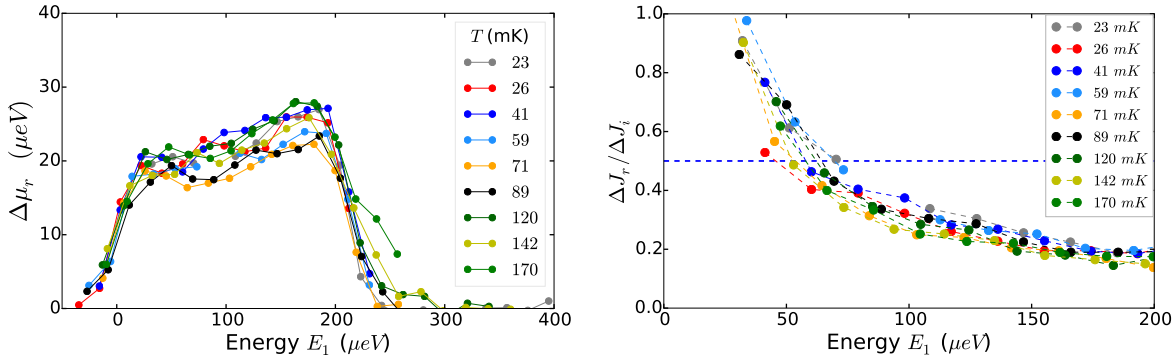

(a) **(b)**

Figure 7.8: **(a)** Electrochemical potential increase $\Delta\mu_r$ measured after the propagation from an ensemble of spectra measured at increasing temperatures. (b)Fraction of the excess heat current $\Delta J_r/\Delta J_i$ that remains on the edge channel after the propagation as a function of the injection energy E_1 measured on the spectrum taken at increasing temperature.

the edge channel as expected.

Second, we have shown that the measurements of the heat current in the edge channel indicate that there is a very large energy leak which is not in agreement with any of the current theoretical models that describes the interaction in the integer quantum Hall regime at filling factor $\nu = 2$. Moreover, this energy leak was consistently observed in all the spectra of the relaxation of the quasiparticle peak suggesting that it is a robust observation and a characteristic of this regime. In addition, such a large energy leak was not observed when we investigated the relaxation of a double step distribution function on chapter 5, on which the hole excitations and electrons excitations not only are low energy excitation but also they contribute symmetrically to the injected excess heat current. When the relaxation of the double step distribution function was measured we observed a small energy leak, in agreement with the results reported in Ref. [52]. Our measurements in both regimes absolutely rule out possible experimental artifacts that could lead to an *apparent* energy leak.

While a constant 25% of energy leak was observed on the relaxation of the double step distribution, here we report that the relaxation of energy resolved excitations leads to an energy leak that strongly depends on the injection energy E_1 of the quasiparticle peak. In fact, the fraction of remaining energy, $\Delta J_r/\Delta J_i$, roughly follows a $1/E_1$ dependence.

Furthermore, a detailed analysis of the relation between the charge current $\Delta\mu_r$ and the remaining heat current ΔJ_r shows that actually the remaining energy corresponds to the energy injected as low energy electron-hole excitations created near μ.

We hope that these unexpected an intriguing observations can provide new useful information to finally identity the complete relaxation mechanism that could explain the missing energy paradox and the role of the interactions in the decoherence in quantum Hall edge channel at filling factor $\nu = 2$.

Chapter 8

Decoupling the Edge States

In this chapter we show that the relaxation of the quasiparticle peak can be weakened by decoupling the two co-propagating edge channels with the help of a depletion gate. We show that when the edge channels are decoupled, the probability for the quasiparticle peak to survive can increase up to 5 times. Furthermore, in this regime the energy leaking out of the system is also strongly reduced. This experiment provides a clear demonstration of the role of the interaction between co-propagating edge channels in the relaxation of quasiparticles emitted in a narow energy band above the Fermi sea.

8.1 The Suppression of the Relaxation

We investigate the effects of decoupling the co-propagating edge states on two samples, ***D31*** and ***E33***, where the short propagation path was designed to have a length $L = 0.75\,\mu m$ and $L = 0.48\,\mu m$ respectively. In chapter 6 we have demonstrated that for these propagation distances it was possible to detect a residual quasiparticle peak that survives the relaxation. Although it was clearly observed in the spectroscopy for a propagation length $L = 0.48\mu m$, we showed that it was hardly detectable when the distance is beyond $L = 0.75\mu m$. We found that a substantial part of the relaxation of the quasiparticle peak takes place in the sub-micrometer scale. In this section we show how the relaxation can be diminished, leading to a better preservation of the quasiparticle peak even at $L = 0.75\mu m$, by decoupling the co-propagating edge channels.

8.1.1 Reducing the Relaxation at $L = 0.75\mu m$

The sample design (Fig.6.1) allows to change, in situ, the propagation distance on the same device by polarizing a surface metallic gate: the electrode ***A2***. When it is fully polarized at *pinch-off* ($V_{A2} \sim -0.5V$) it forces the edge channels to follow a longer path which is designed to be three times larger than the short direct path between the two quantum dots. Conversely, the edge states propagate freely along the short path

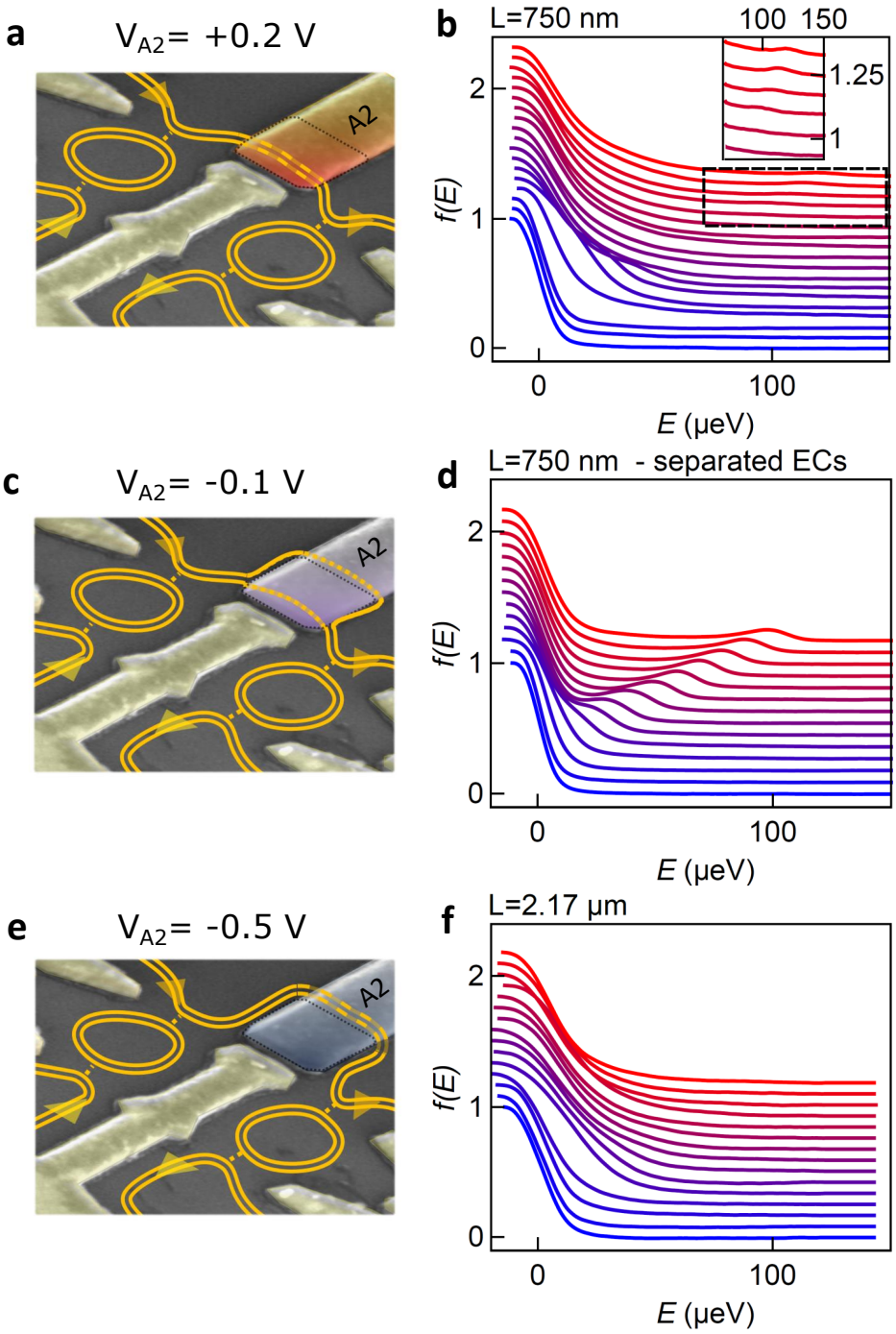

Figure 8.1: **a**, **c**, **e**: False-colour scanning electron micrographs of a typical sample, depicting the trajectories of the edge channels for $V_{A2} = 0.2$ V (**a**, ***A2*** gate highlighted in orange), $V_{A2} = -0.1$ V (**c**, ***A2*** gate highlighted in purple), and $V_{A2} = -0.5$ V (**e**, ***A2*** gate highlighted in blue). In **a**, the two edge channels co-propagate along a $L \approx 750$ nm short path. In **c**, the two edge channels are spatially separated (orange dotted lines) as they flow below the ***A2*** gate. In **e**, the two edge channels co-propagate along a $L \approx 2.17\mu$m long path. **b**, **d**, **f**: Measured $f(E)$ for the configurations depicted in resp. **a**, **c**, and **e**. Each curve, offset for clarity, corresponds to an injection energy increment $\delta E_1 \approx 9\mu eV$, from $E_1 \approx -26\mu eV$ (blue) to $E_1 \approx 122\mu eV$ (red, **b**) and $E_1 \approx 98\mu eV$ (red, **d** and **f**). The inset in **b** is a zoom on the region delimited by the black dashed square.

when the electrode ***A2*** is not negatively polarized ($V_{A2} \geq 0V$). In this way, it was possible to increase the propagation distance in sample ***D31*** from $L = 0.75\,\mu m$ up to $L = 2.17\,\mu m$. However when the electrode ***A2*** is polarized at an intermediate voltage, $-0.5V \leq V_{A2} \leq 0.0V$, we can access to a different regime on which the coupling between the two co-propagating edge states can be tuned.

A schematic representation of these three distinct regimes is shown in the figure 8.1, together with the distribution functions measured after the propagation in the outer edge channel, where a quasiparticle peak was injected as in the previous chapters.

The figures 8.1(a)-(b) correspond to the spectroscopy of the relaxation of the quasiparticle peak after the short propagation distance $L = 0.75\,\mu m$. Similar to the discussion presented in section 6.7, in this regime a residual quasiparticle peak is still observed at high energies $E_1 \sim 130\,\mu eV$ which is emphasized on the inset of fig. 8.1(b) which is a zoom of the region highlighted by the dashed box.

In the intermediate regime, shown in the figure 8.1(c)-(d), the interaction between the two edge channels was weakened, likely by diverting the inner edge channel along the longer path while the outer edge channel, where the quasiparticle peak is injected, propagates still along the short path. In this intermediate regime, the residual quasiparticle peak that is detected is remarkably larger than what it was measured in Fig. 8.1(b), at the same propagation distance, suggesting that the usual relaxation mechanism was considerable suppressed.

Finally, the figure 8.1(e)-(f) shows the last regime where both edge channels are sent along the long path of $L = 2.17\,\mu m$ in which no signatures of the injected quasiparticle peak are detected on the distribution functions measured after the propagation.

Quasiparticle Peak Decay

The relaxation process was seen to generate an exponential decay of the amplitude $\mathcal{T}_{1,c}$ of the quasiparticle peak as a function of the energy E_1 at which it was injected (Section 6.5). Such behavior, characterized by a decaying energy E_{decay}, serves as an indicator to quantitatively characterize the relaxation process. From equation 6.16, the relation $\mathcal{T}_{1,c}/\mathcal{T}_{1,0} = exp(-E_1/E_{decay})$ represents the probability for a particle to propagate on the edge channel through an interacting region without losing energy, namely the *elastic scattering probability*.

In figure 8.2 we show how the exponential decay of the normalized peak height $\mathcal{T}_{1,c}/\mathcal{T}_{1,0}$ is strongly affected when going through the intermediate regime by gradually polarizing the gate ***A2*** from $V_{A2} = +0.2\,V$ up to $V_{A2} = -0.5\,V$. We observe, in figure 8.2b, that the decaying characteristic energy reaches a maximum $E^{max}_{decay} \sim 100\,\mu eV$ at the intermediate regime which is 5 times bigger than the nominal value $E_{decay} \sim 20\,\mu eV$ measured at the same propagation distance in presence of the co-propagating edge channel. It clearly indicates that in the intermediate regime the particles at a given energy are 5 times more likely to reach the detector without losing energy. This represents

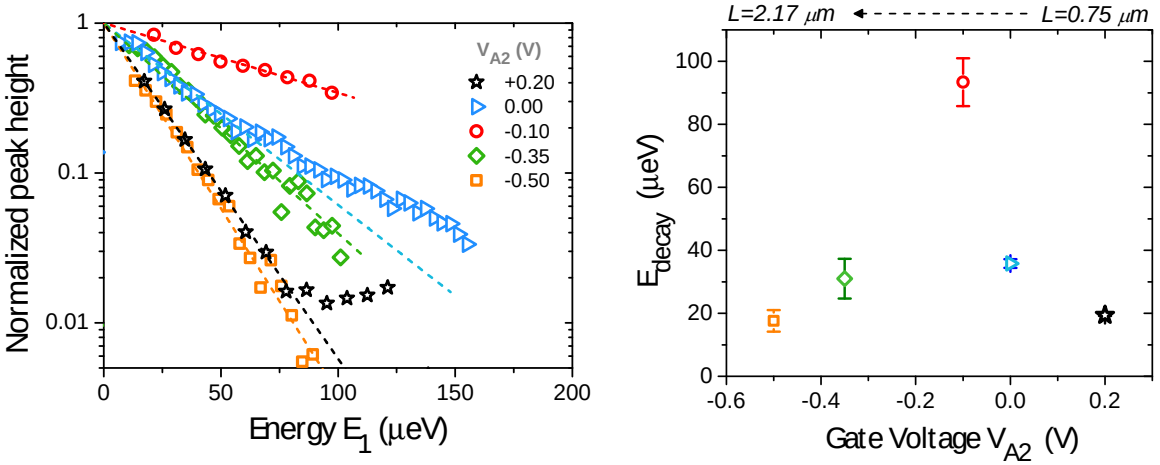

(a) (b)

Figure 8.2: **(a)** Normalized quasiparticle peak height plotted in semilog scale as a function of the injection energy E_1 for the different polarization voltage V_{A2} in gate ***A2*** measured in sample ***D31***. The dashed line are exponential fits. **(b)** Characteristic energy E_{decay} extracted of the exponential decay fit in **(a)** as a function of the polarization voltage V_{A2}.

a remarkable suppression of the relaxation process since it implies that particles can now propagate for a distance that is at least five times longer and still being detected as a residual quasiparticle peak. Therefore these measurements demonstrate that it is possible to tune the coupling between co-propagating edge channels in order to extend the distance over which a quasiparticle peak, injected at a well defined energy, propagates before decaying from a sub-micrometer scale up to several micrometers. With this experiments, we determined the limitations imposed by the relaxation and we demonstrate how that can be considerable improved.

Heat Current

As investigated in chapter 7 the relaxation also induces an energy loss from the outer edge channel which is observed by measuring the heat current that remains after the propagation. In Figure 8.3 we show the ratio between the residual excess heat current ΔJ_r after the propagation and the injected excess heat current ΔJ_i, which represents the fraction of remaining energy in the edge channel where the quasiparticles are injected. As explained before, $\Delta J_r/\Delta J_i = 1.0$ means that the energy is redistributed within the edge channel while the limit $\Delta J_r/\Delta J_i = 0.5$ is expected when full equilibration between the two edge channels is achieved.

We observe that when the system is placed in the intermediate regime, more energy remains in the edge channel, in agreement with the reduction of the relaxation of the quasiparticle peak. However, even when the relaxation is minimized, there is still an energy leakage from the edge channel. It could be attributed in part to the residual path, along which the two edge channel co-propagates next to each other, between the quantum dots' tunneling points and the position at which the edge channels are

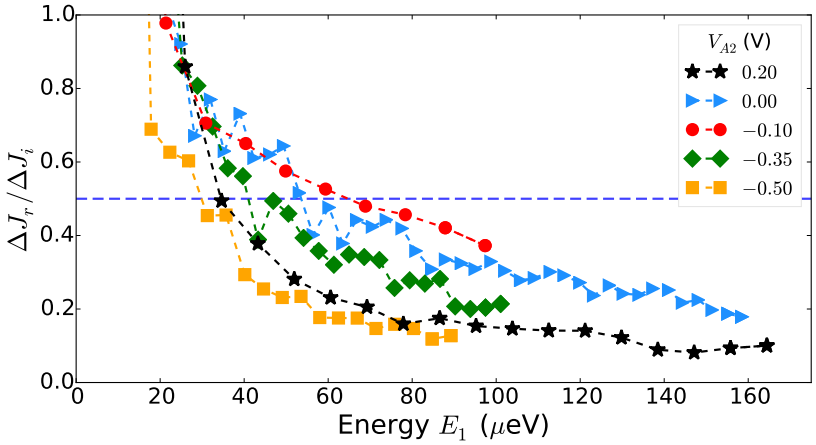

Figure 8.3: Fraction of the excess heat current $\Delta J_r/\Delta J_i$ that remains on the outer edge channel after the propagation as a function of the injection energy E_1 measured at different polarization voltage V_{A2} in the gate ***A2***. The horizontal blue dash line is the lower bound expected for an energy equipartition between two co-propagating edge channels.

effectively decoupled. This residual path can be up to 200 nm long in sample ***D31***.

In addition we still observe that the remaining energy on the edge channel goes below the limit expected at full equilibration between two interacting edge channels, even when the two edge states are maximally decoupled at $V_{A2} = -0.1\,V$.

As done in section 7.3 we can describe the remaining excess heat current ΔJ_r in terms of the injected heat current with the excitations in the quasiparticle peak $\Delta J_{qp}^{(in)} = (E_1 - \mu_r) * \Delta\mu_r$ and the injected heat current with the electron-hole excitations created near the electrochemical potential $\Delta J_{eh}^{(in)} = (\Delta\mu_r)^2/2$ using the empiric equation (Eq. 7.13):

$$\Delta J_r(E_1) = \gamma_{qp}\Delta J_{qp}^{(in)} + \gamma_{eh}\Delta J_{eh}^{(in)} \tag{8.1}$$

Two examples of the fits in the intermediate regime are shown in figure 8.4. Additionally, we show the contribution due to the injected quasiparticle peak in yellow (The first term of Eq. 8.1) and the contribution due to the injected low energy excitations in blue (The second term of Eq. 8.1).

Figure 8.5 shows that both coefficients γ_{qp} and γ_{eh} display a maximum centered at the condition of maximal decoupling of the edge channel that was achieved on this experiment. Notice that at the intermediate regime, both parameters take values that are well above the mean value observed for all previous experiments, which is indicated by the horizontal dashed line together with its standard deviation defining the shaded region. This is also an indication that in the intermediate regime, a large amount of the injected energy remains in the edge channel.

8.1.2 Reducing the Relaxation at $L = 0.48\mu m$

We have performed this experiment as well in the sample ***E33*** on which the short direct path between the quantum dots was designed to have a length $L = 0.48\,\mu m$.

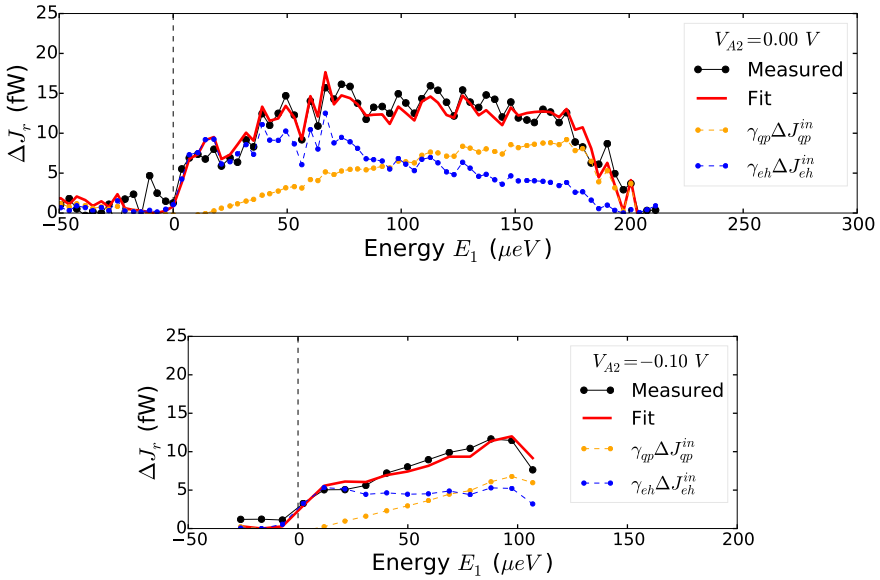

Figure 8.4: Excess heat current ΔJ_r (black symbols) measured after the propagation in the intermediate regime, with $V_{A2} = 0$V (top) and $V_{A2} = -0.1$V (bottom), as a function of the injection energy E_1. The red line corresponds to a fit using the empiric equation 8.1 which links the measured $\Delta J_r(E_1)$ with the measured electrochemical increase $\Delta\mu_r(E_1)$ using two parameter γ_{qp} and γ_{eh}. The yellow (blue) points correspond to the contribution due to the first (second) term in equation 8.1 using the parameters extracted from the fit.

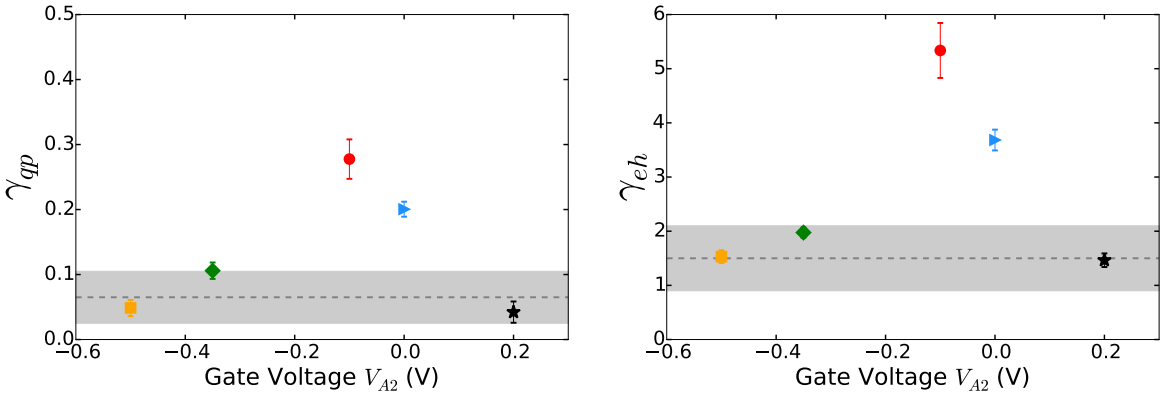

Figure 8.5: As a function of the polarization voltage V_{A2}, we plot the evolution of the coefficients γ_{qp} (left) and γ_{eh} (right) obtained from the empiric fit of the measured excess heat current ΔJ_r as a function of the injection energy E_1 as illustrated in Fig. 8.4. The horizontal dashed line centered in the area shaded in grey, represents the mean value of the parameter and its standard deviation obtained from the ensemble of points presented in the Fig. 7.6 which were measured with both edge channel co-propagating along the path.

Since the propagation length is smaller in this sample, the relaxation undergone by the quasiparticle peak in normal conditions is already weaker. Therefore the difference between the normal regime, where both edge channels co-propagates along the short path, and the intermediate regime, where the edge channels are decoupled, is less pronounced than in sample ***D31*** where the short path has $L = 0.75\,\mu m$.

Quasiparticle Peak Decay

In figure 8.6a we show the evolution of the characteristic energy E_{decay} of the exponential decay of the quasiparticle peak's amplitude as a function of the polarization voltage in the electrode ***A2***. As in sample ***D31***, the decaying energy passes through a maximum value at the intermediate regime, achieved at $V_{A2} = -0.12\,V$.

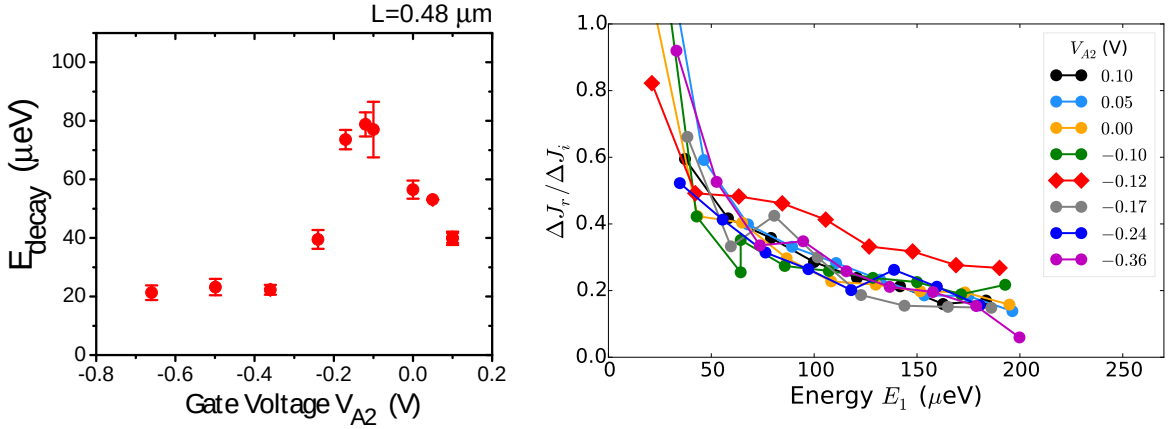

Figure 8.6: **(a)** Characteristic energy E_{decay}, extracted of the exponential fit of the quasiparticle peak's amplitude, plotted as a function of the polarization voltage V_{A2} applied in the gate ***A2*** in sample ***E33***. **(b)** Fraction of the excess heat current $\Delta J_r/\Delta J_i$ that remains on the outer edge channel after the propagation as a function of the injection energy E_1 measured at different polarization voltage V_{A2} measured in sample ***E33***. The horizontal blue dash line is the lower bound expected for an energy equipartition between two co-propagating edge channels.

Heat Current

When looking at the remaining heat current on the edge channel, we observe as well that there is less energy loss in the intermediate regime. This can be clearly seen on the figure 8.6b where we observe the curve measured at the intermediate regime to be well separated from the ensemble of other measurements.

8.1.3 Intermediate Regime vs Distance

The figure 8.7a shows a comparison of the exponential decay of the quasiparticle peak's amplitude in the initial state (full symbols), where both edge channels co-propagates along the short distance, and the optimum intermediate regime (open symbols), where the edge channels are decoupled. We show a comparison of the change observed at the two propagation distances $L = 0.75\,\mu m$ and $L = 0.48\,\mu m$. We observe that when the excitations propagate along a distance $L = 0.75\,\mu m$ in the intermediate regime (open blue circles) there is even less relaxation than if the excitations propagate along the short distance $L = 0.48\,\mu m$ with edge channels co-propagating next to each other.

A similar behavior can be observed in the heat current (Fig. 8.7b): by decoupling the edge states at $L = 0.75\,\mu m$ there is less energy loss than if the system propagates along $L = 0.48\,\mu m$ in normal conditions.

The similarity between the two measurements in the decoupled regime (open squares and open circles), indicates that even if the propagation distance is different in both samples, the relaxation undergone by the quasiparticle peak is similar. This is in agreement with the idea that in both cases there could be a residual short distance along which both edge channels co-propagates. In our sample design it is possible that such residual distance can arise just after the injection point next to the first quantum dot or just before the measurement point next to the second quantum dot.

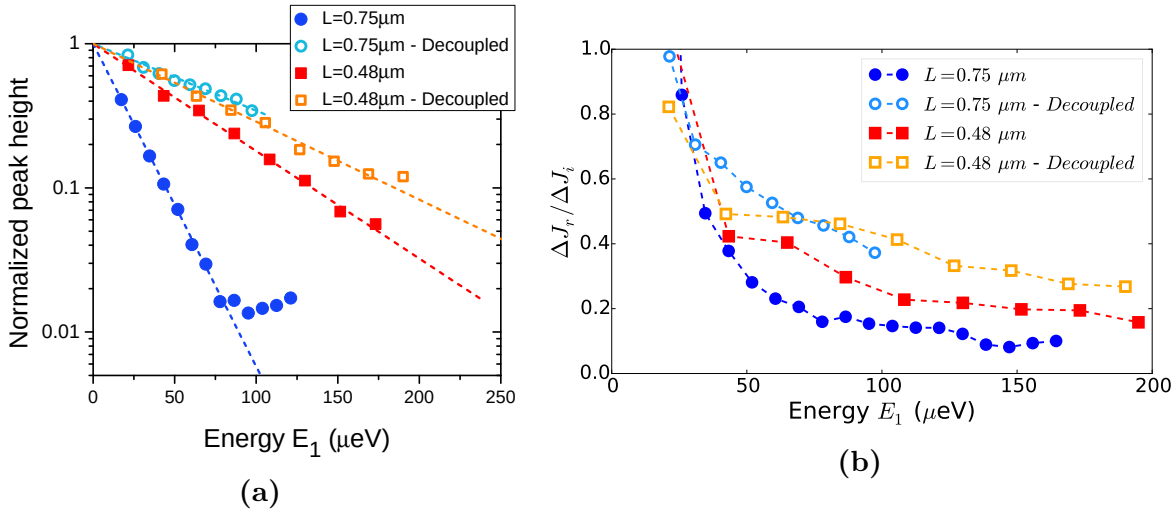

Figure 8.7: **(a)** Comparison of the exponential decay of the normalized quasiparticle peak's amplitude as a function of the injection energy E_1 measured when: the two edge channels propagates together along the short path $L = 0.75\mu$m in sample ***D31*** (filled circles), the two edge channel are maximally decoupled in sample ***D31*** (open circles), the two edge channels co-propagate along the short path $L = 0.48\mu$m in sample ***E33*** (filled squares), the two edge channel are maximally decoupled in sample ***E33*** (open squares). **(b)** Fraction of the excess heat current $\Delta J_r/\Delta J_i$ that remains on the outer edge channel after the propagation measured in the same condition as the data in **(a)** represented respectively with the same symbols.

8.2 Coexistence of Quasiparticle Peaks

When the sample ***D31*** was placed in the intermediate regime ($V_{A2} = -0.1V$) we have observed that, in addition to the spectacular reduction of the relaxation, multiple quasiparticle peaks can propagate simultaneously at different energies. In this section we briefly describe an example of these observations where multiple quasiparticle peaks coexist and survive to the relaxation along the propagation length $L = 0.75\,\mu m$.

Multiple quasiparticle peaks can be injected on the edge channel by using the first quantum dots as an energy filter with many active levels in the bias energy window. We realize this by selecting resonant levels with excited states, meaning that there are

many active levels on the bias energy window; however the charge state of the quantum dot only fluctuates by $\pm 1e$ when particles are transmitted.

In figure 8.8a we show a measurement of the transconductance dI/dV_p as a function of the bias voltage V_{sd} and the plunger gate voltage V_p applied on the first quantum dot which is used to inject the particles. The two most intense lines define the boundaries of adjacent Coulomb diamonds where the dot is in the Coulomb blockade regime with a fixed number charges. In between these boundaries, transport is allowed trough the discrete levels that lies within the bias windows. This measurement shows signatures of the presence of excited states as additional features in between the boundary lines. The figure 8.8b is a trace at fixed bias voltage on which excited states are seen as additional peaks or dips in between the two outermost structures which define the bias window.

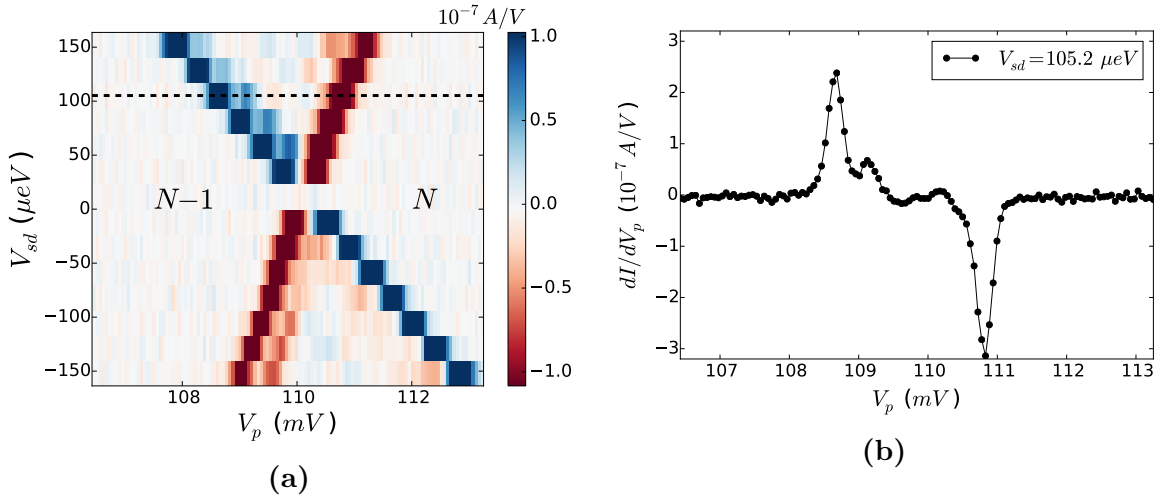

Figure 8.8: **(a)** Transconductance measurement in the first quantum dot as a function of the plunger gate voltage V_p and the bias voltage V_{sd} applied on the dot. **(b)** single horizontal trace of the transconductance measured in **(a)** taken at fixed bias voltage $V_{sd} \approx 105\mu eV$.

The figure 8.9a shows a 2D-plot of the normalized transconductance measured as a function of the detection energy E_2 (x-axis) at different injection energies E_1 (y-axis) using the first quantum dot in a configuration with excited states. Contrary to the usual case where a single diagonal line is observed, this measurement displays multiple parallel diagonal lines at positive energies. Each diagonal line describes an individual quasiparticle peak.

The figure 8.9b shows the distribution functions $f_{r,c}$ measured after the propagation that have been obtained from the spectrum at the different injection energies E_1. We can identify two main quasiparticle peaks in close proximity that are detected around the injection energy E_1. They can be easily seen in the figure 8.10 which is a zoom of the tails of the distributions presented on Fig. 8.9b. Additionally we notice that there is a small third peak around an energy $E = 80\,\mu eV$ that appears on the first three curves labeled with the injection energy $E_1 \in \{0, 10, 20\}\mu eV$. Moreover in this

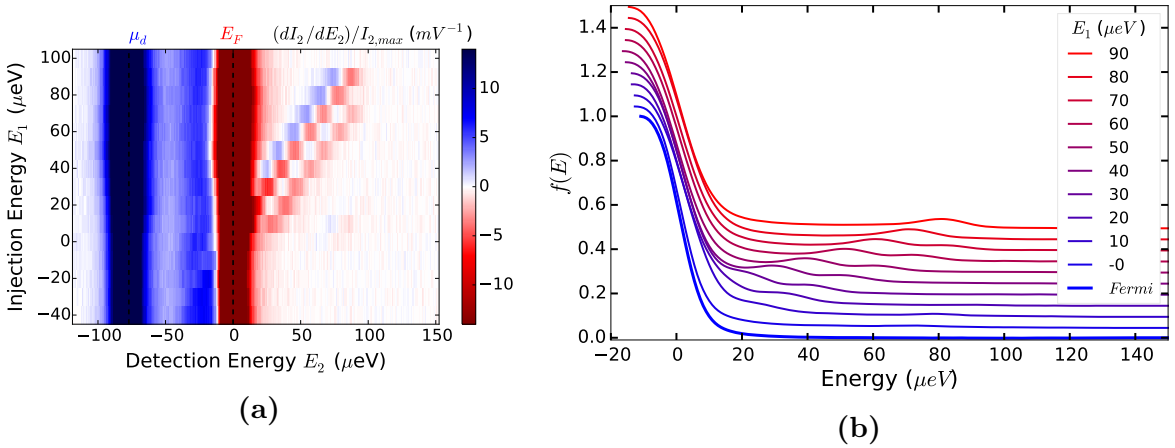

(a) **(b)**

Figure 8.9: **(a)** 2D-plot of the normalized transconductance as a function of the detection energy E_2 (x-axis) at different injection energy E_1 (y-axis) measured in sample ***D31*** with a polarization voltage $V_{A2} = -0.1V$ and with the first quantum dots in a configuration where the resonant level present excited states. **(b)** Distribution functions obtained from **(a)** after integration of the transconductance signal. The curves were vertically shifted for clarity by a constant offset proportional to the injection energy increase $\delta E_1 = 10\mu eV$.

last figure we can see that the different quasiparticle peaks enter and leave the bias energy windows $E \in [0\,,\,94]\mu eV$, defined by the first quantum dot, at different E_1, corresponding to different plunger gate voltage V_p on the first quantum dot.

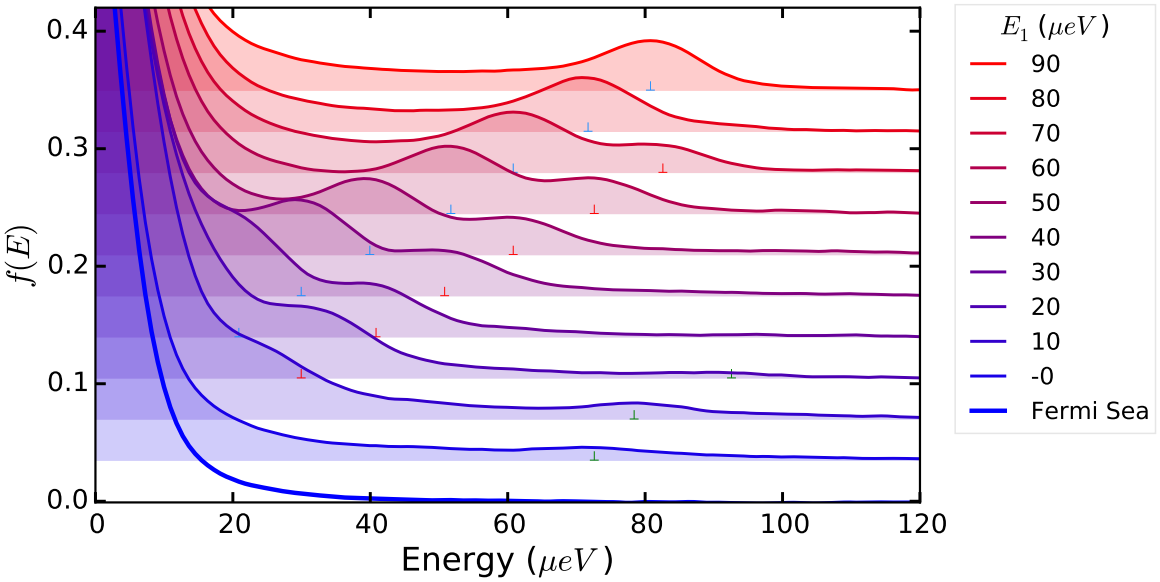

Figure 8.10: Zoom on the tails of the distribution function presented in Fig. 8.9b where different quasiparticle peaks coexist while they propagates.

From these measurements we obtain the position of each quasiparticle peak as a function of the injection energy E_1 which evolves as parallel lines as shown in Figure 8.11a. The position lines are labeled as $E^{(0)}, E^{(1)}, E^{(2)}$ such that the quasiparticle peak at position $E^{(0)}$ is the last one to enter the bias energy windows and the last one to leave it, thus it corresponds to the peak that is closer to the Fermi level on a given

distribution $f_{r,c}$, hence the least energetic peak.

This measurement provides an estimation of the energy difference between the discrete levels: $\Delta E_{21} = E^{(2)} - E^{(1)} = 60\,\mu eV$ and $\Delta E_{10} = E^{(1)} - E^{(0)} = 20\,\mu eV$. The figure 8.11b shows the measurement of the differential conductance on the first quantum dot at the finite bias $V_{sd} = 94\,\mu V$ at which it was implemented on the spectroscopy. The measured ΔE_{21} and ΔE_{10} defines the vertical shaded region at which it is expected to observe signatures of the additional excited states while they successively exceed $E_1 = eV_{sd} = 94\,\mu eV$ leaving the bias energy windows. Indeed, it is in the shaded regions where the differential conductance presents extra features characteristics of excited states, which can lead to an increase or a decrease in the overall conductance depending on the relative coupling of the different excites states. In consequence, it can be inferred that the level structure on the first quantum dot consists of three discrete levels: A ground state that follows $E^{(0)}$, a first excited state at $21\,\mu eV$ that follows $E^{(1)}$ and a second excited state at $80\,\mu eV$ that follows $E^{(2)}$.

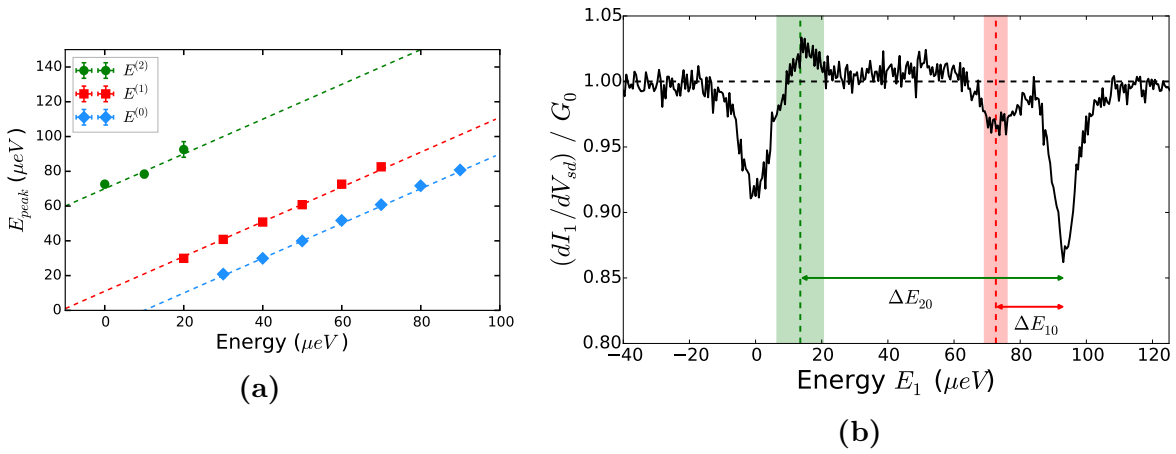

Figure 8.11: **(a)** Evolution of the energies $E^{(0)}$, $E^{(1)}$ and $E^{(2)}$ at which the three quasiparticle peaks are centered as a function of the injection energy E_1 which depends on the plunger gate voltage V_p applied on the first quantum dot. **(b)** Transconductance of the first quantum dot as a function of the injection energy $E_1(V_p1)$ measured in the same conditions at which the spectrum presented in Fig. 8.9 was obtained. The red (green) regions correponds to the energy E_1 at which it is expected to observe signatures of the presence of the first (second) excited state inferred from the data plotted in **a**.

Therefore by implementing a resonant condition in the first quantum dot with excites states we are able to sequentially inject particle on the edge channel at different well defined energies. Notice that particles will have a different probability to tunnel across each excited states, which depends on the coupling between the discrete level and the reservoir, however only one discrete level is active at the time and particles are injected on the edge channel one by one.

Additionally, from the spectrum we measure the evolution of each quasiparticle peak's amplitude which still decays exponentially as shown on figure 8.12. We observe as well that the two better resolved quasiparticle peaks, associated to the two lowest discrete levels $E^{(0)}$ and $E^{(1)}$, have a characteristic decay energy E_{decay} that is enhanced

since the inner edge channel is decoupled from the outer edge where the quasiparticles have been injected. In normal conditions, when the two edge channel co-propagate following the same short path, the decaying energy was only $E_{decay} \approx 20\,\mu eV$.

The coexistence of multiple quasiparticle peaks propagating at different energies was observed several times *only* when the system was in the intermediate regime on which both edge channels are decoupled. However we were not able to conclusively test if this is a fundamental condition to observe the coexistence of several quasiparticle peaks, since we do not have measurements with the first quantum dot showing clear signatures of excited states for other propagation lengths or in other inter edge channel coupling conditions.

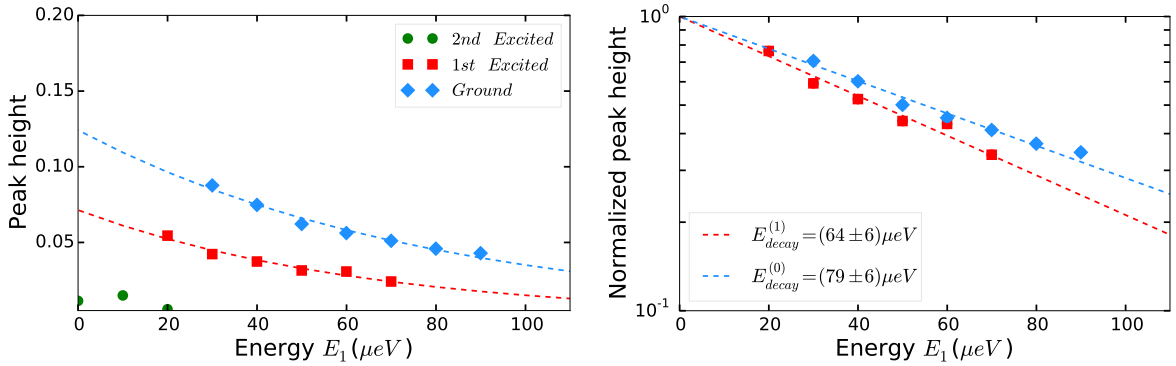

(a) **(b)**

Figure 8.12: **(a)** Evolution as a function of the injection energy $E_1(V_{p1})$ of the amplitude of the three quasiaprticle peaks observed in the measured distribution functions presented in Fig. 8.9. The dashed lines are exponential fits. **(b)** Evolution of the normalized quasiparticle peak's amplitude presented in **a** in semilog scale. The dashed lines are the exponential decay from the extrapolated initial value at $E_1 = 0$.

8.3 Conclusions

In this chapter we demonstrated that the relaxation of the quasiparticle peak injected in the outer edge channel can be weakened up to five times by decoupling this edge channel of the neighboring inner edge channel.

We have shown that it is possible to achieve this regime simply by implementing a surface depletion gate which is used to divert only the inner edge channel along a longer path, leaving the outer edge channel to propagate alone following the short path.

Clear signatures of a reduced relaxation have been observed both in the characteristic energy E_{decay} of the exponential decay undergone by the quasiparticle peak's amplitude and in the remaining excess heat current ΔJ_r measured on the outer edge channel.

These observations address a central aspect in the field of *electron quantum optics* that has not been demonstrated at this level up to now: how far can an electron excitation propagates on the edge channel before decaying?. This question also plays

an important role for the future manipulation of the quantum state of single electron excitation propagating in quantum Hall edge channels which has been proposed as a convenient system to realize flying qubits for quantum computation in solid state systems. With these experiments, we determined the limitations imposed by the relaxation in the integer quantum Hall regime, under standard conditions, and we demonstrated how the relaxation can be considerably reduced extending the lifetime of finite energy excitations at least five times.

Moreover we have shown that multiple quasiparticle peaks, injected at different energies, can coexist and survives to the relaxation along the propagation length $L = 0.75\,\mu m$ when the system is set at the intermediate regime where the edge channels are decoupled.

Chapter 9

Conclusions and Perspectives

This thesis explores the relaxation of a quasiparticle peak injected in the outer edge channel obtained in the integer quantum Hall regime at filling factor $\nu = 2$. We have performed an energy resolved spectroscopy of the relaxation by implementing two quantum dots as energy filters. The first quantum dot continuously injects particles at a given energy E_1 in the range $E_1 \in [0\,;\,200]\mu$eV. The quasiparticles were injected with a Lorentz distribution, with a typical width $\Gamma_1 \sim 10\mu$eV, above the Fermi Sea of the outer edge channel. After a tunable propagation length L in the range of $L \in [0.48\,;\,3.4]\mu$m, where relaxation can take place, we perform the spectroscopy of the distribution of particles in the outer edge channel by implementing a second quantum dot as energy filter. This detection scheme was previously implemented in order to investigate relaxation of a double step distribution function injected in the outer edge channel in the same regime [51, 52].

The main results obtained along this thesis are:

1 - We have quantitatively reproduced the main observations on the relaxation of a double step distribution function previously investigated in Ref. [51, 52]. Our observations are in agreement with the fact that the relaxation of this out of equilibrium state occurs between 1μm and 10μm of propagation, which indicates that we find the same relaxation rate despite the differences in the devices. Moreover we confirm that this relaxation process leads to $\sim 20\%$ of the injected energy to leaks out of the system of the two interacting edge channels.

2 - After a short propagation length $L < 1\mu$m, we have measured a residual quasiparticle peak, which represents the particles that survives to the relaxation. This constitutes the first experimental observation of a quasiparticle peak in a quantum Hall edge channel.

3 - Although the propagation over sub-micrometer lengths leads to a sizable energy relaxation, a residual quasiparticle peak was observed to subsists even at relatively high energies, up to 150μeV.

4 - We have measured that while the width (FWHM) of the quasiparticle peak remains constant as a function of the injection energy E_1, the amplitude of the quasiparticle peak exponentially decreases as a function of E_1. Moreover, we observed that the relaxation process does not affect the energy at which the quasiparticle peak is centered, being always coincident with the injection energy.

5 - We have observed that the characteristic energy E_{decay} of the exponential decay of the quasiparticle peak's amplitude is strongly affected by the propagation length L and the temperature T. On the one hand, when increasing the propagation length from $L = 0.48\mu$m to $L = 0.75\mu$m, the decay energy E_decay decrease from 60μeV to 20μeV. On the other hand, when the temperature is increased from 20mK to 170mK, the decay energy decrease from $E_{decay} \approx 60\mu$eV to $E_{decay} \approx 30\mu$eV.

6 - A comparison of these measurements with the ones obtained after a longer propagation length $1\mu m < L < 3.4\mu m$, where no quasiparticle peak was observed although the distribution was not yet at equilibrium, allows to distinguish two time scales in the relaxation process. During a first step, which occurs over a sub-micrometer distance, the quasiparticle peak gets progressively dissolved as described in **(4)** bringing the injected particles closer to the Fermi sea. As a consequence, the quasiparticle peak evolves into an extended distribution of particles that spread over the whole energy range from the Fermi level $E_F \sim 0\mu$eV up to the injection energy E_1. The second step in the relaxation process, which brings the resulting extended distribution of particles into a Fermi sea, occurs over several micrometers of propagation. We suggest that this second time scale is the same that is involved in the relaxation process of the double step distribution function, which consist of out of equilibrium quasiparticles near the Fermi sea, while the first time scale appears only on the relaxation of the quasiparticle peak, which consist of out-of equilibrium quasiparticles well above of the Fermi sea. These two time scales in the relaxation process were first predicted in the theoretical work presented in Ref. [56].

7 - The measurements of the heat current that remains on the edge channel after the propagation shows that the amount of energy lost during propagation is markedly larger than expected. We observed that up to 70% of the injected energy leaks out of the system of two interacting edge channels. This suggests that relaxation mechanisms towards external degrees of freedom play an important unexpected role in electron quantum optics experiments.

8 - Finally, we have demonstrated that the relaxation of the quasiparticle peak injected in the outer edge channel can be strongly suppressed by decoupling the two co-propagating edge channels. In this regime, it was possible to extend the distance over which the quasiparticle propagates before decaying, from the sub-micrometer scale up to several micrometers.

To conclude, in this thesis we captured the limitations imposed by the energy relax-

ation in quantum Hall edge channels and circumvent them by considerably extending the lifetime of finite energy excitations. However, there remain some open questions indicating that the current understanding of the excitations in the quantum Hall effect is not complete:

1 - So far it was not possible to identify which is the origin of the large energy leak that was observed in the relaxation of the quasiparticle peak. Possible candidates are: bulk excitation as considered in Ref. [54] or the internal degrees of freedom develops in the edge channel as a consequence of the edge reconstruction [93]. Other possible explanations involves non linear dispersion of edge magnetoplasmons in the Luttinger liquid theory [58]. Although our measurement does not allows us to distinguish between different scenarios, they shed some light on this subject in order to better understand the mechanisms that are involved.

2 - Additionally, on the one hand, the exponential decay of the quasiparticle peak amplitude that we observed is not predicted by any of the current models that describe the interactions in this system. On the other hand, we have observed signatures of a quasiparticle peak revival in several of our measurements. Up to our knowledge, such a behavior is only observed in the calculations presented in Ref. [116] where the quasiparticle peak's amplitude decreases with the injection energy E_1 following an oscillatory behavior.

Since this experiment shows that the interaction with the co-propagating edge channel is a key element in the relaxation of the quasiparticle peak as well as it was shown for the double step distribution function [52], as a perspective it would be interesting to perform similar measurements at other filling factors ν. The relaxation of the quasiparticle peak injected in the outer edge channel but at filling factor $\nu = 3$ or $\nu = 1$ would provide useful information to identify the origin of the large energy leak we have seen. Additionally, this experiment could be extended to the fractional quantum Hall regime where it is well known that the Coulomb interaction leads to the formation of excitations with fractional charges.

Appendix A

Injected Heat Current

This appendix present the demonstration that when new particles are injected in the system around a characteristic energy E_1 the injected excess heat current ΔJ has the general form:

$$\Delta J = (E_1 - \mu)\Delta\mu + \frac{1}{2}\Delta\mu^2 \tag{A.1}$$

where $\Delta\mu$ is the increase in the electrochemical potential due to the injected particles.

First, lets consider that the initial state is a distribution function $f_0(E)$, characterized by an electrochemical potential μ_0, which is not necessarily a Fermi distribution.

Then, lets imagine that new particles are injected in the system, with a distribution $P_1(E)$ which can have any functional dependence on the energy. In any realistic experiment $P_1(E)$ is a continuous function. In particular, during the experiments presented in this thesis it was shown that the particles were injected with a Lorentz distribution function, $P_1(E) = L_1(E, E_1)$, centered around the injection energy E_1 given by the resonant level in the quantum dot implemented as the emitter. Therefore, in the general case, the final distribution function $f_1(E)$ after the injection of particles results $f_1(E) = f_0(E) + P_1(E)$ and it is characterized by an electrochemical potential μ_1.

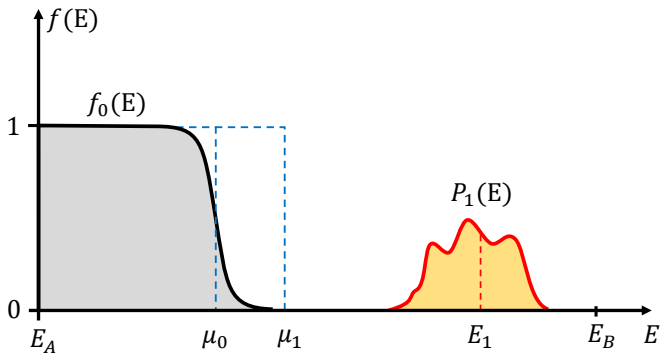

Figure A.1: Distribution functions.

Electrochemical potential increase $\Delta\mu$

The electrochemical potential μ_0 of the initial distribution function $f_0(E)$ is obtained by measuring the area under the distribution from an energy E_A, at which $f_0(E) = 1\ \forall E \leq E_A$, up to the energy E_B at which $f_0(E) = 0\ \forall E \geq E_B$:

$$\mu_0 = E_A + \int_{E_A}^{E_B} f_0(E)\, dE \tag{A.2}$$

In the following, without losing generality, we fix the constants E_A and E_B such that the conditions also holds after the injection of particle, thus $f_1(E) = 1\ \ \forall E \leq E_A$ and $f_1(E) = 0\ \ \forall E \geq E_B$. Additionally, we chose the zero energy point to be E_A. In consequence we can avoid writing the limits of the integration everytime and the electrochemical potential μ_0 simply reads:

$$\mu_0 = \int f_0(E)\, dE \tag{A.3}$$

After the injection of particles, the electrochemical potential μ_1 of the distribution function $f_1(E)$ is:

$$\mu_1 = \int f_1(E) dE = \int \Big[f_0(E) + P_1(E) \Big] dE = \mu_0 + \int P_1(E) dE \tag{A.4}$$

Therefore, the increase in the electrochemical potential $\Delta\mu = \mu_1 - \mu_0$, results:

$$\Delta\mu = \int P_1(E) dE \tag{A.5}$$

Heat current increase ΔJ

The initial distribution function $f_0(E)$ carries a heat current J_0 that can be calculated from the integration:

$$hJ_0 = \int (E_- \mu_0) \Big[f_0(E) - \Theta(\mu_0 - E) \Big] dE \tag{A.6}$$

where we have drop the integration limits E_A and E_B for simplicity and the $\Theta(\mu_0 - E)$ is the Fermi function at zero temperature with electrochemical potential μ_0.

After the injection of particles the heat current J_1 reads:

$$hJ_1 = \int (E_- \mu_1) \Big[f_1(E) - \Theta(\mu_1 - E) \Big] dE \tag{A.7}$$

In the following we will develop this last equation to arrive to the general form (Eq. A.1). First, notice that we can write $\Theta(\mu_1 - E) = \Theta(\mu_0 - E) + \Delta\Theta_{\mu_0,\mu_1}(E)$ where the

rectangular function $\Delta\Theta_{\mu_0,\mu_1}(E)$ is defined as:

$$\Delta\Theta\mu_0,\mu_1(E) = \begin{cases} 1 & \text{if } \mu_0 < E < \mu_1, \\ 0 & \text{if } E < \mu_0 \quad \text{or} \quad \mu_1 < E. \end{cases} \tag{A.8}$$

Therefore the equation A.7 can be written as:

$$hJ_1 = \int \Big[(E-\mu_0)-\Delta\mu\Big] \times \Big\{ \Big[f_0(E)-\Theta(\mu_0-E)\Big] + P_1(E) - \Delta\Theta\mu_0,\mu_1(E) \Big\} dE \tag{A.9}$$

$$\begin{aligned} hJ_1 = & \int (E-\mu_0)\Big[f_0(E)-\Theta(\mu_0-E)\Big]dE \\ & + \int (E-\mu_0)P_1(E)dE - \int (E-\mu_0)\Delta\Theta\mu_0,\mu_1(E)dE \\ & - \int \Delta\mu\Big[f_0(E)-\Theta(\mu_0-E)\Big]dE - \int \Delta\mu P_1(E)dE + \int \Delta\mu\Delta\Theta\mu_0,\mu_1(E)dE \end{aligned} \tag{A.10}$$

The first integral term in the right hand side of eq. A.10 is the heat current in the initial distribution function hJ_0. The second integral can be written in term of a characteristic energy E_1 which is the mean energy at which additional particles are injected:

$$E_1 = \frac{\int EP_1(E)dE}{\int P_1(E)dE} \tag{A.11}$$

In the third and sixth integral terms in the right hand side of equation A.10, the $\Delta\Theta\mu_0,\mu_1(E)$ function reduces the limits of the integration to be done between μ_0 and μ_1. Therefore we have:

$$\begin{aligned} hJ_1 = & hJ_0 + (E_1-\mu_0)\int P_1(E)dE - \int_{\mu_0}^{\mu_1}(E-\mu_0)dE \\ & - \Delta\mu\int \Big[f_0(E)-\Theta(\mu_0-E)\Big]dE - \Delta\mu\int P_1(E)dE + \Delta\mu\int_{\mu_0}^{\mu_1} dE \end{aligned} \tag{A.12}$$

The fourth term in the right hand side in equation A.12 is null since the integrated function is anti-symmetric around μ_0. Additionally, the last two term in equation A.12 cancel each other since $\int P_1(E)dE = \Delta\mu$. Thus, the excess heat current $\Delta J = J_1 - J_0$ is given only by:

$$h\Delta J = (E_1-\mu_0)\Delta\mu - \frac{(E-\mu_0)^2}{2}\Big|_{\mu_0}^{\mu_1} \tag{A.13}$$

$$h\Delta J = (E_1-\mu_0)\Delta\mu - \frac{(\Delta\mu)^2}{2} \tag{A.14}$$

Finally, substituting $\mu_0 = \mu_1 - \Delta\mu$, we obtain:

$$h\Delta J = (E_1 - \mu)\Delta\mu + \frac{(\Delta\mu)^2}{2} \tag{A.15}$$

Therefore this is a very general equation for the increase in the heat current due to the injection of new particles, around a characteristic energy E_1, that increases the electrochemical potential by $\Delta\mu$. Furthermore it does not depends on the particular functional form of the injected distribution of particles $P_1(E)$ and neither on the details of the low energy excitation of the initial distribution function $f_0(E)$ which was not restricted to be a Fermi function.

Appendix B

Propagation Speed and Related Parameters

Currently there are several publications that describes the interactions between two co-propagating edge channels in the integer quantum Hall effect (IQHE) regime based in the Luttinger liquid theory [116, 119, 58, 118, 42, 47]. When investigating the various consequences of the Coulomb interaction, different authors describe the properties of the system using different parameters to characterize the interactions. A central parameter in these works is the propagation speed of the excitations since it defines the relevant energy, length and time scales on the experiment. We notice that, the distinction between some parameters and the actual propagation speed of the excitations was not clear in some cases. Therefore, the purpose of this appendix is to clarify these concepts and their relation among the different descriptions. In particular we focus on the publications that we discuss along the manuscript in relation to our experiment and gives some estimated values.

The bosonization approach in the Luttinger Liquid description allows to write the Hamiltonian of the system $H = H_0 + H_{int}$ in term of a local density density interaction (Section 4.3.3). The non interacting part H_0 accounts for the kinetic energy of the excitations in each edge channel $\alpha = 1, 2$:

$$H_0 = \sum_{\alpha=1,2} \pi\hbar\, v_{d\alpha} \int \rho_\alpha^2(x)\, dx \tag{B.1}$$

where $v_{d\alpha}$ is the drift velocity in each channel within the non interacting description. A explicit distinction, $v_{d1} \neq v_{d2}$ is made because they can be slightly different since they are given by the ratio between the *local* electric field and the the magnetic field.

The interacting term H_{int} in the Hamiltonian accounts for the *intra* and *inter* edge channel Coulomb interaction. The screened Coulomb interaction between a particle at position x_1 in the edge channel α and another particle at position x_2 in the edge channel β is described by a short ranged coupling: $g_{\alpha\beta}(x_1, x_2) = g_{\alpha\beta}\, \delta(x_1 - x_2)$. Thus,

the interacting term reads:

$$H_{int} = \int \rho_\alpha(x) g_{\alpha\beta}\, \rho_\beta(x)\, dx \tag{B.2}$$

Therefore the matrix element $H_{\alpha\beta}$ of the total Hamiltonian $H = H_0 + H_{int}$ can be written as:

$$H_{\alpha\beta} = \pi\hbar \int \rho_\alpha(x) \Big[\delta_{\alpha\beta}\, v_{d\alpha} + g_{\alpha\beta}/\pi\hbar\Big] \rho_\beta(x)\, dx \tag{B.3}$$

And the matrix element $\mathcal{V}_{\alpha\beta}$ of the global coupling is just defined as:

$$\mathcal{V}_{\alpha\beta} = \delta_{\alpha\beta}\, v_{d\alpha} + g_{\alpha\beta}/\pi\hbar \tag{B.4}$$

We can see that the diagonal terms represents the intrachannel interaction and only renormalize the drift velocity in each edge channel. The non-diagonal term describes the interchannel coupling and must be symmetric, $g_{\alpha\beta} = g_{\beta\alpha}$, due to the Onsager-Büttiker relations as discussed in Ref. [57].

Propagation speed in Ref. [57, 116]

In Ref. [57] and [116], the case of two edge channels coupled over a finite length L is described using the scattering formalism. The interacting region is characterized by a scattering matrix S for edge magnetoplasmons in terms of three parameters which play, in this case, the same role as the Luttinger or the Fermi liquids parameters [57]. To Follow the notation in Ref. [57], the term $g_{\alpha\beta}/\pi\hbar$ in eq.B.4 is replaced by the equivalent term: $e^2 V_{\alpha\beta}/h$. Subsequently, they show that the global coupling $\mathcal{V}$ can be written in the matrix representation using the Pauli matrices σ^z and σ^x:

$$\mathcal{V} = \bar{v}\mathbf{1} + \frac{\Delta v}{2}\sigma^z + W\sigma^x \tag{B.5}$$

where the three scalar parameters are defined in terms of the three independent coupling terms $\{V_{11}, V_{22}, V_{12}\}$ that describe the interactions and the non interacting drift velocities:

$$\hat{v} = \frac{v_{d\alpha} + v_{d\beta}}{2} + \frac{e^2}{2h}(V_{11} + V_{22}) \tag{B.6}$$

$$\Delta v = \frac{v_{d\alpha} - v_{d\beta}}{2} + \frac{e^2}{h}(V_{11} - V_{22}) \tag{B.7}$$

$$W = \frac{e^2}{h} V_{12} \tag{B.8}$$

These independent parameters $\{\bar{v}, \Delta v, W\}$ can be combined again in order to define a new set of parameters $\{v_0, v, \varphi\}$ in term of which it is written the plasmon scattering

matrix at finite frequency ω:

$$S(\omega, L) = e^{iL\mathcal{V}^{-1}} = e^{i\omega L/v_0} e^{i\omega L/v(cos\varphi\sigma^z + sin\varphi\sigma^x)} \tag{B.9}$$

where the new parameters are defined as:

$$v_0 = \frac{\hat{v}^2 - \left[\left(\frac{\Delta v}{2}\right)^2 + W^2\right]}{\bar{v}^2} \tag{B.10}$$

$$v = \frac{\bar{v}^2 - \left[\left(\frac{\Delta v}{2}\right)^2 + W^2\right]}{\sqrt{\left(\frac{\Delta v}{2}\right)^2 + W^2}} \tag{B.11}$$

$$tan(\varphi) = \frac{W}{\Delta v/2} \tag{B.12}$$

As described in section 4.3.3, φ is known as the *mixing angle*. In this way, the system is described in term of a new set of independent parameters $\{\varphi, v_c, v_s\}$ by introducing the propagation speeds, v_c and v_s, of the charge (c) and spin (s) modes, the new eigenmodes of the interacting system, that are given by:

$$v_c = \left(\frac{1}{v_0} - \frac{1}{v}\right)^{-1} \tag{B.13}$$

$$v_s = \left(\frac{1}{v_0} + \frac{1}{v}\right)^{-1} \tag{B.14}$$

In the last part of Section 4.3.3 we discussed the calculations obtained with this model presented in Ref. [116, 57]. In particular the Fig. 4.16 shows the probability $Z(E_0)$ that a particle, injected at energy E_0, has to propagate across the interacting region of length L without losing energy. It is important to notice that $Z(E_0)$ is given as a function of $E_0 L/\hbar v$, where v is the parameter defined in Eq. B.11. Importantly, notice that in the non interacting case $W \sim 0$, the parameter v can strongly deviates from the drift velocity, if $v_{d1} \approx v_{d2}$, since it becomes:

$$v = \frac{2v_{d1}v_{d2}}{v_{d1} - v_{d2}} \tag{B.15}$$

Propagation speed in Ref. [119]

In Ref. [119] it is experimentally investigated the relaxation of a double step distribution function created with a biased QPC in the regime of low transparencies ($\tau_{qpc} \ll 1$). As theoretically predicted in Ref. [58] a metastable state should develop at intermediate propagation distances as a consequence of the spin-charge separation. A fundamental parameter to estimated the regime on which the metastable state is expected is given by a velocity parameter v_{sc} that is defined in the experimental work as follow. When

the QPC, based with V_s, is set at a given low transmission τ_{qpc}, it injects particles in the edge channel with an average rate: $e\tau_{qpc}V_s/h$. The uncertainty relation implies that each electron wavepacket has a spread h/eV_s in time and $\Delta x = v_m h/eV_s$ in space, being v_m a typical velocity in the edge channel. Due to the Coulomb interaction the injected wavepackets splits developing the spin and charge modes that propagates at velocities v_s and v_c respectively. The distance $L_s(t)$ between the two component increase with time, and they will be well separated at a time t_s for which $L_s > \Delta x$. This gives $t_s > \Delta x/(v_c - v_s)$. At this time, the charge mode has traveled for a distance $L_{sc} = v_c t_s$ which results:

$$L_{sc} = \frac{v_c v_m}{v_c - v_s}\frac{h}{eV_s} \approx \frac{v_c v_s}{v_c - v_s}\frac{h}{eV_s} = v_{sc}\frac{h}{eV_s} \tag{B.16}$$

where it was taken $v_m \approx v_s$ and it was defined the velocity v_{sc} as:

$$v_{sc} = \frac{v_c v_s}{v_c - v_s} \tag{B.17}$$

In Ref. [119], the length L_{sc} is considered as the length that is required for the spin-charge separation where the metastable state is expected to be observed. L_{sc} is obtained by estimating v_{sc} from several experimental measurements assuming an exponential relation between the measured step width Δ and the propagation distance L:

$$\Delta/eV_s = e^{(-L/L_{sc})} = e^{(-e|V_s|L/hv_{sc})} \tag{B.18}$$

Importantly, notice that the velocity v_{sc} is similar to the parameter v discussed in the previous section in relation with the description in Ref. [116, 57]. In the interacting regime we can write:

$$v = 2\,\frac{v_s v_c}{v_c - v_s} = 2\,v_{sc} \tag{B.19}$$

Propagation speed in Ref. [44]

Ref. [44] is the seminal work in which it was proposed that the development of the spin and charge eigenmodes is responsable for the dephasing that was experimentally observed in Mach-Zehnder interferometers (MZI) at filling factor $\nu = 2$ [35, 33, 34, 36]. According to this work, the temperature dependence of the visibility and the period of its oscillations as a function of the bias voltage (the lobe structure) are determined by an energy scale ϵ given by:

$$\epsilon = 2\frac{v_{sc}}{L_U + L_D} \tag{B.20}$$

where L_U and L_D are the lengths of the two arms in the interferometer. This energy scale ϵ would depend only on the slow mode speed v_s in the case of $v_c \gg v_s$ that is obtained for a long range Coulomb interaction. However, in the general case they

found that the dephasing length l_φ follows:

$$l_\varphi = \frac{v_{sc}\hbar}{\pi k_B T} \tag{B.21}$$

Estimated values

In Ref. [127, 52] it was reported that for GaAs/AlGaAs devices in the integer quantum Hall regime at filling factor $\nu = 2$, a standard drift velocity v_d is found in the range $v_d \in [5, 50] \times 10^4$ m/s. This range was obtained from different sources which concerns only devices where the edges were defined by metal gates as recapitulated in Ref. [127]. Moreover, it was indicated that devices without metal gates can display a typical drift velocity one order of magnitude larger.

Following the procedure described in the section B, the velocity v_{sc} measured in their devices was estimated to be $v_{sc} \sim 2.7 \times 10^4$ m/s. However, by analysis of the data reported in Ref. [52] using the same procedure (Eq. B.18) it indicates $v_{sc} \sim 8.7 \times 10^4$ m/s in that case. Moreover, it is reported that this values are comparable to the range $v_{sc} = [6.0; 7.5] \times 10^4$ m/s obtained from time-of-flight experiments (See [119] and Ref. therein).

Additionally, using Eq. B.21 we can estimate a value for v_{sc} using the experimental determination of the dephasing length $l_\varphi \sim 20\mu$m measured at a temperature $T = 20$ mK [33]. This estimation gives $v_{sc} \sim 17 \times 10^4$ m/s.

Finally, in our experiments we measured an exponential decay of the quasiparticle peak's amplitude as a function of the injection energy E_1. The characteristic energy E_{decay} of such behavior can be scaled with the propagation distance L to obtain a characteristic speed v_{dec}:

$$E_{decay} = \hbar v / L \tag{B.22}$$

As can be seen in the Fig. B.1 from these measurements we obtain a value of the speed $v_{dec} \sim 3.5 \times 10^4$ m/s which is of the order of the speed v_{sc} mentioned before.

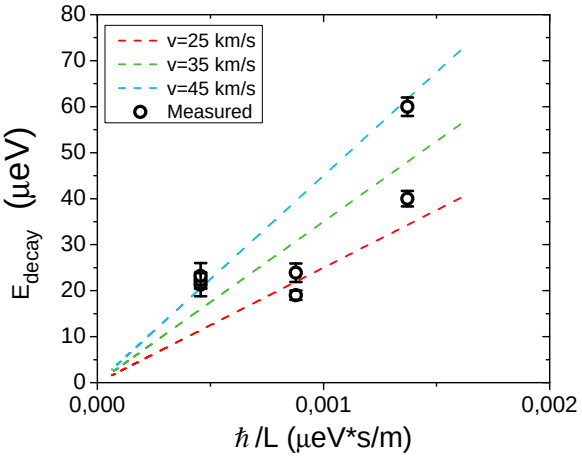

Figure B.1: Characteristic energy E_{decay} measured from the exponential decay of the quasiparticle peak's amplitude in spectra taken at different propagation lengths L.

Reference	Velocity	Corresponding velocity in the other references	Defined as / Related to
us	v_c	- -	Charge mode velocity
	v_s	- -	Spin mode velocity
K. Itoh *et al.* [119]	v_{sc}	$\frac{v_c v_s}{v_c - v_s}$	It defines the minimum length for the spin-charge separation
C. Grenier *et al.* [57,116]	v_+	v_c	Charge mode velocity
	v_-	v_s	Spin mode velocity
	v	$2\, v_{sc}$	They parametrize the scattering matrix for plasmons for two interacting edge channels
	v_0	$2\,\frac{v_c v_s}{v_c + v_s}$	
Ivan P. Levkivskyi *et al.* [44]	u	v_c	Charge mode velocity
	v	v_s	Spin mode velocity
	$\frac{u\, v}{u - v}$	v_{sc}	It defines the energy scale for the temperature dependence and the period of the lobe structure in the visibility of MZI.
	$\frac{u\, v}{u + v}$	$\frac{v_0}{2}$	Related to the phase shift and the phase rigidity in a MZI.

Figure B.2: Comparison between the velocities that are defined in the different references which were discussed in this appendix. Following the corresponding reference, the rightmost column briefly describes in which mechanism each parameter is involved.

Symbols and Constants

T_{ph} : Phonon temperature
T_e : Electronic temperature
$\mathcal{T}$: Transmission probability
μ : Electrochemical potential
Ł : Propagation distance
λ_F : Fermi wavelength
E_F : Fermi energy
e : Electron charge (magnitude) . . . . . $1.602\,10^{-19}\,C$
$\mathbf{v}$: Vector
$\hat{v}$: Scalar operator
$\hat{\mathbf{v}}$: Vectorial operator

References

[1] BJ Van Wees, LP Kouwenhoven, H van Houten, CWJ Beenakker, JE Mooij, CT Foxon, and JJ Harris. Quantized conductance of magnetoelectric subbands in ballistic point contacts. *Phys. Rev. B*, 38:3625, 1988.

[2] BJ Van Wees, H Van Houten, CWJ Beenakker, J Gr Williamson, LP Kouwenhoven, D Van der Marel, and CT Foxon. Quantized conductance of point contacts in a two-dimensional electron gas. *Phys. Rev. Lett.*, 60(9):848, 1988.

[3] DA Wharam, Trevor John Thornton, R Newbury, M Pepper, H Ahmed, JEF Frost, DG Hasko, DC Peacock, DA Ritchie, and GAC Jones. One-dimensional transport and the quantisation of the ballistic resistance. *Journal of Physics C: solid state physics*, 21(8):L209, 1988.

[4] U Meirav, MA Kastner, and SJ Wind. Single-electron charging and periodic conductance resonances in GaAs nanostructures. *Phys. Rev. Lett.*, 65(6):771, 1990.

[5] Marc A Kastner. The single-electron transistor. *Reviews of modern physics*, 64(3):849, 1992.

[6] K Ishibashi, Y Takagaki, K Gamo, S Namba, S Ishida, K Murase, Y Aoyagi, and M Kawabe. Observation of aharonov-bohm magnetoresistance oscillations in selectively doped GaAs-AlGaAs submicron structures. *Solid state communications*, 64(4):573–576, 1987.

[7] CJB Ford, TJ Thornton, R Newbury, M Pepper, H Ahmed, CT Foxon, JJ Harris, and C Roberts. The aharonov-bohm effect in electrostatically defined heterojunction rings. *Journal of Physics C: Solid State Physics*, 21(10):L325, 1988.

[8] JA Simmons, DC Tsui, and G Weimann. Quantum interference effects in high-mobility mesoscopic GaAs/$Al_xGa_{1-x}As$ heterostructures. *Surface Science*, 196(1-3):81–88, 1988.

[9] K v Klitzing, Gerhard Dorda, and Michael Pepper. New method for high-accuracy determination of the fine-structure constant based on quantized hall resistance. *Phys. Rev. Lett.*, 45(6):494, 1980.

[10] Markus Büttiker. Absence of backscattering in the quantum hall effect in multiprobe conductors. *Physical Review B*, 38(14):9375, 1988.

[11] Gwendal Fève, Adrien Mahé, J-M Berroir, Takis Kontos, Bernard Placais, DC Glattli, A Cavanna, Bernard Etienne, and Yong Jin. An on-demand coherent single-electron source. *Science*, 316(5828):1169–1172, 2007.

[12] B Kaestner, V Kashcheyevs, S Amakawa, MD Blumenthal, L Li, TJBM Janssen, G Hein, K Pierz, T Weimann, U Siegner, and HW Schumacher. Single-parameter nonadiabatic quantized charge pumping. *Physical Review B*, 77(15):153301, 2008.

[13] Akira Fujiwara, Katsuhiko Nishiguchi, and Yukinori Ono. Nanoampere charge pump by single-electron ratchet using silicon nanowire metal-oxide-semiconductor field-effect transistor. *Applied Physics Letters*, 92(4):042102, 2008.

[14] Leonid S Levitov, Hyunwoo Lee, and Gordey B Lesovik. Electron counting statistics and coherent states of electric current. *Journal of Mathematical Physics*, 37(10):4845–4866, 1996.

[15] J Dubois, T Jullien, F Portier, P Roche, A Cavanna, Y Jin, W Wegscheider, P Roulleau, and DC Glattli. Minimal-excitation states for electron quantum optics using levitons. *Nature*, 502(7473):659, 2013.

[16] Sylvain Hermelin, Shintaro Takada, Michihisa Yamamoto, Seigo Tarucha, Andreas D Wieck, Laurent Saminadayar, Christopher Bäuerle, and Tristan Meunier. Electrons surfing on a sound wave as a platform for quantum optics with flying electrons. *Nature*, 477(7365):435, 2011.

[17] RPG McNeil, M Kataoka, CJB Ford, CHW Barnes, D Anderson, GAC Jones, I Farrer, and DA Ritchie. On-demand single-electron transfer between distant quantum dots. *Nature*, 477(7365):439, 2011.

[18] A Bertoni, Paolo Bordone, Rossella Brunetti, Carlo Jacoboni, and S Reggiani. Quantum logic gates based on coherent electron transport in quantum wires. *Phys. Rev. Lett.*, 84(25):5912, 2000.

[19] Radu Ionicioiu, Gehan Amaratunga, and Florin Udrea. Quantum computation with ballistic electrons. *International Journal of Modern Physics B*, 15(02):125–133, 2001.

[20] David P DiVincenzo. The physical implementation of quantum computation. *Fortschritte der Physik: Progress of Physics*, 48(9-11):771–783, 2000.

[21] Christopher Bäuerle, D Christian Glattli, Tristan Meunier, Fabien Portier, Patrice Roche, Preden Roulleau, Shintaro Takada, and Xavier Waintal. Coherent

control of single electrons: a review of current progress. *Reports on Progress in Physics*, 81(5):056503, 2018.

[22] LD Landau. The theory of a fermi liquid. *Soviet Physics Jetp-Ussr*, 3(6):920–925, 1957.

[23] LD Landau. Oscillations in a fermi liquid. *SOVIET PHYSICS JETP-USSR*, 5(1):101–108, 1957.

[24] LD Landau. On the theory of the fermi liquid. *Sov. Phys. JETP*, 8(1):70, 1959.

[25] S Tomonaga. Elementary theory of quantum-mechanical collective motion of particles, i. *Progress of Theoretical Physics*, 13(5):467–481, 1955.

[26] JM Luttinger. *J. Math. Phys.*, 4:1154, 1963.

[27] JM Luttinger. Analytic properties of single-particle propagators for many-fermion systems. *Physical Review*, 121(4):942, 1961.

[28] FDM Haldane. Luttinger liquid theory'of one-dimensional quantum fluids. i. properties of the luttinger model and their extension to the general 1d interacting spinless fermi gas. *Journal of Physics C: Solid State Physics*, 14(19):2585, 1981.

[29] Heinz J Schulz, Gianaurelio Cuniberti, and Pierbiagio Pieri. Fermi liquids and luttinger liquids. In *Field theories for low-dimensional condensed matter systems*, pages 9–81. Springer, 2000.

[30] Johannes Voit. One-dimensional fermi liquids. *Reports on Progress in Physics*, 58(9):977, 1995.

[31] Xiao-Gang Wen. Chiral luttinger liquid and the edge excitations in the fractional quantum hall states. *Physical Review B*, 41(18):12838, 1990.

[32] Yang Ji, Yunchul Chung, D Sprinzak, M Heiblum, D Mahalu, and Hadas Shtrikman. An electronic mach–zehnder interferometer. *Nature*, 422(6930):415, 2003.

[33] Preden Roulleau, F Portier, P Roche, A Cavanna, G Faini, U Gennser, and D Mailly. Direct measurement of the coherence length of edge states in the integer quantum hall regime. *Phys. Rev. Lett.*, 100(12):126802, 2008.

[34] Preden Roulleau, F Portier, DC Glattli, P Roche, A Cavanna, G Faini, U Gennser, and D Mailly. Finite bias visibility of the electronic mach-zehnder interferometer. *Physical Review B*, 76(16):161309, 2007.

[35] I Neder, M Heiblum, Y Levinson, D Mahalu, and V Umansky. Unexpected behavior in a two-path electron interferometer. *Phys. Rev. Lett.*, 96(1):016804, 2006.

[36] LV Litvin, Andreas Helzel, H-P Tranitz, Werner Wegscheider, and Christoph Strunk. Edge-channel interference controlled by landau level filling. *Physical Review B*, 78(7):075303, 2008.

[37] Izhar Neder, Nissim Ofek, Y Chung, M Heiblum, D Mahalu, and V Umansky. Interference between two indistinguishable electrons from independent sources. *Nature*, 448(7151):333, 2007.

[38] P Roulleau, F Portier, P Roche, A Cavanna, G Faini, U Gennser, and D Mailly. Noise dephasing in edge states of the integer quantum hall regime. *Phys. Rev. Lett.*, 101(18):186803, 2008.

[39] PA Huynh, F Portier, H Le Sueur, G Faini, U Gennser, D Mailly, F Pierre, W Wegscheider, and P Roche. Quantum coherence engineering in the integer quantum hall regime. *Phys. Rev. Lett.*, 108(25):256802, 2012.

[40] Adrien Mahé, FD Parmentier, Erwann Bocquillon, J-M Berroir, DC Glattli, Takis Kontos, Bernard Plaçais, Gwendal Fève, A Cavanna, and Yong Jin. Current correlations of an on-demand single-electron emitter. *Physical Review B*, 82(20):201309, 2010.

[41] Erwann Bocquillon, Vincent Freulon, J-M Berroir, Pascal Degiovanni, Bernard Plaçais, A Cavanna, Yong Jin, and Gwendal Fève. Coherence and indistinguishability of single electrons emitted by independent sources. *Science*, 2013.

[42] Claire Wahl, Jérôme Rech, Thibaut Jonckheere, and Thierry Martin. Interactions and charge fractionalization in an electronic hong-ou-mandel interferometer. *Phys. Rev. Lett.*, 112(4):046802, 2014.

[43] A Marguerite, Ch Cabart, C Wahl, B Roussel, V Freulon, D Ferraro, Ch Grenier, J-M Berroir, B Plaçais, T Jonckheere, et al. Decoherence and relaxation of a single electron in a one-dimensional conductor. *Physical Review B*, 94(11):115311, 2016.

[44] Ivan P Levkivskyi and Eugene V Sukhorukov. Dephasing in the electronic mach-zehnder interferometer at filling factor $\nu = 2$. *Physical Review B*, 78(4):045322, 2008.

[45] Izhar Neder. Fractionalization noise in edge channels of integer quantum hall states. *Phys. Rev. Lett.*, 108(18):186404, 2012.

[46] E Berg, Y Oreg, E-A Kim, and F Von Oppen. Fractional charges on an integer quantum hall edge. *Phys. Rev. Lett.*, 102(23):236402, 2009.

[47] S Tewari, P Roulleau, C Grenier, Fabien Portier, A Cavanna, U Gennser, D Mailly, and P Roche. Robust quantum coherence above the fermi sea. *Physical Review B*, 93(3):035420, 2016.

[48] H Pothier, S Guéron, Norman O Birge, D Esteve, and MH Devoret. Energy distribution function of quasiparticles in mesoscopic wires. *Phys. Rev. Lett.*, 79(18):3490, 1997.

[49] Nadya Mason, Yung-Fu Chen, Travis Dirks, Gassem Al-Zoubi, and Norman Birge. Non-equilibrium tunneling spectroscopy in carbon nanotubes. In *APS Meeting Abstracts*, 2009.

[50] Clemens Rössler, Simon Burkhard, Tobias Krähenmann, Marc Röösli, Peter Märki, Julien Basset, Thomas Ihn, Klaus Ensslin, Christian Reichl, and Werner Wegscheider. Spectroscopy of equilibrium and nonequilibrium charge transfer in semiconductor quantum structures. *Physical Review B*, 90(8):081302, 2014.

[51] C Altimiras, H Le Sueur, U Gennser, A Cavanna, D Mailly, and F Pierre. Non-equilibrium edge-channel spectroscopy in the integer quantum hall regime. *Nature Physics*, 6(1):34, 2010.

[52] H Le Sueur, C Altimiras, U Gennser, A Cavanna, D Mailly, and F Pierre. Energy relaxation in the integer quantum hall regime. *Phys. Rev. Lett.*, 105(5):056803, 2010.

[53] C Altimiras, H Le Sueur, U Gennser, A Cavanna, D Mailly, and F Pierre. Tuning energy relaxation along quantum hall channels. *Phys. Rev. Lett.*, 105(22):226804, 2010.

[54] Anders Mathias Lunde, Simon E Nigg, and Markus Büttiker. Interaction-induced edge channel equilibration. *Physical Review B*, 81(4):041311, 2010.

[55] Pascal Degiovanni, Ch Grenier, Gwendal Fève, Carles Altimiras, Helene Le Sueur, and Frederic Pierre. Plasmon scattering approach to energy exchange and high-frequency noise in $\nu = 2$ quantum hall edge channels. *Physical Review B*, 81(12):121302, 2010.

[56] D Ferraro, B Roussel, Ch Cabart, E Thibierge, G Fève, Ch Grenier, and P Degiovanni. Real-time decoherence of landau and levitov quasiparticles in quantum hall edge channels. *Phys. Rev. Lett.*, 113(16):166403, 2014.

[57] Charles Grenier. *Electronic quantum optics*. Theses, Ecole normale supérieure de lyon - ENS LYON, June 2011.

[58] Ivan P Levkivskyi and Eugene V Sukhorukov. Energy relaxation at quantum hall edge. *Physical Review B*, 85(7):075309, 2012.

[59] Sadao Adachi. GaAs, AlAs, and $Al_xGa_{1-x}As$: Material parameters for use in research and device applications. *Journal of Applied Physics*, 58(3):R1–R29, 1985.

[60] Loren Pfeiffer, KW West, HL Stormer, and KWl Baldwin. Electron mobilities exceeding 10^7 cm^2/vs in modulation-doped GaAs. *Applied Physics Letters*, 55(18):1888–1890, 1989.

[61] Neil W Ashcroft and N David Mermin. Solid state physics (holt, rinehart and winston, new york, 1976). 403, 2005.

[62] Alexander Tzalenchuk, Samuel Lara-Avila, Alexei Kalaboukhov, Sara Paolillo, Mikael Syväjärvi, Rositza Yakimova, Olga Kazakova, TJBM Janssen, Vladimir Fal'Ko, and Sergey Kubatkin. Towards a quantum resistance standard based on epitaxial graphene. *Nature nanotechnology*, 5(3):186, 2010.

[63] David Ferry and Stephen Marshall Goodnick. *Transport in nanostructures*. Number 6. Cambridge university press, 1999.

[64] Daijiro Yoshioka. *The quantum Hall effect*, volume 133. Springer Science & Business Media, 2013.

[65] Steven M Girvin. The quantum hall effect: novel excitations and broken symmetries. In *Aspects topologiques de la physique en basse dimension. Topological aspects of low dimensional systems*, pages 53–175. Springer, 1999.

[66] Thierry Martin and Shechao Feng. Suppression of scattering in electron transport in mesoscopic quantum hall systems. *Phys. Rev. Lett.*, 64(16):1971, 1990.

[67] G Müller, Dieter Weiss, AV Khaetskii, K Von Klitzing, S Koch, H Nickel, W Schlapp, and R Lösch. Equilibration length of electrons in spin-polarized edge channels. *Physical Review B*, 45(7):3932, 1992.

[68] M Dobers, K v Klitzing, J Schneider, G Weimann, and K Ploog. Electrical detection of nuclear magnetic resonance in GaAs-$Al_xGa_{1-x}As$ heterostructures. *Phys. Rev. Lett.*, 61(14):1650, 1988.

[69] BE Kane, LN Pfeiffer, and KW West. Evidence for an electric-field-induced phase transition in a spin-polarized two-dimensional electron gas. *Physical Review B*, 46(11):7264, 1992.

[70] Keith R Wald, Leo P Kouwenhoven, Paul L McEuen, Nijs C van der Vaart, and CT Foxon. Local dynamic nuclear polarization using quantum point contacts. *Phys. Rev. Lett.*, 73(7):1011, 1994.

[71] R Landauer. R. landauer, ibm j. res. dev. 1, 223 (1957). *IBM J. Res. Dev.*, 1:223, 1957.

[72] Rolf Landauer. Electrical resistance of disordered one-dimensional lattices. *Philosophical magazine*, 21(172):863–867, 1970.

[73] M Büttiker, Y Imry, R Landauer, and S Pinhas. Generalized many-channel conductance formula with application to small rings. *Physical Review B*, 31(10):6207, 1985.

[74] M Büttiker. Four-terminal phase-coherent conductance. *Phys. Rev. Lett.*, 57(14):1761, 1986.

[75] M Buttiker. Symmetry of electrical conduction. *IBM Journal of Research and Development*, 32(3):317–334, 1988.

[76] R Landauer and Th Martin. Equilibrium and shot noise in mesoscopic systems. *Physica B: Condensed Matter*, 175(1-3):167–177, 1991.

[77] Markus Buttiker. Coherent and sequential tunneling in series barriers. *IBM Journal of Research and Development*, 32(1):63–75, 1988.

[78] D Sprinzak, E Buks, M Heiblum, and Hadas Shtrikman. Controlled dephasing of electrons via a phase sensitive detector. *Phys. Rev. Lett.*, 84(25):5820, 2000.

[79] Stefan Oberholzer, E Bieri, C Schönenberger, Marcella Giovannini, and Jérôme Faist. Positive cross correlations in a normal-conducting fermionic beam splitter. *Phys. Rev. Lett.*, 96(4):046804, 2006.

[80] P Roulleau, F Portier, P Roche, A Cavanna, G Faini, U Gennser, and D Mailly. Tuning decoherence with a voltage probe. *Phys. Rev. Lett.*, 102(23):236802, 2009.

[81] Supriyo Datta. Steady-state quantum kinetic equation. *Physical Review B*, 40(8):5830, 1989.

[82] Supriyo Datta. A simple kinetic equation for steady-state quantum transport. *Journal of Physics: Condensed Matter*, 2(40):8023, 1990.

[83] Shechao Feng. Quantum transport in the presence of phase-breaking scattering: generalized landauer formula. *Physica A: Statistical Mechanics and its Applications*, 168(1):439–446, 1990.

[84] Sébastien Jezouin, Z Iftikhar, A Anthore, FD Parmentier, U Gennser, A Cavanna, A Ouerghi, Ivan P Levkivskyi, E Idrisov, EV Sukhorukov, et al. Controlling charge quantization with quantum fluctuations. *Nature*, 536(7614):58, 2016.

[85] Hermann Grabert and Michel H Devoret. *Single charge tunneling: Coulomb blockade phenomena in nanostructures*, volume 294. Springer Science & Business Media, 2013.

[86] CWJ Beenakker. Theory of coulomb-blockade oscillations in the conductance of a quantum dot. *Physical Review B*, 44(4):1646, 1991.

[87] DV Averin, AN Korotkov, and KK Likharev. Theory of single-electron charging of quantum wells and dots. *Physical Review B*, 44(12):6199, 1991.

[88] LP Kouwenhoven, NC Van der Vaart, AT Johnson, W Kool, CJPM Harmans, JG Williamson, AAM Staring, and CT Foxon. Single electron charging effects in semiconductor quantum dots. *Zeitschrift für Physik B Condensed Matter*, 85(3):367–373, 1991.

[89] NC Van der Vaart, SF Godijn, Yu V Nazarov, CJPM Harmans, JE Mooij, LW Molenkamp, and CT Foxon. Resonant tunneling through two discrete energy states. *Phys. Rev. Lett.*, 74(23):4702, 1995.

[90] Frank Hohls, M Pepper, JP Griffiths, GAC Jones, and DA Ritchie. Ballistic electron spectroscopy. *Applied Physics Letters*, 89(21):212103, 2006.

[91] Daniela Pfannkuche and Sergio E Ulloa. Selection rules for transport excitation spectroscopy of few-electron quantum dots. *Phys. Rev. Lett.*, 74(7):1194, 1995.

[92] Edgar Bonet, Mandar M Deshmukh, and DC Ralph. Solving rate equations for electron tunneling via discrete quantum states. *Physical Review B*, 65(4):045317, 2002.

[93] DB Chklovskii, BI Shklovskii, and LI Glazman. Electrostatics of edge channels. *Physical Review B*, 46(7):4026, 1992.

[94] A Yacoby, HF Hess, TA Fulton, LN Pfeiffer, and KW West. Electrical imaging of the quantum hall state. *Solid state communications*, 111(1):1–13, 1999.

[95] E Ahlswede, P Weitz, J Weis, K Von Klitzing, and K Eberl. Hall potential profiles in the quantum hall regime measured by a scanning force microscope. *Physica B: Condensed Matter*, 298(1-4):562–566, 2001.

[96] E Ahlswede, J Weis, K v Klitzing, and K Eberl. Hall potential distribution in the quantum hall regime in the vicinity of a potential probe contact. *Physica E: Low-dimensional Systems and Nanostructures*, 12(1-4):165–168, 2002.

[97] Michael R Geller and Giovanni Vignale. Universal equilibrium currents in the quantum hall fluid. *Physical Review B*, 52(19):14137, 1995.

[98] Eduard V Devyatov. Edge states in the regimes of integer and fractional quantum hall effects. *Physics-Uspekhi*, 50(2):197, 2007.

[99] DJ Thouless. Edge voltages and distributed currents in the quantum hall effect. *Phys. Rev. Lett.*, 71(12):1879, 1993.

[100] IL Aleiner and LI Glazman. Novel edge excitations of two-dimensional electron liquid in a magnetic field. *Phys. Rev. Lett.*, 72(18):2935, 1994.

[101] RC Ashoori, HL Stormer, LN Pfeiffer, KW Baldwin, and K West. Edge magnetoplasmons in the time domain. *Physical Review B*, 45(7):3894, 1992.

[102] NB Zhitenev, RJ Haug, K v Klitzing, and K Eberl. Time-resolved measurements of transport in edge channels. *Phys. Rev. Lett.*, 71(14):2292, 1993.

[103] G Ernst, RJ Haug, J Kuhl, KV von Klitzing, and K Eberl. Acoustic edge modes of the degenerate two-dimensional electron gas studied by time-resolved magnetotransport measurements. *Phys. Rev. Lett.*, 77(20):4245, 1996.

[104] Hiroshi Kamata, Takeshi Ota, Koji Muraki, and Toshimasa Fujisawa. Voltage-controlled group velocity of edge magnetoplasmon in the quantum hall regime. *Physical Review B*, 81(8):085329, 2010.

[105] T H Hansson. *Fermi and Luttinger liquids*. Lecture notes for the 2011 Nordita winter school, 2011.

[106] Daniel C Mattis and Elliott H Lieb. Exact solution of a many-fermion system and its associated boson field. *Journal of Mathematical physics*, 6(2):304–312, 1965.

[107] Yaroslav Tserkovnyak, Bertrand I Halperin, Ophir M Auslaender, and Amir Yacoby. Interference and zero-bias anomaly in tunneling between luttinger-liquid wires. *Physical Review B*, 68(12):125312, 2003.

[108] OM Auslaender, H Steinberg, A Yacoby, Y Tserkovnyak, BI Halperin, KW Baldwin, LN Pfeiffer, and KW West. Spin-charge separation and localization in one dimension. *Science*, 308(5718):88–92, 2005.

[109] Seigo Tarucha, Takashi Honda, and Tadashi Saku. Reduction of quantized conductance at low temperatures observed in 2 to 10 μm-long quantum wires. *Solid state communications*, 94(6):413–418, 1995.

[110] Thierry Giamarchi. *Quantum physics in one dimension*, volume 121. Oxford university press, 2004.

[111] Marc Bockrath, David H Cobden, Jia Lu, Andrew G Rinzler, Richard E Smalley, Leon Balents, and Paul L McEuen. Luttinger-liquid behaviour in carbon nanotubes. *Nature*, 397(6720):598, 1999.

[112] M Grayson, DC Tsui, LN Pfeiffer, KW West, and AM Chang. Continuum of chiral luttinger liquids at the fractional quantum hall edge. *Phys. Rev. Lett.*, 80(5):1062, 1998.

[113] Xiao-Gang Wen. Gapless boundary excitations in the quantum hall states and in the chiral spin states. *Physical Review B*, 43(13):11025, 1991.

[114] Erwann Bocquillon, Vincent Freulon, François D Parmentier, Jean-Marc Berroir, Bernard Plaçais, Claire Wahl, Jérome Rech, Thibaut Jonckheere, Thierry Martin, Charles Grenier, et al. Electron quantum optics in ballistic chiral conductors. *Annalen der Physik*, 526(1-2):1–30, 2014.

[115] Pascal Degiovanni, Ch Grenier, and Gwendal Fève. Decoherence and relaxation of single-electron excitations in quantum hall edge channels. *Physical Review B*, 80(24):241307, 2009.

[116] Charles Grenier, Rémy Hervé, Gwendal Fève, and Pascal Degiovanni. Electron quantum optics in quantum hall edge channels. *Modern Physics Letters B*, 25(12n13):1053–1073, 2011.

[117] Erwann Bocquillon, Vincent Freulon, P Degiovanni, B Plaçais, A Cavanna, Y Jin, G Fève, et al. Separation of neutral and charge modes in one-dimensional chiral edge channels. *Nature communications*, 4:1839, 2013.

[118] Hiroyuki Inoue, Anna Grivnin, Nissim Ofek, Izhar Neder, Moty Heiblum, Vladimir Umansky, and Diana Mahalu. Charge fractionalization in the integer quantum hall effect. *Phys. Rev. Lett.*, 112(16):166801, 2014.

[119] Kosuke Itoh, Ryo Nakazawa, Tomoaki Ota, Masayuki Hashisaka, Koji Muraki, and Toshimasa Fujisawa. Signatures of a nonthermal metastable state in copropagating quantum hall edge channels. *Phys. Rev. Lett.*, 120(19):197701, 2018.

[120] AS Goremykina and EV Sukhorukov. Fermi-edge singularity and related interaction induced phenomena in multilevel quantum dots. *Physical Review B*, 95(15):155419, 2017.

[121] Tobias Krähenmann, Livio Ciorciaro, Christian Reichl, Werner Wegscheider, Leonid Glazman, Thomas Ihn, and Klaus Ensslin. Fermi edge singularities

in transport through lateral GaAs quantum dots. *New Journal of Physics*, 19(2):023009, 2017.

[122] EB Foxman, U Meirav, PL McEuen, MA Kastner, O Klein, PA Belk, DM Abusch, and SJ Wind. Crossover from single-level to multilevel transport in artificial atoms. *Physical Review B*, 50(19):14193, 1994.

[123] P Torresani, MJ Martínez-Pérez, S Gasparinetti, J Renard, G Biasiol, L Sorba, F Giazotto, and S De Franceschi. Nongalvanic primary thermometry of a two-dimensional electron gas. *Physical Review B*, 88(24):245304, 2013.

[124] HL Edwards, Q Niu, and AL De Lozanne. A quantum-dot refrigerator. *Applied Physics Letters*, 63(13):1815–1817, 1993.

[125] HL Edwards, Q Niu, GA Georgakis, and AL De Lozanne. Cryogenic cooling using tunneling structures with sharp energy features. *Physical Review B*, 52(8):5714, 1995.

[126] JR Prance, CG Smith, JP Griffiths, SJ Chorley, D Anderson, GAC Jones, I Farrer, and DA Ritchie. Electronic refrigeration of a two-dimensional electron gas. *Phys. Rev. Lett.*, 102(14):146602, 2009.

[127] Carles Altimiras. *Inelastic mechanisms in mesocopic circuits realized in two dimensional electron gases*. Theses, Université Paris 11, October 2010.

Relax Team. Ramiro Rodriguez, François Parmentier, Patrice Roche.

Arg Team. Sofia, Raul, Ayelen, Ramiro, Mery, Matias.

université PARIS-SACLAY
ÉCOLE DOCTORALE
Physique en île-de-France (EDPIF)

Titre: Relaxation en énergie d'électrons émis au-dessus de la mer de Fermi d'un canal de bord de l'effet Hall quantique

Mots clés: Relaxation, Spectroscopie, États de bord, L'effet Hall Quantique, Boite Quantiques

Résumé: Les canaux de bord unidimensionnels, chiraux et sans dissipation de l'effet Hall quantique forment l'analogue électrique des fibres optiques, permettant la réalisation d'expériences d'optique quantique électronique où l'on manipule de manière cohérente les trajectoires des paquets d'ondes électroniques. Une série récente de travaux expérimentaux et théoriques a mis en lumière de forts effets de décohérence et de relaxation en énergie provoqués par les interactions entre canaux de bord co-propageants. Dans cette thèse, nous étudions comment les électrons, injectés sur une fenêtre d'énergie étroite au-dessus de la mer de Fermi d'un canal de bord, perdent leur énergie alors qu'ils se propagent à l'échelle du micromètre. Pour ce faire, nous implémentons deux boites quantiques comme filtres d'énergie pour effectuer une spectroscopie à énergie résolue de la relaxation dans le régime de Hall quantique au facteur de remplissage deux. Nous avons observé une relaxation remarquable et démontré qu'elle peut être considérablement supprimée modifiant le couplage entre les canaux de bord.

Title: Relaxation of Quasiparticles Injected Above the Fermi Sea of a Quantum Hall Edge Channel

Keywords: Relaxation, Spectroscopy, Edge Channel, Quantum Hall Effect, Quantum Dots

Abstract: The one-dimensional, chiral and dissipationless edge channels of the quantum Hall effect form the electrical analogue of optical fibers, allowing the implementation of electron quantum optics experiments where one coherently manipulates the trajectories of electronic wave packets. A recent series of experimental and theoretical works have put into light strong effects of decoherence and energy relaxation caused by interactions between co-propagating edge channels. In this thesis we investigate how the electrons, injected on a narrow energy window above the Fermi Sea of an edge channel, lose the energy while they propagate in the micrometer scale. We implement two quantum dots as energy filters to perform an energy resolved spectroscopy of the relaxation in the quantum Hall regime at filling factor two. We observed a remarkable energy relaxation and also demonstrate that the relaxation can be considerably suppressed by tuning the coupling between edge channels.

Université Paris-Saclay
Espace Technologique / Immeuble Discovery
Route de l'Orme aux Merisiers RD 128 / 91190 Saint-Aubin, France